



University of Kentucky
UKnowledge

Theses and Dissertations--Physics and
Astronomy

Physics and Astronomy


2022

UNDERSTANDING THE PHYSICS OF GALAXY CLUSTERS OUT TO THEIR VIRIAL RADII AND BEYOND

Arnab Sarkar

University of Kentucky, arnab.sarkar@uky.edu

Author ORCID Identifier:

 <https://orcid.org/0000-0002-5222-1337>

Digital Object Identifier: <https://doi.org/10.13023/etd.2022.358>

[Right click to open a feedback form in a new tab to let us know how this document benefits you.](#)

Recommended Citation

Sarkar, Arnab, "UNDERSTANDING THE PHYSICS OF GALAXY CLUSTERS OUT TO THEIR VIRIAL RADII AND BEYOND" (2022). *Theses and Dissertations--Physics and Astronomy*. 102.
https://uknowledge.uky.edu/physastron_etds/102

This Doctoral Dissertation is brought to you for free and open access by the Physics and Astronomy at UKnowledge. It has been accepted for inclusion in Theses and Dissertations--Physics and Astronomy by an authorized administrator of UKnowledge. For more information, please contact UKnowledge@lsv.uky.edu.

STUDENT AGREEMENT:

I represent that my thesis or dissertation and abstract are my original work. Proper attribution has been given to all outside sources. I understand that I am solely responsible for obtaining any needed copyright permissions. I have obtained needed written permission statement(s) from the owner(s) of each third-party copyrighted matter to be included in my work, allowing electronic distribution (if such use is not permitted by the fair use doctrine) which will be submitted to UKnowledge as Additional File.

I hereby grant to The University of Kentucky and its agents the irrevocable, non-exclusive, and royalty-free license to archive and make accessible my work in whole or in part in all forms of media, now or hereafter known. I agree that the document mentioned above may be made available immediately for worldwide access unless an embargo applies.

I retain all other ownership rights to the copyright of my work. I also retain the right to use in future works (such as articles or books) all or part of my work. I understand that I am free to register the copyright to my work.

REVIEW, APPROVAL AND ACCEPTANCE

The document mentioned above has been reviewed and accepted by the student's advisor, on behalf of the advisory committee, and by the Director of Graduate Studies (DGS), on behalf of the program; we verify that this is the final, approved version of the student's thesis including all changes required by the advisory committee. The undersigned agree to abide by the statements above.

Arnab Sarkar, Student

Dr. Yuanyuan Su, Major Professor

Dr. Christopher Crawford, Director of Graduate Studies

UNDERSTANDING THE PHYSICS OF GALAXY CLUSTERS OUT TO THEIR
VIRIAL RADII AND BEYOND

DISSERTATION

A dissertation submitted in partial
fulfillment of the requirements for
the degree of Doctor of Philosophy
in the College of Arts and Sciences
at the University of Kentucky

By
Arnab Sarkar
Lexington, Kentucky

Advisors: Dr. Yuanyuan Su (University of Kentucky)
&
Dr. Scott W. Randall (Center for Astrophysics | Harvard & Smithsonian)
2022

Copyright© Arnab Sarkar 2022

<https://orcid.org/0000-0002-5222-1337>

ABSTRACT OF DISSERTATION

UNDERSTANDING THE PHYSICS OF GALAXY CLUSTERS OUT TO THEIR VIRIAL RADII AND BEYOND

In the hierarchical structure formation model, galaxy clusters grow and evolve via mergers and accretion from the surrounding cosmic web, leaving distinctive marks in the gas properties, metallicity, and dynamical state at the outskirts of clusters, which needs to be probed to better understand the growth of a cluster. I probed the gas properties of four nearby galaxy groups MKW4, Antlia, RXJ1159, and ESO3060170 out to their virial radii using deep *Suzaku* and mostly snapshot *Chandra* observations. I found the gas entropy profiles of MKW4 follow a power-law at its outskirts - as expected from purely gravitational structure formation model. I measured an enclosed baryon fraction of 11% at the outskirts of MKW4, remarkably smaller than the cosmic baryon fraction of 15%, suggesting galaxy groups due to their shallow gravitation potential are vulnerable to baryon loss. I measured the average Fe abundance of four groups at their outskirts, which is remarkably uniform and strikingly similar to that of massive clusters and fully consistent with the numerical predictions from the IllustrisTNG cosmological simulation. This result support an early-enrichment scenario among galactic systems over an order of magnitude in mass even before their formation. I also studied the gas dynamics of a early-stage merging galaxy cluster, Abell 98, using deep *Chandra* observations. I reported the first unambiguous detection of an axial merger shock, which unveils a critical epoch in the formation of a massive galaxy cluster when two subclusters are caught in the early phase of the merging process. I also detected X-ray emission from the the warm-hot intergalactic medium (WHIM) filament, lies between two subclusters of Abell 98.

KEYWORDS: X-ray observations, Galaxy clusters, Intra-cluster medium

Arnab Sarkar

September 22, 2022

UNDERSTANDING THE PHYSICS OF GALAXY CLUSTERS OUT TO THEIR
VIRIAL RADII AND BEYOND

By
Arnab Sarkar

Dr. Yuanyuan Su (University
of Kentucky)

&

Dr. Scott W. Randall (Center
for Astrophysics | Harvard
& Smithsonian)

Director of Dissertation

Dr. Christopher Crawford

Director of Graduate Studies

September 22, 2022

Date

To my loving wife ...

ACKNOWLEDGMENTS

Foremost, I am beyond grateful to my advisors, Dr. Yuanyuan Su and Dr. Scott W. Randall, for their unwavering support and guidance over the past several years. Their patience, motivation, enthusiasm, and immense knowledge provided me with invaluable help both in my academic endeavors and as well as in my development as a scientist. They have my deepest gratitude for their countless hours of collaboration, instruction, and feedback - even in weekend days.

It is impossible to extend enough thanks to my family, especially my parents and my sister, who gave me the encouragement I needed throughout this process.

The highest form of thanks is owed to my incredible wife, Priyanka, for her unconditional love, endless support, and encouragement she has given me through the most difficult parts of my life. Thank you for always being by my side since our undergraduate days - for this I will be eternally grateful!

I would also like to mention my cat, Mithai, for all the entertainment and emotional support!

CONTENTS

Acknowledgments	iii
List of Tables	vii
List of Figures	viii
Chapter 1 Introduction	1
1.1 Why X-ray?	1
1.2 Telescopes	3
1.2.1 <i>Suzaku</i>	3
1.2.2 <i>Chandra</i>	5
Chapter 2 Joint <i>Suzaku</i> and <i>Chandra</i> observations of the MKW4 galaxy group out to the virial radius	7
2.1 Introduction	7
2.2 Observations and data reduction	8
2.2.1 <i>Suzaku</i>	9
2.2.2 <i>Chandra</i>	15
2.3 Results	15
2.3.1 Density and temperature profile	15
2.3.2 Entropy and pressure profile	18
2.3.3 Mass and gas fraction	20
2.4 Systematic uncertainties	22
2.5 Discussion	25
2.5.1 Entropy profile	25
2.5.2 Gas mass fraction	26
2.5.3 Azimuthal Scatter	29
2.6 Summary	30
Chapter 3 Chemical abundances in the outskirts of nearby galaxy groups mea- sured with joint <i>Suzaku</i> and <i>Chandra</i> observations	33
3.1 Introduction	33
3.2 Observations and Spectral analysis	36
3.3 Results	38
3.3.1 Fe abundance profiles	38
3.3.2 Chemical composition	41
3.3.3 Iron mass-to-light ratios	42
3.3.4 Supernovae yields	43
3.4 Systematic uncertainties	44
3.5 Discussion	44
3.5.1 Early enrichment scenario	44

3.5.2	Early enrichment population	45
3.5.3	Chemical composition of galaxy groups	46
3.6	Summary	46
Chapter 4	Discovery of a pre-merger shock in an intercluster filament in Abell 98	53
4.1	Introduction	53
4.2	Data analysis	54
4.2.1	Imaging analysis	54
4.2.2	Spectral analysis	57
4.3	Detection of Filament emission	57
4.4	Discussion and Conclusion	60
4.4.1	Nature of the shock front	60
4.4.2	Electron-ion equilibrium	61
4.4.3	Filament emission	61
Chapter 5	Gas sloshing and cold fronts in pre-merging galaxy cluster Abell 98	66
5.1	Introduction	66
5.2	Data preparation	67
5.3	Imaging analysis	69
5.3.1	A98N	69
5.3.2	A98S	71
5.4	Spectral analysis	74
5.4.1	Global ICM properties	74
5.4.2	Temperature map	76
5.4.3	A98N: East and North cold fronts	77
5.4.4	A98S: cold front, tail, and western SB edge	77
5.5	Summary	80
Chapter 6	Improved Fe II emission line models for AGN using new atomic datasets	82
6.1	Introduction	82
6.2	Basic ingredients	84
6.2.1	Fe II atomic datasets	84
6.2.2	AGN SEDs	87
6.3	Applications	89
6.3.1	Modelling of the BLR cloud	89
6.3.2	The effects of microturbulence	92
6.3.3	Fe II/Mg II ratio	93
6.3.4	Eigenvector 1	96
6.4	Summary	98
Chapter 7	Conclusions	100
Bibliography	102

Vita 129

LIST OF TABLES

2.1	Observational log	9
2.2	X-ray background components of outer regions ^a	14
2.3	Properties of MKW4	22
2.4	Comparison of our results with other works	23
2.5	Systematic error of gas properties at R_{200}	24
3.1	Observational log	35
3.2	Properties of the groups	36
4.1	<i>Chandra</i> observation log	63
5.1	<i>Chandra</i> observation log	67
6.1	Solar abundances used in CLOUDY	85

LIST OF FIGURES

1.1	Artistic diagram of Bremsstrahlung radiation in the ICM, where X-ray photons are emitted due to the acceleration of electrons caused by ions. Figure is taken from wikipedia.	2
1.2	Fully integrated <i>Suzaku</i> satellite before launch.	3
1.3	A photo of one of the four XIS camera onboard <i>Suzaku</i>	4
1.4	Assembly of the <i>Chandra</i> telescope.	5
1.5	Advanced CCD Imaging Spectrometer (ACIS) onboard <i>Chandra</i>	5
2.1	Left: <i>Suzaku</i> mosaic image of MKW4 in the 0.5-2 keV energy band with NXB subtracted and exposure corrected. Green annuli represent the regions used for spectra extraction. Magenta circle indicates $R_{200} = 33.2'$ (884 kpc). Right: <i>Chandra</i> mosaic image of MKW4 center (ACIS-S3) and three outer regions (ACIS-I) in the 0.5-2.0 keV energy band. The image of MKW4 is smoothed with a Gaussian kernel and a number of radii of 30. Blue boxes represent the <i>Suzaku</i> FOV. Green elliptical regions are the resolved point sources. Magenta circle indicates R_{200}	9
2.2	Surface brightness profiles of MKW4 derived from the <i>Suzaku</i> XIS image in the 0.5 - 2.0 keV energy band in three different directions. The profiles have been corrected for exposure, instrumental background (NXB), and the point sources detected with <i>Chandra</i> . Black solid line is the best-fit β -profile.	11
2.3	<i>Suzaku</i> XIS 1 spectra of MKW4 for representative regions of central and two outer bins in north and east directions. Black dots are the data points. Cyan, red, black, green, and yellow lines are the best-fit ICM emission, resolved CXB, unresolved CXB, MW, and LHB components, respectively. Magenta line is the model of the best-fit ICM emission and X-ray background components together.	12
2.4	Left: Triangle down: surface brightness of point sources resolved by <i>Chandra</i> . Triangle up: surface brightness of point sources obtained from mock <i>Suzaku</i> sky. Magenta dotted: total surface brightness limit of resolved+unresolved point sources taken from Moretti et al. (2009). Cyan dashed: expected surface brightness limit of unresolved point sources with 1σ error (shaded) calculated using Equations 2.3 and 2.4. Star: estimated surface brightness of unresolved point sources from <i>Suzaku</i> fitting. Right: Blue: spectroscopic temperature profile of MKW4 in the north-east direction obtained from spectral fitting of the <i>Suzaku</i> data only. Red: same profile obtained from the joint fitting of <i>Suzaku</i> and <i>Chandra</i> data. Magenta dashed line indicates R_{200} of MKW4.	13

2.5	Deprojected density profiles of MKW4 in north (orange), east (blue), and north-east (green) directions. Shaded regions indicate 1σ uncertainties. Red triangles: the best-fit normalizations for the <code>apec</code> thermal component obtained from spectral analysis. Black triangles: the normalizations of the <code>apec</code> thermal component calculated from the resulting 3D density profile.	16
2.6	Deprojected temperature profiles of MKW4 in north (orange), east (blue), and north-east (green) directions. The 2D temperature profiles of MKW4, estimated using Equation 2.6, are indicated in black. Shaded regions indicate 1σ uncertainties. Temperatures obtained from the <code>apec</code> thermal component by fitting the spectra extracted from the <i>Chandra</i> and <i>Suzaku</i> data are shown in yellow and red respectively. Magenta and cyan dashed lines show the average temperature profiles derived for groups in Loken et al. (2002) and Sun et al. (2009) respectively.	16
2.7	3D density (left) and temperature (right) profiles of MKW4 in three different directions.	17
2.8	3D entropy profiles of MKW4 in north (orange), east (blue), and north-east (green) directions. Shaded regions indicate 1σ uncertainties. Magenta dashed line represents the entropy profile derived from gravity only cosmological simulation (Voit et al., 2005) using Equation 2.10.	19
2.9	3D pressure profiles of MKW4 in north (orange), east (blue), and north-east (green) directions. Shaded regions indicate 1σ uncertainties. Magenta dashed line represents the semi-analytical universal pressure profile (Arnaud et al., 2010), derived using Equation 2.13.	19
2.10	The X-ray hydrostatic mass profile (M_{total}) of MKW4 derived using Equation 2.14. Red dashed line shows best-fit NFW mass profile obtained by integrating Equation 2.16. Shaded region indicates 1σ error.	21
2.11	The gas mass fraction of MKW4 in north (orange), east (blue), and north-east (green) directions. Red dashed line: cosmic baryon fraction estimated by <i>Planck</i> (Planck Collaboration et al., 2014). Magenta dashed line: cosmic baryon fraction estimated by <i>WMAP</i> (Komatsu et al., 2011).	23
2.12	Orange: The entropy profile of MKW4 in north direction with 1σ error. Red: The baseline entropy profile estimated using Equation 2.10. Magenta: The entropy profile scaled with f_{gas} as shown in Equation 2.17.	27

- 2.13 The f_{gas} is plotted with the cluster temperature at R_{200} . Open circles represent f_{gas} obtained using *Suzaku* only and filled circles represent f_{gas} obtained using *XMM-Newton* + *Planck* or *Suzaku* + *Chandra*. Color codes for different clusters are shown in the plot. The f_{gas} for A1644, A1795, A2029, A2142, A2255, A2319, A3158, A644, and A85 are taken from Eckert et al. (2019). We obtain f_{gas} of PKS0745-191 from Walker et al. (2012), RX J1159+5531 from Su et al. (2015), UGC 03957 from Thölken et al. (2016), Coma from Mirakhor and Walker (2020a), Perseus from Simionescu et al. (2011), Antlia from Wong et al. (2016), Virgo from Simionescu et al. (2017), A2199 from Mirakhor and Walker (2020b), Centaurus from Walker et al. (2013), and ESO 3060170 from Su et al. (2013). Red and magenta dashed lines shows cosmic baryon fraction estimated using *Planck* (Planck Collaboration et al., 2014) and *WMAP* (Komatsu et al., 2011) respectively. 28
- 2.14 Azimuthal scatter of gas properties at R_{200} of MKW4. We compare our results with azimuthal variations in other clusters, e.g., A1246: Sato et al. (2014); A1689: Kawaharada et al. (2010); A1835: Ichikawa et al. (2013); A2744: Ibaraki et al. (2014); PKS0745-191: George et al. (2009); RJX1159+5531: Su et al. (2015); Coma: Simionescu et al. (2013); Perseus: Urban et al. (2014). Dashed brown line: the azimuthal variation in relaxed simulated clusters from Vazza et al. (2011). Dotted brown line: the azimuthal variation in perturbed simulated clusters from Vazza et al. (2011). 31
- 3.1 Left: Fe profiles obtained from the 2T *vaptec* model. All abundances are in the solar unit. We assume a solar abundance table of Asplund et al. (2009). Yellow shaded region represents the measurement of Fe abundance in 10 massive clusters (Urban et al., 2017). Black shaded region shows average Fe abundance profile with 16–84 percentile error, obtained from 41 galaxy groups in TNG100. Right: Iron abundances at $R > 0.25R_{200}$ of individual groups. The red shaded region indicates average iron abundance for $0.25-1.0R_{200}$ with 1σ uncertainty. The black shaded region represents average iron abundance at $R > 0.25R_{200}$ for 41 galaxy groups in TNG100. Open circles represent Fe abundance at R_{200} of Antlia and MKW4, measured jointly. 37
- 3.2 X/Fe ratios as a function of radius for individual metals. The red shaded region represents the average X/Fe excluding central $R < 0.25R_{200}$ region. The blue shaded region represents the average X/Fe for the central $R < 0.25R_{200}$ region. Black shaded region shows the average X/Fe profile of 41 galaxy groups in TNG100. 40

3.3	<p><i>Left:</i> Radial profiles of IMLR with K_s-band luminosity for groups in our sample and the Perseus cluster. We obtain IMLR of Perseus from Matsushita et al. (2013). <i>Right:</i> The averaged f_{SNIa} for the four groups at $R < 0.25R_{200}$ and $0.25R_{200} < R < R_{200}$. Green shaded region represents the measurement scatter obtained from a large number of groups (Mernier et al., 2017). Yellow shaded region indicates the limit of f_{SNIa} at the massive cluster core (de Plaa et al., 2007). Vertical dotted line indicates $0.25R_{200}$.</p>	41
3.4	<p><i>Left:</i> Effective Fe yield as a function of cluster/group mass within R_{500}. Circles represent Fe yield for the cluster in the sample of Ghizzardi et al. (2021), squares represent the groups in the sample of Renzini and Andreon (2014), triangles represent NGC 1550, Hydra A, and Coma in the sample of Sasaki et al. (2014). Yellow shaded region shows the expected value estimated from the SN yields derived from Maoz and Graur (2017) and Renzini and Andreon (2014). The brown shaded region shows the expected value calculated assuming higher SNIa rate from Freundlich and Maoz (2021). <i>Right:</i> Effective Fe yield as a function of cluster/group mass within R_{200}.</p>	42
3.5	<p>Top left: NXB subtracted and exposure corrected mosaic <i>Suzaku</i> image of MWK4 in the 0.5-2 keV energy band. Magenta circle indicates R_{200}. Green annuli represent the regions used for spectra extraction. Top right: mosaic <i>Chandra</i> image of MKW4 in the 0.5-7.0 keV energy band. The resolved point sources are marked in green elliptical regions. Middle and Bottom: radial profiles of different elements from the group center to the outskirts. Vertical dotted line indicate $0.25R_{200}$.</p>	47
3.6	<p>Antlia; same as Figure 3.5.</p>	48
3.7	<p>RXJ 1159; same as Figure 3.5.</p>	49
3.8	<p>ESO 3060170; same as Figure 3.5</p>	50
3.9	<p>Best-fit results of the spectral analysis for the outermost regions of four groups. We show only XIS1 spectra. Red, black, cyan, green, yellow colored lines indicate best-fit resolved CXB, unresolved CXB, ICM emission, GH, LHB components, respectively. Blue line shows the best-fit ICM emission and X-ray background together. <i>Top panel:</i> Black data points are for MKW4. Orange data points are for Antlia. Solid line represents MKW4 and dashed line represents Antlia. <i>Bottom panel:</i> spectra for RXJ1159 and ESO3060170.</p>	51
4.1	<p><i>Chandra</i> exposure corrected and background subtracted image of A98 in the 0.5–2 keV energy band. White and cyan regions are used for the analysis of the filament emission. Centers of A98N and A98S are marked in black.</p>	55

4.2	<p><i>Top-left:</i> Similar to Figure 4.1 but zoom in to A98N and smoothed with $\sigma=2''$ Gaussian. Green regions used for spectral analysis. <i>Top-right:</i> GGM image of A98N with $\sigma=16''$ Gaussian kernel. White dashed curve shows southern shock front. <i>Middle left:</i> surface brightness profile of A98N in south direction with $1-\sigma$ errorbars. Inset figure shows the 3D density profile. <i>Middle-right:</i> projected temperature, <i>bottom-left:</i> 3D density, <i>bottom-right:</i> pressure profiles of A98N in south direction.</p>	56
4.3	<p><i>left:</i> Black shows the surface brightness profile across the bridge measured using <i>Chandra</i>. Red indicates the sum of the surface brightness profiles of the diffuse, extended emission extracted from the <i>Suzaku</i> observations. Blue represents the residual filament emission. <i>Right:</i> projected temperature profile across the bridge, measured with a 1-T model. Red and green shaded regions indicate the hot component and cool component temperatures, respectively, measured with a 2-T model.</p>	58
4.4	<p>Comparison of the temperature profile across the shock front with the predicted electron temperature profiles based on instant collisionless model (red) and Coulomb collisional model (blue). Yellow ellipse indicates the relevant post-shock electron temperature for comparing with two models.</p>	59
5.1	<p>Merged, exposure corrected, and background subtracted <i>Chandra</i> ACIS-I image of northern (A98N) and central (A98S) sub-clusters of A98 in the 0.5–2.0 energy band. The image has been smoothed with a $\sigma=2''$ Gaussian kernel. The dual structure of A98S is clearly visible. Yellow circles represent the regions used for the measurement of global ICM properties of both sub-clusters.</p>	68
5.2	<p><i>Left:</i> Residual image of A98N in the 0.5-2 keV energy band obtained after subtracting azimuthal averaged surface brightness profile from the Figure 5.1. The image has been smoothed with a $1.5''$ Gaussian kernel. A spiral pattern can clearly be seen travelling clock-wise if traced inward. Green sectors are used for spectral analysis. <i>Right:</i> Gaussian gradient magnitude filtered image of A98N smoothed by $\sigma = 8$ pixels and each pixel = $0.492''$. The north and east cold fronts are marked by white arrow.</p>	70
5.3	<p><i>Left:</i> Northern sector surface brightness profile of A98N in the 0.5 - 2 keV energy band fitted with a broken power-law model. The best-fit deprojected density profile is shown in inset figure. All error bars are at $1-\sigma$ level. <i>Right:</i> similar to the <i>left</i> figure, but for eastern sector.</p>	72
5.4	<p><i>Left:</i> Unsharp-masked image of A98Sa and A98Sb created by subtracting images smoothed by 2D Gaussians with $\sigma = 2''$ and $20''$. Green regions are used for the spectral analysis. The ‘tail’ is marked with magenta arrow. <i>Right:</i> Gaussian gradient magnitude filtered image of A98S. The image is smoothed by $\sigma = 13''$. A sharp gradient is clearly visible to SW of the A98Sa and marked by white curve. Green sectors are used for spectral analysis.</p>	73

5.5	Residual image of excess X-ray emission of A98Sa and A98Sb with 1.4 GHz radio contours overlaid in green. The image was created by subtracting two 2D elliptical β -models from an unbinned image with point sources excluded. White, yellow, black arrows indicate the spiral structure, the bifurcation of spiral pattern, and the ‘tail’ of X-ray emission, respectively.	74
5.6	<i>Left:</i> Azimuthal surface brightness profile in the 0.5 - 2 keV energy band centered on the A98Sa core. Black represents the surface brightness at individual angles and red represents the binned surface brightness in 90° sectors. The north and south sectors contain the northern and southern lobe of the WAT. East sector contains the second BCG, A98Sb. <i>Right:</i> Eastern sector (as shown in Figure 5.4) surface brightness profile of A98Sb in the 0.5 - 2 keV energy band fitted with a broken power-law model. Deprojected density profile is shown in inset figure.	75
5.7	Projected temperature map of A98N/A98S. Units are in keV. The individual sub-cluster centers are marked by white crosses. The warmer gas ‘arc’ can be seen to the south of A98N. A98N and A98Sb have cool central cores, whereas A98Sa has a warmer, roughly isothermal core.	76
5.8	<i>Top panel:</i> Northern sector projected temperature, deprojected electron density, and projected electron pressure profiles centered on the A98N core. The metallicity was fixed to 0.4 Z_{\odot} . The projected pressure profile was estimated using the deprojected densities and projected temperatures. Vertical dashed line represents the position of the surface brightness edges. <i>Bottom panel:</i> similar as above but for eastern sector.	78
5.9	Eastern sector projected temperature, deprojected electron density, and projected electron pressure profiles centered on the A98Sb core. The metallicity was fixed to 0.4 Z_{\odot} . The projected pressure profile was estimated using the deprojected densities and projected temperatures. Vertical dashed line represents the position of the surface brightness edge.	79
5.10	<i>Left:</i> western sector surface brightness profile of A98Sa in the 0.5-2 keV energy band fitted with a broken power-law model. Deprojected density profile is shown in inset figure. <i>Right:</i> western sector projected temperature profiles of A98Sa. Black and red represent the uncertainties estimated with 68% and 90% confidence level, respectively. The red data points are shifted to the right for the purpose of clarity and comparison. Vertical dashed line represents the position of the surface brightness edge.	80
6.1	Diagram showing the energy levels of various models of the Fe II atom. From left to right : dataset derived by Verner et al. (1999), Bautista et al. (2015), Tayal and Zatsarinny (2018), and Smyth et al. (2019). The horizontal dashed lines indicate the H I and Fe II ionization limits. The energy of the Ly α transition, an important source of photoexcitation of Fe II, is also indicated, along with the thermal energy corresponding to 10 ⁴ K.	86

6.2	Comparing different SEDs used in CLOUDY. Red dashed line: SED derived by Mathews and Ferland (1987). Blue dashed line: SED derived by Korista et al. (1997). Cyan solid line: Jin et al. (2012) SED.	87
6.3	Comparing CLOUDY predicted Fe II spectra in 0.1–0.58 μm wavelength band using three different Fe II datasets and a fixed SED (Jin et al., 2012). Red dotted line: Fe II spectra using Verner et al. (1999) dataset. Blue dashed line: Tayal and Zatsarinny (2018) dataset. Cyan solid line: Smyth et al. (2019) dataset. Ranges of y-axis are different in all sub-figures.	88
6.4	Comparing CLOUDY predicted Fe II spectra in 0.1–0.58 μm wavelength bands using three different AGN SEDs and a fixed Fe II dataset (Smyth et al., 2019). Red dotted line: Fe II spectra using Mathews and Ferland (1987) SED. Blue dashed line: Korista et al. (1997) SED. Cyan solid line: Jin et al. (2012) SED. Ranges of y-axis are different in all sub-figures. . .	89
6.5	Blue spectrum shows a typical Fe II spectra in UV using Smyth et al. (2019) dataset, Jin et al. (2012) SED. The Spikes and Gap are marked with vertical dashed lines.	89
6.6	Contour plot of the Spike/gap ratio and equivalent width (EW) derived from photoionization model using the Smyth et al. (2019) Fe II dataset and Jin et al. (2012) AGN SED. Left: Spike/gap ratio of the Fe II UV bump in the $n_{\text{H}} - \Phi$ plane. Right: EW of Fe II UV bump in the $n_{\text{H}} - \Phi$ plane. An axis indicating the distance of Fe II emitting cloud from the central black hole is also added.	90
6.7	Spike/gap ratio and EW of the Fe II emission in the UV as a function V_{turb} . Green line: the Spike/gap ratio and EW of Fe II UV bump corresponding to $V_{\text{turb}} = 100$ km/s. These values are consistent with observation. Any turbulence greater than 100 km/s will reproduce the observed Fe II emission.	93
6.8	Similar to Figure 6.6 except $V_{\text{turb}} = 100$ km/s. Large regions of parameter space reproduce the observed Spike/Gap ratio ~ 1.4 and $\text{EW} > 400\text{\AA}$ of the IZW 1 in the UV band.	94
6.9	<i>Left:</i> panel (a) shows a comparison between the observed Fe II UV template (Vestergaard and Wilkes, 2001) and the CLOUDY predicted Fe II UV spectrum with $V_{\text{turb}} = 0$ km/s. Panel (b) shows the same comparison with $V_{\text{turb}} = 100$ km/s. <i>Right:</i> panel (c) compares the Fe II optical template (Véron-Cetty et al., 2004) to the CLOUDY predicted spectrum with $V_{\text{turb}} = 0$ km/s. Panel (d) presents the same comparison except $V_{\text{turb}} = 100$ km/s. The turbulent model largely reproduces the template.	95
6.10	$I(\text{Fe II})/I(\text{Mg II})$ as a function of the Fe abundances. We show that the Fe II/Mg II ratio for two different UV bands – 2000 \AA - 3000 \AA and 2200 \AA - 3090 \AA band, as described in Verner et al. (2003) and De Rosa et al. (2011), respectively.	96

6.11 Panel (a) and (b): red circles show the EW of the Fe II UV bump and the Fe II optical band as a function of L/L_{Edd} respectively. Panel (c): red and blue triangles represent the $I(\text{Fe II})/I(\text{Mg II})$ and $I(\text{Fe II})(\text{UV})/I(\text{Fe II})(\text{Optical})$ as a function of L/L_{Edd} , respectively. For both plots we use our best obtained model parameters. Green circles and magenta squares are the observed $I(\text{Fe II})/I(\text{Mg II})$ ratios taken from De Rosa et al. (2011) and Shin et al. (2019) respectively. 97

Chapter 1 Introduction

Clusters of galaxies or galaxy clusters are the massive structures in our Universe that consist of hundreds if not thousands of galaxies bound together by gravity. They typically have masses between 10^{13} - $10^{15} M_{\odot}$. Thus, they are the largest gravitationally bound systems in our Universe. Galaxy clusters sit at the crossroads between cosmology and astrophysics and offer powerful probes of the expansion of the Universe and the growth of large-scale structures. According to the most successful structure formation models, the cosmological constant dominated cold dark matter models, structures form in our Universe through gravitational instabilities (citation). This model predicts that galaxy clusters form and grow hierarchically by the mergers and accretion of smaller groups and clusters.

Even though the name is “galaxy” cluster, galaxies only make up about 5% of the total mass of a cluster. Meanwhile, about 80% of the mass in a cluster comes from dark matter, which holds everything else together. One of the critical features of galaxy clusters is the intra-cluster medium (ICM) since it makes up 15% of the total mass, the second most massive contribution to cluster mass. ICM hosts most of the visible matter in the Universe in the form of hot, X-ray emitting plasma, which permeates much of the space between galaxies.

1.1 Why X-ray?

Due to their massive structures, the gas trapped inside galaxy clusters heats up to a temperature where the electrons have been stripped from their atoms, making ICM in the form of hot plasma. The typical ICM gas temperature lies in 10^6 - 10^8 K. At this temperature, ICM shines brightly in X-ray. Most X-ray emissions from the ICM arise in a physical process called Bremsstrahlung radiation - a type of electromagnetic radiation produced when a charged particle is accelerated caused by an electric field or another charged particle. The total power radiated in this process can be estimated by

$$P = \frac{q^2 \gamma^4}{6\pi \epsilon_0 c} \left(\vec{\dot{\beta}} \cdot \vec{\dot{\beta}} + \frac{(\vec{\beta} \cdot \vec{\dot{\beta}})^2}{1 - \beta^2} \right), \quad (1.1)$$

where, q is the charge of the accelerated particle, $\beta = \frac{\text{velocity of charged particle (v)}}{\text{speed of light (c)}}$, $\dot{\beta}$ is the time derivative of β , γ is the Lorentz factor, and ϵ_0 is the vacuum permittivity. In the ICM, the free electrons are accelerated by the ions in the plasma, which produces continuum X-ray photons, as seen in Figure 1.1. Since most of the electrons in the ICM follow Maxwellian velocity distribution, the X-ray emission from ICM refers to thermal Bremsstrahlung emission. X-ray emission from galaxy clusters also contain emission lines from partially ionized atoms, which can be used to probe the chemical composition, and certain physical properties of the ICM.

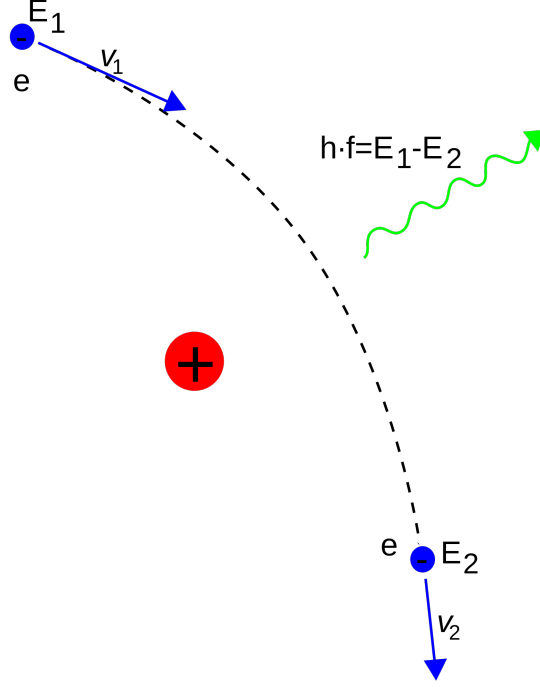


Figure 1.1: Artistic diagram of Bremsstrahlung radiation in the ICM, where X-ray photons are emitted due to the acceleration of electrons caused by ions. Figure is taken from wikipedia.

Using X-ray observations of galaxy clusters one can measure the flux density $F(x, y)$, as a function of direction, x , y , in the sky. The $F(x, y)$ is related to the X-ray emissivity, ϵ , as follows (Molnar, 2016)

$$F(x, y) = \frac{1}{4\pi D_L^2} \int_{\nu_1/(1+z)}^{\nu_2/(1+z)} \int_{z_1}^{z_2} \epsilon_\nu(\rho, T_g, Z_{ab}) dz' d\nu, \quad (1.2)$$

where D_L is the luminosity distance to the cluster at redshift z , $\rho(\mathbf{r})$, $T_g(\mathbf{r})$, and Z_{ab} are the gas density, temperature, and the abundance of heavy elements, respectively. The inner integral of Equation 1.2 is along the line of sight (along z axis) and the outer integral is over the observed frequency band. The emissivity, ϵ_ν , at a given frequency ν , depends on electron, and ion number densities and gas temperature as follows

$$\epsilon_\nu(\rho, T_g, Z_{ab}) = n_e \sum_{i,Z} n_{i,Z} \Lambda_\nu(T_e, Z_i), \quad (1.3)$$

where $n_e(\mathbf{r})$, $n_{i,Z}(\mathbf{r})$, and $\Lambda_\nu(T_e, Z_i)$ are the electron, ion number densities, and cooling function, respectively. In practice, one can assume a simple geometry for cluster, e.g., spherical or ellipsoidal, but such approximation breaks down for dynamically active clusters, which impacts significantly on the ICM properties. X-ray observations of ICM, therefore, provides plethora of information on gas properties (e.g., temperature, density), chemical composition, and the geometry of the cluster itself.

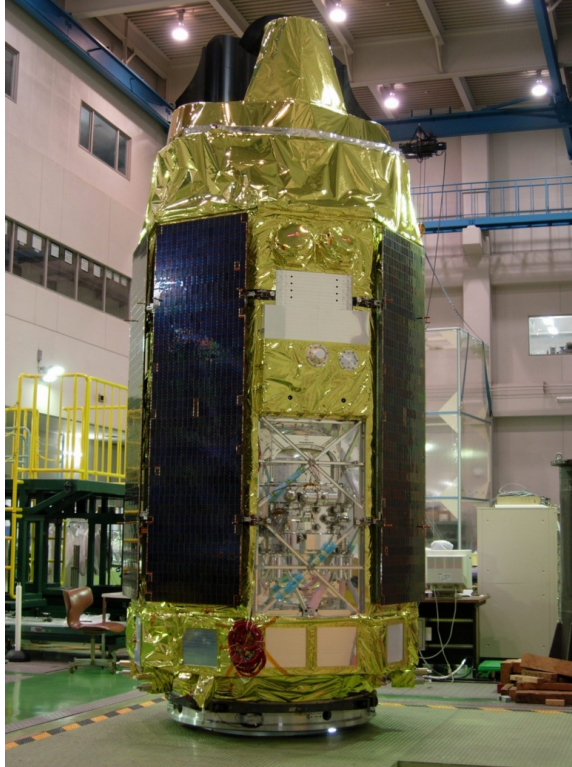


Figure 1.2: Fully integrated *Suzaku* satellite before launch.

1.2 Telescopes

X-rays from astrophysical sources can not reach Earth's surface since they are easily absorbed by the Earth's atmosphere. Earth's atmosphere contains water vapor, which is opaque to X-rays. This is good for all the life forms on the Earth, as large doses of X-rays are dangerous and can cause cell mutations. However, this also means it is impossible to observe X-rays from astrophysical sources with ground-based instruments. We must get into Earth's orbit to detect those X-rays coming from space. After decades long endeavors, On December 12, 1970, an X-ray satellite named X-ray Explorar was launched into a 500-mile high orbit from Earth's surface. Later, the X-ray Explorar was renamed Uhuru - a Swahili word that means "freedom". That was the beginning. In the last half of a century, several X-ray telescopes with advanced capabilities have been sent into Earth's orbit, which has led to exciting discoveries. For my thesis, I analyzed X-ray observations of ICM of several galaxy clusters/groups using two telescopes, *Suzaku* (now defunct) and *Chandra* (currently operating).

1.2.1 *Suzaku*

Suzaku (named after mythical Vermilion bird of the south) was developed jointly by JAXA (Japanese space agency) and NASA to probe high energy X-ray sources, as seen in Figure 1.2. It was launched on July 10, 2005 into a low earth orbit - 550 km from the earth surface. *Suzaku* carries four X-ray Imaging Spectrometers (XIS), one

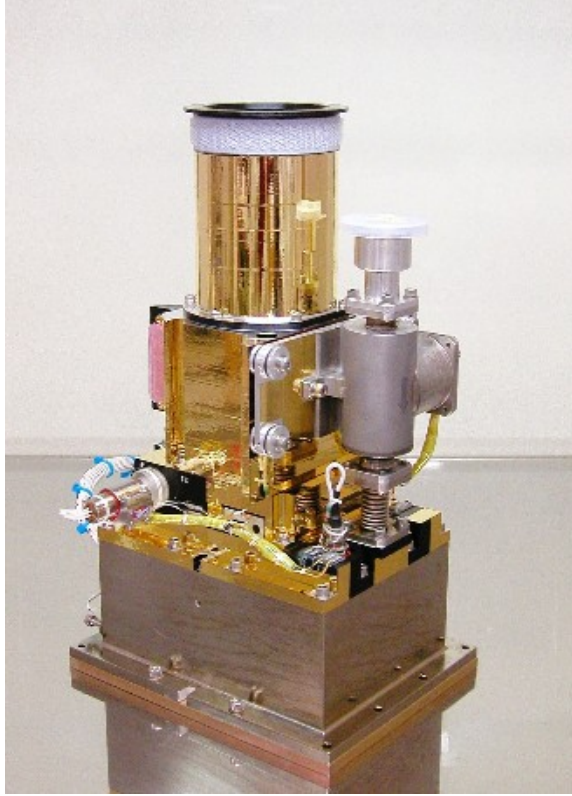


Figure 1.3: A photo of one of the four XIS camera onboard *Suzaku*.

high resolution X-ray Spectrometer (XRS), and one Hard X-ray Detector (HXD). The prime instrument on this mission, XRS, was inoperable due to a cryogen (coolant) loss on July 29, 2005. However, other two instruments were fully operable.

XIS consists of four charge coupled devices (CCD) X-ray imaging spectrometers - XIS0, 1, 2, and 3. Figure 1.3 shows a XIS camera onboard *Suzaku*. The XIS operates in photon-counting mode, in which X-ray event is discriminated from the others and its arrival time, position, and energy are recorded. They provide X-ray images of the source over an $18' \times 18'$ region in the energy range 0.4-10 keV with a typical energy resolution of 120 eV. For observing faint X-ray emission from ICM, I primarily use *Suzaku* XIS observation, as described in next chapters. X-ray observations of faint ICM greatly suffers from particle background - a type of X-ray emission caused by the interaction between the chemical composition of spacecraft body and highly energetic charged particles in solar flare and in cosmic rays. This type of background X-ray photons are very hard to distinguish from the actual X-ray photons that comes from astrophysics sources. Due to the low earth orbit of *Suzaku*, most of the highly energetic charged particles are shielded off by the earth atmosphere, only few reaching to the telescope. This greatly reduces the particle background. Also *Suzaku* has far better spectral sensitivity at ~ 1 keV than any of its predecessors, enabling us to precisely measure the gas properties and chemical composition of the ICM at the faintest part of the galaxy clusters.



Figure 1.4: Assembly of the *Chandra* telescope.

1.2.2 *Chandra*

Chandra X-ray observatory has been NASA's flagship mission for X-ray astronomy since its launch on July 23, 1999. Figure 1.4 shows the telescope assembly. It carries four major scientific instruments - a High Resolution Camera (HRC), one Advanced CCD Imaging Spectrometer (ACIS), two Transmission Grating Spectrometers. ACIS consists of an array of CCDs, as seen in Figure 1.5, are capable of producing high resolution X-ray images and as well as spectrum. With a angular resolution of $0.5''$, ACIS is about 100 times more sensitive to the faint X-ray sources and produces detailed image of the sources compared to any of the previous X-ray telescopes. It collects X-ray photons in a $18' \times 18'$ region over an energy range of 0.2-10 keV.

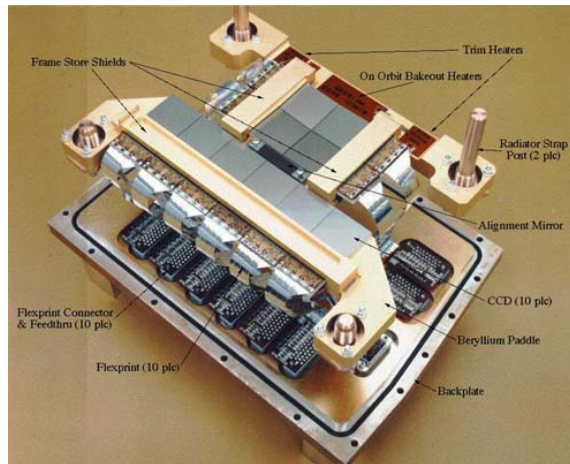


Figure 1.5: Advanced CCD Imaging Spectrometer (ACIS) onboard *Chandra*.

Due to its superb angular resolution, *Chandra* is extremely useful in analysing gas properties and gas dynamics in smaller scale with unprecedented details and in resolving Cosmic X-ray Background. Cosmic X-ray background (CXB) is a type of sky X-ray background emission from the distant AGNs, which dominates in 2-10 keV

energy range. Thus, one needs to carefully distinguish the CXB emission from the ICM emission, otherwise it causes large systematic uncertainties in the measuring the gas properties and chemical composition of the ICM. *Chandra*'s improved sensitivity than any of its predecessors makes possible to study black holes, supernovae, galaxy clusters in detail and advance our understanding of the origin, evolution, and destiny of our Universe.

Chapter 2 Joint *Suzaku* and *Chandra* observations of the MKW4 galaxy group out to the virial radius

2.1 Introduction

A significant fraction of all the baryons of the Universe, including more than half of the galaxies, reside in groups and low mass clusters (e.g., Eke et al., 2004; Springel and Hernquist, 2003). In the standard CDM structure formation model, clusters continue to grow and evolve through mergers and accretions, largely along cosmic filaments, in their outer regions (Walker et al., 2019). These processes may leave distinctive marks in the gas properties at cluster outskirts, including inhomogeneous gas density distributions, turbulent gas motions, and electrons that are not in thermodynamic equilibrium with the ions in the intra-cluster medium (ICM). Groups are expected to be more evolved than massive clusters, as their sound crossing times are short compared to the Hubble time ($0.1\text{--}0.5 H_0^{-1}$, Paul et al., 2017). However, due to their shallower gravitational potential wells, groups are more sensitive to non-gravitational processes, such as galactic winds, star formation, and feedback from active galactic nuclei (AGN, e.g., Lovisari et al., 2015; Pratt et al., 2010; Mathews and Guo, 2011; Humphrey et al., 2012; Thölken et al., 2016). Probing the gas properties of galaxy groups out to their virial radii thus provides a powerful approach to investigating their growth and evolution.

In galaxy cluster studies, entropy, as a function of radius, records the thermal history of the ICM (e.g., Borgani et al., 2005; McCarthy et al., 2010). Entropy is empirically defined as $K(r)=T/n_e^{2/3}$, where n_e and T are the electron density and gas temperature, respectively. A growing number of X-ray observations have been made for cluster outskirts (e.g., Simionescu et al., 2017; Ghirardini et al., 2018). The majority of these works study the properties of massive galaxy clusters ($T_X > 3$ keV), while there is a lack of detailed studies of the outskirts of galaxy groups. The studies of massive clusters have brought up unexpected results (e.g., Urban et al., 2014; Simionescu et al., 2017; Ghirardini et al., 2018) such as the flattening or even a drop of entropy profiles between R_{500}^\dagger and R_{200} relative to the expectation from numerical simulations of the gravitational collapse model (Voit et al., 2005). Several explanations have been proposed to explain the deviation of entropy profiles from the self-similar value, e.g., the breakdown of thermal equilibrium between electrons and protons (Akamatsu et al., 2011) or inhomogeneous gas density distribution (gas clumping) at cluster outskirts (Nagai and Lau, 2011). Accretion shocks at the cluster outskirts tend to heat the heavier ions faster than electrons, causing thermal non-equilibrium between electrons and ions and leading to a lower gas entropy (e.g., Akamatsu et al., 2011; Hoshino et al., 2010). Unresolved cool gas clumps were invoked by Simionescu et al. (2011) and Nagai and Lau (2011) to explain the observed entropy flattening, since the denser, cooler clumps have a higher emissivity than the

[†] r_Δ = radius from cluster core where matter density is Δ times the critical density of the Universe.

local ICM. The clumping factor is defined as

$$C = \frac{\langle n_e^2 \rangle}{\langle n_e \rangle^2}, \quad (2.1)$$

where n_e is the electron density. Simionescu et al. (2011) estimate a clumping factor of $C \approx 16$ for the Perseus cluster. Bonamente et al. (2013) and Walker et al. (2012) report $C \approx 7$ for Abell 1835 and $C \approx 9$ for PKS 0745-191, respectively. In contrast, a handful of observations have indicated that low mass clusters ($T_X < 3$ keV) show little to no flattening in their entropy profiles (e.g., RXJ1159, Su et al. 2015; A1750, Bulbul et al. 2016a; UGC 03957, Thölken et al. 2016), presumably because groups have lower clumping factors at their outskirts. Galaxy groups may provide essential constraints on whether their entropy profiles behave in a self-similar way compared to galaxy clusters.

MKW4 is a cool core cluster at $z \sim 0.02$ with a global temperature of 1.6 keV (Sun et al., 2009). It contains nearly 50 member galaxies, including NGC 4073, the brightest group galaxy (BGG). The NGC 4073 is about 1.5 times brighter than the second-brightest galaxy in the group (O’Sullivan et al., 2003). Unlike massive clusters, the outskirts of galaxy groups are relatively unexplored due to their low surface brightness. The typical ICM surface brightness in group outskirts falls below 20% of the total emission. The measurement of their gas properties is therefore extremely challenging. The now-defunct *Suzaku* X-ray telescope with its low particle background helped unravel this new frontier. However, *Suzaku* can only resolve point sources down to a flux level of 10^{-13} erg cm $^{-2}$ s $^{-1}$ due to its modest PSF ($\sim 3'$), which causes significant statistical and systematic uncertainties in the measurement of gas properties at the group outskirts. Thanks to the superb angular resolution of *Chandra*, even with the modest exposures it increases the number of detected point sources by 1 dex, which allows tighter constraints on the cosmic X-ray background (CXB) uncertainties (Miller et al., 2012).

We utilize deep *Suzaku* and snapshot *Chandra* observations to probe the thermal properties of MKW4 out to its virial radius in multiple directions, which we present in this paper. The metallicity distribution of MKW4 will be presented in a following paper. Using NASA/IPAC Extragalactic Database,[‡] we calculate a luminosity distance of 83 Mpc ($1'' = 0.443$ kpc) for $z = 0.02$, adopting a cosmology of $H_0 = 70$ km s $^{-1}$ Mpc $^{-1}$, $\Omega_\Lambda = 0.7$, and $\Omega_m = 0.3$. All reported uncertainties in this paper are at 1σ confidence level unless mentioned otherwise.

2.2 Observations and data reduction

MKW4 has been mapped with 6 *Suzaku* pointings from its center out to the virial radii in the north, east, and north-east directions, as shown in Figure 2.1. It has also been observed with a deep *Chandra* ACIS-S observation at its center and three snapshot *Chandra* ACIS-I observations overlapping with the three outer *Suzaku* pointings in three directions. Below we describe the data reduction processes and spectral fitting for each of the observations.

[‡]<http://ned.ipac.caltech.edu>

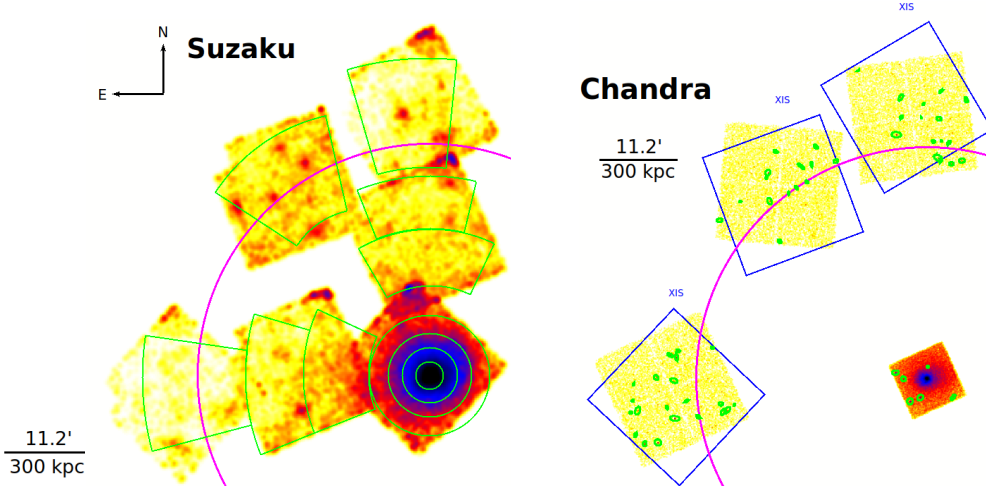


Figure 2.1: Left: *Suzaku* mosaic image of MWK4 in the 0.5-2 keV energy band with NXB subtracted and exposure corrected. Green annuli represent the regions used for spectra extraction. Magenta circle indicates $R_{200} = 33.2'$ (884 kpc). Right: *Chandra* mosaic image of MKW4 center (ACIS-S3) and three outer regions (ACIS-I) in the 0.5-2.0 keV energy band. The image of MKW4 is smoothed with a Gaussian kernel and a number of radii of 30. Blue boxes represent the *Suzaku* FOV. Green elliptical regions are the resolved point sources. Magenta circle indicates R_{200} .

Table 2.1: Observational log

Name	Obs Id	Instrument	Obs Date	Exposure time (ks)	RA ($^{\circ}$)	DEC ($^{\circ}$)	P.I.
<i>Suzaku</i> central	808066010	XIS0, XIS1, XIS3	2013 Dec 30	34.6	181.1346	1.9097	F. Gastaldello
<i>Suzaku</i> Offset 1	805081010	XIS0, XIS1, XIS3	2010 Nov 30	77.23	181.1270	2.2181	F. Gastaldello
<i>Suzaku</i> N2	808067010	XIS0, XIS1, XIS3	2010 Nov 30	97	181.1504	2.5206	Y. Su
<i>Suzaku</i> Offset 2	805082010	XIS0, XIS1, XIS3	2010 Nov 30	80	181.4270	1.8972	Y. Su
<i>Suzaku</i> E1	808065010	XIS0, XIS1, XIS3	2013 Dec 29	100	181.7142	1.8506	F. Gastaldello
<i>Suzaku</i> NE	809062010	XIS0, XIS1, XIS3	2013 Dec 29	87.5	181.4583	2.3361	Y. Su
<i>Chandra</i> central	3234	ACIS-S	2002 Nov 24	30	181.1283	1.9286	Y. Fukazawa
<i>Chandra</i> N	20593	ACIS-I	2019 Feb 25	14	181.1369	2.5209	Y. Su
<i>Chandra</i> E	20592	ACIS-I	2018 Nov 17	15	181.7146	1.8715	Y. Su
<i>Chandra</i> NE	20591	ACIS-I	2019 Mar 08	14	181.4548	2.3585	Y. Su

2.2.1 Suzaku

MKW4 has been mapped with three X-ray Imaging Spectrometer (XIS) instruments onboard *Suzaku* – two front-illuminated CCDs (XIS0, XIS3), and one back-illuminated CCD (XIS1). The observation logs are summarized in Table 4.1. All three XIS instruments were in the normal clocking mode without window and burst options during the observations.

Data reduction

The *Suzaku* data was reduced using HEASoft 6.25, CIAO 4.11, and the XIS calibration database (CALDB) version 20181010. We followed a standard data reduction thread

§ to process all the event files. The 5×5 mode event files were converted to the 3×3 mode event files and combined with the other 3×3 mode event files. The resulting event files were filtered for calibration source regions and bad pixels with `cleansis`. We selected events with GRADE 0, 2, 3, 4, and 6. Light curves were filtered for flares using the `lc_clean` task of CIAO 4.11. The resolved point sources were identified visually. We did not exclude those sources while extracting spectra, because exclusion would result in a very low photon count available for the spectral analysis. We instead took the advantage of *Chandra* observations to estimate their position, flux and incorporated them in the background fit (discussed in Section 3.2).

We extracted spectra from four concentric annuli, $0' - 2'$, $2' - 4'$, $4' - 6'$, and $6' - 8.6'$ for the central pointing. We extracted spectra from two partial annuli $12.4' - 29'$, $29' - 48.3'$ for the pointings in the north direction and from $8.6' - 26'$, $26' - 45'$ for the pointings in the east direction. For the north-east direction, we extracted spectra from a partial annulus of $27' - 42'$. All annuli had widths ranging from 8 kpc at the central region to 223 kpc at the outermost bin. We generated redistribution matrix files (RMF) for all regions and detectors using FTOOL `xisrmfgen` and instrumental background files (NXB) using FTOOL `xisnxbgen`. The ancillary response files (ARF) were generated using `xissimarfgen` by providing an appropriate β -image derived from the *Chandra* surface brightness profile of MKW4 at the central region. Another ARF was produced to model the X-ray background by considering uniform sky emission in a circular region of $20'$ radius. An exposure corrected and NXB subtracted mosaic image of MKW4 in the 0.5-2 keV energy band is shown in Figure 2.1. We obtained *Suzaku* surface brightness profiles of MKW4 in three different directions, as shown in Figure 2.2. We fitted the profiles with a single β -model (Cavaliere and Fusco-Femiano, 1976; Arnaud, 2009):

$$S(r) = S_0 \left[1 + \left(\frac{r}{r_c} \right)^2 \right]^{-3\beta+1/2}, \quad (2.2)$$

which yielded the best-fit $(\beta, r_c) = (0.515 \pm 0.001, 30 \pm 2.5 \text{ kpc})$.

Spectral analysis

Spectral analysis was performed using `XSPEC--12.10.1` and C-statistics. Each spectrum was rebinned to guarantee 20 photons per bin to aid the convergence and the computational speed. Spectra extracted from the XIS0, XIS1, and XIS3 were simultaneously fitted. The spectral fitting was restricted to the 0.4 - 7.0 keV energy band for XIS1, and to the 0.6 - 7.0 keV energy band for XIS0 and XIS3 (e.g., Mitsuda et al., 2007). We fitted each spectrum with an ICM emission model plus a multi-component X-ray background model. The ICM emission model contains a thermal `apec` component associated with a photoelectric absorption (`phabs`) component - `phabs` \times `apec`, as shown in Figure 2.3. The temperature, abundance, and normalization of the `apec` component were allowed to vary independently for regions at the group center and

§<https://heasarc.gsfc.nasa.gov/docs/suzaku/analysis/abc/>

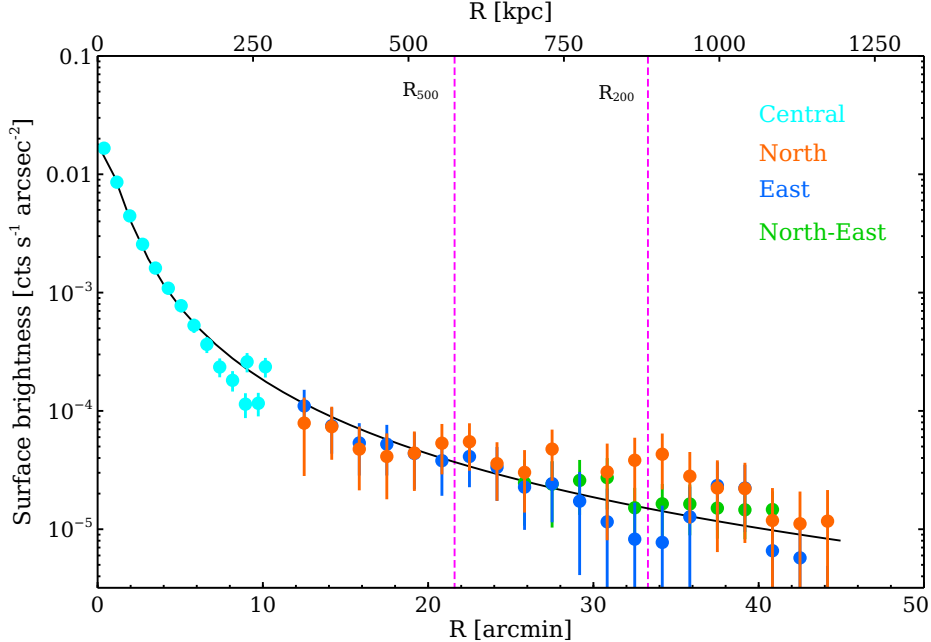


Figure 2.2: Surface brightness profiles of MKW4 derived from the *Suzaku* XIS image in the 0.5 - 2.0 keV energy band in three different directions. The profiles have been corrected for exposure, instrumental background (NXB), and the point sources detected with *Chandra*. Black solid line is the best-fit β -profile.

at the intermediate radii. For those three regions at R_{200} , we find it necessary to fix their abundances at $0.2 Z_{\odot}$. Similar metallicity was observed at R_{200} for the RX J1159+5531 group (Su et al., 2015). We discuss the systematic uncertainties caused by this choice of abundance in Section 2.4.

To model the X-ray background, we adopted $\text{phabs} \times (\text{pow}_{\text{resolved CXB}} + \text{pow}_{\text{unresolved CXB}} + \text{apec}_{\text{MW}}) + \text{apec}_{\text{LHB}}$, where $\text{pow}_{\text{resolved CXB}}$ and $\text{pow}_{\text{unresolved CXB}}$ are the power-law components to model the resolved CXB and unresolved CXB, respectively. The thermal apec_{MW} and apec_{LHB} represent two foreground components to account for emissions from the Milky Way (MW) and Local Hot Bubble (LHB), respectively. We made use of the *Chandra* observations that cover the *Suzaku* pointings of the outskirts of MKW4 to mitigate much of the CXB contribution. We detected a total of 78 point sources with *Chandra* (see Figure 2.1). Point sources that fall onto the ACIS-S1, S2, and S4 chips are not included in our analysis. The faintest point source was detected at a flux of $8.1 \times 10^{-15} \text{ erg cm}^{-2} \text{ s}^{-1}$. We converted the count rates of resolved point sources to the fluxes assuming a power-law model with a photon index of 1.41 (De Luca and Molendi, 2004). We produced mock *Suzaku* observations for the resolved point sources using *xissim*, based on their positions and fluxes determined with *Chandra*. An exposure time of 100 ks was set to ensure good photon statistics. We extracted spectra from the mock *Suzaku* observations using the same extraction regions used for the actual *Suzaku* observations. Figure 2.4 (left) compares the surface brightnesses of the actual point sources resolved by *Chandra* and that of

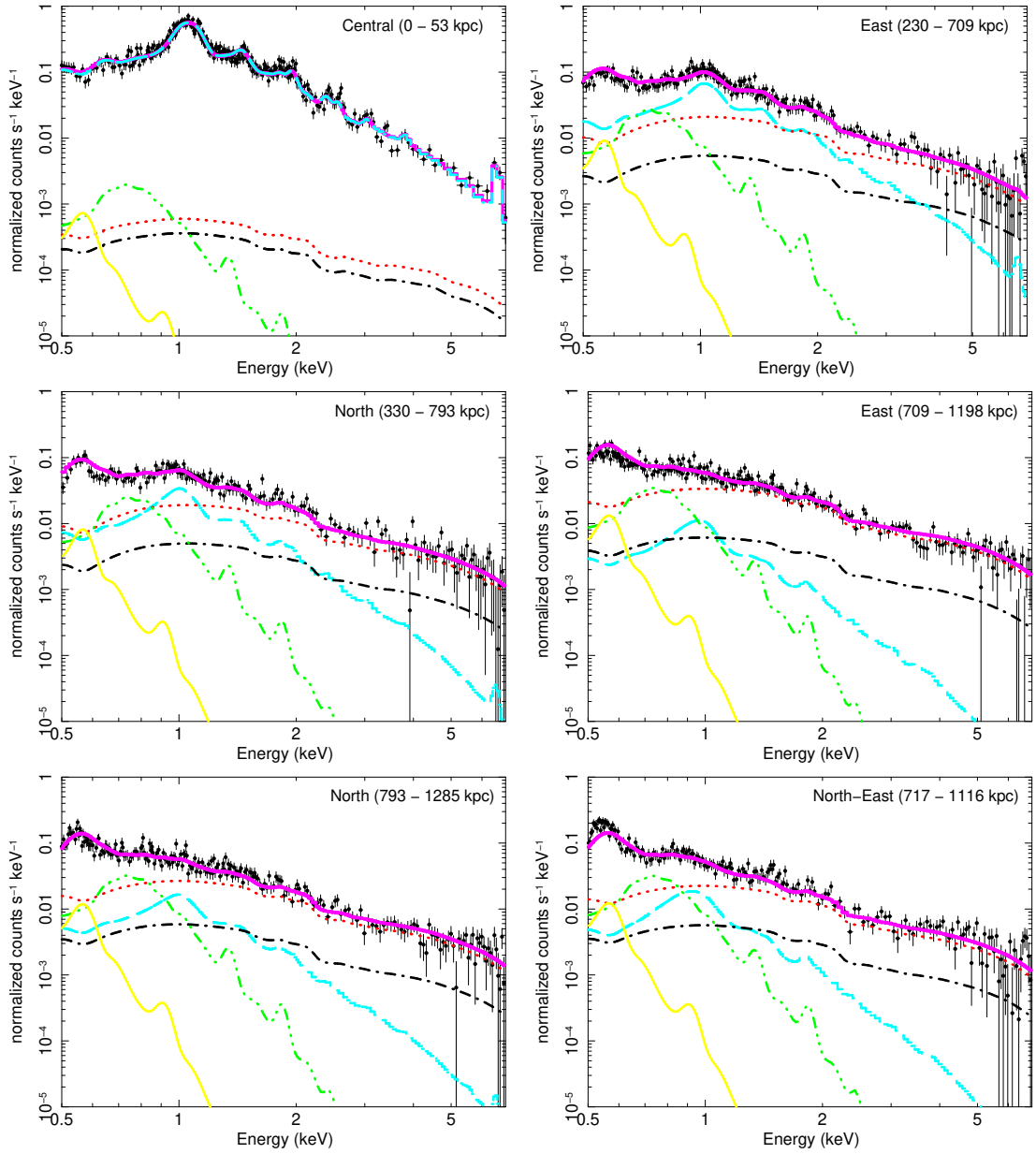


Figure 2.3: *Suzaku* XIS 1 spectra of MKW4 for representative regions of central and two outer bins in north and east directions. Black dots are the data points. Cyan, red, black, green, and yellow lines are the best-fit ICM emission, resolved CXB, unresolved CXB, MW, and LHB components, respectively. Magenta line is the model of the best-fit ICM emission and X-ray background components together.

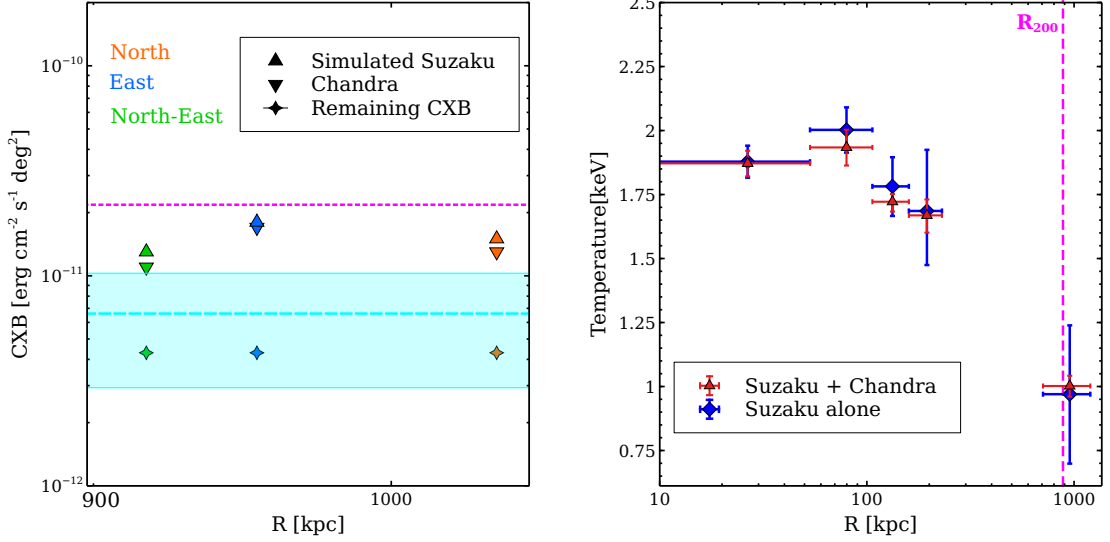


Figure 2.4: *Left*: Triangle down: surface brightness of point sources resolved by *Chandra*. Triangle up: surface brightness of point sources obtained from mock *Suzaku* sky. Magenta dotted: total surface brightness limit of resolved+unresolved point sources taken from Moretti et al. (2009). Cyan dashed: expected surface brightness limit of unresolved point sources with 1σ error (shaded) calculated using Equations 2.3 and 2.4. Star: estimated surface brightness of unresolved point sources from *Suzaku* fitting. *Right*: Blue: spectroscopic temperature profile of MKW4 in the north-east direction obtained from spectral fitting of the *Suzaku* data only. Red: same profile obtained from the joint fitting of *Suzaku* and *Chandra* data. Magenta dashed line indicates R_{200} of MKW4.

the simulated *Suzaku* observations, which are in good agreement with each other. We fitted the mock spectra with an absorbed power-law model ($\text{phabs} \times \text{pow}$) with a photon index of 1.41. The resulting best-fit normalizations were used as the normalizations of the resolved component ($\text{pow}_{\text{resolved CXB}}$) in the background model and kept frozen. Figure 2.4 (*right*) compares the spectral temperature profiles (discussed in Section 2.3) obtained with *Suzaku* observations alone and with joint *Suzaku* and *Chandra* observations of MKW4 in the north-east direction. The significant improvement of uncertainties demonstrates that the addition of *Chandra* observations can help to constrain the CXB and increase the accuracy of the measurement of ICM properties at the outskirts (e.g., Miller et al., 2012). For the regions with no *Chandra* coverages (two regions of intermediate radii in north and east directions), we let the normalizations of $\text{pow}_{\text{resolved CXB}}$ component to vary independently.

The normalizations of $\text{pow}_{\text{unresolved CXB}}$ component were allowed to vary collectively for different regions, assuming little fluctuations in the surface brightness of the remaining unresolved point sources. We obtained a best-fit normalization of $4.2 \times 10^{-12} \text{ erg cm}^{-2} \text{ s}^{-1} \text{ deg}^{-2}$ for the unresolved point sources in the 2.0 - 10.0 keV energy band, as shown in Figure 2.4. The normalization of unresolved CXB can be

Table 2.2: X-ray background components of outer regions^a

Name	CXB ^b	LHB ^c	MW ^d
<i>Suzaku</i> East	11.25 ^{+0.12} _{-0.13}	13.9 ^{+1.1} _{-1.3}	6.21 ^{+0.32} _{-0.35}
<i>Suzaku</i> North	9.51 ^{+0.12} _{-0.12}	—	—
<i>Suzaku</i> North-East	8.63 ^{+0.12} _{-0.12}	—	—

^a Results for the normalizations of various components (non-instrumental) of X-ray background for a circular region with 20' radii. The LHB and MW components for *Suzaku* North and *Suzaku* North-East directions are linked to the *Suzaku* East.

^b Normalization of power-law component ($\Gamma=1.41$) for resolved + unresolved cosmic X-ray background in the units of 10^{-4} photons s^{-1} cm^{-2} keV^{-1} at 1 keV.

^c Normalization of the unabsorbed **ap**ec thermal component ($kT = 0.08$ keV, $abun = 1Z_{\odot}$) integrated over line of sight, $1/4\pi[D_A(1+z)]^2 \int n_e n_H dV$ in the units of 10^{-18} cm^{-5} .

^d Normalization of the absorbed **ap**ec thermal component ($kT = 0.2$ keV, $abun = 1Z_{\odot}$) integrated over line of sight, $1/4\pi[D_A(1+z)]^2 \int n_e n_H dV$ in the units of 10^{-18} cm^{-5} .

estimated as (Moretti et al., 2009) -

$$F_{CXB} = 2.18 \pm 0.13 \times 10^{-11} - \int_{S_{min}}^{S_{max}} \left(\frac{dN}{dS} \right) \times S dS, \quad (2.3)$$

in units of $erg\ cm^{-2}\ s^{-1}\ deg^{-2}$, assuming a total CXB surface brightness of $2.18 \pm 0.13 \times 10^{-11}$ $erg\ cm^{-2}\ s^{-1}\ deg^{-2}$ in the 2.0 - 10.0 keV energy band. We adopted an analytical form of the integral source flux distribution from Moretti et al. (2003) -

$$N(> S) = N_{S(H)} \left[\frac{(2 \times 10^{-15})^{\alpha_{1,S(H)}}}{S^{\alpha_{1,S(H)}} + S_{0,H}^{\alpha_{1,S(H)} - \alpha_{2,S(H)}} S^{\alpha_{2,S(H)}}} \right], \quad (2.4)$$

where $\alpha_{1,S(H)} = 1.57_{-0.08}^{+0.10}$, $\alpha_{2,S(H)} = 0.44_{-0.13}^{+0.12}$, $S_{0,H} = 4.5_{1.7}^{+3.7} \times 10^{-15}$ $erg\ cm^{-2}\ s^{-1}$, and $N_{S(H)} = 5300_{-1400}^{+2850}$ are the best-fit parameters with a 68% confidence level. We estimated the flux limit for unresolved point sources to be $6.61 \pm 3.68 \times 10^{-12}$ $erg\ cm^{-2}\ s^{-1}\ deg^{-2}$. This flux is consistent with the flux obtained from spectral fitting.

To constrain the temperature and surface brightness of Local Hot Bubble (**ap**ec_{LHB}) and Milky Way (**ap**ec_{MW}) foregrounds, we used the ROSAT All-Sky Survey (RASS) data in an annulus region of 0.9° - 1.2° from the group center where no group emission was expected. We extracted spectra using the HEASARC X-ray background tool[‡]. The RASS spectrum was fitted simultaneously with the *Suzaku* data. The background fitting results are shown in Figure 2.3 and listed in Table 2.2.

[‡]<http://heasarc.gsfc.nasa.gov/cgi-bin/Tools/xraybg/xraybg.pl>

2.2.2 Chandra

MKW4 was observed using *Chandra* with one ACIS-S pointing at the group center and three ACIS-I pointings overlapping with the outer regions observed with *Suzaku*. The observation logs are listed in Table 4.1.

Data reduction

The *Chandra* data reduction was performed using HEASoft 6.25, CIAO-4.11, and a *Chandra* calibration database (CALDB 4.8.3). We followed a standard data reduction thread [§]. All data were reprocessed from the level 1 events using `chandra_repro`, which applied the latest gain, charge transfer inefficiency correction, and filtering from bad grades. The light curves were filtered using `lc_clean` script to remove periods affected by flares. The resulting filtered exposure times are listed in Table 4.1. Point sources were identified with `wavdetect` using a range of wavelet radii between 1 and 16 pixels to maximize the number of detected point sources. The detection threshold was set to 10^{-6} , which guaranteed detection of $\lesssim 1$ spurious source per CCD. Detected point sources were confirmed visually. Figure 2.1 shows the adaptively smoothed ACIS-S3 image of MKW4 in the 0.5 - 2.0 keV energy band.

We extracted spectra from 6 adjoining, concentric annuli centered at the X-ray centroid in the *Chandra* ACIS-S3 chip. The widths of the annular regions were chosen to contain approximately the same number of background-subtracted counts of 2000 for better spectral analysis. Count-weighted spectral response matrices (ARFs and RMFs) were generated using `mkwarf` and `mkacisrmf` tasks for each annulus. The blanksky background was produced by the `blanksky` tool for background subtraction. The blanksky background was tailored based on the count rate in the 9.5 - 12.0 keV energy band relative to the observation.

Spectral analysis

All spectra were fitted simultaneously to model the ICM properties of different regions. We modeled the ICM emission with a single thermal `apec` model associated with a photoelectric absorption model- `phabs` \times `apec`. Photoionization cross-sections were taken from Balucinska-Church and McCammon (1992). We obtained the galactic hydrogen column density, $N_{\text{H}} = 1.72 \times 10^{20} \text{ cm}^{-2}$ at the direction of MKW4, using HEASARC N_{H} tool ^{††}. All ICM emission components were allowed to vary independently.

2.3 Results

2.3.1 Density and temperature profile

We derive the deprojected (3D) gas density and temperature profiles of MKW4 assuming analytical prescriptions for 3D gas density and temperature. We follow the

[§]<http://cxc.harvard.edu/ciao/threads/index.html>

^{††}<http://heasarc.gsfc.nasa.gov/cgi-bin/Tools/w3nh/w3nh.pl>

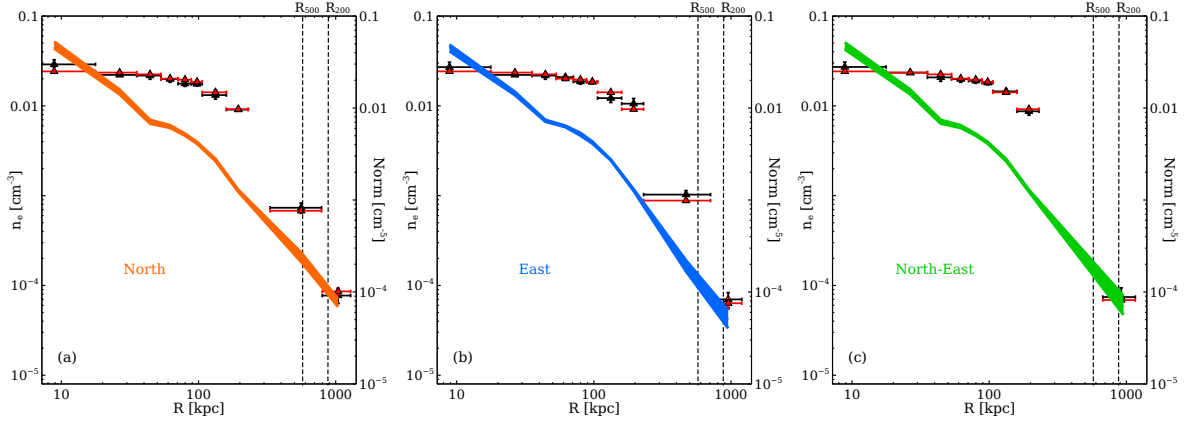


Figure 2.5: Deprojected density profiles of MKW4 in north (orange), east (blue), and north-east (green) directions. Shaded regions indicate 1σ uncertainties. Red triangles: the best-fit normalizations for the *apec* thermal component obtained from spectral analysis. Black triangles: the normalizations of the *apec* thermal component calculated from the resulting 3D density profile.

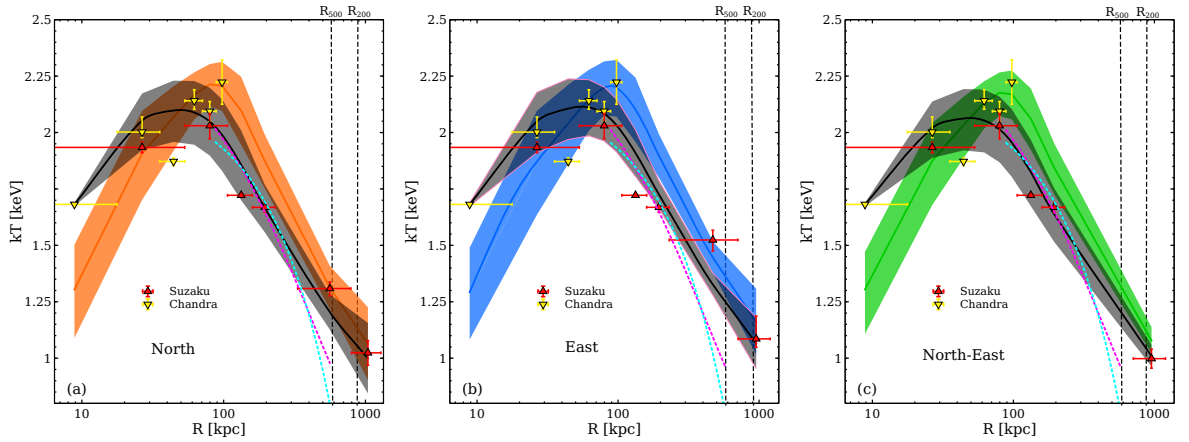


Figure 2.6: Deprojected temperature profiles of MKW4 in north (orange), east (blue), and north-east (green) directions. The 2D temperature profiles of MKW4, estimated using Equation 2.6, are indicated in black. Shaded regions indicate 1σ uncertainties. Temperatures obtained from the *apec* thermal component by fitting the spectra extracted from the *Chandra* and *Suzaku* data are shown in yellow and red respectively. Magenta and cyan dashed lines show the average temperature profiles derived for groups in Loken et al. (2002) and Sun et al. (2009) respectively.

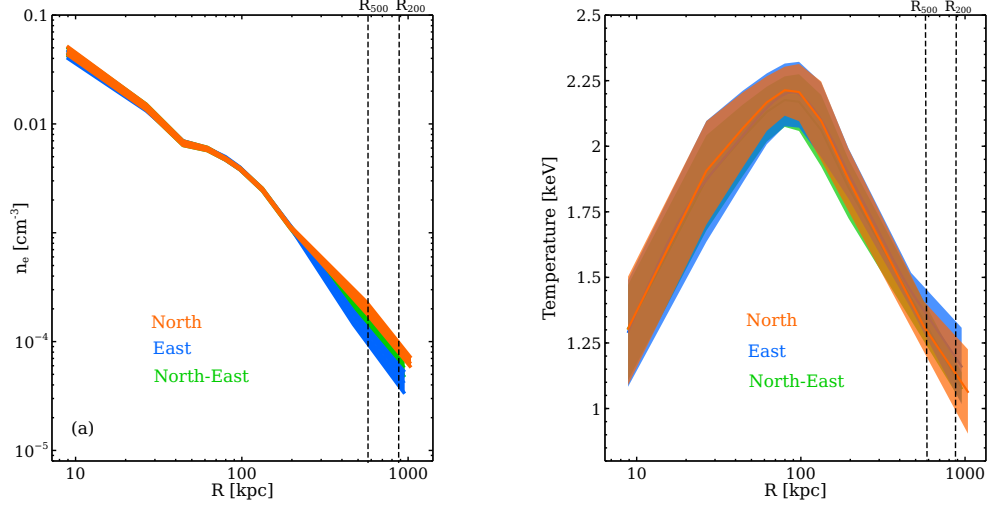


Figure 2.7: 3D density (left) and temperature (right) profiles of MKW4 in three different directions.

analytical expressions described in Vikhlinin et al. (2006). The normalization of the `apec` thermal component relates to the ICM density as: $\text{norm} = \int n_e n_p dl$, where the density profile of electrons (n_e) and protons (n_p) can analytically be described as:

$$n_e n_p(r) = \frac{n_{01}^2}{(1 + r^2/r_{c1}^2)^{3\beta_1}} + \frac{n_{02}^2}{(1 + r^2/r_{c2}^2)^{3\beta_2}}. \quad (2.5)$$

We obtain the 3D density profile of MKW4 by projecting the 3D analytic model given in Equation 2.5 along the line of sight and fit it to the measured 2D normalizations of thermal `apec` component obtained from the spectral analysis, assuming $n_e = 1.2n_p$ and The uncertainties are calculated using Monte Carlo simulations with 1000 to 2000 realizations.

The resulting 3D density profiles are shown in Figure 2.5. A comparison between the normalizations obtained from spectral analysis and the normalizations obtained from the Equation 2.5 are also shown in Figure 2.5. Figure 2.7 compares the 3D density profiles of MKW4 in three different directions.

We derive the 3D temperature profile by fitting the spectral temperature (2D spectroscopic temperature, T_{2D}) obtained from thermal `apec` component with the following analytic function (Vikhlinin et al., 2006):

$$T_{2D} = \frac{\int n_e^2 T_{3D}^{\frac{1}{4}} dV}{\int n_e^2 T_{3D}^{-\frac{3}{4}} dV}, \quad (2.6)$$

where

$$T_{3D}(r) = T_0 \frac{(x + T_{\min}/T_0)}{(x + 1)} \times \frac{(r/r_t)^{-a}}{(1 + r^b/r_t^b)^{c/b}}, \quad (2.7)$$

and $x = \left(\frac{r}{r_{\text{cool}}}\right)^{a_{\text{cool}}}$.

Figure 2.6 represents the projected (T_{2D}) and deprojected (T_{3D}) temperature profiles of MKW4 from its center out to the virial radii in north, east, and north-east directions.

The uncertainties in temperatures are also calculated using Monte Carlo simulations. The deprojected temperature profiles of MKW4 decline from 2.20 keV at $0.1R_{200}$ to 1.14 keV at R_{200} . A similar temperature drop was found in other groups (e.g., Su et al., 2015). The projected temperatures measured with *Suzaku* and *Chandra* are consistent for the overlapping regions. Figure 2.7 compares the 3D temperature profiles of MKW4 in three different directions.

Our temperature profile agrees well with the *Chandra* temperature profiles of MKW4 out to R_{2500} , as given by Vikhlinin et al. (2006) (V06) and Sun et al. (2009) (S09) as well as the measurement obtained with *XMM-Newton* by Gastaldello et al. (2007) (G07) out to $\sim 0.6R_{500}$. We measure a gas temperature at R_{500} between those of V06 and S09 and consistent with the *Suzaku* measurement using the two intermediate pointings (Sasaki et al., 2014). We compare the projected temperature profiles of MKW4 to the empirical profiles derived for groups by Sun et al. (2009):

$$\frac{T}{T_{2500}} = (1.22 \pm 0.02) - (0.79 \pm 0.04) \frac{R}{R_{500}}, \quad (2.8)$$

and by Loken et al. (2002):

$$\frac{T}{T_{2500}} = (1.37 \pm 0.03) - \left(1 + \frac{R}{R_{500}}\right)^{-(1.34 \pm 0.21)}, \quad (2.9)$$

as shown in Figure 2.6. Both profiles show good agreement with the projected temperature profile of MKW4 out to $\sim R_{2500}$. Their values at R_{500} exceed what is measured for MKW4 by 30% and 60%, respectively. These empirical profiles are determined with a large number of galaxy groups with a sizable scatter. Many of them do not have their temperatures actually measured out to R_{500} .

2.3.2 Entropy and pressure profile

We derive the 3D entropy and pressure profiles of MKW4 from 3D density and temperature profiles, as shown in Figures 2.8 and 2.9. We compare our entropy profiles with a baseline profile derived from purely gravitational structure formation (Voit et al., 2005) and assuming a hydrostatic equilibrium-

$$K_{\text{gra}}(R) = 1.32 K_{200} \left(\frac{R}{R_{200}}\right)^{1.1}, \quad (2.10)$$

and the normalization K_{200} is defined as-

$$K_{200} = 362 \frac{G M_{200} \mu m_p}{2R_{200}} \left(\frac{1}{\text{keV}}\right) E(z)^{-4/3} \times \left(\frac{\Omega_m}{0.3}\right)^{-4/3} \text{keV cm}^{-2}, \quad (2.11)$$

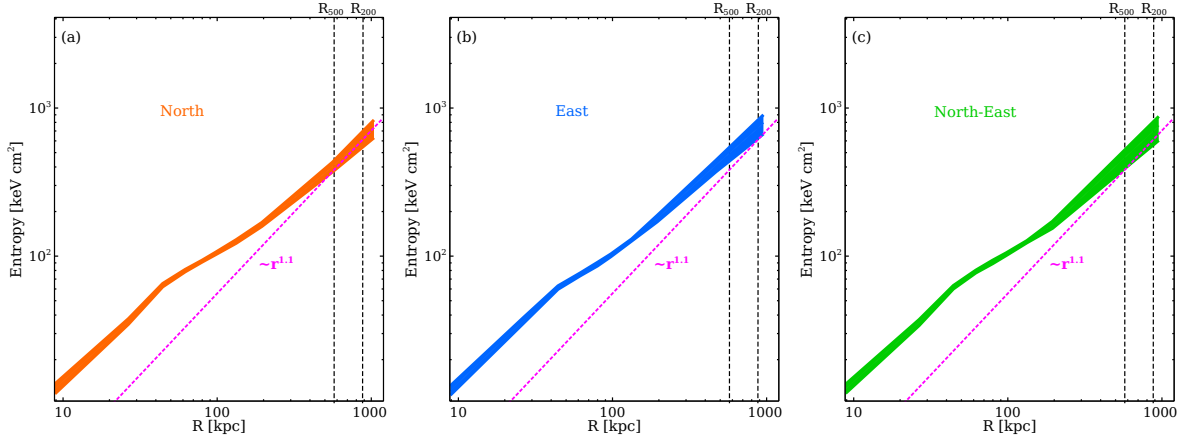


Figure 2.8: 3D entropy profiles of MKW4 in north (orange), east (blue), and north-east (green) directions. Shaded regions indicate 1σ uncertainties. Magenta dashed line represents the entropy profile derived from gravity only cosmological simulation (Voit et al., 2005) using Equation 2.10.

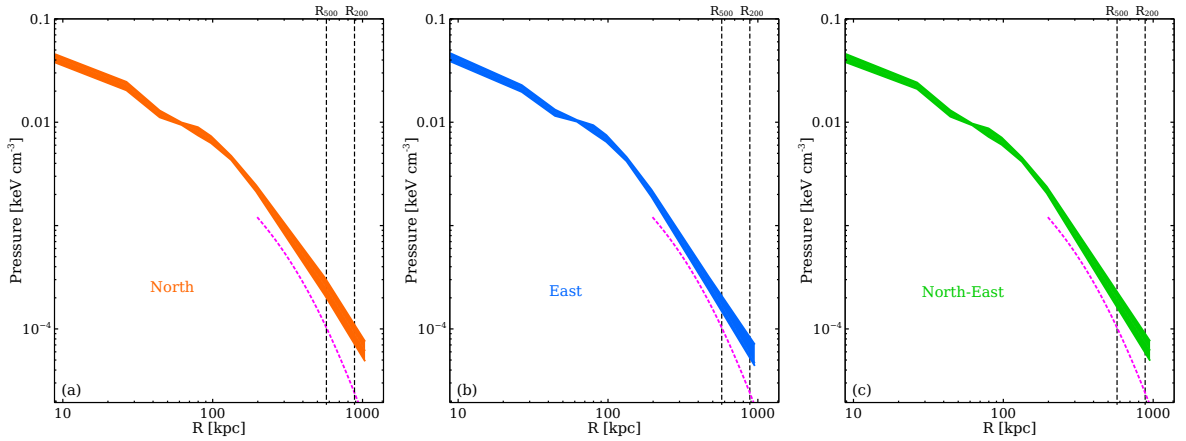


Figure 2.9: 3D pressure profiles of MKW4 in north (orange), east (blue), and north-east (green) directions. Shaded regions indicate 1σ uncertainties. Magenta dashed line represents the semi-analytical universal pressure profile (Arnaud et al., 2010), derived using Equation 2.13.

$$\text{where, } E(z) = \sqrt{\Omega_m (1+z)^3 + \Omega_\Lambda}. \quad (2.12)$$

The m_p is proton mass and $\mu \sim 0.6$ is the mean molecular weight. The 3D entropy profiles of MKW4 increase monotonically with radius in three directions, as seen in Figure 2.8. We observe apparent entropy excesses towards the central region (up to $\sim 0.5R_{200}$) of MKW4 relative to the baseline profile. At larger radii, the entropy profiles of MKW4 are consistent with the baseline profile, i.e., its slope attains a value of ~ 1.1 between R_{500} and R_{200} in all observed directions.

The 3D pressure profiles of MKW4 are shown in Figure 2.9. We compare the measured pressure profiles to a semi-analytical universal pressure profile (Arnaud et al., 2010) defined as -

$$P(r) = P_{500} \left[\frac{M_{500}}{3 \times 10^{14} h_{70}^{-1} M_\odot} \right]^{\alpha_p + \alpha'_p(x)} \times \frac{P_0}{(c_{500}x)^\gamma [1 + (c_{500}x)^\alpha]^{\frac{(\beta-\alpha)}{\alpha}}} \quad (2.13)$$

where $x = \frac{R}{R_{500}}$, $\alpha'_p(x) = 0.10 - (\alpha_p + 0.10) \frac{(x/0.5)^3}{[1+(x/0.5)^3]}$. The P_{500} is the pressure at R_{500} and M_{500} (see Table 3.2) is the total hydrostatic mass within R_{500} . We adopt

$$[P_0, c_{500}, \alpha, \beta, \gamma, \alpha_p] = [8.403h_{70}^{-3/2}, 1.177, 0.3081, 1.0510, 5.4905, 0.12 \pm 0.10]$$

from Arnaud et al. (2010). Sun et al. (2011) adopted similar parameters and found that the Arnaud et al. (2010) pressure profile is also representative for galaxy groups. The 3D pressure profiles of MKW4 in all directions from $0.35R_{500}$ out to $\sim 0.65R_{500}$ show good agreement with this universal pressure profile but exceed it by more than 50% at R_{500} .

2.3.3 Mass and gas fraction

We derive the X-ray hydrostatic mass of MKW4 and its gas mass within a specific radius (R) from the group center, incorporating the above 3D density and temperature profiles in the following equations-

$$M_{\text{tot}}(< R) = -\frac{kT_{3D}R}{G\mu m_p} \left(\frac{d \ln \rho_{\text{gas}}}{d \ln R} + \frac{d \ln T_{3D}}{d \ln R} \right) \quad (2.14)$$

$$M_{\text{gas}}(< R) = 4\pi \int_0^R \rho_g(r') r'^2 dr', \quad (2.15)$$

where $\rho_{\text{gas}} = 1.92\mu m_H n_e$ is the gas density, and m_H is the proton mass. The resulting hydrostatic mass profile of MKW4 is shown in Figure 2.10. We obtain $M_{\text{tot}}(< R_{500}) \approx 6.5 \pm 1.0 \times 10^{13} M_\odot$ and $M_{\text{tot}}(< R_{200}) \approx 9.7 \pm 1.5 \times 10^{13} M_\odot$. Our measured

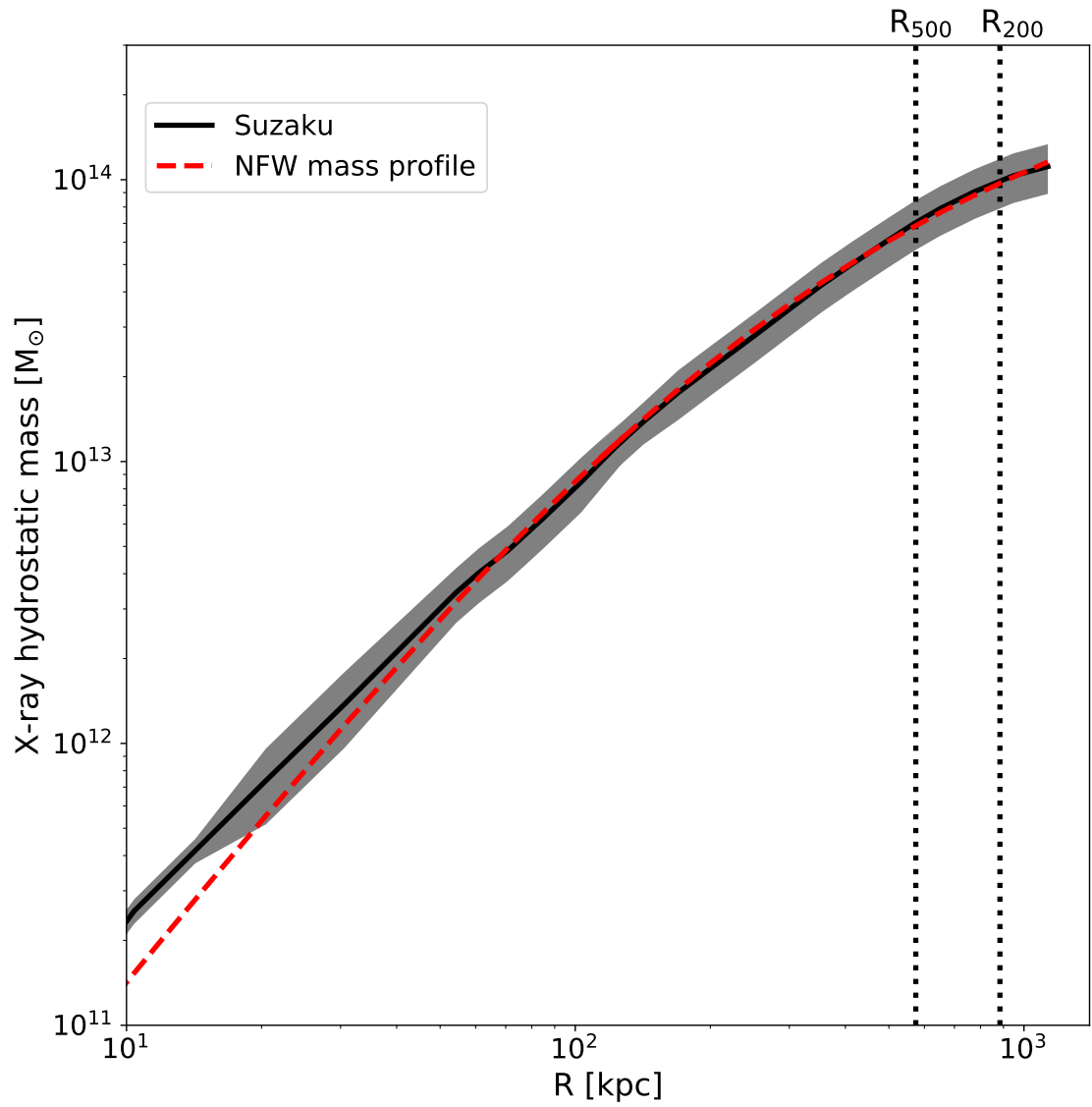


Figure 2.10: The X-ray hydrostatic mass profile (M_{total}) of MKW4 derived using Equation 2.14. Red dashed line shows best-fit NFW mass profile obtained by integrating Equation 2.16. Shaded region indicates 1σ error.

Table 2.3: Properties of MKW4

T_{2500}^a (keV)	T_{500} (keV)	T_{200} (keV)	R_{2500} (kpc)	R_{500} (kpc)	R_{200} (kpc)	M_{500}^b ($10^{13} M_{\odot}$)	M_{200} ($10^{13} M_{\odot}$)	$f_{\text{gas}, 2500}^c$	$f_{\text{gas}, 500}$	$f_{\text{gas}, 200}$	c_{500}	c_{200}
$1.71_{-0.08}^{+0.09}$	1.36 ± 0.09	$1.14_{-0.13}^{+0.16}$	274 ± 10	574 ± 20	884 ± 17	6.5 ± 1.0	9.7 ± 1.5	0.05 ± 0.01	0.07 ± 0.01	0.090 ± 0.011	$3.09_{-0.39}^{+0.52}$	$4.75_{-0.60}^{+0.80}$

^a T_{Δ} = deprojected temperature at R_{Δ} .

^b M_{Δ} = total X-ray hydrostatic mass within R_{Δ} .

^c $f_{\text{gas}, \Delta}$ = enclosed gas mass fraction at R_{Δ} .

hydrostatic mass within R_{500} is between that given by Vikhlinin et al. (2006) ($7.7 \pm 1.0 \times 10^{13} M_{\odot}$) and those of Gastaldello et al. (2007) ($4.3 \pm 0.2 \times 10^{13} M_{\odot}$) and Sun et al. (2009) ($4.8 \pm 0.7 \times 10^{13} M_{\odot}$).

We fit our hydrostatic mass profile to the NFW mass density profile (Navarro et al., 1997):

$$\rho(r) = \frac{\rho_s}{(r/r_s)(1 + r/r_s)^2}, \quad (2.16)$$

as shown in Figure 2.10. We obtain a best-fit r_s of 186 ± 23 kpc, which gives the central mass concentrations of $c_{500} = 3.09_{-0.39}^{+0.52}$ at R_{500} and $c_{200} = 4.75_{-0.60}^{+0.80}$ at R_{200} . We also obtain the sparsity, the ratio of masses at two overdensities (Corasaniti et al., 2018), $S_{200,500} = 1.49 \pm 0.31$. Our measurement of $S_{200,500}$ for MKW4 is closely align with the typical $S_{200,500}$ of 1.5 found for galaxy clusters in N-body simulation (Corasaniti et al., 2018).

We obtain its enclosed gas mass and estimate the gas mass fraction $f_{\text{gas}} = \frac{M_{\text{gas}}}{M_{\text{tot}}}$ for each direction, as shown in Figure 2.11. At $\sim R_{500}$, the measured gas mass fraction of MKW4 is below 10% in all directions, similar to the other galaxy groups (e.g., Vikhlinin et al., 2006; Sun et al., 2009; Humphrey et al., 2012; Thölken et al., 2016). At a radii larger than R_{500} , f_{gas} grows slowly and attains a value of 0.092 ± 0.009 in the north, 0.087 ± 0.012 in the east, and 0.090 ± 0.011 in the north-east at R_{200} . These gas mass fractions are surprisingly low compared to the cosmic baryon fraction of 0.15 (Planck Collaboration et al., 2014) and 0.17 (Komatsu et al., 2011). A brief comparison of the mass and f_{gas} of MKW4 between our work and previous studies is listed in Table 2.4.

2.4 Systematic uncertainties

We investigate changes of the best-fit gas density, temperature, entropy, pressure, and enclosed gas mass fraction at R_{200} introduced by a variety of systematic effects. Below we focus on the systematic uncertainties related to the entropy. All other gas properties are listed in Table 2.5.

We consider two different sources of systematic uncertainties associated with the CXB. First, we allow the best fit normalization of the CXB component in the background model to vary by 20% with a fixed power-law slope of $\Gamma = 1.41$ (De Luca and Molendi, 2004), which leads to a maximum change in gas entropy by $\sim 18\%$ at R_{200} for the north, east, and north-east directions (see ΔCXB in Table 2.5). Second, we fix the CXB power-law slope to $\Gamma = 1.3$ and 1.5, respectively. Adopting $\Gamma = 1.3$ has

Table 2.4: Comparison of our results with other works

Name	R_{500} (kpc)	M_{500}^{\ddagger} $\times 10^{13} (M_{\odot})$	$f_{\text{gas}, 2500}^{\dagger}$	$f_{\text{gas}, 500}^{\dagger}$	C_{500}
This work	574 ± 20	6.5 ± 1.0	0.05 ± 0.01	0.07 ± 0.01	$3.09^{+0.52}_{-0.39}$
S09 [§]	538^{+24}_{-29}	$4.85^{+0.71}_{-0.68}$	$0.047^{+0.002}_{-0.003}$	0.086 ± 0.009	$3.93^{+1.16}_{-0.78}$
G07	527 ± 8	4.27 ± 0.18	—	—	6.4 ± 0.5
V06	634 ± 28	7.7 ± 1.0	0.045 ± 0.002	0.062 ± 0.006	2.54 ± 0.15

$^{\ddagger}M_{\Delta}$ = total X-ray hydrostatic mass within R_{Δ} .

$^{\dagger}f_{\text{gas}, \Delta}$ = enclosed gas mass fraction at R_{Δ} .

[§] S09, G07, and V06 are referred to Sun et al. (2009), Gastaldello et al. (2007), and Vikhlinin et al. (2006) respectively.

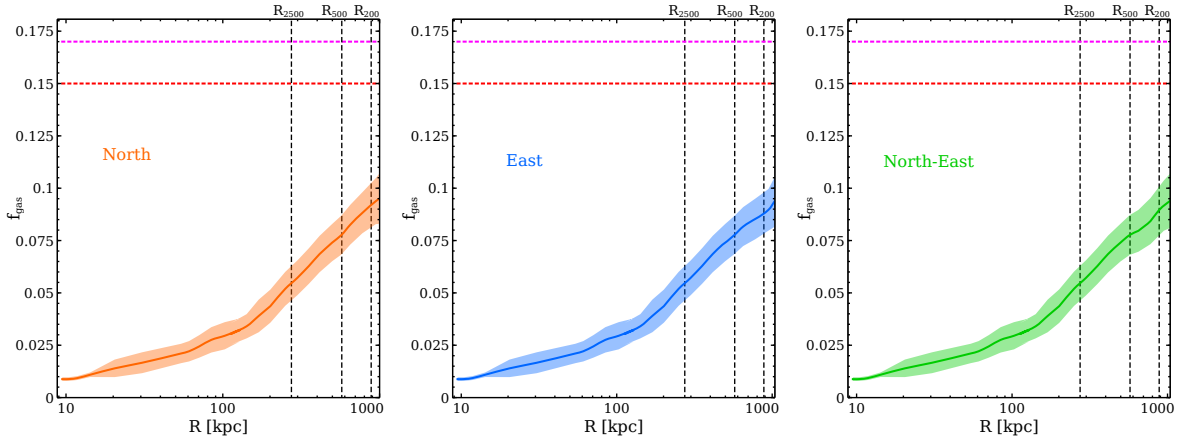


Figure 2.11: The gas mass fraction of MKW4 in north (orange), east (blue), and north-east (green) directions. Red dashed line: cosmic baryon fraction estimated by *Planck* (Planck Collaboration et al., 2014). Magenta dashed line: cosmic baryon fraction estimated by *WMAP* (Komatsu et al., 2011).

Table 2.5: Systematic error of gas properties at R_{200}

	Test	Temperature keV	Density 10^{-5} cm^{-3}	Entropy keV cm^2	Pressure $10^{-5} \text{ keV cm}^{-3}$	f_{gas}
	Best fit	1.13 ± 0.14	8.85 ± 1.5	630 ± 82	9.2 ± 2.8	0.092 ± 0.009
North	ΔCXB	+0.06, -0.04	+0.08, -0.46	-4, +176	+0.17, -0.36	± 0.004
	$\Delta\text{CXB-}\Gamma$	+0.14, -0.04	-0.24, -0.13	-26, +116	-0.8, +0.003	± 0.001
	Δabun	+0.06, -0.04	+0.22, -0.46	-22, +177	+0.03, -0.36	+0.0007, -0.008
	ΔN_{H}	-0.04, +0.06	-0.22, -0.15	+31, +30	-0.09, +0.4	-0.002, +0.009
	$\Delta\text{distance}$	± 0.03	± 0.2	± 66	± 0.34	± 0.008
	ΔMW	+0.084, +0.024	+0.001, -0.19	-51, +72	+0.20, +0.16	+0.001, +0.001
	ΔLHB	± 0.09	± 0.05	± 165	± 0.16	± 0.01
	Δsolar	+0.02, +0.14	-0.66, -0.23	+159, -28	± 0.78	+0.01, +0.02
	Best fit	1.17 ± 0.15	5.6 ± 1.2	712 ± 100	6.55 ± 1.3	0.087 ± 0.012
East	ΔCXB	+0.28, -0.1	+1.52, +0.84	+71, -141	+2.4, -0.03	+0.006, -0.001
	$\Delta\text{CXB-}\Gamma$	-0.2, +0.28	+1.06, +1.27	-249, +107	-0.27, +2.08	-0.006, +0.005
	Δabun	+0.28, -0.10	+0.85, +1.55	-68, +143	-0.02, +2.44	+0.005, -0.001
	ΔN_{H}	-0.01, +0.05	+0.12, +0.13	-63, -55	+0.13, +0.88	+0.003, +0.02
	$\Delta\text{distance}$	± 0.02	± 0.34	± 39	± 0.06	± 0.002
	ΔMW	-0.06, +0.16	+0.9, +0.43	-186, +167	+0.23, +0.49	-0.01, +0.03
	ΔLHB	± 0.01	± 0.62	± 82	± 0.17	± 0.001
	Δsolar	+0.06, -0.1	+0.16, +1.27	+111, -191	-0.11, +0.36	-0.003, +0.008
	Best fit	1.12 ± 0.07	6.7 ± 1.8	682 ± 134	7.54 ± 1.7	0.090 ± 0.011
North-East	ΔCXB	+0.09, -0.25	+1.2, -0.36	-5, +130	+1.4, -0.3	-0.01, -0.005
	$\Delta\text{CXB-}\Gamma$	+0.06, -0.25	-1.4, -1.27	+210, -44	-1.7, -2.8	+0.003, -0.004
	Δabun	-0.15, -0.07	-0.74, -1.8	-39, +213	-1.8, -2.6	-0.003, -0.004
	ΔN_{H}	-0.05, +0.06	-0.14, -0.13	-34, +40	-0.80, -0.70	-0.004, 0.007
	$\Delta\text{distance}$	± 0.05	± 1.4	± 152	± 2.1	± 0.003
	ΔMW	-0.15, +0.05	-0.67, -0.95	-61, +200	-0.93, -0.61	-0.004, -0.008
	ΔLHB	± 0.03	± 0.78	± 201	± 0.57	± 0.002
	Δsolar	-0.07, -0.25	-2.0, -1.2	+235, -60	-2.8, +2.7	± 0.004

ΔCXB : vary the normalization of the CXB component by 20%, while keeping the slope of the power law, $\Gamma = 1.4$.

$\Delta\text{CXB-}\Gamma$: set the slope of the power law for CXB component at $\Gamma = 1.3$ and 1.5, respectively.

Δabun : set the metal abundance at $0.1 Z_{\odot}$ and $0.3 Z_{\odot}$, respectively for outermost bin.

ΔN_{H} : vary the galactic hydrogen column density by 20%.

$\Delta\text{distance}$: vary the redshift parameter by 5%.

ΔMW : vary the normalization for apec_{MW} by 10%.

ΔLHB : vary the normalization for apec_{LHB} by 10%.

Δsolar : set the solar abundance table to Anders and Grevesse (1989) and Lodders (2003), respectively.

little effect on our results for the north direction, while the gas entropy varies by $\sim 30\%$ for the other two directions. Adopting $\Gamma = 1.5$, the gas entropy is increased by $\sim 14\%$ for the north and east directions, while no significant changes are observed for the north-east direction.

We examine the impacts on gas properties due to variations in the MW and LHB foreground components by varying the normalization of each component by 10% (see ΔMW and ΔLHB in Table 2.5). We find that the variation in the MW component changes the gas entropy by 22% in the east and 27% in the north-east. The 10% variation in the LHB component changes the entropy by 20% in the north and 27% in the north-east.

We adopt the solar abundance table of Asplund et al. (2006) for the spectral analysis, as shown in Figure 2.3. Here, we experiment with two different solar abundance tables of Anders and Grevesse (1989) and Lodders (2003) to find their impacts on the measurement of gas properties. Results are listed in Table 2.5 under $\Delta solar$. Using the Anders and Grevesse (1989) solar abundance table, the gas entropy increases by 20% in the north, 13% in the east, and 32% in the north-east directions. In contrast, using the Lodders (2003) abundance table, the entropy does not change significantly in the north and north-east directions but decreases by 20% in the east.

In the spectral analysis, we find it necessary to fix the ICM metallicity at $0.2 Z_{\odot}$ for regions at R_{200} . Here, we estimate the uncertainties in the measurements of gas properties associated with the possible variation of the ICM metallicity. We repeat the spectral analysis by fixing the metallicity at $0.1 Z_{\odot}$ and $0.3 Z_{\odot}$ (see $\Delta abun$ in Table 2.5). Fixing the metal abundance at $0.1 Z_{\odot}$ has little impact on gas properties at the outskirts of MKW4, while adopting a metallicity of $0.3 Z_{\odot}$ increases the gas entropy by $\sim 20\%$ in the north, 15% in the east, and 25% in the north-east directions.

2.5 Discussion

Combining the deep *Suzaku* observations with the *Chandra* ACIS-S and ACIS-I observations of MKW4, we measured its gas properties from the group center out to the virial radii in three directions. Its entropy profiles at larger radii are consistent with the self-similar value predicted by gravitational collapse alone (Voit et al., 2005). We estimated the enclosed gas mass fraction of MKW4 as a function of radial distance from the group center and obtained a surprisingly low value within R_{200} compared to clusters. Below we discuss the implications of these results in detail.

2.5.1 Entropy profile

The entropy profile describes the thermal history of the ICM. Previous works on massive clusters ($T_X > 3$ keV) have measured entropy profiles that flatten between R_{500} and R_{200} and even tend to fall below the self-similar value predicted by gravitational collapse alone (e.g., Simionescu et al., 2011; Bonamente et al., 2013; Walker et al., 2012). The explanations proposed for the unexpected entropy profiles include clumpy ICM and electron-ion non-equilibrium, either of which can be induced as galaxy clusters accrete cold gas from cosmic filaments. Using numerical simulations,

Nagai and Lau (2011) predict that massive clusters with $M_{200} > 10^{14} M_{\odot} h^{-1}$ contain a significant fraction of clumpy gas at larger radii due to frequent merging events, which biases low the entropy by overestimating the gas density. We do not observe any flattening in the entropy profiles of MKW4 between R_{500} and R_{200} . Our results suggest that the merger rate is comparably lower for MKW4 because of the shallow gravitational potential well, which makes the ICM less clumpy at its outskirts. This also supports the fact that clumping factors are smaller in the low mass clusters ($M_{200} < 10^{14} M_{\odot} h^{-1}$) and groups, as suggested by Su et al. (2015), Thölken et al. (2016), and Bulbul et al. (2016a). The entropy profiles of MKW4 instead follow the baseline profile (Voit et al., 2005), indicating its gas dynamics at the outskirts may be mainly regulated by gravity.

Another explanation for entropy flattening is electron-ion thermal non-equilibrium. A shock wave resulting from any recent merger and accretion event at the outskirts tends to heat the heavy-ions faster than electrons, causing the ion temperature to exceed the electron temperature. This thermal non-equilibrium could bias low the gas entropy. Numerical simulations show that the discrepancy between electron and ion temperature is more severe in more massive and rapidly growing clusters (e.g., Avestruz et al., 2015; Walker et al., 2019). The well behaved entropy profiles of MKW4 suggest that it is a relatively undisturbed system and has experienced few recent mergers.

Despite the agreement between the entropy profiles of MKW4 and the baseline profile (Voit et al., 2005) at larger radii, we observe apparent entropy excess at the center of MKW4. Pratt et al. (2010) and Le Brun et al. (2014) advocate that the AGN feedback could elevate entropy profiles at the center of galaxy clusters by pushing a substantial fraction of baryons out of R_{200} . Pratt et al. (2010) also corrects the entropy profiles for the redistribution of hot gas due to AGN feedback, as follows-

$$K_{\text{corrected}} = K_{\text{measured}} \times \left(\frac{f_{\text{gas}}}{f_{\text{b}}} \right)^{2/3}. \quad (2.17)$$

We scale the measured entropy profile of MKW4 in north direction as Equation 2.17, adopting a cosmic baryon fraction of $f_{\text{b}} = 0.15$ from the Planck Collaboration et al. (2014), as shown in Figure 2.12. We find the scaled entropy profile follows closely with the baseline profile, even out to the virial radii, suggesting that the redistribution of the group gas due to the AGN feedback may have shaped its gas entropy (Mathews and Guo, 2011).

2.5.2 Gas mass fraction

The enclosed gas mass fraction (f_{gas}) of MKW4 slowly rises from the group center and reaches $\sim 7\%$ within R_{500} , consistent with the previous *Chandra* studies of MKW4 (Vikhlinin et al., 2006) and the f_{gas} of other groups (e.g., Humphrey et al., 2012; Su et al., 2013; Lovisari et al., 2015; Su et al., 2015; Thölken et al., 2016). We obtain a f_{gas} of $\sim 9\%$ within R_{200} for MKW4, which is remarkably small compared to the cosmic baryon fraction (f_{b}) of 15%. We estimate the stellar mass of MKW4 using Two

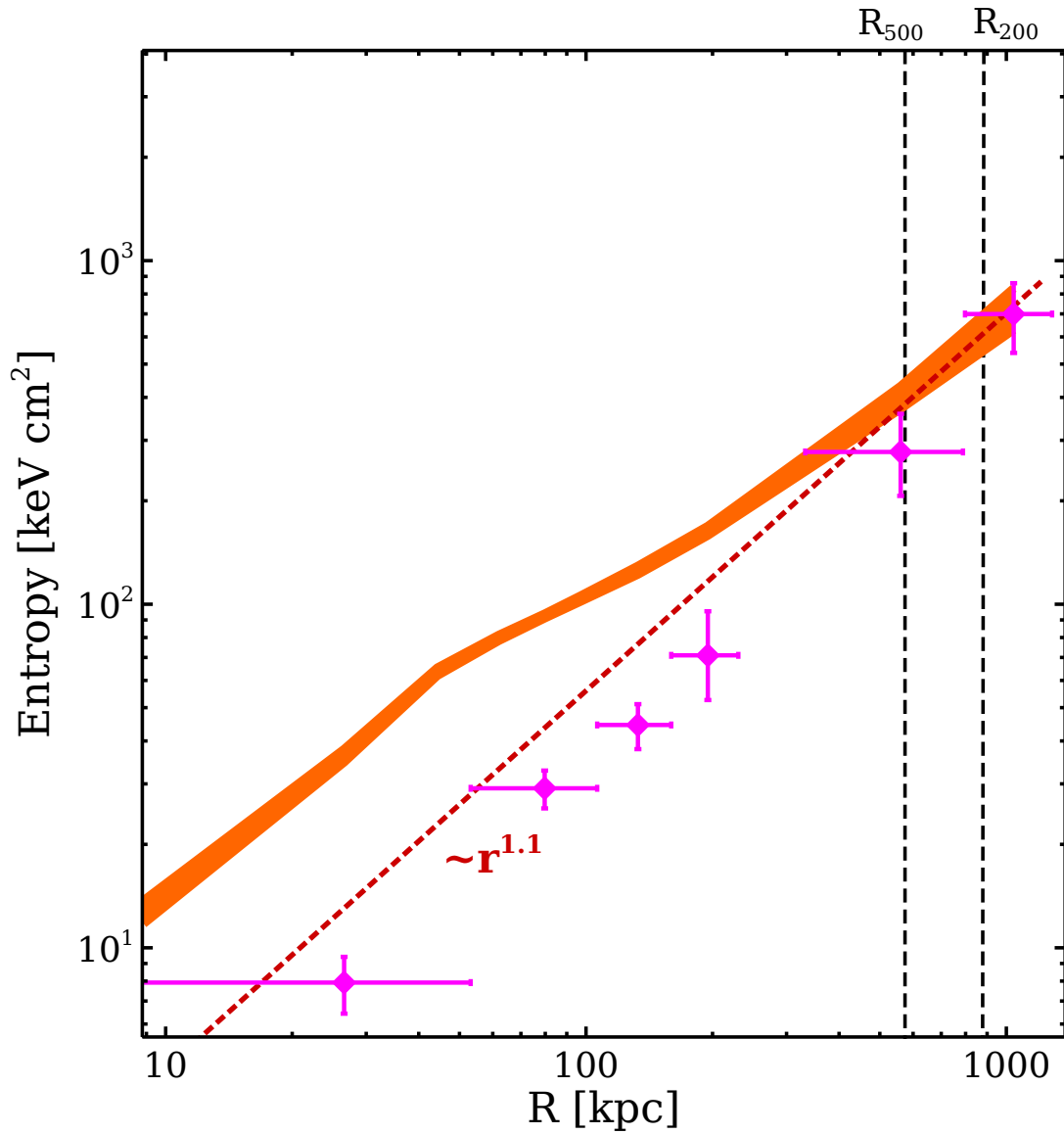


Figure 2.12: Orange: The entropy profile of MKW4 in north direction with 1σ error. Red: The baseline entropy profile estimated using Equation 2.10. Magenta: The entropy profile scaled with f_{gas} as shown in Equation 2.17.

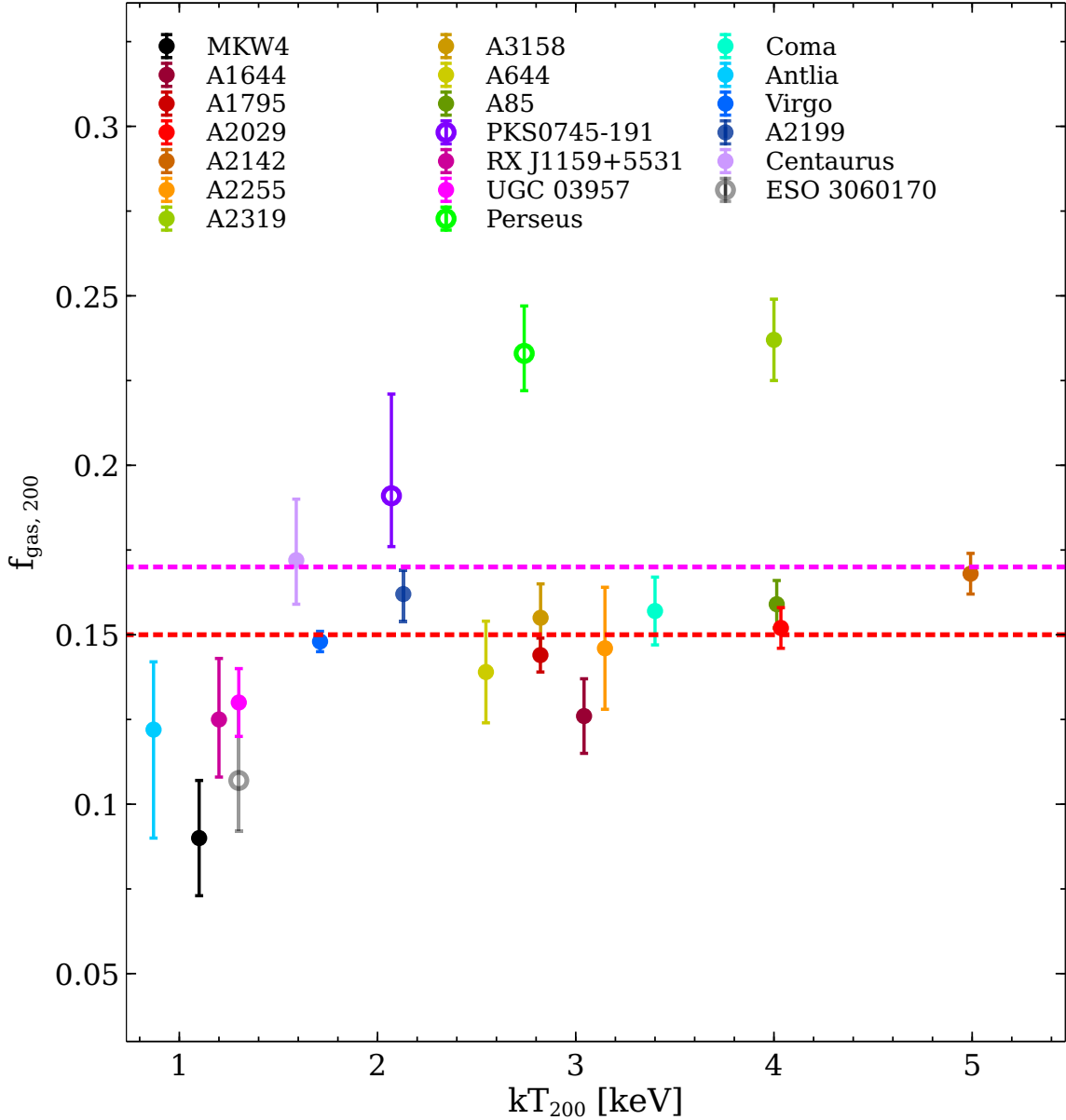


Figure 2.13: The f_{gas} is plotted with the cluster temperature at R_{200} . Open circles represent f_{gas} obtained using *Suzaku* only and filled circles represent f_{gas} obtained using *XMM-Newton* + *Planck* or *Suzaku* + *Chandra*. Color codes for different clusters are shown in the plot. The f_{gas} for A1644, A1795, A2029, A2142, A2255, A2319, A3158, A644, and A85 are taken from Eckert et al. (2019). We obtain f_{gas} of PKS0745-191 from Walker et al. (2012), RX J1159+5531 from Su et al. (2015), UGC 03957 from Thölken et al. (2016), Coma from Mirakhor and Walker (2020a), Perseus from Simionescu et al. (2011), Antlia from Wong et al. (2016), Virgo from Simionescu et al. (2017), A2199 from Mirakhor and Walker (2020b), Centaurus from Walker et al. (2013), and ESO 3060170 from Su et al. (2013). Red and magenta dashed lines shows cosmic baryon fraction estimated using *Planck* (Planck Collaboration et al., 2014) and *WMAP* (Komatsu et al., 2011) respectively.

Micron All-Sky Survey (2MASS[§]) data in K_s band, assuming a stellar mass-to-light ratio of ~ 1 (Bell et al., 2003). We find that the stellar mass contributes nearly 2% to the total hydrostatic mass, which leads to an enclosed baryon fraction (f_b) of $\sim 11\%$ within R_{200} of MKW4, still significantly lower than the cosmic f_b .

Similar discrepancies have been found in galaxies (e.g., Fukugita et al., 1998; Hoekstra et al., 2005; Dai et al., 2010), the so called “missing baryon problem”, which remains a grand challenge problem in understanding the galaxy evolution (e.g., Fukugita et al., 1998; Dai et al., 2010). In the case of MKW4, internal heating caused by AGN feedback may have pushed the hot gas towards larger radii or even expelled it from the system (e.g., Metzler and Evrard, 1994; Bower et al., 2008), which reduces the amount of hot gas, hence the baryon fraction. Alternatively, a significant amount of hot gas associated with the individual galaxies may have condensed and cooled out of the X-ray emitting ICM and reside in the Circumgalactic Medium (CGM) in the form of cold gas (e.g., Fielding et al., 2017) that is undetectable in X-ray and near-infrared (K_s band). Massive systems such as clusters of galaxies typically have a f_b consistent with the cosmic f_b at the virial radii (e.g., Walker et al., 2012; Bonamente et al., 2013), while the f_b of galaxies is approximately 7% (Hoekstra et al., 2005) at their virial radii.

We note that MKW4, as a galaxy group, has a f_b within R_{200} between those of galaxies and clusters. We compare our estimated f_{gas} at R_{200} ($f_{\text{gas},200}$) with those of other clusters and groups as a function of cluster temperature at R_{200} , as shown in Figure 2.13. The $f_{\text{gas},200}$ of lower-mass clusters tend to stay below the cosmic baryon fraction. In contrast, the intermediate and higher-mass clusters have $f_{\text{gas},200}$ consistent with the cosmic baryon fraction. Gravitational potential may have played a critical role in retaining hot baryons inside a galaxy cluster.

The measured $f_{\text{gas},200}$ of PKS 0745, Perseus, and A2319 exceed the cosmic baryon fraction. The $f_{\text{gas},200}$ of PKS 0745 and Perseus were measured with *Suzaku* alone, which may introduce positive bias in the gas mass measurement due to unresolved cool gas clumps at their outskirts. A2319 is a merging cluster, for which Ghirardini et al. (2018) report a substantial non-thermal pressure support at its outskirts, which may have biased the hydrostatic mass low. Our estimated $f_{\text{gas},200}$ in MKW4 is consistent with other groups of similar masses, as seen in Figure 2.13. The low $f_{\text{gas},200}$ found in MKW4 implies that its X-ray hydrostatic mass is unlikely to be underestimated at R_{200} .

2.5.3 Azimuthal Scatter

Azimuthal variations in the ICM properties may arise for different reasons, including unresolved substructures, mergers, and gas clumping (e.g., Miller et al., 2012; Su et al., 2015). We adopt the formula given by Vazza et al. (2011) to evaluate the azimuthal scatter of different gas properties at the outskirts of MKW4 and compare

[§]<https://irsa.ipac.caltech.edu/applications/2MASS/IM/interactive.html>

our results with the other clusters and groups-

$$S_c(r) = \sqrt{\frac{1}{N} \sum_i \frac{[y_i(r) - Y(r)]^2}{[Y(r)]^2}}, \quad (2.18)$$

where $y_i(r)$ is the radial profile of a quantity for the i^{th} -section, $Y(r)$ is the azimuthal average of that quantity, and N is the total number of sections. We obtain azimuthal scatters of gas properties at R_{200} of MKW4, as shown in Figure 2.14. We find $S_c(R_{200}) = 0.041 \pm 0.012$ in temperature, 0.191 ± 0.036 in density, 0.052 ± 0.019 in entropy, 0.149 ± 0.037 in pressure, and 0.020 ± 0.009 in the gas mass fraction.

Numerical simulations show that the azimuthal variation in gas density and temperature rises to $\sim 10\%$ at R_{200} for relaxed clusters, while it increases to $\sim 50\text{-}80\%$ for perturbed clusters (Vazza et al., 2011), as shown in Figure 2.14. The azimuthal scatters of the gas properties at the outskirts of MKW4 are consistent with the expectation for relaxed clusters. We also compare our results with a number of galaxy clusters observed with *Suzaku* out to R_{200} with $N = 3$ or more azimuthal coverages, as shown in Figure 2.14. The azimuthal variations in temperature and entropy of MKW4 are significantly smaller among those clusters. The similar ICM properties at R_{200} in the north, east, and north-east directions confirm that MKW4 is a spherically symmetric relaxed system, and the hydrostatic equilibrium is likely to be a good approximation even out to its virial radii.

2.6 Summary

We have analysed joint *Suzaku* and *Chandra* observations of the galaxy group MKW4 and measured its ICM properties from its center out to the virial radius. We have derived the radial profiles of gas density, temperature, entropy, pressure, and gas mass fraction in three different directions. Our findings are summarized below.

- Using *Chandra* observations of MKW4, we have resolved much of the CXB at its center and three outskirt regions. We are able to model the contamination from point sources in *Suzaku* data and greatly reduce the uncertainties in the measurement of ICM properties.
- The 3D gas densities of MKW4 decline to $\sim 10^{-5} \text{ cm}^{-3}$ at its outskirts and are consistent among the three directions. The 3D temperature profiles decline from 2.2 keV at $0.1R_{200}$ to ~ 1.14 keV at the virial radius. The temperature profiles of MKW4 in the three directions follow the universal profiles derived by Loken et al. (2002) and Sun et al. (2009).
- The entropy profiles of MKW4 follow the baseline profile (Voit et al., 2005) beyond R_{500} in the north, east, and north-east directions, which indicates that the gas dynamics at the group outskirts is mainly regulated by the gravitational collapse. Our results also show entropy excess towards the group center compared to the baseline profile, suggesting that the central AGN of MKW4 may have redistributed the hot gas.

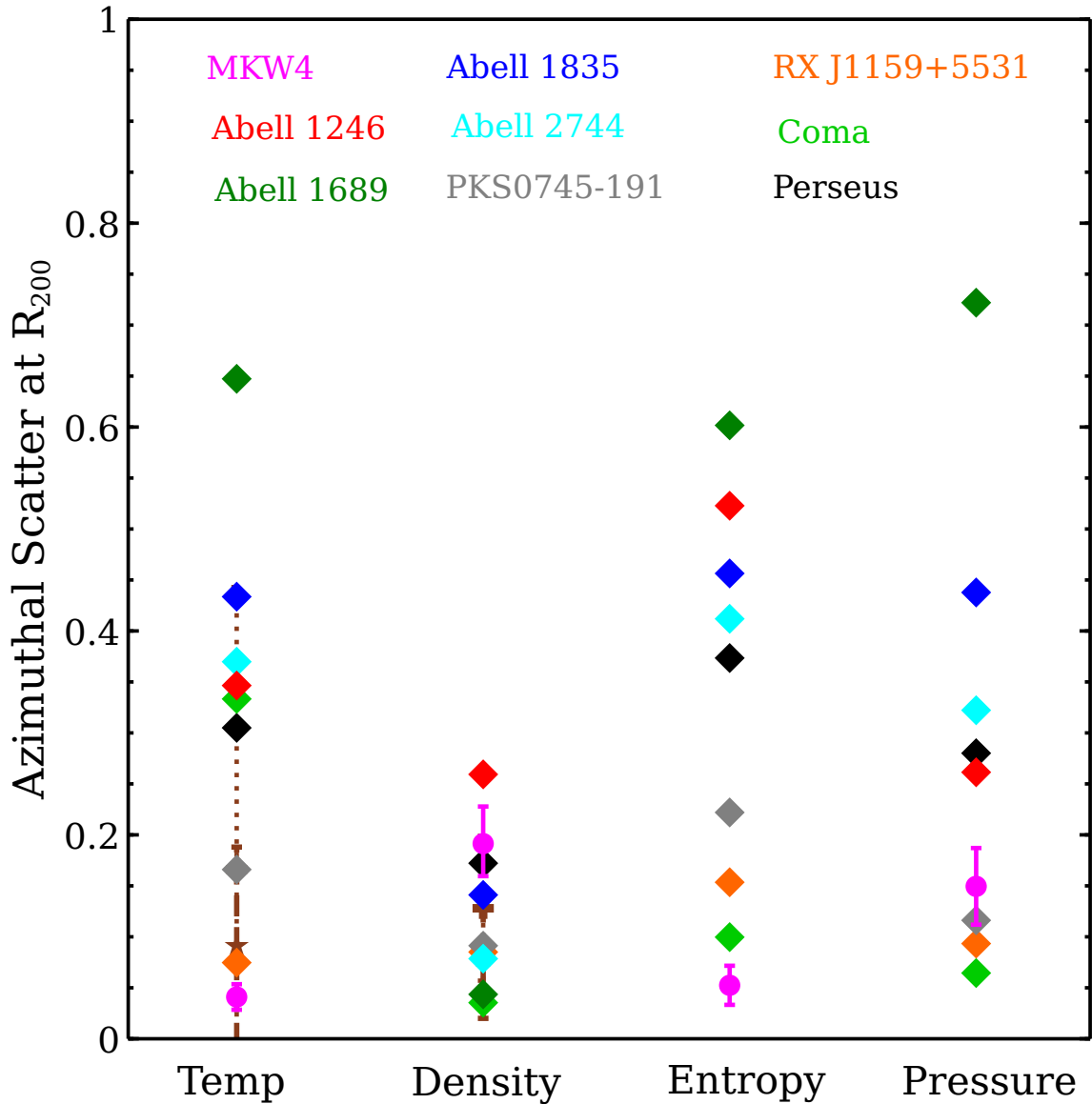


Figure 2.14: Azimuthal scatter of gas properties at R_{200} of MKW4. We compare our results with azimuthal variations in other clusters, e.g., A1246: Sato et al. (2014); A1689: Kawaharada et al. (2010); A1835: Ichikawa et al. (2013); A2744: Ibaraki et al. (2014); PKS0745-191: George et al. (2009); RJX1159+5531: Su et al. (2015); Coma: Simionescu et al. (2013); Perseus: Urban et al. (2014). Dashed brown line: the azimuthal variation in relaxed simulated clusters from Vazza et al. (2011). Dotted brown line: the azimuthal variation in perturbed simulated clusters from Vazza et al. (2011).

- We estimated the total X-ray hydrostatic mass of MKW4, $M_{\text{tot}}(< R_{500}) \approx 6.5 \pm 1.0 \times 10^{13} M_{\odot}$ and $M_{\text{tot}}(< R_{200}) \approx 9.7 \pm 1.5 \times 10^{13} M_{\odot}$. Our measurement shows that its baryon fraction is only $\sim 11\%$ at the virial radii, which is lower than the cosmic baryon fraction (Komatsu et al., 2011; Planck Collaboration et al., 2014). The lower baryon fraction implies that the central AGN feedback or galactic winds may have expelled much of its hot gas at its early epoch, or/and the hot gas associated with the individual galaxies may have condensed and cooled out of the X-ray emitting ICM and reside in the CGM in the form of cold gas.
- The azimuthal scatter in gas properties at the outskirts of MKW4 is small, suggesting that it is a remarkably relaxed system and the bulk of its ICM is likely to be in hydrostatic equilibrium.

Chapter 3 Chemical abundances in the outskirts of nearby galaxy groups measured with joint *Suzaku* and *Chandra* observations

3.1 Introduction

Big Bang nucleosynthesis primarily produced all the hydrogen and helium of the Universe and few lighter elements like Li and Be. Heavier elements are later forged in stars. Clusters of galaxies with their deep gravitational potential wells retain substantial X-ray emitting hot gas ($T \sim 10^7\text{--}10^8$ K), the so called intracluster medium (ICM) (Ettori and Fabian, 1999). A dominant fraction of metals in the local Universe can be found in the ICM, making them a unique astrophysical laboratory to probe the nucleosynthesis and chemical enrichment histories of the Universe (Biffi et al., 2018; Mernier et al., 2018a).

The enrichment processes in the ICM remains an open question. In the late enrichment scenarios (after the cluster is assembled), the ICM metal distributions are expected to be non-uniform with a significant amount of azimuthal scatters (Domainko et al., 2006). For instance, the galactic materials can be stripped off from the galaxies and deposited in the ICM as the infalling galaxies interacting with the dense gas (e.g., Gunn and Gott, 1972; Fabjan et al., 2010), which enriches the ICM along the directions of infalling galaxies. Also, the metals dispersed into the ICM at later times should broadly follow the spatial distributions of galaxies, leading to flat metal mass-to-light ratios (Matsushita et al., 2013). Neither of these is consistent with the observations. Nearby massive clusters, such as Perseus, show a remarkably homogeneous Fe abundance of $\sim 0.3 Z_{\odot}$ at $R > 0.25R_{200}^{\dagger}$ (Urban et al., 2017; Werner et al., 2013). Previous studies, using *Chandra*, *Suzaku*, and *XMM-Newton* observations, have reported steep iron mass-to-light ratios (IMLRs) for several galaxy clusters out to $0.2\text{--}0.5R_{200}$ (e.g., Matsushita et al., 2007; Sato et al., 2009; Simionescu et al., 2011), which indicates that metal mass is more extended than the distribution of cluster galaxies. Although, the ICM can achieve a uniform distribution of metals in the late enrichment process via large scale sloshing motion, the steep entropy profiles of galaxy clusters may prevent the efficient mixing up of metals across the large radial bins (Domainko et al., 2006; Werner et al., 2013; Ghizzardi et al., 2014).

The observed uniform Fe abundances and steep IMLR profiles suggest an early enrichment scenario in which most of the enrichment occurred in the proto-cluster environment (e.g., Fabjan et al., 2010; Biffi et al., 2017). This process is primarily driven by the galactic winds and active galactic nuclei (AGN) feedback at the epoch of the peak star formation (around $z \sim 2\text{--}3$; Madau and Dickinson, 2014). The strong galactic winds and AGN activity may have expelled much of the metals from the inter-stellar medium (ISM) and uniformly mixed the inter-galactic gas even before the cluster is assembled.

[†] R_{Δ} the radius from within which the average matter density is Δ times the critical density of the Universe.

With the better understanding of the stellar nucleosynthesis over the past decades, it is now evident that most of the lighter elements like O, Mg, and Ne are synthesized by massive stars and expelled into the ICM by core-collapsed supernovae (SNcc) (e.g., Nomoto et al., 2006), while the heavier elements like Ar, Ca, Fe, and Ni are primarily produced by Type Ia supernovae (SNe Ia) (e.g., Iwamoto et al., 1999; Sarkar et al., 2021a). Elements like Si and S are produced relatively comparably by both SNe Ia and SNcc (e.g., de Plaa et al., 2007). Therefore, the metal abundance pattern of heavier elements strongly depends on the SNe Ia explosion mechanism and the abundances of lighter elements depend on the stellar initial mass function (IMF) of galaxies (Mernier et al., 2015, 2016b). The measurement of the abundance profiles of those metals is crucial to constrain supernovae models and to probe the chemical enrichment history of the ICM.

The α -capture (such as O, Mg, Ne, Si, S) and Fe peak elements (such as Cr, Mn, Fe, Co, Ni) can be observed from their emission lines in X-ray. Most of these emission lines originate from the K and L – shell transitions in highly ionised plasma (see Chakraborty et al. 2020a,b). Since the ICM is very close to collisional ionization equilibrium and optically thin, the equivalent widths of those emission lines can easily be converted to element abundances (Böhringer and Werner, 2010; Mernier et al., 2016a; Urban et al., 2017). Using *Chandra* observations, Rasmussen and Ponman (2007) have found that Si/Fe ratio increases with radius, strongly suggesting an excess of SNe Ia contribution at cluster center, while SNcc contribution dominates at the outskirts. Later on, however, it was observed in M87 that the Si abundance profile is even more centrally peaked than Fe (Million et al., 2011). Most recently, an extensive *Suzaku* investigation of the nearby Virgo cluster reveals a SNIa fraction of 12–37% throughout its ICM, which challenges the pure SNcc enrichment at the cluster outskirts (Simionescu et al., 2015). Nowadays, the current view is same abundance profiles for all elements.

The enrichment process in lower mass systems (groups) is even less clear (Gastaldello et al., 2021). With deep gravitational potential wells, galaxy clusters behave like closed-box systems, holding all of the metals ever produced by the stars inside their virial radius (e.g., de Plaa et al., 2007) In contrast, galaxy groups have shallow gravitational potential well, which makes them vulnerable to losing material via non-gravitational processes, such as galactic winds driven by supernovae (SNe) and AGN feedback (e.g., Rasmussen and Ponman, 2007; Lovisari et al., 2015; Thölken et al., 2016). These processes may expel much of its enriched gas out of the system (Sarkar et al., 2021b). Using *ASCA* data, Makishima et al. (2001) found that the IMLRs in galaxy groups within $0.5 R_{200}$ increases with their masses, while those of galaxy clusters are not mass dependent and are systematically higher than groups. The detailed study of metal budgets out to the virial radius of groups are relatively unexplored due to their low surface brightness. The emission from the outskirts of groups is typically dominated by X-ray background, which makes the measurement of metal abundances very challenging (Rasmussen and Ponman, 2009). *Suzaku*, with its stable particle background and higher spectral sensitivity below 1 keV (Koyama et al., 2007), can measure the metal abundances more precisely at R_{200} and beyond. The inclusion of snapshot *Chandra* observations resolves much of the Cosmic X-ray

Table 3.1: Observational log

Name	Obs Id	Obs Date	Exp. (ks)
<i>Suzaku</i>			
MKW4 central	808066010	2013 Dec 30	34.6
MKW4 Offset 1	805081010	2010 Nov 30	77.23
MKW4 N2	808067010	2010 Nov 30	97
MKW4 Offset 2	805082010	2010 Nov 30	80
MKW4 E1	808065010	2013 Dec 29	100
MKW4 NE	809062010	2013 Dec 29	87.5
Antlia E0	802035010	2007 Nov 19	55
Antlia E1	807066010	2012 Jun 13	20
Antlia E2	807067010	2012 Jun 14	21
Antlia E3	807068010	2012 Jun 15	19
Antlia E4	807069010	2012 Jun 16	17
Antlia E5	807070010	2012 Jun 17	39
Antlia EB	807071010	2012 Jun 18	38
RXJ1159 N	804051010	2009 May 02	84
RXJ1159 S	807064010	2012 May 27	81
	807064020	2012 Dec 18	21
RXJ1159 E	809063010	2014 May 29	96
RXJ1159 W	809064010	2014 May 31	94
ESO3060170 central	805075010	2010 May	27
ESO3060170 offset	805075060	2010 May	70
<i>Chandra</i>			
MKW4 central	3234	2002 Nov 24	30
MKW4 N2	20593	2019 Feb 25	14
MKW4 E1	20592	2018 Nov 17	15
MKW4 NE	20591	2019 Mar 08	14
Antlia E1	15090	2013 Nov 20	7
Antlia E2	15089	2013 Nov 22	7
Antlia E3	15088	2013 Jul 02	7
Antlia E4	15086	2013 Nov 04	7
Antlia E5	15085	2013 Apr 05	7
Antlia EB	15087	2013 Nov 04	7
RXJ1159 central	4964	2004 Feb 11	76
RXJ1159 NW	14026	2012 Aug 09	50
RXJ1159 NE	14473	2012 Aug 12	37
	14027	2012 Aug 09	13
ESO3060170 central	3188	2002 March 08	14.06
ESO3060170 offset	17219	2015 Oct 09	9.84

Table 3.2: Properties of the groups

Name	peak temp (keV)	R ₂₀₀ (kpc)	z	scale (1") (kpc)	CC/NCC
MKW4	2.2	884	0.02	0.443	CC
Antlia	2.3	887	0.009	0.213	NCC
RXJ1159	2.5	871	0.081	1.583	CC
ESO3060170	2.7	1150	0.0358	0.73	CC

Background (CXB), which is crucial to pin down the systematic uncertainty.

In this paper, we study the metal abundances of four galaxy groups MKW4, Antlia, RXJ1159+5531 (hereafter RXJ1159), and ESO3060170 from their centers out to R₂₀₀ with *Suzaku* and *Chandra*. Their peak temperatures (just outside the group core at $\sim 0.25 R_{200}$) are 2.2 keV, 2.3 keV, 2.5 keV, and 2.7 keV, respectively. To our knowledge, they are the lowest mass systems that have their gas properties constrained at R₂₀₀. MKW4, RXJ1159, and ESO3060170 are cool core systems, while Antlia is a non-cool-core group. The thermodynamic properties of these four galaxy groups out to their virial radii are reported in Sarkar et al. (2021b), Wong et al. (2016), Su et al. (2015), and Su et al. (2013), respectively. Unlike massive galaxy clusters, these groups do not show obvious flattening of their entropy profiles at large radii. We use NASA/IPAC Extragalactic Database[‡] to estimate the luminosity distance for MKW4, Antlia, RXJ1159, and ESO3060170, by adopting a cosmology of H₀ = 70 km s⁻¹ Mpc⁻¹, $\Omega_{\Lambda} = 0.7$, and $\Omega_{\text{m}} = 0.3$. Table 3.2 outlines the physical properties of four groups. We assume a solar abundance table of Asplund et al. (2009) throughout this paper. All uncertainties are reported at 1 σ confidence level.

3.2 Observations and Spectral analysis

MKW4 has been observed with *Suzaku* and *Chandra* in three different directions (north, east, and north-east). Antlia and ESO3060170 have been mapped in one direction, east and south, respectively. RXJ1159 has been observed with full azimuthal coverage. The detailed observations are listed in Table 4.1. The exposure corrected and background subtracted mosaic *Suzaku* images of four groups in the 0.5–2.0 keV energy band are shown in Figures 3.5, 3.6, 3.7, and 3.8, respectively. We followed the data reduction procedure described in Sarkar et al. (2021b) for MKW4, Wong et al. (2016) for Antlia, Su et al. (2015) for RXJ1159, and Su et al. (2013) for ESO3060170. In short, we extracted spectra from several annular regions from the center out to the virial radius of each group, as marked in green annular sectors in Figures 3.5, 3.6, 3.7, and 3.8. We generated redistribution matrix files (RMF) and instrumental background files (NXB) for all regions and detectors. For each region, one ancillary response file (ARF) was generated using a β -profile image to model the ICM component; another ARF was produced for a uniform emission in a circular region of 20' radius to model the sky X-ray background.

[‡]<http://ned.ipac.caltech.edu>

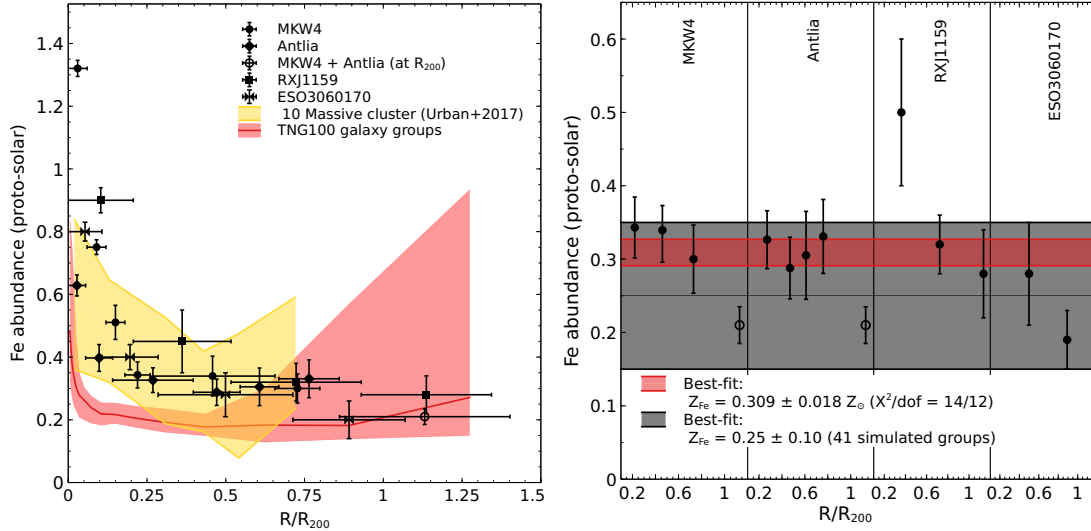


Figure 3.1: Left: Fe profiles obtained from the 2T vapec model. All abundances are in the solar unit. We assume a solar abundance table of Asplund et al. (2009). Yellow shaded region represents the measurement of Fe abundance in 10 massive clusters (Urban et al., 2017). Black shaded region shows average Fe abundance profile with 16–84 percentile error, obtained from 41 galaxy groups in TNG100. Right: Iron abundances at $R > 0.25R_{200}$ of individual groups. The red shaded region indicates average iron abundance for 0.25-1.0 R_{200} with 1σ uncertainty. The black shaded region represents average iron abundance at $R > 0.25R_{200}$ for 41 galaxy groups in TNG100. Open circles represent Fe abundance at R_{200} of Antlia and MKW4, measured jointly.

Spectral analysis was performed using XSPEC--12.10.1 and Cash statistics (Cash, 1979). We fit the spectra extracted from XIS0, XIS1, and XIS3 simultaneously. For MKW4, the spectral fitting was restricted to the energy range of 0.4 - 7 keV for XIS1 and 0.6 - 7 keV for XIS0 and XIS3 (Sarkar et al., 2021b), while the energy range of 0.5-7 keV was used for the other three groups. We fit each spectrum with a multi-component X-ray background model and a thermal emission model. For X-ray background model, we adopted $-\text{phabs}(\text{pow}_{\text{resolvedCXB}} + \text{pow}_{\text{unresolvedCXB}} + \text{apec}_{\text{MW}}) + \text{apec}_{\text{LHB}}$. The $\text{pow}_{\text{resolvedCXB}}$ component represents the point sources resolved by *Chandra*[§]. A mosaic image of *Chandra* observations of each group in the 0.5–7.0 keV energy band is shown in Figures 3.5, 3.6, 3.7, and 3.8 with all resolved point sources marked in green elliptical regions. The second power-law component ($\text{pow}_{\text{unresolvedCXB}}$) describes the unresolved point sources. The two thermal apec components model the foreground emissions from Milky Way (apec_{MW}) and Local Hot Bubble (apec_{LHB}).

To account for the ICM emission for each annulus, two thermal vapec components associated with a photoelectric absorption (phabs) component - $\text{phabs} \times (\text{vapec} +$

[§]We produce synthetic *Suzaku* observations for each point source using xissim based on their position and flux determined by *Chandra*. We extract spectra from these synthetic *Suzaku* observations using the same extraction regions as the radial profiles. Those spectra are then fit to a powerlaw model with an index of 1.41 to obtain the normalization of $\text{pow}_{\text{resolvedCXB}}$.

vaptec) were fitted to the spectra of each group* The galactic hydrogen column densities in the direction of MKW4, Antlia, RXJ1159, and ESO3060170 were obtained using HEASARC N_{H} tool[¶]. We link the temperature of the cooler component of each region to half that of the hotter component. The normalizations of both components are allowed to vary freely. The best-fit spectral models for the outermost regions of the four groups are shown in Figure 3.9.

For MKW4 and Antlia, we fit spectra from the regions at different azimuthal directions simultaneously. We let the temperatures and normalizations to vary freely among different regions, while linking the abundances of the regions that are at the same distance from the group center. We allow the abundances of O, Mg, Si, S, Fe, and Ni to vary freely, while rest of the elements were varied collectively. The abundances of Ar and Ca were linked to S. For Antlia, we are unable to constrain the S abundance for E2 and E3, for which we set Si=S. For the outer three regions of MKW4 at R_{200} and the outer two regions of Antlia at R_{200} (E4 and E5), we did not find any good constraint on their metal abundances when fitted individually. Therefore, we performed a simultaneous fitting for all those 5 regions. Their temperatures and normalizations were allowed to vary freely but with their metallicities linked. The virial temperatures of MKW4 and Antlia are nearly the same. Both groups display entropy profiles rising all the way to R_{200} . The distance of MKW4 is twice that of Antlia, which makes the outermost regions of MKW4 ($R = 706\text{-}1200$ kpc) cover almost the same physical radial range as the outermost two regions in Antlia ($R = 828\text{-}1302$ kpc). It is therefore reasonable to assume that they have similar metallicities at R_{200} .

For RXJ1159 and ESO3060170 we set their Ni abundance to $1 Z_{\odot}$ (the best-fit for MKW4 and Antlia) as we could not find a good spectral fit when letting it vary freely. The rest of the elements were allowed to vary as described for MKW4 and Antlia. We also find it necessary to link the abundance of region 3 to region 4, and region 5 to region 6 for ESO3060170 (the temperature and normalization of each region is free to vary). We did not perform any deprojection during spectral fitting since it may introduce systematic noise (Nulsen and Böhringer, 1995; McLaughlin, 1999). The best-fit Fe, O, Mg, Si, S, and Ni profiles of each group are shown in Figures 3.5, 3.6, 3.7, and 3.8.

3.3 Results

3.3.1 Fe abundance profiles

We obtain the abundance profiles of Fe from the centers of these four groups out to their R_{200} , as shown in Figure 3.1 and Figures 3.5, 3.6, 3.7, and 3.8. Within

*The Fe abundance measurement is biased low when fitting multi-phase gas with a single temperature model (e.g., Buote and Fabian, 1998; Buote, 2000; Gastaldello et al., 2021). Given *Suzaku*'s modest angular resolution, each radial bin covers a sizable physical region, likely associated with temperature variation even at cluster outskirts. When fitting a single temperature spectrum generated with Xspec *fakeit* to our 2T model, no bias to the metal abundance measurement is found. Therefore, our model should not introduce any bias if even the gas is single phase.

¶<http://heasarc.gsfc.nasa.gov/cgi-bin/Tools/w3nh/w3nh.pl>

0.25 R_{200} , their Fe abundances all increase towards their centers with MKW4 showing the strongest gradient reaching $1.3 Z_{\odot}$. This may be partially due to the smaller radial bin width that has been resolved for MKW4. The Fe abundance profile of Antlia is much flatter at $R > 0.05R_{200}$ with the smallest Fe increase to $0.6 Z_{\odot}$ at $R < 0.05R_{200}$. Unlike the other three groups, Antlia is a non-cool-core system. The mechanism that has disrupted their cores, such as major merger, may have redistributed their central metal content at $R > 0.05R_{200}$ (e.g., Murray et al., 2018; Lovisari and Reiprich, 2019).

Despite the fact that these systems show a variety of Fe abundances at their centers, the Fe abundance profiles start to converge outside their cores. At the group outskirts, the Fe abundances are mostly consistent within uncertainties. We measure an average Fe abundance of $0.309 \pm 0.018 Z_{\odot}$ ($\chi^2 = 14$ for 12 degrees of freedom) over the radii of 0.25–1.0 R_{200} . This is strikingly similar to what was found for 10 nearby massive clusters with a Z_{Fe} of $0.316 \pm 0.012 Z_{\odot}$ ($\chi^2 = 28.85$ for 25 degrees of freedom) over their 0.25–1.0 R_{200} (Urban et al., 2017) using the same Solar abundance table of Asplund et al. (2009).

We compare the measured Fe abundance at $R > 0.25R_{200}$ of four groups with that of simulated groups, as shown in Figure 3.1. We use IllustrisTNG100, which is a simulation run in the IllustrisTNG project (e.g., Naiman et al., 2018; Springel et al., 2018; Nelson et al., 2018; Marinacci et al., 2018; Pillepich et al., 2018), to make prediction for iron abundance at group outskirts. The simulated volume is $(110.7 \text{ Mpc})^3$ providing 41 simulated groups, which are defined as Friend-of-Friend halos within the mass range $M_{200} \sim 5 \times 10^{13} - 4 \times 10^{14} M_{\odot}$ at $z=0$. The abundance is measured within the range of $[0.25-1]R_{200}$ and it is computed as an X-ray emission-weighted quantity, in which the X-ray emission of each simulated gas cell is obtained based on the gas thermodynamics, e.g. gas density, temperature, and metallicity, assuming a APEC plasma model.

We compare the Fe radial profiles of four groups derived in this work with the average Fe profile predicted by the TNG100 simulations. The mean emission-weighted Fe profile, derived from a sample of 41 simulated galaxy groups in the considered mass range, shown in grey in Figure 3.1, agrees well with our observations at $R > 0.5R_{200}$. At $R < 0.5R_{200}$, simulations predict lower Fe abundances by a factor of ~ 2 compared to the observations. Similar discrepancies also been found by Mernier et al. (2018b) and Leccardi and Molendi (2008), while comparing the Fe abundance profiles with the hydrodynamic simulations. Planelles et al. (2014) argue that this discrepancy can be explained by the outdated assumptions on the SNe yields, the assumed initial mass function, the fraction of binary systems, and/or the SNe efficiency of releasing metals into the ICM (Mernier et al., 2018b).

Simulations show large scatter in the Fe profile at the central region and at the outskirts, as seen in Figure 3.1 left. While the former one reflects the diversity of the group cores, the latter could be explained due to the presence of satellites and high-density clumps at the outskirts. The average Fe abundance of simulated groups in $0.25R_{200} < R < R_{200}$ is in agreement with the observations, as shown in Figure 3.1 right.

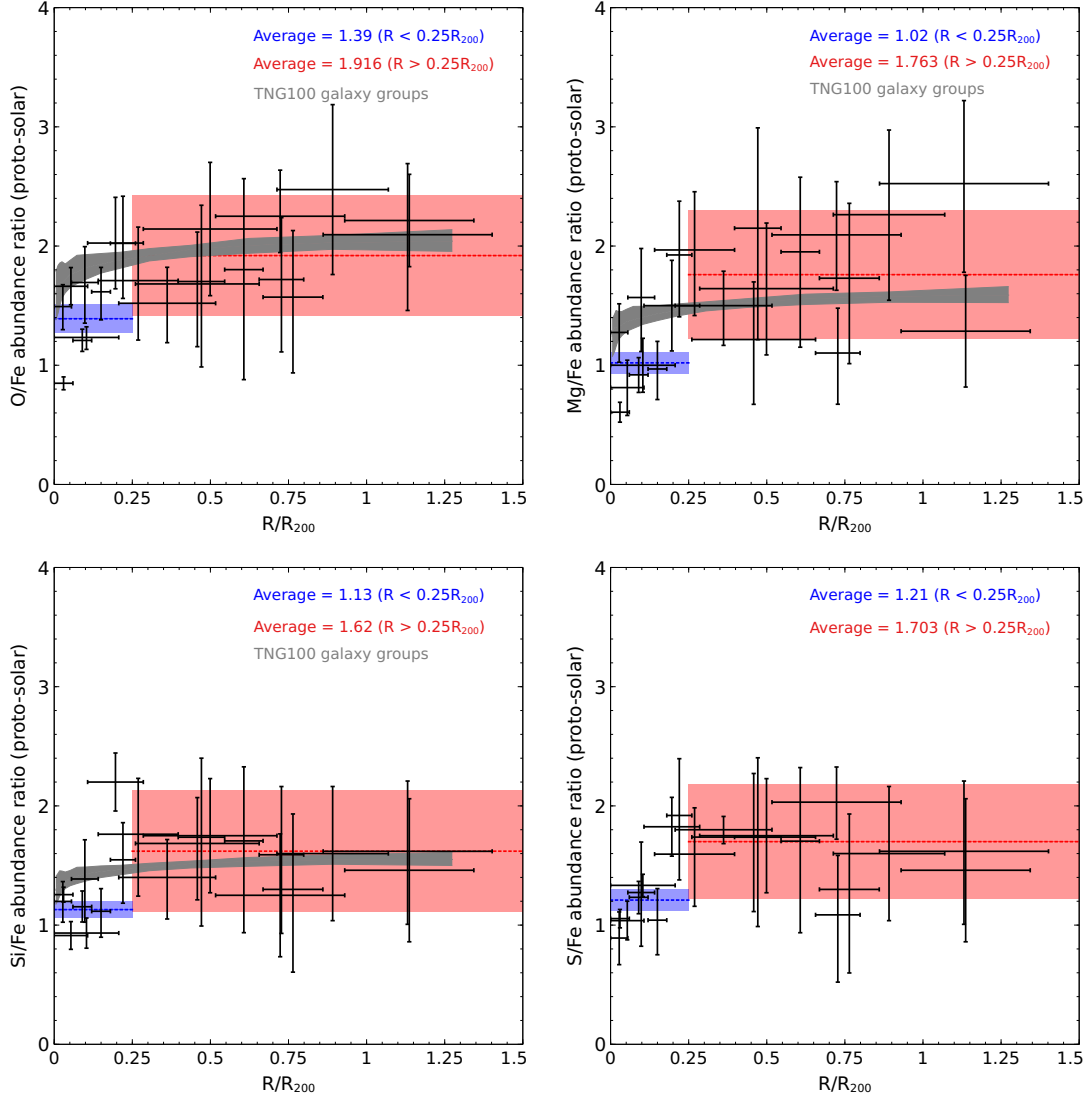


Figure 3.2: X/Fe ratios as a function of radius for individual metals. The red shaded region represents the average X/Fe excluding central $R < 0.25R_{200}$ region. The blue shaded region represents the average X/Fe for the central $R < 0.25R_{200}$ region. Black shaded region shows the average X/Fe profile of 41 galaxy groups in TNG100.

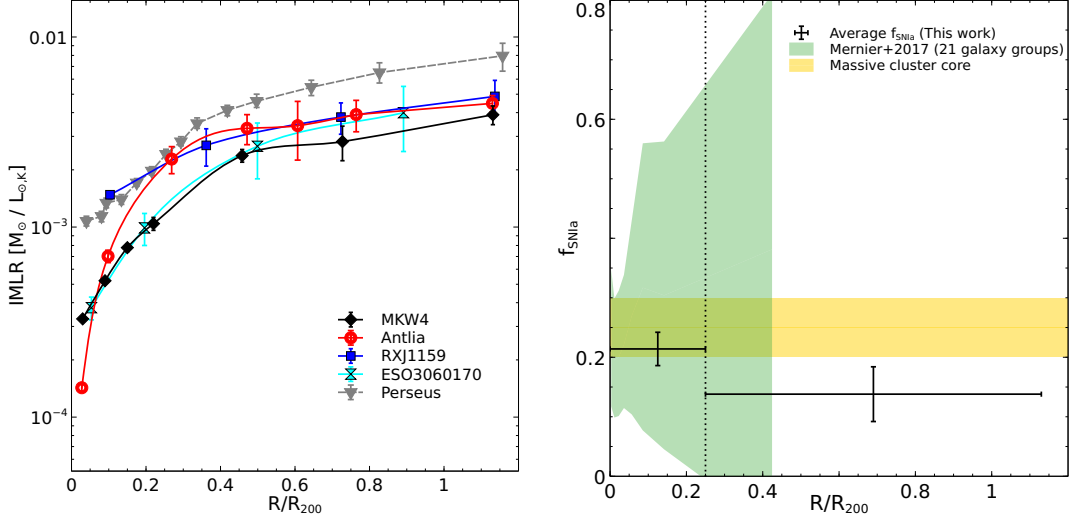


Figure 3.3: *Left*: Radial profiles of IMLR with K_s-band luminosity for groups in our sample and the Perseus cluster. We obtain IMLR of Perseus from Matsushita et al. (2013). *Right*: The averaged f_{SNIa} for the four groups at $R < 0.25R_{200}$ and $0.25R_{200} < R < R_{200}$. Green shaded region represents the measurement scatter obtained from a large number of groups (Mernier et al., 2017). Yellow shaded region indicates the limit of f_{SNIa} at the massive cluster core (de Plaa et al., 2007). Vertical dotted line indicates $0.25R_{200}$.

3.3.2 Chemical composition

In addition to Fe, we have further constrained the abundance profiles of O, Mg, S, Si, and Ni as shown in Figures 3.5, 3.6, 3.7, and 3.8. We derive their abundance ratios relative to Fe as a function of radius from the centers out to the virial radii as shown in Figure 3.2. The uncertainties are calculated using Monte Carlo simulations with 2000 - 3000 realizations. We observe that the X/Fe ratios are consistent with the solar abundance within $R < 0.25R_{200}$, with $\text{O/Fe} = 1.39 \pm 0.12$ ($\chi^2/\text{degrees of freedom} = 16.7/6$), $\text{Mg/Fe} = 1.02 \pm 0.09$ ($\chi^2/\text{degrees of freedom} = 17.6/5$), $\text{Si/Fe} = 1.13 \pm 0.07$ ($\chi^2/\text{degrees of freedom} = 10.5/6$), $\text{S/Fe} = 1.21 \pm 0.09$ ($\chi^2/\text{degrees of freedom} = 11.6/7$), and $\text{Ni/Fe} = 1.82 \pm 0.29$ ($\chi^2/\text{degrees of freedom} = 16.5/4$), which is similar to what have been measured for group centers such as the CHEERS project (Mernier et al., 2018b). The X/Fe ratios over $0.25R_{200} < R < R_{200}$ are somewhat super solar with $\text{O/Fe} = 1.92 \pm 0.51$ ($\chi^2/\text{degrees of freedom} = 5.2/12$), $\text{Mg/Fe} = 1.76 \pm 0.54$ ($\chi^2/\text{degrees of freedom} = 10/12$), $\text{Si/Fe} = 1.62 \pm 0.51$ ($\chi^2/\text{degrees of freedom} = 8/12$), $\text{S/Fe} = 1.70 \pm 0.48$ ($\chi^2/\text{degrees of freedom} = 6/12$), and $\text{Ni/Fe} = 3.60 \pm 1.50$ ($\chi^2/\text{degrees of freedom} = 3.4/6$).

We compare the O/Fe, Mg/Fe, and Si/Fe ratios of four groups with that of simulated groups, as shown in Figure 3.2. Since TNG simulations does not include S abundance, we could not compare measured S/Fe ratio with the simulation. Our measured abundance ratios for O/Fe, Mg/Fe, and Si/Fe are consistent with the simulated groups within their 1σ error bars.

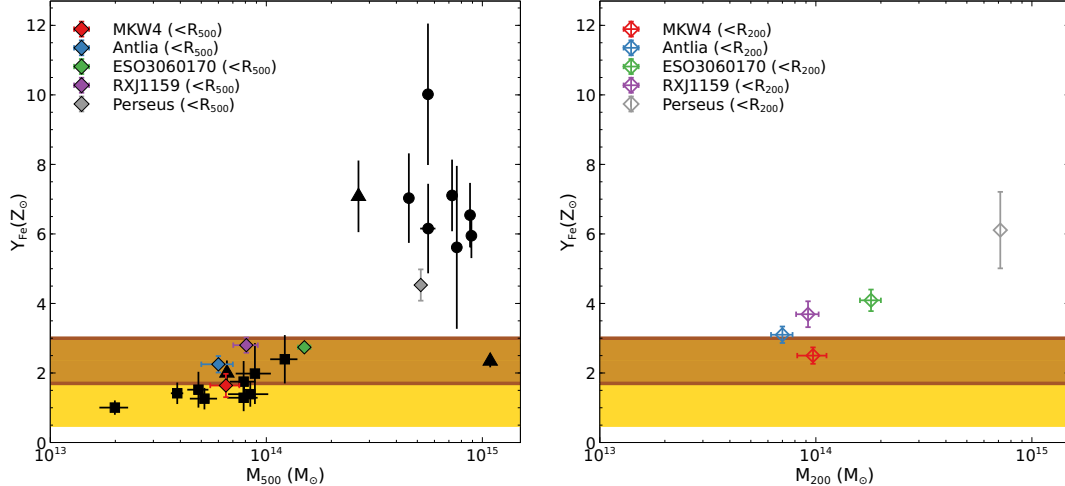


Figure 3.4: *Left*: Effective Fe yield as a function of cluster/group mass within R_{500} . Circles represent Fe yield for the cluster in the sample of Ghizzardi et al. (2021), squares represent the groups in the sample of Renzini and Andreon (2014), triangles represent NGC 1550, Hydra A, and Coma in the sample of Sasaki et al. (2014). Yellow shaded region shows the expected value estimated from the SN yields derived from Maoz and Graur (2017) and Renzini and Andreon (2014). The brown shaded region shows the expected value calculated assuming higher SNIa rate from Freundlich and Maoz (2021). *Right*: Effective Fe yield as a function of cluster/group mass within R_{200} .

3.3.3 Iron mass-to-light ratios

We investigate the IMLR from the centers out to the virial radii of these groups to compare the Fe distribution in the IGrM with their stellar mass profiles. We use the metal abundance profiles obtained in this work and the deprojected density profiles of MKW4, Antlia, RXJ1159, and ESO3060170 derived in Sarkar et al. (2021b), Wong et al. (2016), Su et al. (2015), and Su et al. (2013), respectively, to calculate the accumulated iron mass within a specific radius for each group. We estimate the K_s -band luminosity of each group using Two Micron All-Sky Survey (2MASS[‡]). We obtain a $2^\circ \times 2^\circ$ mosaic image centered at each group from the 2MASS data catalogue. We adopt the Galactic extinction (A_K) values for both groups from NASA/IPAC Extragalactic Database[†]. We deproject the K_s -band luminosity with radius and the resultant luminosity profiles are used to calculate the cumulative IMLR. Figure 3.3 shows the IMLR of MKW4, Antlia, RXJ1159, and ESO3060170 from their centers out to the virial radii. The radial profiles of IMLR increase with radius for all groups, suggesting that their metal distribution is more extended than the galaxy light out to R_{200} . Their IMLR within R_{500} are within the scatter of what have been found for other groups (e.g., Sato et al., 2009), although that of RXJ1159 at $0.1 R_{200}$ is exceptionally high. The accumulated IMLR of these groups converge to $(4-5) \times 10^{-3}$

[‡]<https://irsa.ipac.caltech.edu/applications/2MASS/IM/interactive.html>

[†]<http://ned.ipac.caltech.edu>

$M_{\odot}/L_{K\odot}$ at R_{200} , which is half that of the Perseus cluster.

We estimate the Fe yield (Y_{Fe}), which is the ratio of total Fe mass released by stars to the total stellar mass formed for a given stellar population, as follows (Renzini and Andreon, 2014; Ghizzardi et al., 2021; Gastaldello et al., 2021)

$$Y_{\text{Fe},500} = \frac{M_{\text{Fe},500}^{\text{star}} + M_{\text{Fe},500}}{M_{\text{star},500}(0)} \quad (3.1)$$

where $M_{\text{Fe},500}$ is the Fe mass within R_{500} , $M_{\text{Fe},500}^{\text{star}}$ is the Fe mass locked into the stars within R_{500} , $M_{\text{star},500}(0)$ is the mass of gas within R_{500} that went into stars and whose present mass is reduced by a factor r_0^{-1} , i.e., $M_{\text{star},500}(0) = r_0 M_{\text{star},500}$ (Gastaldello et al., 2021), where r_0 is the return factor. We adopt $r_0 = 1/0.58$ following Renzini and Andreon (2014) and Gastaldello et al. (2021). Figure 3.4 shows the effective Fe yield of four galaxy groups within R_{500} and R_{200} , respectively. We compare Fe yield of four groups within R_{500} with the sample of clusters studied in Ghizzardi et al. (2021), the sample of groups studied in Renzini and Andreon (2014), and the systems studied in Sasaki et al. (2014). We adopt the expected values as estimated in Gastaldello et al. (2021). The Fe yields within R_{200} of four groups are significantly higher than that of R_{500} , which suggest that at the group scale feedback redistributes metals, may pushing (or preventing from collapse) a consistent fraction of them, out to R_{200} and beyond.

3.3.4 Supernovae yields

The yields of SNe Ia and SNcc are the major contributors to the metal enrichment of the ICM. We fit our measured metallicity distributions to the metallicity patterns predicted by several theoretical SNe Ia and SNcc nucleosynthesis models, following Mernier et al. (2016b). We fit the average metal abundance ratios of O/Fe, Mg/Fe, Si/Fe, and S/Fe for these groups to a combination of a single SNe Ia and a single SNcc model and allow the relative number of SNe Ia over the total number of SNe (denoted as f_{SNIa}) free to vary (Werner et al., 2006). Mernier et al. (2016b) and Simionescu et al. (2019) pointed out that existing SNe yield models cannot successfully reproduce the observed Ni/Fe ratios, which in turn introduces large errors in fitting parameters. We, therefore, exclude the Ni/Fe ratio from the fitting process. Since the α -capture elements—O, Mg are primarily produced by the SNcc and Si, S are produced by both SNcc and SNe Ia, their relative abundances compared to Fe, which is a major SNe Ia product, are sensitive to the fitting parameters. Our measured average abundance patterns for MKW4 and Antlia fit best with the delayed detonation (DDT) SNe Ia model of Badenes et al. (2006) and with the “classical” mass-dependent SNcc model of Nomoto et al. (2006) with a progenitor metallicity of $Z_{\text{init}} = 0.02 Z_{\odot}$. For RXJ1159 and ESO3060170, we obtain a best-fit by using SNe Ia model of Badenes et al. (2006) and SNcc model of Nomoto et al. (2013) and Sukhbold et al. (2016), respectively. We assume the SNcc yields are produced by the population of massive stars having a Salpeter IMF (Salpeter, 1955) with a common Z_{init} (e.g., Mernier et al., 2016b) throughout this paper. We next fit the metal abundance patterns at each radial bin of four groups to obtain their f_{SNIa} from the centers out to the virial radii. Figure 3.3

shows the f_{SNIa} averaged over two radial bins of $0 - 0.25R_{200}$ and $0.25 - 1.0R_{200}$. The derived f_{SNIa} decreases from 0.214 ± 0.028 at their centers to 0.138 ± 0.046 at the outskirts. Those values are broadly consistent with those of the core of massive galaxy clusters of 20%–30% (de Plaa et al., 2007; Simionescu et al., 2009) and our Milky Way of 15% (Tsujiimoto et al., 1995). We note that the SNe yields constitute a key source of bias in the above analysis. The SNe yield models suffer indeed from uncertainties up to a factor of 2 (e.g., Wiersma et al., 2009) and as a consequence the derived estimation of f_{SNIa} should be interpreted with caution (e.g., de Grandi and Molendi, 2009; Mernier et al., 2018b).

3.4 Systematic uncertainties

We test our results against possible systematic uncertainties introduced during spectral analysis, following Sarkar et al. (2021b). One of the most important and uncertain components of the X-ray background is CXB. To examine the systematic uncertainty associated with the CXB, we vary the normalization of the unresolved CXB component by 10% with a fixed power-law slope of $\Gamma = 1.41$. We obtain that the associated impacts on all the metal abundances are within the statistical error limit. Next, we estimate the systematic uncertainties introduced by two foreground components—MW and LHB. We vary their best-fit normalizations by 10%, which does not lead to any significant change in the measured metal abundances. Finally, we experiment with a 20% variation in Galactic column density (N_{H}), which also has no significant impact on the measured metal abundances.

3.5 Discussion

Using joint *Suzaku* and *Chandra* observations, we derived the abundance profiles of Fe, O, Mg, S, Si, and Ni for four nearby galaxy groups from their centers out to the virial radii. To our best knowledge, this is the first time that such measurements have been made for such low-mass systems. In the previous section, we show that our results are stable against various sources of systematic uncertainties. Below we compare the results with what we know from massive galaxy clusters and discuss the implications of our findings.

3.5.1 Early enrichment scenario

Previous studies have reported a universal Fe abundance of $\sim 0.3 Z_{\odot}$ at outskirts of nearby massive clusters using *Suzaku* observations (e.g., Werner et al., 2013; Urban et al., 2017). It has also been shown that no significant redshift evolution of the global metallicity ($R < R_{500}$) is found for high-redshift samples (e.g., McDonald et al., 2016; Mantz et al., 2017; Liu et al., 2020). These findings all point to an early-enrichment scenario that the ICM is enriched during the peak of star formation at $z = 2 - 3$ before the formation of galaxy clusters. The state-of-the-art hydrodynamical simulations have verified that the ICM can be substantially enriched during the peak of the star formation at $2 < z < 3$ (e.g., Biffi et al., 2017, 2018). Early AGN feedback may

have played an important role in displacing the metal-enriched gas produced within galaxies throughout the ICM (Truong et al., 2019).

We are able to constrain the metallicity profiles out to R_{200} for four galaxy groups with a temperature ~ 2.5 keV and with a mass of an order of magnitude smaller than massive clusters. We found a nearly flat Fe abundance profile over the radii of 0.25 - $1.0 R_{200}$, as shown in Figure 3.1, with an average $Z_{\text{Fe}} = 0.309 \pm 0.018 Z_{\odot}$, which is remarkably similar to that of the massive clusters. This $\text{Fe} \sim 0.3 Z_{\odot}$ uniform abundance distribution has also been found at the outskirts of two poor clusters, UGC 03957 (Thölken et al., 2016) and Virgo (Simionescu et al., 2015), whose peak temperatures are ~ 3.5 keV, which is between groups and clusters.

In addition to Fe, other elements (O, Mg, Si, S, and Ni) also have nearly constant abundance throughout the outskirts of the groups in spite of the larger uncertainties. Our findings consistent with the same enrichment mechanism may be at work among systems at various different mass scales. In a hierarchical Universe, low mass systems form earlier than more massive systems. For metals to be deposited and well mixed before the gravitational collapse of galaxy groups, the timeline of the early-enrichment scenario including the formation of SNIa (and their progenitor stars) needs to be pushed back further (e.g., Maoz et al., 2014; Biffi et al., 2018).

3.5.2 Early enrichment population

A conundrum in the enrichment study is that the total metals observed in rich clusters cannot be explained by the visible stellar component as shown in Figure 3.4 (also see E Blackwell et al., 2021; Ghizzardi et al., 2021). This discrepancy invokes an external and universal source of metals even *before* the star formation episode – an Early Enrichment Population (EEP) which is not visible today (Mantz et al., 2017). The time scale of this enrichment epoch is not well constrained but possibly at $3 < z < 10$ and such an early stellar population may be directly observable with JWST.

Our findings demonstrate that once the Fe abundance is measured out to R_{200} , the current stellar content of galaxy groups is insufficient to produce their total metals as well. Nevertheless, within both R_{500} and R_{200} , the effective Fe yields of groups are significantly smaller than those of rich clusters. In addition to Fe yields, this difference between groups and clusters is also reflected in their iron-mass-to-light ratios. As shown in Figure 3.3, we have derived the accumulated IMLR of these groups out to R_{200} . Compared to the Perseus cluster, galaxy groups contain twice as much stellar lights for their metals. The small IMLR of groups relative to clusters may be attributed to the relatively shallower potential well of groups making them unable to retain all the enriched gas against non-thermal processes such as AGN feedback. As shown in Sarkar et al. (2021b), the accumulated gas mass to total mass ratios within R_{200} are consistent with the cosmic baryon fraction for galaxy clusters, which are systematically higher than those of galaxy groups. Furthermore, groups and clusters may have different star formation history. IGrM has a lower temperature and density than ICM and therefore providing a less hostile environment for the member galaxies. The higher star formation rate in galaxy groups may partially explain the small IMLR (Davé et al., 2008).

3.5.3 Chemical composition of galaxy groups

The additional constraints on O, Mg, Si, and S allow us to derive the chemical components and SNIa fraction of galaxy groups. The abundance ratios of O/Fe, S/Fe, Si/Fe, and Mg/Fe of the four groups in our sample are shown in Figure 3.2. Largely caused by the abrupt change in the slope of the Fe abundance profile, we observe different chemical compositions between group centers and group outskirts. The X/Fe ratios within $0.25R_{200}$ are consistent with the Solar chemical composition, for which we derive a f_{SNIa} of 0.214 ± 0.028 . This is in agreement with the average gas abundance ratios of cluster cores (de Plaa et al., 2007) and 44 nearby systems within $R < R_{500}$ (dominated by galaxy clusters) in the CHEERS sample (Mernier et al., 2017). A similar chemical composition for gas has been found at the centers of the Perseus cluster using microcalorimeter on board *Hitomi* (Simionescu et al., 2019) as well as in NGC 1404, an early-type galaxy, through a joint *XMM-Newton* EPIC, RGS, and *Chandra*-ACIS study (Mernier et al., 2022). It is intriguing that ICM, IGrM, and even ISM metallicities trace the same metal abundance pattern as our Solar System, rather than that of their own dominant galaxies. This seems to further imply a common origin of the metals among these systems. Alternatively, this also means that the stellar population we see today in clusters and groups (i.e. mainly red-and-dead population) has very little to do with the metal content of their hot halos.

Over the radii of 0.25 - $1.0R_{200}$ the X/Fe ratios are generally super solar ranging from 1.6 to 1.9, for which we derive that the SNIa fraction is 0.138 ± 0.046 , allowing us to rule out a pure SNcc enrichment by 3σ . The Fe abundance at the outskirts is unlikely to be significantly underestimated since we have employed a 2T model to mitigate the “Fe-bias” and we have obtained a measured Z_{Fe} similar to that of the rich clusters. It is worth noting that the large uncertainties and scatters of the measurements do not allow us to claim a clear discrepancy from the solar value for S/Fe, Si/Fe, and Mg/Fe, while the O line can not be well resolved by CCD-like detectors such as XIS. Extensive *Suzaku* study of the outskirts of the Virgo cluster reveals a super solar value for Mg/Fe of 1.2–1.6, while their Si/Fe and S/Fe ratios are 0.6-0.8 and 0.8-1.2, respectively. The X/Fe ratios may scatter among different systems. The results can be further complicated by the various sources of systematic effects associated with the observations of the background dominated regimes.

3.6 Summary

We analyzed joint *Suzaku* and *Chandra* observations of four nearby groups – MKW4, Antlia, RXJ1159+5531, and ESO3060170. *Suzaku* observations were used to constrain their gas properties and *Chandra* data were used to refine the results by mitigating the uncertainties introduced by the CXB. We have derived abundance profiles of O, Mg, Si, S, Fe, and Ni out to the R_{200} for the first time for such low-mass systems. Our results are summarized below.

- The metal abundances at the central region of Antlia are significantly lower than those of MKW4, RXJ1159+5531, and ESO3060170. Unlike the other

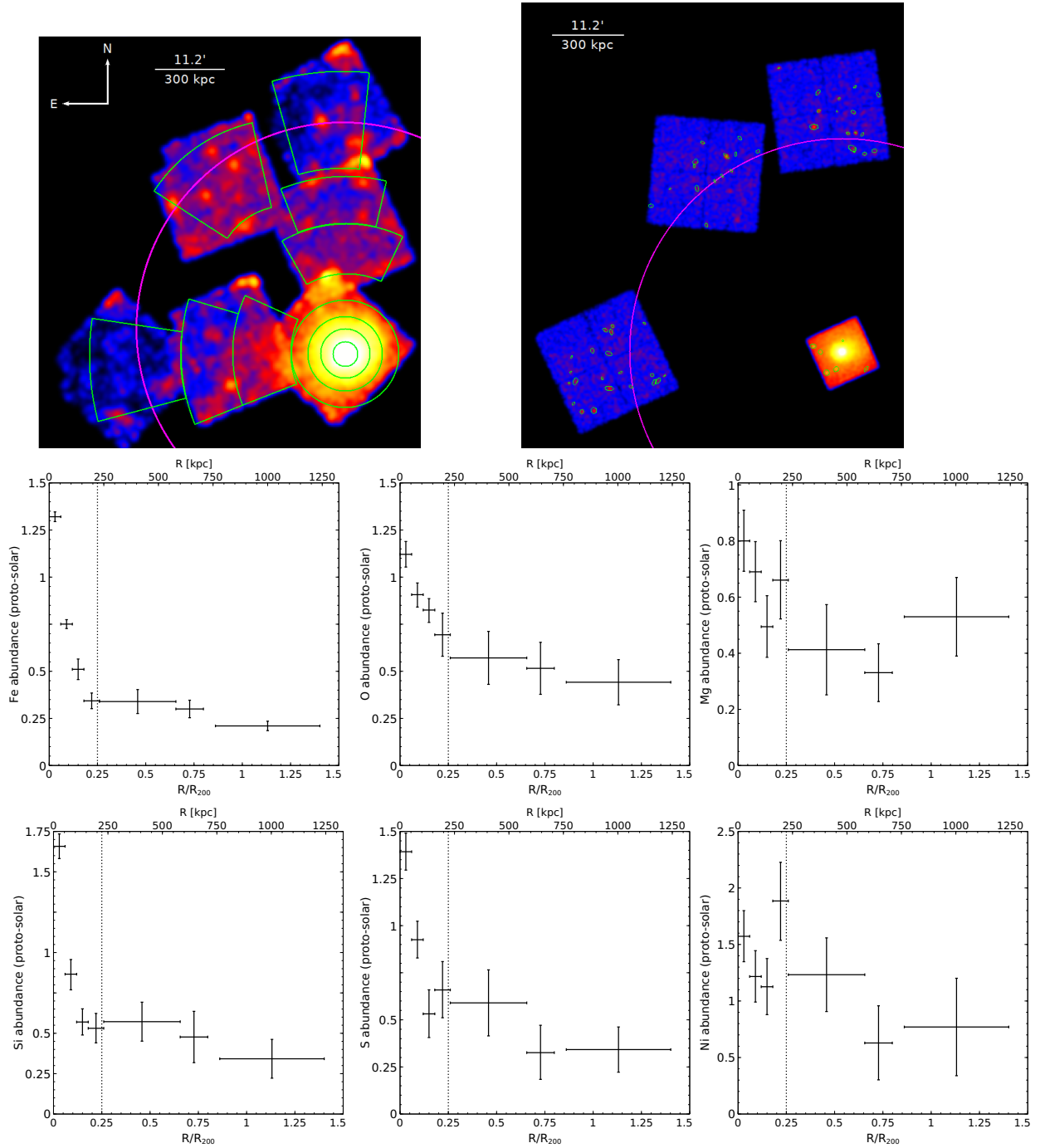


Figure 3.5: Top left: NXB subtracted and exposure corrected mosaic *Suzaku* image of MWK4 in the 0.5-2 keV energy band. Magenta circle indicates R_{200} . Green annuli represent the regions used for spectra extraction. Top right: mosaic *Chandra* image of MKW4 in the 0.5-7.0 keV energy band. The resolved point sources are marked in green elliptical regions. Middle and Bottom: radial profiles of different elements from the group center to the outskirts. Vertical dotted line indicate $0.25R_{200}$.

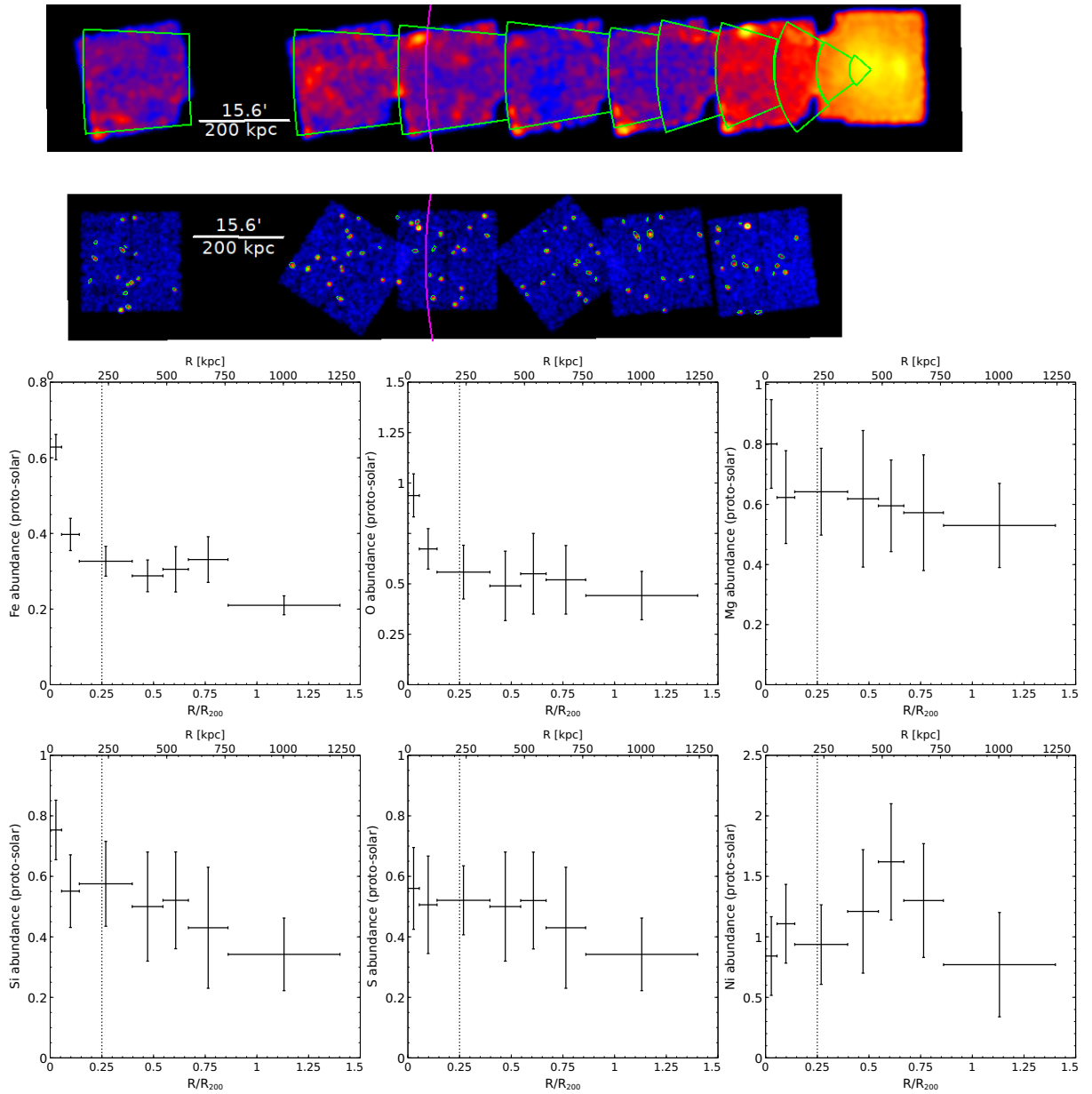


Figure 3.6: Antlia; same as Figure 3.5.

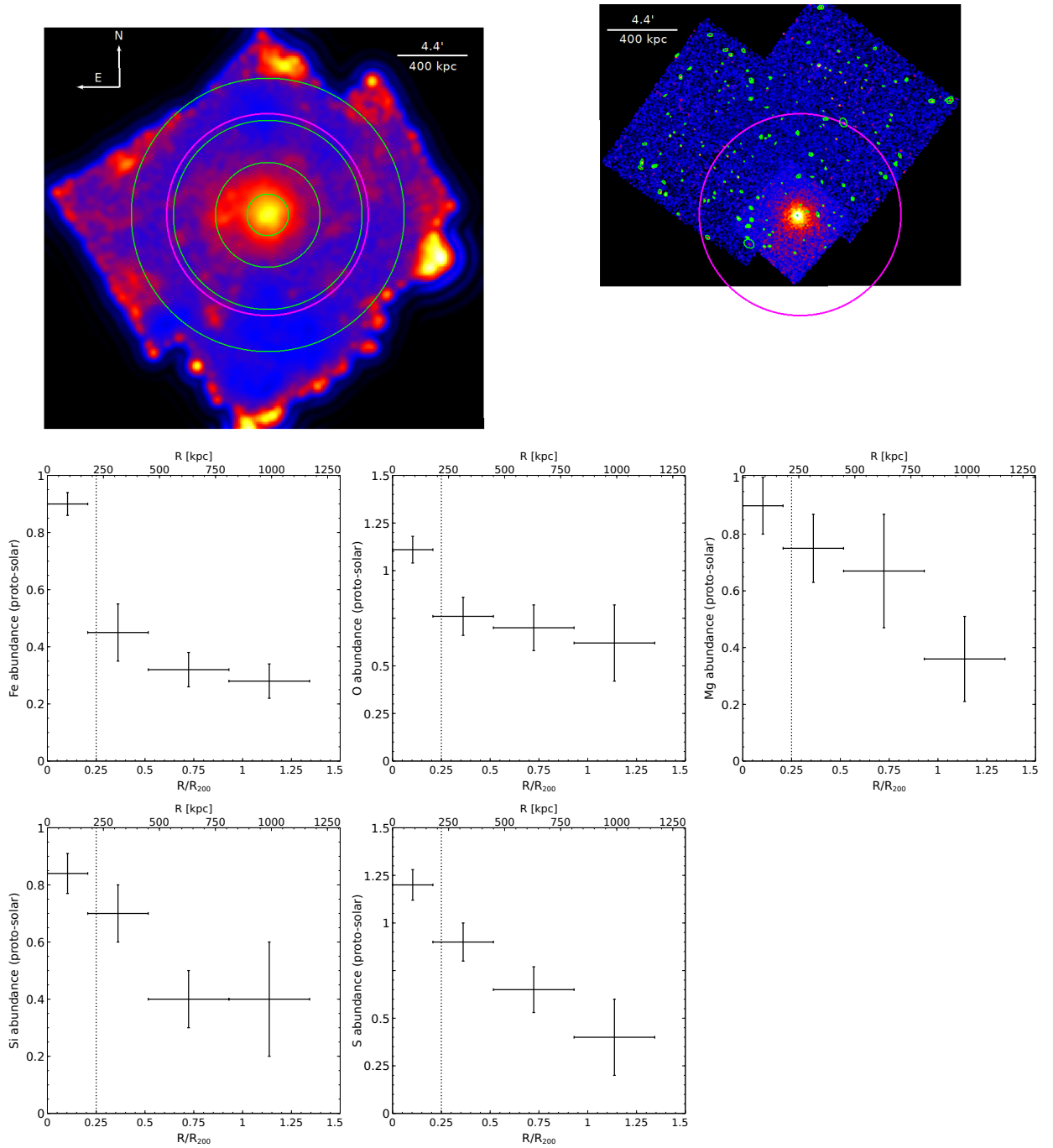


Figure 3.7: RXJ 1159; same as Figure 3.5.

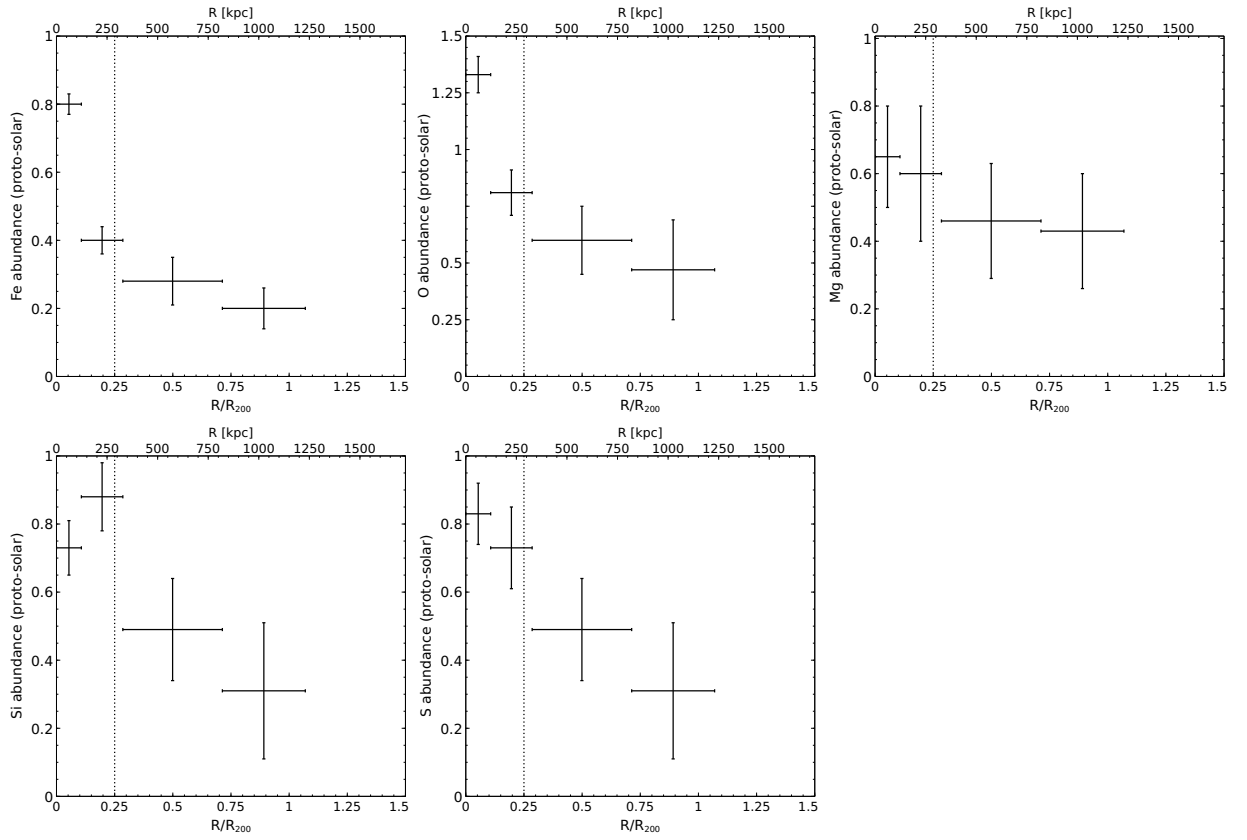
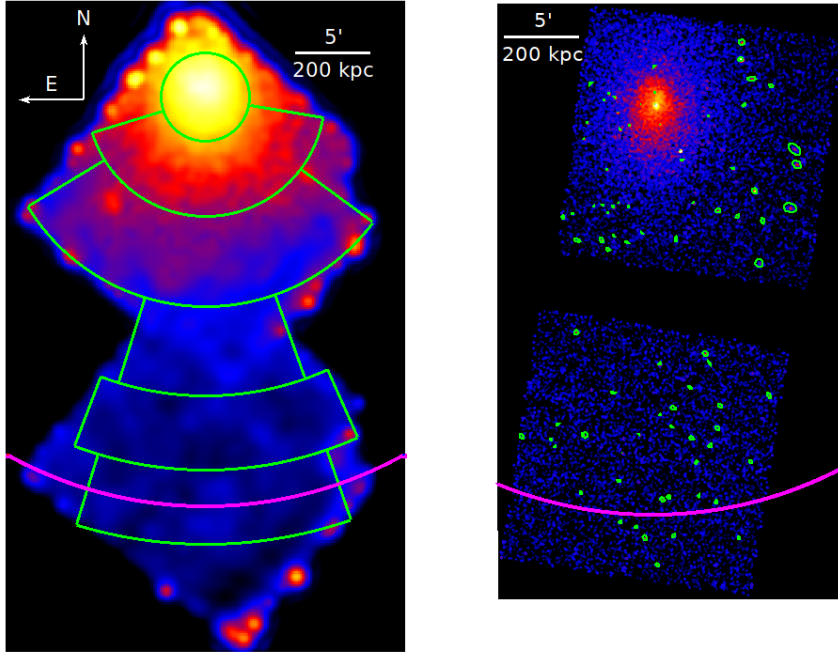


Figure 3.8: ESO 3060170; same as Figure 3.5

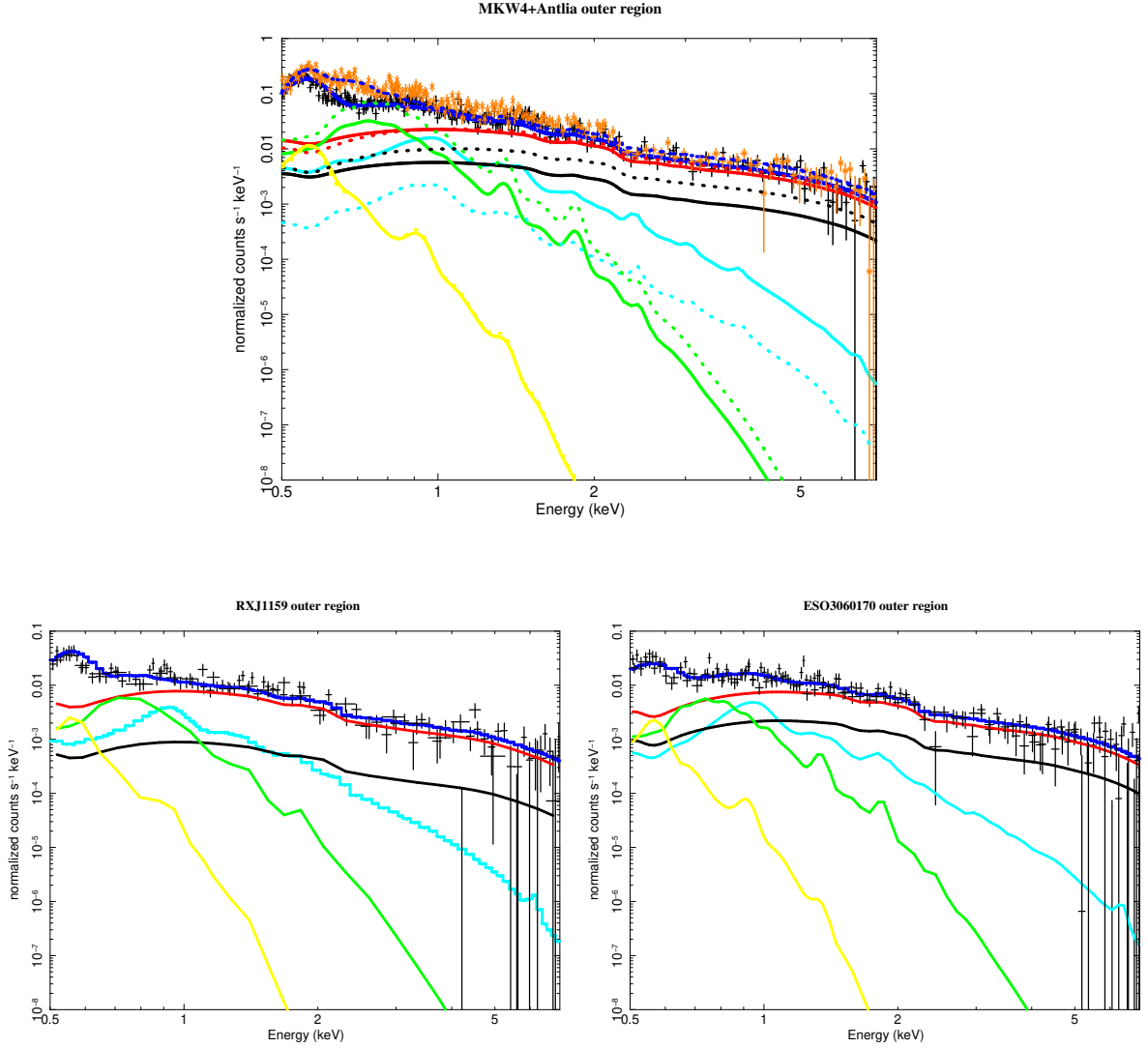


Figure 3.9: Best-fit results of the spectral analysis for the outermost regions of four groups. We show only XIS1 spectra. Red, black, cyan, green, yellow colored lines indicate best-fit resolved CXB, unresolved CXB, ICM emission, GH, LHB components, respectively. Blue line shows the best-fit ICM emission and X-ray background together. *Top panel:* Black data points are for MKW4. Orange data points are for Antlia. Solid line represents MKW4 and dashed line represents Antlia. *Bottom panel:* spectra for RXJ1159 and ESO3060170.

three systems, Antlia is a non cool-core group. Like observed in massive system equivalents (i.e. non-cool core clusters), more frequent merging events may have disrupted its core and erased much of the centrally peaked metallicity.

- At group outskirts ($0.25-1.0R_{200}$), we measure flat metal abundance profiles for all four groups with an average Fe abundance of $Z_{\text{Fe}} = 0.309 \pm 0.018 Z_{\odot}$ ($\chi^2 = 14$ for 12 degrees of freedom), which is remarkably consistent with what was found in rich clusters, and the predictions from IllustrisTNG for galaxy groups. The uniform metal distribution suggests that the same early enrichment process may have been at work before the gravitational collapse of groups and clusters. Early AGN feedback is likely to have played an important role in transporting metals from galaxies to the hot gas as well as efficiently mixing the enriched gas throughout the proto cluster/group gas at $z = 2 - 3$. It is also plausible that an early-enrichment population is responsible for contaminating the proto cluster/group gas even before the formation of the current stellar components at $3 < z < 10$.
- We derive the accumulated iron mass-to-light ratios from the center out to the R_{200} of these groups. Their IMLR increase with radius, indicating that the enriched gas is more extended than the stellar distribution. Near the R_{200} , the accumulated IMLR of these groups are consistent with each other at $4-5 \times 10^{-3} M_{\odot}/L_{K\odot}$. However, these values are significantly lower than the accumulated IMLR of Perseus at R_{200} , which may imply that groups could not retain all of their enriched gas due to their shallower potential wells, and/or a halo-mass dependent star formation history.
- We compare the effective Fe yields of groups within R_{500} and R_{200} , and the theoretical expectation. The iron yields measured out to R_{200} of four groups show a tension with respect to the expected values from empirical supernovae yields and in contrast with what can be observed within R_{500} . A significant amount of metals are found at the outskirts of groups. When the Fe abundance is measured out to R_{200} , the visible stellar component in the groups is insufficient to produce the observed metals, which may pose a challenge for the chemical enrichment models in the same fashion as the one already known for clusters.
- The O/Fe, Mg/Fe, Si/Fe, and S/Fe ratios at the group centers are nearly solar and consistent with the chemical composition measured at cluster centers. The hot gas in the systems that are orders of magnitude different in mass traces the same metal abundance pattern as our Solar System, rather than that of their own dominant galaxies. The derived SNIa fraction is 14% at their outskirts, allowing as to rule out a pure core collapsed supernovae enrichment before the gravitational collapse of galaxy groups.

Chapter 4 Discovery of a pre-merger shock in an intercluster filament in Abell 98

4.1 Introduction

Clusters of galaxies are primarily assembled and grow via accretion, gravitational infall, and mergers of smaller substructures and groups. In such merging events, a significant fraction of kinetic energy dissipates (on a Gyr timescale) in the intra-cluster medium (ICM) via shocks and turbulence (Markevitch et al., 1999). Such shocks are the major heating sources for the X-ray emitting ICM plasma (Markevitch and Vikhlinin, 2007). Shock fronts provide an essential observational tool in probing the physics of transport processes in the ICM, including electron-ion equilibration and thermal conduction, magnetic fields, and turbulence (e.g., Markevitch, 2006; Markevitch and Vikhlinin, 2007; Botteon et al., 2016, 2018).

Despite the intrinsic interest and significance of merger shocks, X-ray observations of merger shocks with a sharp density edge and an unambiguous jump in temperature are relatively rare. Currently, only a handful of merger shock fronts have been identified by *Chandra*, such as 1E 0657-56 (Markevitch et al., 2002), Abell 520 (Markevitch et al., 2005), Abell 2146 (Russell et al., 2010, 2012), Abell 2744 (Owers et al., 2011), Abell 754 (Macario et al., 2011), Abell 2034 (Owers et al., 2014), Abell 665 (Dasadia et al., 2016).

Cosmic filaments are thought to connect the large-scale structures of our universe (e.g., Dolag et al., 2006; Werner et al., 2008; Alvarez et al., 2018; Reiprich et al., 2021). Several independent searches for baryonic mass have confirmed discrepancies in baryonic content between the high and low redshift universe (e.g., Fukugita et al., 1998; Fukugita and Peebles, 2004), with fewer baryons being detected in the local Universe. They concluded that a significant fraction of these missing baryons may be “hidden” in the WHIM, in cosmic filaments that connect clusters and groups. The WHIM has a temperature in the 10^5 - 10^7 K (or, $kT \sim 0.01$ - 1 keV) regime, and relatively low surface brightness (e.g., Cen and Ostriker, 1999; Davé et al., 1999, 2001; Smith et al., 2011).

Abell 98 (hereafter A98) is a richness class III early-stage merger with three subclusters: central (A98S; $z \approx 0.1063$), northern (A98N; $z \approx 0.1042$), and southern (A98SS; $z \approx 0.1218$). The northern and southern subclusters are at projected distances of ~ 1.1 Mpc and 1.4 Mpc from the central subcluster, respectively (e.g., Abell et al., 1989; Jones and Forman, 1999; Burns et al., 1994; Paterno-Mahler et al., 2014). The central subcluster is undergoing a separate late-stage merger, with two distinct X-ray cores. Previous observations using *Chandra* and *XMM-Newton* showed that A98N is a cool core cluster with a marginal detection of a warm gas arc, consistent with the presence of a leading bow shock, but that the exposure time was insufficient to confirm this feature (Paterno-Mahler et al., 2014)

To investigate further, we analyzed deep (~ 227 ks) *Chandra* observations of A98N and A98S. In this letter, we report on the detection of an intercluster filament con-

necting A98N and A98S, and of a leading bow shock in the region of the filament, associated with the early-stage merger between A98N and A98S. We adopted a cosmology of $H_0 = 70 \text{ km s}^{-1} \text{ Mpc}^{-1}$, $\Omega_\Lambda = 0.7$, and $\Omega_m = 0.3$, which gives a scale of $1'' = 1.913 \text{ kpc}$ at the redshift $z = 0.1042$ of A98. Unless otherwise stated, all reported error bars are at 90% confidence level.

4.2 Data analysis

Abell 98 was observed twice with *Chandra* for a total exposure time of $\sim 227 \text{ ks}$. The observation logs are listed in Table 4.1. We discuss the detailed data reduction processes in Section 4.4.3.

4.2.1 Imaging analysis

The image showing the both A98N and A98S in the 0.5-2 keV energy band is shown in Figure 4.1. We derived a Gaussian Gradient Magnitude (GGM) filtered image of A98, zooming in the northern subcluster, as shown in Figure 4.2. The GGM-filtered image provides a powerful tool to reveal sub-structures and any associated sharp features in the cluster core, as well as at larger cluster radii (Walker et al., 2016). The intensity of the GGM images indicates the slope of the local surface brightness gradient, with steeper gradients showing up as brighter regions. The GGM image we present here is filtered on a length scale of 32 pixels. Each pixel is $0.492''$ wide. We observe a rapid change in the magnitude of the surface brightness gradient at $\sim 400 \text{ kpc}$ to the south of the A98N center, as seen in Figure 4.2.

GGM images often show artifacts from the filtering process, particularly in low surface brightness regions. Therefore, we next test for the presence of the edge feature indicated in Figure 4.2 by extracting a surface brightness profile across the edge. Figure 4.2 shows the resulting radial surface brightness profile as a function of distance from the A98N core in the 0.5-2 keV energy band. We observe an edge in the X-ray surface brightness profile at about 420 kpc ([0:46:23.14, +20:33:46.32](#)) from the A98N core. The distance of the edge from the A98N core is consistent with the edge observed in the GGM image, which suggests the abrupt change in the gradient corresponds to the surface brightness edge.

The shape of the extracted surface brightness profile across the edge is consistent with what is expected from a projection of a 3D density discontinuity (Markevitch et al., 2000). To quantify the surface brightness edge, we fit the surface brightness profile by projecting a 3D discontinuous double power-law model along the line of sight, defined as

$$n_e(r) \propto \begin{cases} \left(\frac{r}{r_{edge}}\right)^{-\alpha_1}, & \text{if } r < r_{edge} \\ \frac{1}{jump} \left(\frac{r}{r_{edge}}\right)^{-\alpha_2}, & \text{if } r \geq r_{edge} \end{cases} \quad (4.1)$$

where $n_e(r)$ is the 3D electron density at a radius r , r_{edge} is the radius of the putative edge, $jump$ is the density jump factor, and α_1 and α_2 are the slopes before and after

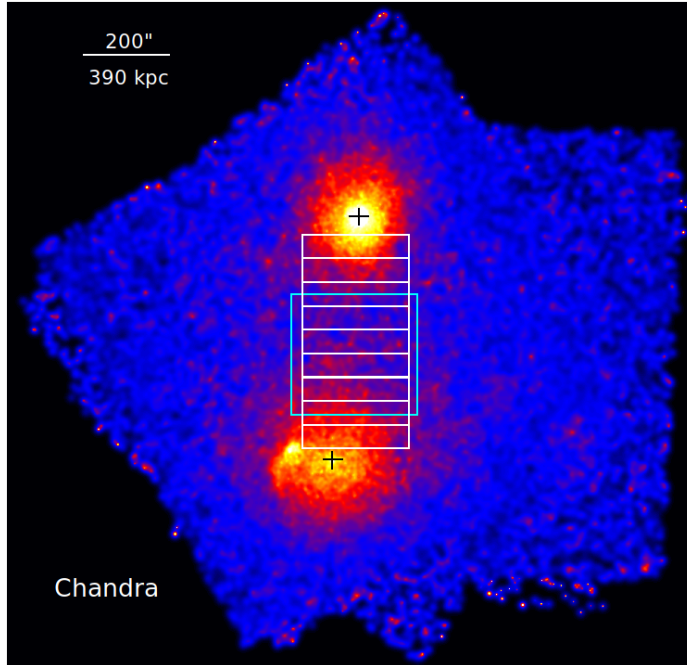


Figure 4.1: *Chandra* exposure corrected and background subtracted image of A98 in the 0.5–2 keV energy band. White and cyan regions are used for the analysis of the filament emission. Centers of A98N and A98S are marked in black.

the edge, respectively. A constant term was also added to the model to account for any residual background, after blanksky subtraction. The best-fit value of this term was consistent with zero, suggesting we successfully eliminated sky and particle background. We project the estimated emission measure profile onto the sky plane and fit the observed surface brightness profile by using least square fitting technique with α_1 , α_2 , r_{edge} , and the *jump* as free parameters. Figure 4.2 shows the best-fit model and the 3D density profile (inset). The best-fit power-law indices across the edge are $\alpha_1 = 0.76 \pm 0.01$ and $\alpha_2 = 0.83 \pm 0.02$, respectively ($\chi^2/\text{dof} = 57/21$). The density jumps, across the edge, by a factor of $\rho_2/\rho_1 = 2.5 \pm 0.3$, where suffix 2 and 1 represent the regions inside and outside of the front. Assuming that the edge is a shock front, this density jump corresponds to a Mach number of $\mathcal{M} = 2.3 \pm 0.3$, estimated from the Rankine-Hugoniot jump condition, defined as

$$\mathcal{M} = \left[\frac{2r}{\gamma + 1 - r(\gamma - 1)} \right]^{\frac{1}{2}}, \quad (4.2)$$

where $r = \rho_2/\rho_1$ and for a monoatomic gas $\gamma = 5/3$. The edge radius, obtained from the fit, is 420 ± 25 kpc. We estimated the uncertainties by allowing all the other model parameters to vary freely. The best-fit edge radius is consistent with the distance of the GGM peak from the A98N center.

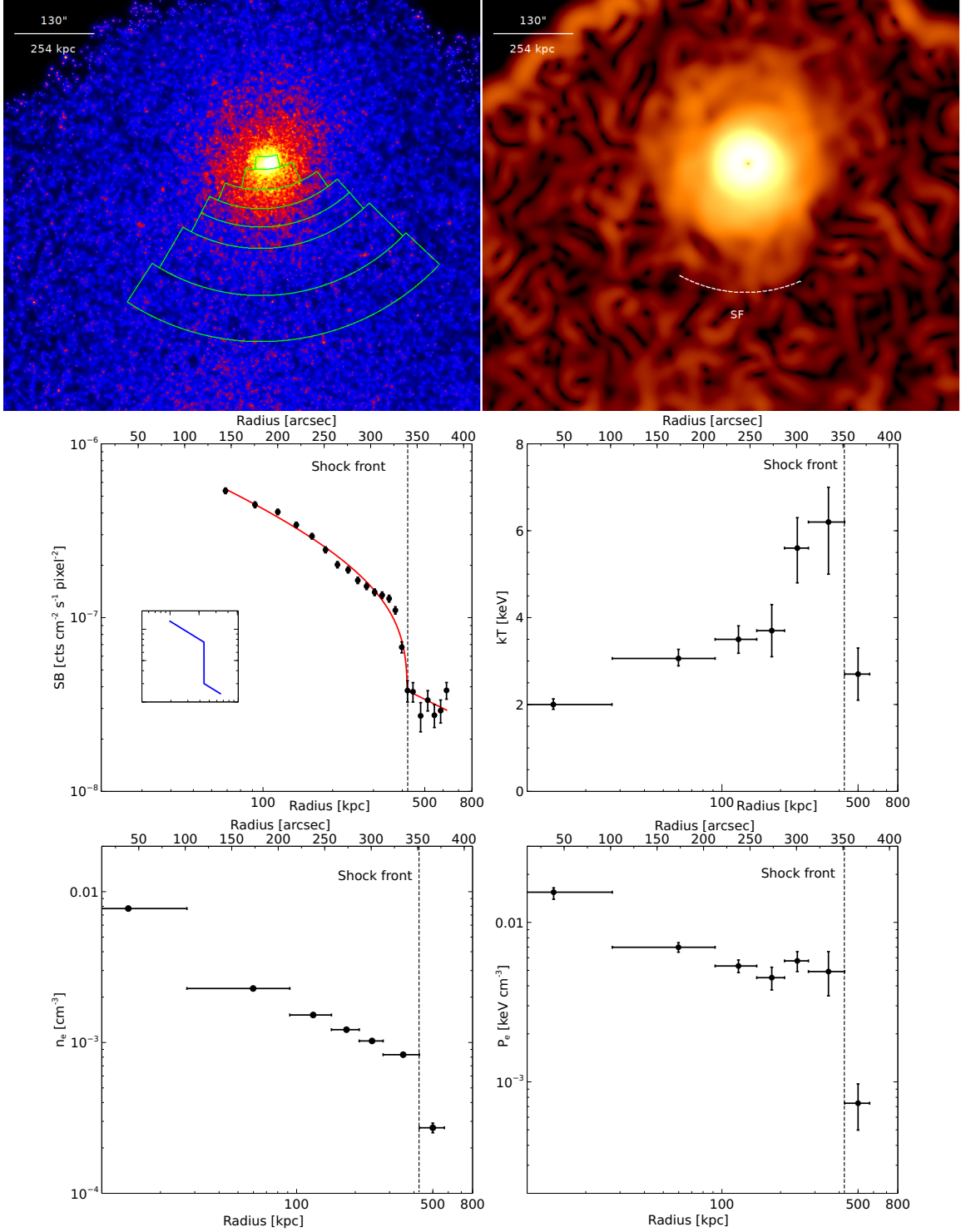


Figure 4.2: *Top-left*: Similar to Figure 4.1 but zoom in to A98N and smoothed with $\sigma=2''$ Gaussian. Green regions used for spectral analysis. *Top-right*: GGM image of A98N with $\sigma=16''$ Gaussian kernel. White dashed curve shows southern shock front. *Middle left*: surface brightness profile of A98N in south direction with 1- σ errorbars. Inset figure shows the 3D density profile. *Middle-right*: projected temperature, *bottom-left*: 3D density, *bottom-right*: pressure profiles of A98N in south direction.

4.2.2 Spectral analysis

To measure the temperature across the surface brightness edge, the southern sector was divided into seven regions, as shown in Figure 4.2. Each region contains a minimum of 2300 background-subtracted counts. We set this lower limit to guarantee adequate counts to measure the temperature uncertainty within 25% in the faint region at a 90% confidence level. For each region, we extracted spectra from individual observations and fitted them simultaneously. The spectra were grouped to contain a minimum of 20 counts per spectral channel. The blank-sky-background spectra were subtracted from the source spectra before fitting (Dasadia et al., 2016). We fitted the spectra from each region to an absorbed single-temperature thermal emission model, PHABS(APEC) (Smith et al., 2001). The redshift was fixed to $z=0.1042$, and the absorption was fixed to the Galactic value of $N_H=3.06\times 10^{20}$ cm $^{-2}$ (Kalberla et al., 2005). The spectral fitting was performed using XSPEC in the 0.6-7 keV energy band, and the best-fit parameters were obtained by reducing C-statistics. We fixed the metallicity to an average value of $0.4 Z_\odot$ since it was poorly constrained if left free (Russell et al., 2010). We adopted solar abundance table of Asplund et al. (2009).

Figure 4.2 shows the best-fit projected temperatures. The projected temperature increases steadily from the A98N core up to ~ 200 kpc, then jumps to a peak of $\sim 6.4^{+1.0}_{-1.5}$ keV at ~ 420 kpc, which then plummets to $2.7^{+0.5}_{-0.5}$ keV beyond the surface brightness edge. Across the edge, the temperature decreases by a factor of $\sim 2.3 \pm 0.6$, confirming the outer edge as a shock front. We estimated the electron pressure by combining the temperature and electron density, as shown in Figure 4.2. As expected, we found a significant decrease in pressure by a factor of $\sim 7 \pm 2$ at the shock front. The observed temperature drop corresponds to a Mach number of $\mathcal{M} = 2.2 \pm 0.4$, consistent with the Mach number derived from the density and pressure jump. Mach numbers from both methods are consistent with each other, bolstering the shock detection. We estimated a pre-shock sound speed of $c_s \sim 848 \pm 80$ km/s, which gives a shock speed of $v_{shock} = c_s \mathcal{M} \approx 1900 \pm 180$ km/s.

4.3 Detection of Filament emission

Early-stage, major mergers between two roughly equal mass subclusters are expected to typically have their merger axis aligned with the filaments of the cosmic web (see Alvarez et al. (2018) for further discussion). To search for faint X-ray emission associated with the filament between A98N and A98S, we extracted a surface brightness profile from nine box regions across the bridge between A98N and A98S in the 0.5-2 keV energy band (see Figure 4.1). Figure 4.3 shows the surface brightness profile of the bridge. This surface brightness profile includes the emission from the extended ICM of both subclusters, and from the filament. To account for only the extended ICM emission from both subclusters, we extracted surface brightness profiles from similar regions placed in the opposite directions of the filament, using *Suzaku* observations of A98 (Alvarez et al., 2022b), assuming in each that the contribution from the neighboring subcluster is negligible. We used *Suzaku* observations because the existing *Chandra* observations do not cover the part of the sky needed for such

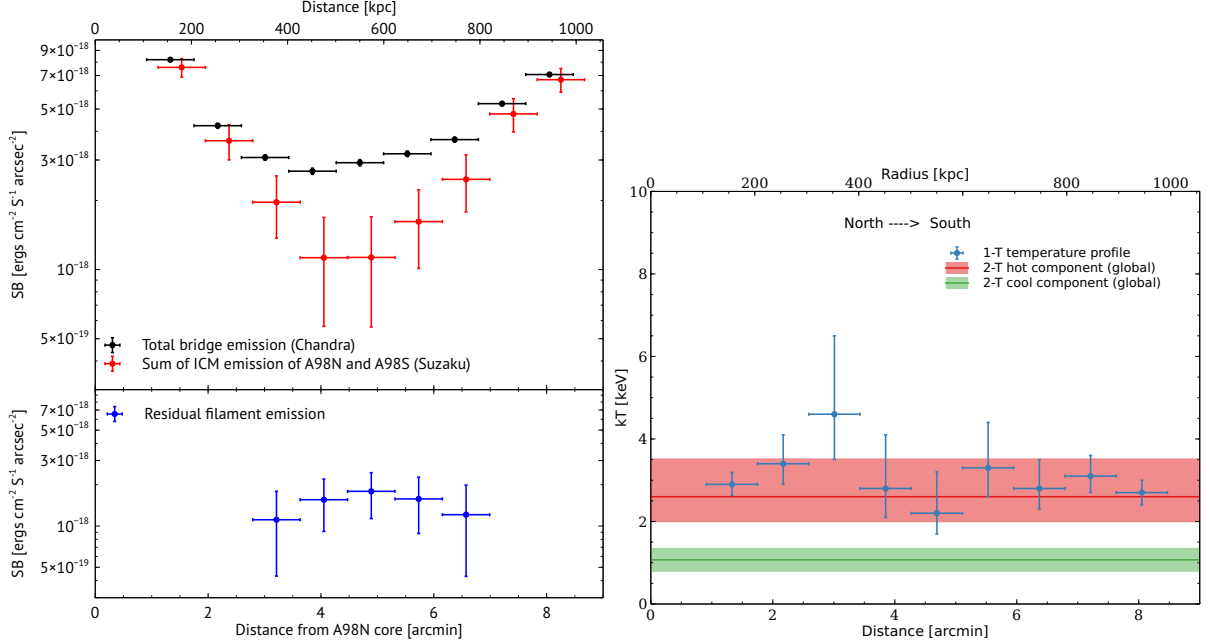


Figure 4.3: *left*: Black shows the surface brightness profile across the bridge measured using *Chandra*. Red indicates the sum of the surface brightness profiles of the diffuse, extended emission extracted from the *Suzaku* observations. Blue represents the residual filament emission. *Right*: projected temperature profile across the bridge, measured with a 1-T model. Red and green shaded regions indicate the hot component and cool component temperatures, respectively, measured with a 2-T model.

analysis. These two diffuse surface brightness profiles are then subtracted from the surface brightness profile of the bridge, yielding the surface brightness profile of the filament. We use *WebPIMMS** to convert *Suzaku* and *Chandra* count rates to physical units ($\text{erg}/\text{cm}^2/\text{s}/\text{arcsec}^2$) in the 0.5-2 keV energy band. We assumed a thermal APEC model with absorption fixed to $N_H = 3.06 \times 10^{20} \text{ cm}^{-2}$, abundance $Z = 0.2Z_\odot$, and temperature $kT = 2.6 \text{ keV}$ (as discussed later).

Figure 4.3 shows the resulting surface brightness profile of the filament in the 0.5-2 keV energy band. We detected excess X-ray surface brightness in the region of the bridge with a $\sim 3.2\sigma$ significance level. Similar excess emission along the bridge with somewhat lower significance ($\sim 2.2\sigma$) was also found by Alvarez et al. (2022b) using only *Suzaku* data. Being very nearby to both subcluster cores, where emission is dominated by the respective subcluster, we could not detect any significant filament emission from the first two and last two regions. This excess X-ray emission suggests the presence of a filament along the bridge connecting A98N and A98S.

To measure the temperature across the bridge region, we adopted similar regions used for the surface brightness profile of the bridge. The spectra were then fitted to a single-temperature APEC model (1-T), keeping the metallicity fixed to $0.2 Z_\odot$. Figure

*<https://heasarc.gsfc.nasa.gov/cgi-bin/Tools/w3pimms/w3pimms.pl>

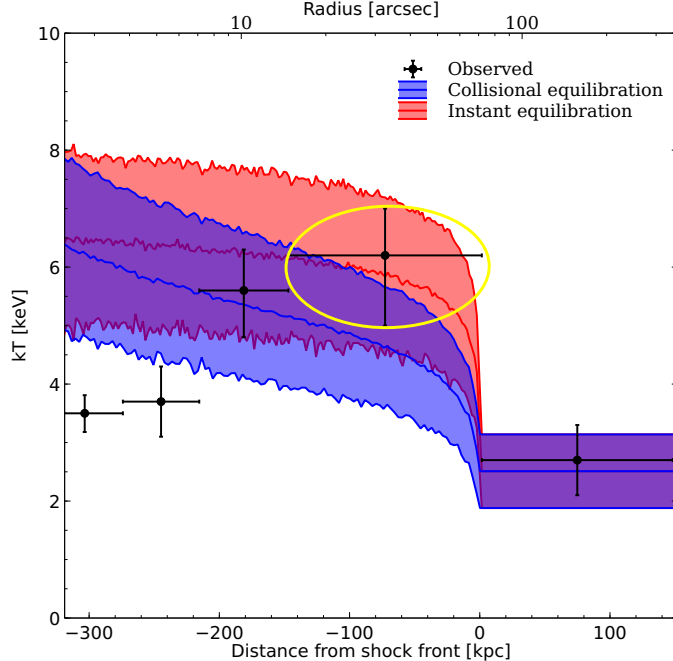


Figure 4.4: Comparison of the temperature profile across the shock front with the predicted electron temperature profiles based on instant collisionless model (red) and Coulomb collisional model (blue). Yellow ellipse indicates the relevant post-shock electron temperature for comparing with two models.

4.3 shows the projected temperature profile. The temperatures across the bridge are consistent within their $\sim 2.7\sigma$ (90%) uncertainty, except for third region where we detected a shock. We next measured the global properties of the bridge using a $0.6 \text{ Mpc} \times 0.7 \text{ Mpc}$ box region (632 kpc from the A98N and 505 kpc from the A98S; shown with cyan in Figure 4.1). Using a single temperature emission model for the bridge region, we obtained a temperature of $1.8_{-0.4}^{+0.7} \text{ keV}$ and an abundance of $0.22_{-0.16}^{+0.12} Z_{\odot}$. Our measured temperature of the bridge is consistent with the temperatures obtained by Paterno-Mahler et al. (2014) using *XMM-Newton* and relatively short exposure *Chandra* observations. We next estimated the electron density of the bridge using

$$n_e = \left[1.73 \times 10^{-10} \times N \sin(i) \times (1+z)^2 \times \left(\frac{D_A}{\text{Mpc}} \right)^2 \left(\frac{r}{\text{Mpc}} \right)^{-2} \left(\frac{l_{obs}}{\text{Mpc}} \right)^{-1} \right]^{1/2} \text{ cm}^{-3},$$

where N is APEC normalization, D_A is the angular diameter distance, r and l_{obs} are the radius and the projected length of the filament, respectively. We obtained electron density of $n_e = 4.2_{-0.8}^{+0.9} \times 10^{-4} \text{ cm}^{-3}$, assuming the filament is in the plane of the sky ($i = 90^\circ$) and has cylindrical symmetry, since for $i \ll 90^\circ$ we would not expect to detect a clear leading merger shock edge. Our measured temperature and electron density are higher than the expected temperature ($\lesssim 1 \text{ keV}$) and electron density ($\sim 10^{-4} \text{ cm}^{-3}$) for the WHIM (e.g., Bregman, 2007; Werner et al., 2008; Eckert et al., 2015; Alvarez et al., 2018; Hincks et al., 2022).

The surface brightness profiles seen in Figure 4.3 show that the emission from the filament itself is much fainter than the diffuse, extended cluster emission. A low-

density gas emission is expected together with the ICM emission at the bridge region. We, therefore, adopted a two-temperature emission model for the bridge and obtained a temperature of $kT_{hot} = 2.60_{-0.62}^{+0.93}$ keV for the hotter component and $kT_{cool} = 1.07 \pm 0.29$ keV for the cooler component. The higher temperature gas is probably mostly the overlapping extended ICM of the subclusters seen in projection. The two-temperature model was a marginal improvement over the one-temperature model with an F-test probability of 0.08. The emission measure of the cooler component corresponds to an electron density of $n_e = 1.30_{-0.31}^{+0.28} \times 10^{-4} \text{ cm}^{-3}$, assuming the filament is in the plane of the sky. From the temperature and electron density of the cooler component, we obtain an entropy of $\sim 416 \text{ keV cm}^2$. Our measured temperature, density, and entropy of the cooler component are consistent with what one expects for the hot, dense part of the WHIM (e.g., Eckert et al., 2015; Bulbul et al., 2016b; Alvarez et al., 2018; Reiprich et al., 2021). *Suzaku* observations also show similar emission to the north of A98N, beyond the virial radius, in the region of the putative large scale cosmic filament (Alvarez et al., 2022b). We also check for any systematic uncertainties in measuring the filament temperature, abundance, and density by varying the scaling parameter of blanksky background spectra by $\pm 5\%$. We find no significant changes.

4.4 Discussion and Conclusion

4.4.1 Nature of the shock front

Our deep *Chandra* observations reveal that the overall system is complex, with A98S dominated by a later-stage merger ongoing along the east-west direction (Sarkar et al. in prep). Previously, Paterno-Mahler et al. (2014) argued that the surface brightness excess along the southern direction of A98N is more likely a shock with a Mach number, $\mathcal{M} \gtrsim 1.3$. With the new data, we found that the temperature increases by a factor of ~ 2.3 (from 2.7 keV to 6.4 keV) across the surface brightness edge, confirming it is a shock front propagating along the merger axis (N/S direction). This is the first unambiguous detection of axial merger shock in an early-stage merger (i.e., pre-core-passage), as opposed to the late-stage merger (i.e., post-core-passage), where several previous observations found axial shocks (e.g., Russell et al., 2010, 2012; Dasadia et al., 2016).

Axial shock detection in an early-stage merging cluster is a long-standing missing piece of the puzzle of cluster formation. Previous *Chandra* observations of the pre-merger system, 1E 2216/1E 2215, detected an equatorial shock (Gu et al., 2019). Equatorial shocks are driven by the adiabatically expanding overlap region between the outskirts of the merging subclusters. They propagate along the equatorial plane, perpendicular to the merger axis. This is in contrast to axial shocks, which are driven by, and ahead of, the infalling subclusters. Gu et al. (2019) did not detect any axial shock in 1E 2216/1E 2215. There are conflicting findings from simulations on which merger shock should form first. Recent hydrodynamical simulations of binary cluster mergers by Zhang et al. (2021) showed the formation of axial merger shocks in the early stages of the merging process. In contrast, simulations by Ha et al. (2018) indicated that equatorial shock forms long before the axial shock.

To date, it is unclear what is driving the apparent discrepancy between the formation of equatorial and axial shocks, although the parameters of the merger (e.g., mass ratio, total mass, impact parameter) likely play a role. Our *Chandra* observation of the shock front in A98 is the ‘first’ unambiguous axial shock detection in an early stage merging system, prior to core passage. We detect no equatorial shocks, but it is possible that they are present and the current observations are not deep enough to detect them. With this discovery, we caught two subclusters in a crucial epoch of the merging process, which will reveal any missing link to the shock formation process in pre-merger systems and provide a yardstick for future simulations.

4.4.2 Electron-ion equilibrium

The electron heating mechanism behind a shock front is still up for debate. The collisional equilibrium model predicts that a shock front propagating through a collisional plasma heats the heavier ions dissipatively. Electrons are then compressed adiabatically, and subsequently come to thermal equilibrium with the ions via Coulomb collisions after a timescale defined in Equation 4.3 (Spitzer, 1962; Sarazin, 1988; Etori and Fabian, 1998; Markevitch and Vikhlinin, 2007). By contrast, the instant equilibrium model predicts that electrons are strongly heated at the shock front, and their temperature rapidly rises to the post-shock gas temperature, similar to the ions (Markevitch, 2006; Russell et al., 2012). The electron and ion temperature jumps at the shock front are determined by the Rankine-Hugoniot jump conditions. Markevitch (2006) showed that the observed temperature profile across the shock front of the Bullet cluster supports the instant equilibrium model. Russell et al. (2012) found that the temperature profile across one shock front of Abell 2146 supports the collisional model while another shock supports the instant model. However, in all cases the measurement errors prevented a conclusive determination. [Later, Russell et al. \(2022\) with deeper *Chandra* observations found both shocks in Abell 2146 favor the collisional model.](#)

Here, we compare the observed temperature profile across the shock front of A98 with the predicted temperature profiles from collisional and instant equilibrium models. We estimate the model electron temperatures and project them along the line of sight, as described in Section 4.4.3. The resulting temperature profiles are shown in Figure 4.4. The observed post-shock electron temperature appears to be higher than the temperature predicted by the collisional equilibrium model and favors the instant equilibrium model, although we cannot rule out the collisional equilibration model due to the large uncertainty in the post-shock electron temperature.

4.4.3 Filament emission

We detected 3.2σ excess X-ray emission along the bridge connecting two sub-clusters (A98N and A98S), also detected by Alvarez et al. (2022b) (with lower significance) using *Suzaku*. Our measured surface brightness of the cooler component ranges between $(0.9\text{--}2.8) \times 10^{-15} \text{ erg cm}^{-2} \text{ s}^{-1} \text{ arcmin}^{-2}$ in the 0.5–2 keV energy band, which is equivalent to $(1.2\text{--}3.6) \times 10^{-15} \text{ erg cm}^{-2} \text{ s}^{-1} \text{ arcmin}^{-2}$ in the 0.2–10 keV energy

band. Using high-resolution cosmological simulations, Dolag et al. (2006) predicted that the X-ray surface brightness of the WHIM filaments should be $\sim 10^{-16}$ erg cm $^{-2}$ s $^{-1}$ arcmin $^{-2}$ with a zero metallicity in the 0.2-10 keV energy band. However, an increased metallicity could induce more line emission, increasing the surface brightness of the filament. A similar conclusion was drawn by Werner et al. (2008) while explaining their observed surface brightness of the WHIM filament, higher than that of cosmological simulation. Our measured surface brightness of the filament is consistent with the surface brightness of the WHIM filament obtained for A222/223 and A1750 (Bulbul et al., 2016b).

Using a 2-T plasma emission model, we measured the temperature of the cooler component of the filament, $kT_{\text{cool}} = 1.07 \pm 0.29$ keV. The 2-T model was a marginal improvement over the 1-T model with an F-test probability of 0.08. Similar filament temperatures were measured for A2744 (0.86–1.72 keV; Eckert et al., 2015), A222/223 (0.66–1.16 keV; Werner et al., 2008), and A1750 (Bulbul et al., 2016b). We obtained a best-fit filament electron density of $n_e = 1.30_{-0.31}^{+0.28} \times 10^{-4}$ cm $^{-3}$, assuming the filament is in the sky plane. If the filament has an inclination angle (i) with the line of sight, the electron density will be lower by a factor of $(\sin i)^{-1/2}$. Previous studies also found similar electron densities for the hot, dense part of the WHIM in several other galaxy clusters, e.g., 0.88×10^{-4} cm $^{-3}$ for A399/401 (Hincks et al., 2021), 1.08×10^{-4} cm $^{-3}$ for A3391/3395 (Alvarez et al., 2018), 10^{-4} cm $^{-3}$ for A2744 and A222/223 (Eckert et al., 2015; Werner et al., 2008). We estimated a baryon over-density of $\rho/\langle\rho\rangle \sim 240$ associated with the gas in the filament, which is consistent with the expected over-density for a WHIM filament (Bregman, 2007). Assuming a cylindrical geometry for the filament, we estimated the associated gas mass to be $M_{\text{gas}} = 3.8_{-0.6}^{+0.8} \times 10^{11} M_{\odot}$.

Our measured temperature and average density of the cooler component are remarkably consistent with what one expects for the hot, dense part of the WHIM, suggesting that this gas corresponds to the hottest, densest parts of the WHIM. X-ray observations of the emission from WHIM filaments are relatively rare because they have lower surface brightness than the ICM. They offer crucial observational evidence of hierarchical structure formation. Using numerical simulations, Davé et al. (2001) predicted that the gas in a WHIM filament has a temperatures in the range $10^{5.5}$ – $10^{6.5}$ K. A similar conclusion was drawn by Lim et al. (2020) using the kinetic S–Z effect in groups of galaxies. Since our detected filament lies in the overlapping ICM of both sub-clusters, the gas may have been heated by the shock and adiabatic compression.

Appendix

A1. Data reduction processes

Abell 98 was observed twice with *Chandra* ACIS-I in VFAINT mode, in September 2009 for 37 ks split into two observations and later in September 2018 – February 2019 for 190 ks divided into eight observations. The combined exposure time is ~ 227 ks (detailed observation logs are listed in Table 4.1). The *Chandra* data reduction

Table 4.1: *Chandra* observation log

Obs ID	Obs Date	Exp. time (ks)	PI
11876	2009 Sep 17	19.2	S. Murray
11877	2009 Sep 17	17.9	S. Murray
21534	2018 Sep 28	29.5	S. Randall
21535	2019 Feb 19	24.7	S. Randall
21856	2018 Sep 26	30.5	S. Randall
21857	2018 Sep 30	30.6	S. Randall
21880	2018 Oct 09	9.9	S. Randall
21893	2018 Nov 11	17.9	S. Randall
21894	2018 Nov 14	17.8	S. Randall
21895	2018 Nov 14	28.6	S. Randall

was performed using CIAO version 4.12 and CALDB version 4.9.4 provided by the Chandra X-ray Center (CXC). We have followed a standard data analysis thread [§].

All level 1 event files were reprocessed using the `chandra_repro` task, employing the latest gain and charge transfer inefficiency corrections, and standard grade filtering. VFaint mode was applied to improve the background screening. The light curves were extracted and filtered using the `lc_clean` script to identify and remove periods affected by flares. The filtered exposure times are listed in Table 4.1. We used the `reproject_obs` task to reproject all observations to a common tangent position and combine them. The exposure maps in the 0.5-2.0 keV energy bands were created using the `flux_obs` script by providing a weight spectrum. The weight spectrum was generated using the `make_instmap_weights` task with an absorbed APEC plasma emission model and a plasma temperature of 3 keV. To remove low signal-to-noise areas near chip edges and chip gaps, we set the pixel value to zero for those pixels with an exposure of less than 15% of the combined exposure time.

Point sources were identified using `wavdetect` with a range of wavelet radii between 1–16 pixels to maximize the number of detected point sources. We set the detection threshold to $\sim 10^{-6}$, for which we expect $\lesssim 1$ spurious source detection per CCD. We used blank-sky observations provided by the CXC to model the non-X-ray background and emission from the foreground structures (e.g., Galactic Halo and Local Hot Bubble) along the observed direction. The blanksky-background was generated using the `blanksky` task and then reprojected to match the coordinates of the observations. The resulting blanksky-background was normalized so that the hard band (9.5 - 12 keV) count rate matched the observations.

A2. Electron heating mechanism

When a shock front propagates through a plasma, it heats the ions dissipatively in a layer that has a width of few ion-ion collisional mean free paths. On the other hand,

[§]<http://cxc.harvard.edu/ciao/threads/index.html>

having very high thermal velocity compared to the shock, the electron temperature does not jump by the same high factor as the ion temperature. The electrons are compressed adiabatically at first in merger shocks and subsequently equilibrate with the ions via Coulomb scattering after a timescale (Spitzer, 1962; Sarazin, 1988) given by,

$$t_{eq}(e, p) \approx 6.2 \times 10^8 \text{yr} \left(\frac{T_e}{10^8 \text{K}} \right)^{3/2} \left(\frac{n_e}{10^{-3} \text{cm}^{-3}} \right)^{-1} \quad (4.3)$$

where T_e and n_e are the electron temperature and density, respectively.

Alternatively, the instant collisionless shock model predicts that the electrons and ions reach thermal equilibrium on a timescale much shorter than t_{eq} after passing the shock front, where the post-shock electron temperature is determined by the pre-shock electron temperature and the RH jump conditions (Markevitch and Vikhlinin, 2007). We use the best-fit density profile shown in Figure 4.2 to project this model electron temperature along the line of sight analytically (Russell et al., 2012).

In the collisional equilibration model, the electron temperature rises at the shock front through adiabatic compression,

$$T_{e,2} = T_{e,1} \left(\frac{\rho_2}{\rho_1} \right)^{\gamma-1} \quad (4.4)$$

where ρ_1 and ρ_2 are the gas density in the pre-shock and post-shock regions, and $\gamma = 5/3$. Electron and ion temperatures then subsequently equilibrate via Coulomb collision at a rate given by,

$$\frac{dT_e}{dt} = \frac{T_i - T_e}{t_{eq}} \quad (4.5)$$

where T_i is the ion temperature. Since the total kinetic energy density is conserved, the local mean gas temperature, T_{gas} is constant with time, where T_{gas} is given by,

$$T_{gas} = \frac{n_e T_e + n_i T_i}{n_i + n_e} = \frac{1.1 T_e + T_i}{2.1} \quad (4.6)$$

where n_i is the ion density.

We integrate Equation 4.5 by using Equation 4.3 and 4.6 to obtain the model electron temperature analytically. Finally, we project the model electron temperature profile along the line of sight (Ettori and Fabian, 1998) by,

$$\langle T \rangle = \int_{b^2}^{\infty} \frac{\epsilon(r) T_e(r) dr^2}{\sqrt{r^2 - b^2}} \bigg/ \int_{b^2}^{\infty} \frac{\epsilon(r) dr^2}{\sqrt{r^2 - b^2}} \quad (4.7)$$

where $\epsilon(r)$ is the emissivity at physical radius r and b is the distance from the shock front.

The emissivity-weighted electron temperature should be close to what one observes with a perfect instrument with a flat energy response across the relevant energy range. Since this is not the case, we convolve the instant and collisional model electron temperatures with the response of the telescope to predict what we expect to measure (Russell et al., 2012). We first estimate the emissivity-weighted electron temperature

using the above models and corresponding emission measure using the best-fit density discontinuity model (Equation 4.3) in a small volume dV . We then sum the emission measures with similar temperatures for each annulus using a temperature binning of 0.1 keV. We simulate spectra in XSPEC using a multi-temperature absorbed `apex` model. We fix the temperature of each component with the median temperature of each bin and calculate the normalization based on the summed emission measure in that temperature bin. We also fix the abundance to $0.4 Z_{\odot}$, n_{H} to galactic value, and redshift to 0.1043. To estimate the expected projected temperature in this annulus, we finally fit this simulated spectra with a single temperature absorbed `apex` model with abundance, n_{H} , and redshift fixed as above.

We adopt the Monte Carlo technique with 1000 realizations to measure uncertainty in model electron temperatures. Assuming a Gaussian distribution of the pre-shock temperature, which is the largest source of uncertainty, we repeated the model and projected temperature calculations 1000 times with a new value of pre-shock temperature each time. The resulting instant and collisional model temperature profiles with 1σ uncertainty are shown in Figure 4.4.

Chapter 5 Gas sloshing and cold fronts in pre-merging galaxy cluster Abell 98

5.1 Introduction

Abell 98 (hereafter A98) is an early-stage merger (Forman et al., 1981) with three main sub-clusters, A98S (central), A98N (northern), and A98SS (southern). Previous studies have reported a shock front associated with the northern sub-cluster and a filament connecting the northern and central sub-clusters (e.g., Alvarez et al., 2022a; Sarkar et al., 2022). In this work, we focus on the substructures at the central regions of both sub-clusters (northern and central).

Cluster mergers along large scale filaments leave imprints on the intra-cluster medium (ICM) in the form of shocks, cold fronts, and gas sloshing spirals (e.g., Markevitch et al., 2001, 2002; Ascasibar and Markevitch, 2006; Markevitch and Vikhlinin, 2007). Numerical simulations show that when a subhalo passes the density peak of the central cluster with a nonzero impact parameter, it accelerates the DM and gas peaks towards it. At first, they travel together, but as the gas peak moves through the surrounding gas, the ICM velocity field around the main cluster core decelerates the gas peak due to the ram pressure, resulting in a separation between the DM and gas peaks. While the DM peak continues moving towards the receding subhalo, the gas peak is held back. During the core passage, the direction of this motion rapidly changes, leading to an abrupt change in the ram-pressure force exerted on the gas peak, which overshoots the potential minimum. Eventually, the gas peak turns around and starts sloshing back and forth around the DM peak. This sloshing motion can be inferred from imaging studies, which reveal the presence of sharp discontinuity in the surface brightness and temperature. In these features, the brighter (denser) side of the surface brightness discontinuity is colder than the fainter (less dense) side; hence the “cold front”, as opposed to the shock front (e.g., Markevitch et al., 2000; Vikhlinin et al., 2001).

Gas sloshing motion can induce multiple cold fronts at different radii, growing over time and combining into a spiral pattern, known as a “gas sloshing” spiral (e.g., Ascasibar and Markevitch, 2006; Markevitch and Vikhlinin, 2007; Roediger et al., 2011). These spiral structures are commonly observed in a multitude of galaxy clusters, such as A1763 (Douglass et al., 2018), A2029 (Paterno-Mahler et al., 2013), A2052 (Blanton et al., 2011), and Fornax cluster (Su et al., 2017). Measurements of gas properties across the cold fronts reveal that the gas pressure stays almost the same across these cold fronts, as observed in several galaxy clusters, e.g., A2029 (Clarke et al., 2004), Perseus (Ichinohe et al., 2019), A2142 (Rossetti et al., 2013), and in galaxy groups (Gastaldello et al., 2013). This leaves little to no room for the relative gas motion, as ram pressure forces would increase the gas pressure inside of the cold front. Though there is pressure equilibrium across the cold fronts, observations exhibit that the gas outside the edge is nearly at hydrostatic equilibrium, but the gas inside the edge is not (e.g., Fabian et al., 2001; Markevitch and Vikhlinin, 2007).

A98 is an early-stage merger at a average redshift of $z \approx 0.1042$ (Paterno-Mahler et al., 2014). Previous observations confirm that this is a system of Bautz-Morgan type II-III and richness of class 3 (Abell et al., 1989). The central sub-cluster A98S is at a redshift of $z \approx 0.1063$ and hosts a wide-angle tail (WAT) radio source (4C 20.04; O’Donoghue et al., 1993). The other two sub-clusters, A98N ($z \approx 0.1043$) and A98SS ($z \approx 0.1218$), are at a projected distance of ~ 1.1 Mpc north and 1.4 Mpc south from the central sub-cluster, respectively. (e.g., Jones and Forman, 1999; Burns et al., 1994). A98N is a cool core cluster with an asymmetric warmer gas arc in the southern direction (Paterno-Mahler et al., 2014). In paper I (Sarkar et al., 2022), we investigated this scenario in detail. We reported a shock front with a Mach number of $\mathcal{M} \approx 2.3$ at about 420 kpc from the A98N core. We also detected the shock-heated gas with a temperature of $6.4_{-1.5}^{+1.0}$ keV in the southern direction of A98N.

The primary goals of this paper are to map the thermodynamic structure and reveal any sub-structures associated with the central regions of A98N and A98S. We investigate the surface brightness edges near A98N and A98S and measure gas properties across them. We organize the paper as follows: in Section 5.2, we describe the data reduction procedures; in Section 5.3, we analyse the actual, residual, the Gaussian Gradient Magnitude (GGM) image, and report the surface brightness profiles and electron density jumps; in Section 5.4, we show results from the spectral analysis, including the gas properties profiles; finally, in Section 5.5 we discuss and summarize our results.

Throughout this paper, we adopt a cosmology of $H_0 = 70 \text{ km s}^{-1} \text{ Mpc}^{-1}$, $\Omega_\Lambda = 0.7$, and $\Omega_m = 0.3$. Unless otherwise stated, all reported error bars correspond to a 90% confidence level.

Table 5.1: *Chandra* observation log

Obs ID	Obs Date	Exp. time (ks)	PI
11876	2009 Sep 17	19.2	S. Murray
11877	2009 Sep 17	17.9	S. Murray
21534	2018 Sep 28	29.5	S. Randall
21535	2019 Feb 19	24.7	S. Randall
21856	2018 Sep 26	30.5	S. Randall
21857	2018 Sep 30	30.6	S. Randall
21880	2018 Oct 09	9.9	S. Randall
21893	2018 Nov 11	17.9	S. Randall
21894	2018 Nov 14	17.8	S. Randall
21895	2018 Nov 14	28.6	S. Randall

5.2 Data preparation

Abell 98 was observed with *Chandra* during two epochs, once in September 2009 for 37 ks split into two observations and later in September 2018 – February 2019 for 190

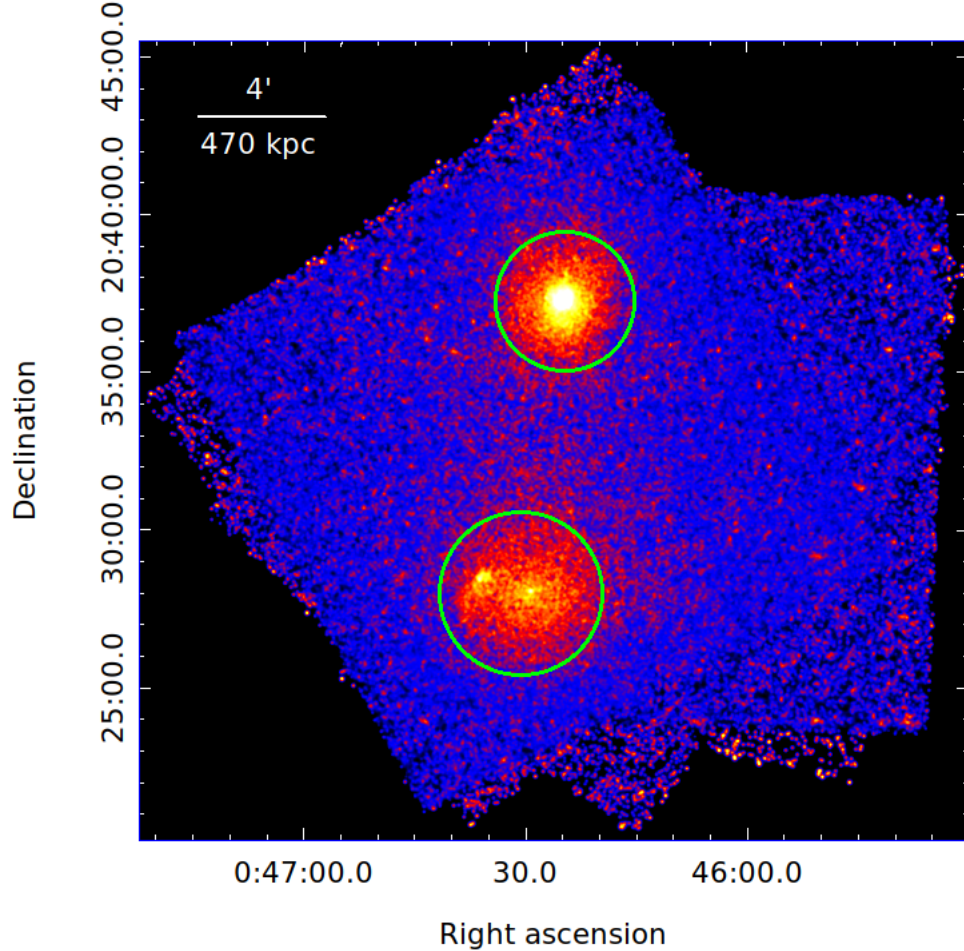


Figure 5.1: Merged, exposure corrected, and background subtracted *Chandra* ACIS-I image of northern (A98N) and central (A98S) sub-clusters of A98 in the 0.5–2.0 energy band. The image has been smoothed with a $\sigma=2''$ Gaussian kernel. The dual structure of A98S is clearly visible. Yellow circles represent the regions used for the measurement of global ICM properties of both sub-clusters.

ks divided into eight observations. The combined exposure time is ~ 227 ks (detailed observation logs are listed in Table 5.1). We performed the *Chandra* data reduction with CIAO version 4.12 and CALDB version 4.9.4 distributed by the Chandra X-ray Center (CXC). We have followed a standard data analyzing thread [§].

All level 1 event files were reprocessed using the `chandra_repro` task by employing the latest gain, charge transfer inefficiency correction, and filtering out the bad grades. VFaint mode was used to improve the background screening. Light curves were extracted and filtered using the `lc_clean` script to identify and remove periods affected by flares. The filtered exposure times are listed in Table 4.1. We used the `reproject_obs` task to reproject all observations to a common tangent position and combine them. The exposure maps in the 0.5–2.0 keV energy bands were created using

[§]<http://cxc.harvard.edu/ciao/threads/index.html>

the `flux_obs` script by providing a weighting spectrum. The weight spectrum was generated using the `make_instmap_weights` task with an absorbed APEC plasma emission model and a plasma temperature of 3 keV. To remove the hot pixels, we set the pixel value to zero for those pixels with an exposure of less than 15% of the combined exposure time.

Point sources were identified using `wavdetect` with a range of wavelet radii between 1–16 pixels. We set the detection threshold to $\sim 10^{-6}$, which guaranteed $\lesssim 1$ spurious source detection per CCD. We used blanksky background observations to model the non-*X*-ray background, emission from foreground structures (e.g., Galactic Halo and Local Hot Bubble) along the observed direction and unresolved faint background sources. The blanksky background files were generated using the `blanksky` task and then reprojected to match the coordinates of the observations. We finally normalized the resulting blanksky background to match the 9.5–12 keV count rates in our observations.

5.3 Imaging analysis

Figure 5.1 shows a slightly smoothed image of A98N (northern sub-cluster) and A98S (central sub-cluster) in the 0.5-2 keV band, obtained after co-adding all ten observations and by applying the correction for exposure non-uniformity. As reported by earlier studies, the cluster is an early-stage merger, with the merger axis likely aligned along a local N-S large-scale filament connecting A98N and A98S (e.g., Paterno-Mahler et al., 2014; Alvarez et al., 2022a; Sarkar et al., 2022).

5.3.1 A98N

We obtain a residual image of A98N to search for any faint substructures, e.g., associated with gas sloshing or merger shocks. The residual image is created by subtracting the azimuthally averaged surface brightness at each radius (centered on A98N), as shown in Figure 5.2. The residual image shows an apparent surface brightness excess spiraling clockwise (if traced inward from large radius), a classic signature of gas sloshing, and is brightest to the north/north-east of the cluster center. The farthest visible arc of the spiral extends out to 140 kpc south from the cluster center. Similar gas sloshing spiral have also observed in other galaxy clusters, e.g., A2029 (Paterno-Mahler et al., 2013), Perseus (Fabian et al., 2011), A1763 (Douglass et al., 2018), A2319 (Ichinohe et al., 2021), and A2142 (Roediger et al., 2012).

The sloshing spiral in A98N indicates it experienced a separate merger, unassociated with the on-going early-stage merger between A98N and A98S, probably in the past few Gyr based on the timescale for the formation of the sloshing spirals seen in simulations (ZuHone et al., 2010). Spiral patterns are understood to have formed when a cool-core system experiences a infall of a subcluster with a non-zero impact parameter. Simulations of the formation of spiral patterns show that during the formation process, the relative velocity between gas density and dark matter peak stays below 400 km/s (Ascasibar and Markevitch, 2006), and the average offset between gas density-dark matter peaks is below 30 kpc (Johnson et al., 2010).

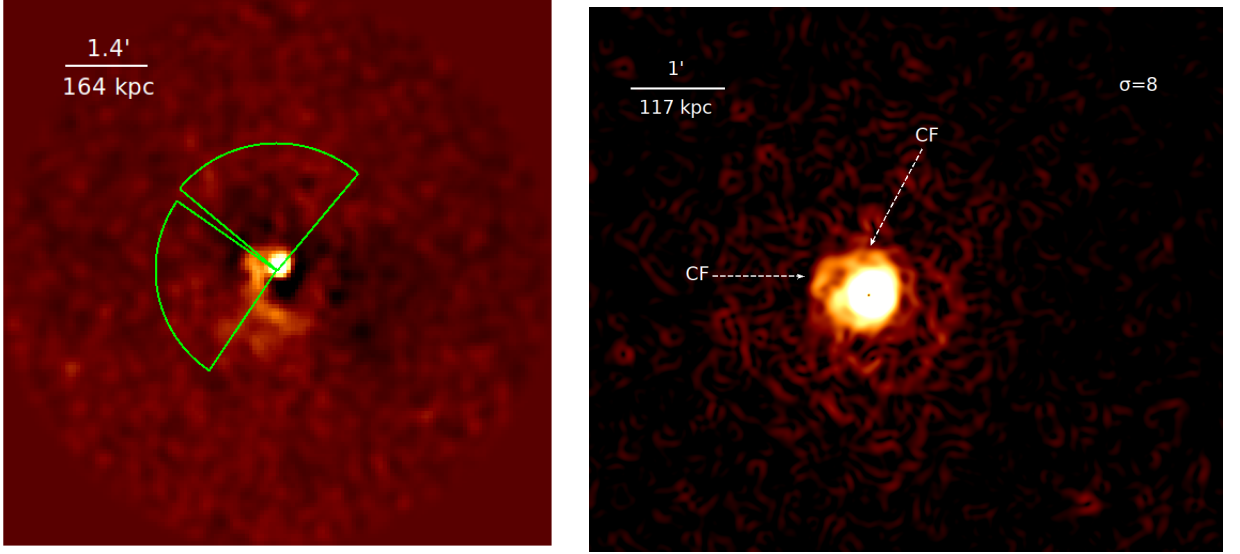


Figure 5.2: *Left*: Residual image of A98N in the 0.5-2 keV energy band obtained after subtracting azimuthal averaged surface brightness profile from the Figure 5.1. The image has been smoothed with a $1.5''$ Gaussian kernel. A spiral pattern can clearly be seen travelling clock-wise if traced inward. Green sectors are used for spectral analysis. *Right*: Gaussian gradient magnitude filtered image of A98N smoothed by $\sigma = 8$ pixels and each pixel = $0.492''$. The north and east cold fronts are marked by white arrow.

Additionally, the winding direction of a spiral (when traced inward from large radii) reveals the infalling subcluster’s trajectory since the direction of angular momentum of spiraling-in gas is the same as that of the infalling subcluster (ZuHone et al., 2011; Douglass et al., 2018). The clockwise winding spiral pattern seen in A98N indicates that the perturbing subcluster may have passed the A98N core from the west to the north-west on the southern side.

Next, to reveal any substructures and associated sharp features in the A98N core, we obtained a GGM filtered image of A98N with a filtering length scale of 8 pixels. Each pixel is $0.492''$ wide. Figure 5.2 shows the GGM image of the A98N core. We observe two regions with relatively large surface brightness gradients in the core, peaking at ~ 60 kpc to the north and 70 kpc to the east of the A98N core (indicated by the white arrows in Figure 5.2), sharply declining at larger radii. To determine the significance of these apparent features, we extracted surface brightness profiles in the east and north directions in 90° sectors. The energy band is restricted to 0.5-2 keV to minimize the effect of variation of X-ray emissivity with temperature while maximizing the signal-to-noise ratio. We match the centers of the curvature of the surface brightness edges to the center of the sectors. Figure 5.3 shows the extracted surface brightness profiles in the east and north directions.

Both surface brightness profiles exhibit discontinuities and overall shapes that are consistent with what is expected from a projected spherical density discontinuity

(Markevitch et al., 2000). We fit each profile with a broken power-law model

$$n(r) \propto \begin{cases} \left(\frac{r}{r_{edge}}\right)^{-\alpha_1}, & \text{if } r < r_{edge} \\ \frac{1}{jump} \left(\frac{r}{r_{edge}}\right)^{-\alpha_2}, & \text{if } r \geq r_{edge} \end{cases} \quad (5.1)$$

where $n(r)$, r_{edge} , and $jump$ represent 3D electron density at a radius r , the radius of the putative edge, and the density jump factor, respectively. α_1 and α_2 are the slopes before and after the edge, respectively. We project the estimated emission measure profile onto the sky plane and fit the observed surface brightness profile by varying the slopes, edge radius, and the magnitude of the jump (similar to what we did for the shock front in paper I; Sarkar et al. 2022). Figure 5.3 displays the best-fit models (red) and the 3D density profiles (inset) for both directions. For the east direction, we obtain best-fit power-law indices of $\alpha_1 = 0.70 \pm 0.01$ and $\alpha_2 = 1.0 \pm 0.01$. The associated density jump across the edge is $\rho_2/\rho_1 = 1.38 \pm 0.03$, where suffix 2 and 1 represent the regions inside and outside of the edge, respectively. Similarly, for the north direction, we find a best-fit power-law index of $\alpha_1 = 0.80 \pm 0.03$ and $\alpha_2 = 1.10 \pm 0.03$ with a corresponding density jump of 1.47 ± 0.01 . We obtain the best-fit edge radius of 70 ± 6 kpc for the east edge and 60 ± 4 kpc for the north edge, as measured with respect to the centroid of the central X-ray surface brightness peak. Both edge radii are consistent with the position of the steep gradients seen in the GGM image (Figure 5.2). We estimate the uncertainty of each parameter by allowing all the other model parameters to vary freely.

5.3.2 A98S

Figure 5.1 reveals that the central sub-cluster (A98S) hosts two distinct surface brightness peaks. Paterno-Mahler et al. (2014) showed that the western peak coincides with a WAT AGN. Using the SDSS-r magnitude of the galaxy distribution of A98, they concluded that these two surface brightness peaks are likely to be associated with two BGCs from two merging subclusters. We denote the western sub-cluster as A98Sa and the eastern sub-cluster as A98Sb. Figure 5.1 exhibits that the X-ray emission is extended from east to west and appears to cut off abruptly northeast of the A98Sb. To better highlight these features, we create an unsharp-mask image in the following way. We smoothed the background subtracted and exposure corrected X-ray image by 2D Gaussian kernels with $\sigma = 2''$ and $20''$. Both images are then subtracted to obtain the unsharp-masked image, as shown in Figure 5.4. Unsharp-masked image features the different substructures in the ICM of A98S. A98S appears to be separated into three concentrations of X-ray emitting gas: the two sub-cluster cores (A98Sa and A98Sb) and a “tail” of emission to the southeast originating from the central region of A98Sb. The unsharp-masked image also reveals a surface brightness edge northeast of A98Sb. In contrast, A98Sa shows a relatively uniform morphology with no prominent surface brightness edges.

We next examine the surface brightness edge seen in the northeast of A98Sb by extracting a surface brightness profile across the edge, as shown in Figure 5.6 (right).

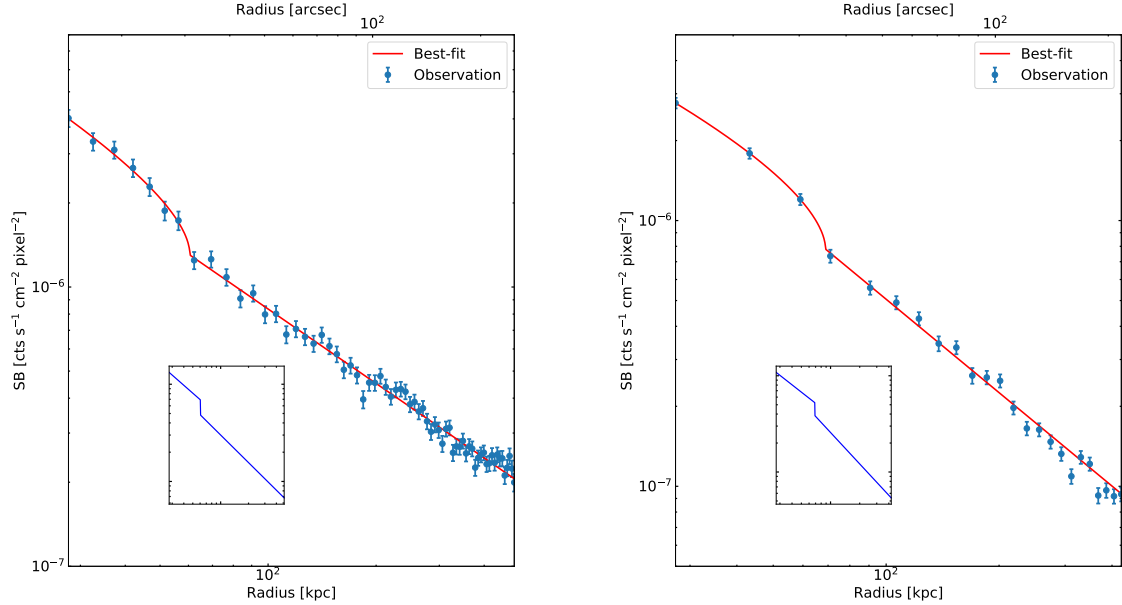


Figure 5.3: *Left*: Northern sector surface brightness profile of A98N in the 0.5 - 2 keV energy band fitted with a broken power-law model. The best-fit deprojected density profile is shown in inset figure. All error bars are at $1\text{-}\sigma$ level. *Right*: similar to the *left* figure, but for eastern sector.

The surface brightness profile shows a discontinuity similar to what we have seen in A98N. We fit the profile with a broken power-law model, as detailed in Section 5.3.1. Figure 5.6 displays the best-fit model (in red) and 3D density profile (inset). We obtain a best-fit power-law index of $\alpha_1 = 0.650 \pm 0.003$ and $\alpha_2 = 0.7 \pm 0.1$. The associated density jump across the edge is $\rho_2/\rho_1 = 2.8 \pm 0.2$ with a best-fit edge radius of 28 ± 2 kpc.

To further investigate any faint substructure associated with both sub-cluster cores (A98Sa and A98Sb), we obtain a β -model subtracted image of A98S. We use two 2D elliptical β -models centered at both sub-cluster cores to fit the surface brightness image in the 0.5-2 keV energy band. We also include a constant in the model to account for the sky background and any residual particle background. The model is fitted in *Sherpa*, and the best-fit parameters are obtained by minimizing the Cash statistic (Cash, 1979). The best-fit 2D β -model image is then subtracted from the source image of A98S, leaving the residual image shown in Figure 5.5.

Figure 5.5 reveals a spiral structure likely to be associated with the gas sloshing resulted from recent fly-by of a subhalo near the central region of A98Sb. The excess emission from the “tail” seen in the residual and unsharp-masked image may suggest a trail of materials that has been ram pressure stripped in the gravitational potential. Alternatively, the spiral structure and the tail may be due to ram pressure stripping, as the subcluster orbits in the main cluster’s potential, and the tail is potentially

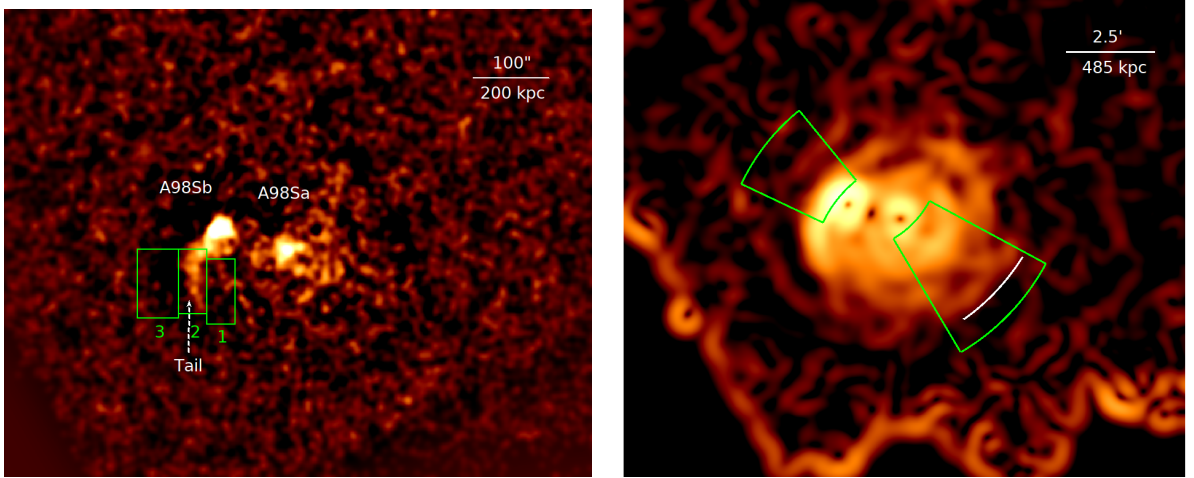


Figure 5.4: *Left*: Unsharp-masked image of A98Sa and A98Sb created by subtracting images smoothed by 2D Gaussians with $\sigma = 2''$ and $20''$. Green regions are used for the spectral analysis. The ‘tail’ is marked with magenta arrow. *Right*: Gaussian gradient magnitude filtered image of A98S. The image is smoothed by $\sigma = 13''$. A sharp gradient is clearly visible to SW of the A98Sa and marked by white curve. Green sectors are used for spectral analysis.

influenced by ICM “whether” (e.g. bulk turbulence). Both scenarios could be true. A further deeper observation is required to probe the feature in detail.

Compared to A98Sb, A98Sa shows a relatively regular morphology. Since there are clear radio lobes, one might expect cavities in the ICM evacuated by these lobes (references). A weak detection of cavities at the location of the lobes was reported in Paterno-Mahler et al. (2014). We therefore extract an azimuthal surface brightness profile, shown in Figure 5.6, centering at the A98Sa core with a radius of $\sim 150''$. The sharp increase in the surface brightness to the east with a peak at $\sim 165^\circ$ is due to the surface brightness peak associated with A98Sb. Similar results were obtained by Paterno-Mahler et al. (2014). However, we do not find any significant difference between the surface brightness in any other directions. Since A98Sa hosts a WAT radio source, the absence of any substantial decrement in the surface brightness at north and south directions indicates that either the radio lobes are filled with X-ray emitting gas, or the jet axis is far enough from the plan of the sky to prevent a detection. Several previous studies also found jets and lobes in other merging galaxy clusters, such as A2199 (Nulsen et al., 2013), A1682 (Clarke et al., 2019), A1446 (Douglass et al., 2008), A562 (Douglass et al., 2011; Gómez and Calderón, 2020), and A1775 (Hu et al., 2021).

The GGM image of A98S shown in Figure 5.4 features a possible surface brightness edge at about 370 kpc southwest of A98Sa. We extract a surface brightness profile across the edge and fit that profile using a broken power-law model, as seen in Figure 5.10. We obtain best-fit power-law indices of $\alpha_1 = 0.7 \pm 0.1$ and $\alpha_2 = 0.9 \pm 0.2$. The electron density jumps by a factor of 1.7 ± 0.5 across the edge. We find the best-fit

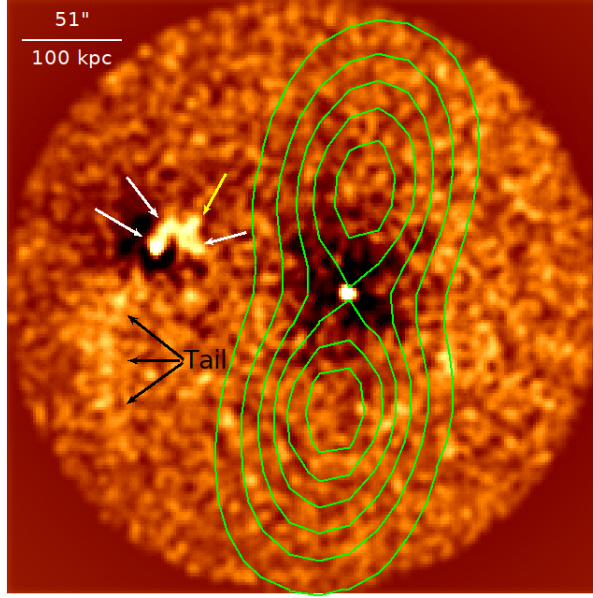


Figure 5.5: Residual image of excess X-ray emission of A98Sa and A98Sb with 1.4 GHz radio contours overlaid in green. The image was created by subtracting two 2D elliptical β -models from an unbinned image with point sources excluded. White, yellow, black arrows indicate the spiral structure, the bifurcation of spiral pattern, and the ‘tail’ of X-ray emission, respectively.

edge radius of 375 ± 10 kpc coincides with the apparent rapid change in the surface brightness gradient seen in GGM image. We discuss the spectral properties of the surface brightness edges seen in A98Sa and A98Sb in Section 5.4.4.

5.4 Spectral analysis

5.4.1 Global ICM properties

To constrain the global properties of both sub-clusters, we first extracted spectra from two circular regions centering at both sub-cluster cores with a radius of $\sim 2'$ for A98N and $3'$ for A98S (roughly similar regions as seen in Paterno-Mahler et al. 2014). Both regions contain $\gtrsim 32000$ background-subtracted counts in the 0.6-7 keV energy band and contain a vast majority of the cluster emission after eliminating the point sources, which is imperative to probe the global properties of both sub-clusters. The background spectra were hard-band scaled (10–12 keV) and subtracted from the source spectra before fitting. We restricted the spectral fitting to the 0.6-7 keV energy band and binned the spectra to contain a minimum of 40 counts per bin. We fixed the redshift to $z = 0.1042$ and the absorption to the galactic value $N_H = 3.06 \times 10^{20} \text{ cm}^{-2}$ (Kalberla et al., 2005). The spectral analysis was performed using *Xspec* version 12.11.1. All resolved point sources were excluded before the spectral analysis. For each sub-cluster, a single-temperature fit to the observed spectra using an absorbed thermal plasma emission model (i.e. *phabs* \times *apec*) produced a good fit (Smith et al.,

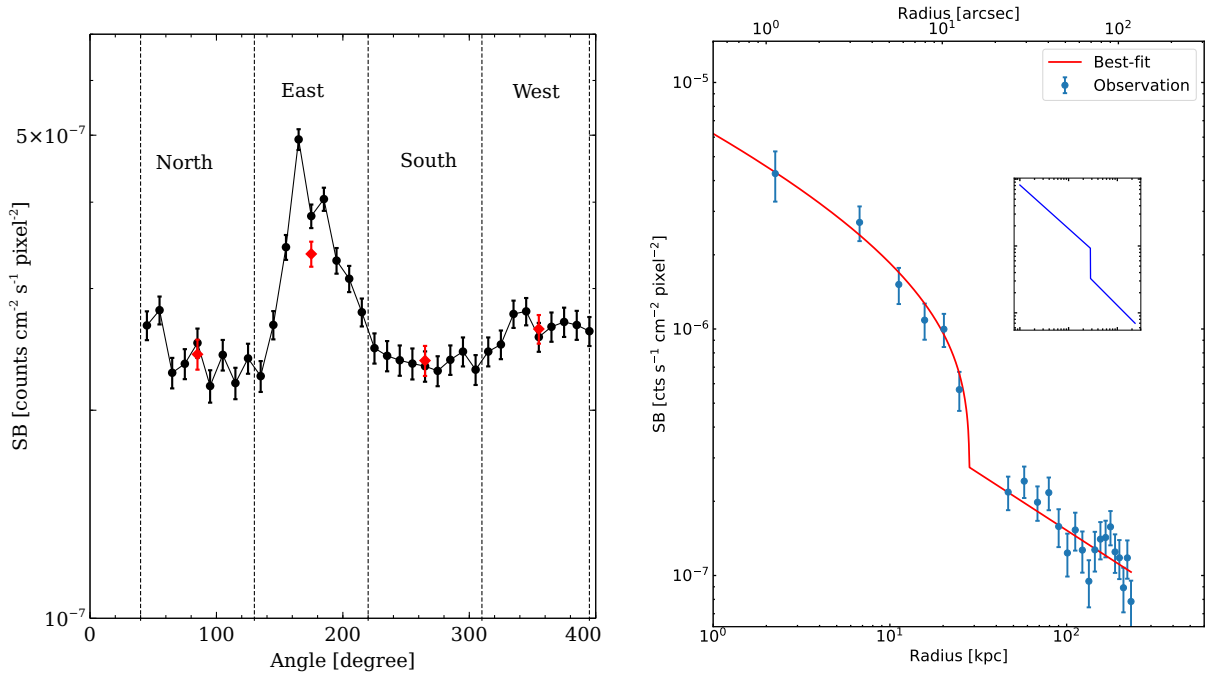


Figure 5.6: *Left*: Azimuthal surface brightness profile in the 0.5 - 2 keV energy band centered on the A98Sa core. Black represents the surface brightness at individual angles and red represents the binned surface brightness in 90° sectors. The north and south sectors contain the northern and southern lobe of the WAT. East sector contains the second BCG, A98Sb. *Right*: Eastern sector (as shown in Figure 5.4) surface brightness profile of A98Sb in the 0.5 - 2 keV energy band fitted with a broken power-law model. Deprojected density profile is shown in inset figure.

2001). We used solar abundance table given in Asplund et al. (2009).

For A98N, we measured a temperature of 3.05 ± 0.09 keV and a metal abundance of $0.63 \pm 0.10 Z_{\odot}$ with a χ^2/dof of 786/761. Additionally, spectral fitting to the central sub-cluster (A98S) yielded a best-fit temperature of 3.04 ± 0.12 keV and an abundance of $0.42 \pm 0.10 Z_{\odot}$ with a χ^2/dof of 870/886. In both cases, the hydrogen column density was fixed to the Galactic value, $N_H = 3.06 \times 10^{20} \text{ cm}^{-2}$, estimated using the LAB survey (Kalberla et al., 2005). Paterno-Mahler et al. (2014) also reported the temperature and abundance of both sub-clusters using a 38 ks *Chandra* observation and a 37 ks *XMM-Newton* observation. For both sub-clusters, our measured temperatures and abundances are consistent with those of Paterno-Mahler et al. (2014).

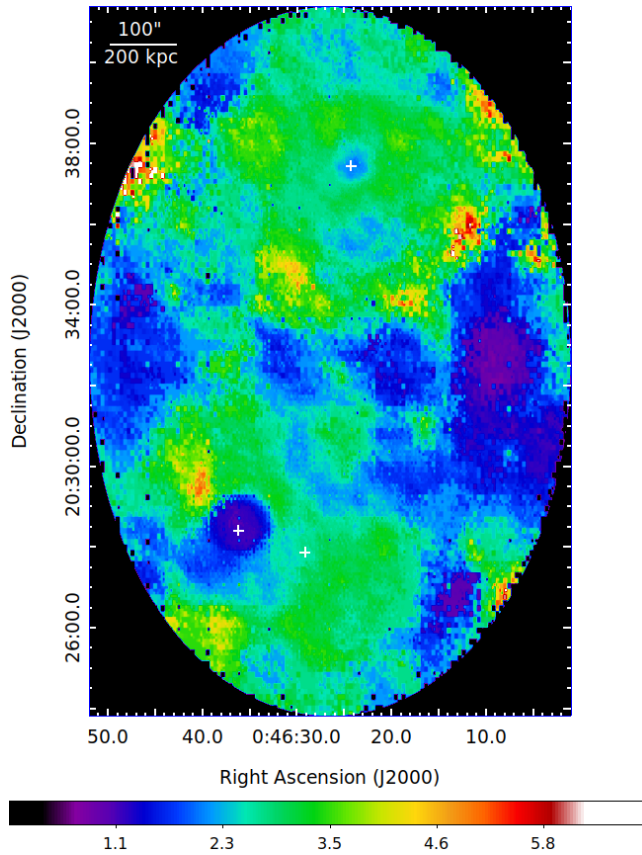


Figure 5.7: Projected temperature map of A98N/A98S. Units are in keV. The individual sub-cluster centers are marked by white crosses. The warmer gas ‘arc’ can be seen to the south of A98N. A98N and A98Sb have cool central cores, whereas A98Sa has a warmer, roughly isothermal core.

5.4.2 Temperature map

For understanding the thermodynamic structures of the ICM in A98N and A98S, we constructed a temperature map following the techniques described in Randall et al. (2008, 2009). We extracted an elliptical region containing both sub-clusters and binned the image with 10 background-subtracted counts per pixel to aid the computational speed. For each pixel, we extracted spectra from a circular region with a radius set such that the region contains ~ 2300 background-subtracted source counts in the 0.5-7 keV energy band. This particular number of source counts was adopted to ensure that the uncertainty in temperature measurements in the fainter regions of the ICM was $\lesssim 25\%$. We generated appropriate response and ancillary response files for each region, and the background spectra were subtracted from the source spectra.

Figure 5.7 shows the temperature map of A98N/A98S. A98N and A98Sb appear to

have cool cores with hot gas enclosing them, which is expected for cool core clusters. In contrast, A98Sa appears to have a warm core with a uniform gas temperature of ~ 3.7 keV within 20 kpc of the core. This may imply that A98a was transformed into a non cool-core cluster during a previous merger.

The northern sub-cluster has an asymmetric ‘arc’ of hot gas with a temperature of > 3.5 keV, which is clearly visible in Figure 5.7. This arc radius (~ 400 kpc) is consistent with the radius of the shock front that we reported in paper I (Sarkar et al., 2022), suggesting the ‘arc’ consists of shock heated gas. The uncertainties in the temperature map range from $\lesssim 15\%$ for brighter regions and stay between 20-25% for the fainter regions. Since each region in the temperature map contains a fixed source count, the extraction regions are larger in the fainter parts of the ICM, making the temperature map highly smoothed.

5.4.3 A98N: East and North cold fronts

We extracted spectra from the eastern and northern sectors in A98N to measure the temperature and density changes across the surface brightness edges seen in Figure 5.3. Each sector was divided into five individual bins. These bins were positioned to measure the gas properties on either side of the surface brightness edges while maintaining a minimum of 3000 background-subtracted counts in each extracted spectrum. We set this lower limit to guarantee enough photon counts for good spectral fitting and constraints on the parameters. Spectra were extracted from those bins in each sector.

We fixed the metallicity to an average value of $0.4 Z_{\odot}$ since it was poorly constrained if left free (Russell et al., 2010). The best-fit parameters were obtained by minimizing the Cash statistics. Figure 5.8 shows the radial profiles of the best-fit projected temperatures and pressures obtained across the eastern and northern edges. The temperature of the gas increases from the A98N core to the larger radii in both directions. Our measurements confirm the electron density jumps detected in the surface brightness profile analysis, but the temperature and pressure profiles appear continuous across the edges. However, the cooler gas inside of the edges is more consistent with a cold front interpretation. Similar cold fronts are also found in other clusters such as Bullet cluster (Markevitch et al., 2002), A2142 (Markevitch et al., 2000), A3667 (Vikhlinin et al., 2001), A2146 (Russell et al., 2010), A2256 (Ge et al., 2020), A2554 (Erdim and Hudaverdi, 2019), Perseus (Walker et al., 2017, 2020), and in many other (Botteon et al., 2018).

5.4.4 A98S: cold front, tail, and western SB edge

A98S consists of two individual sub-clusters, A98Sa and A98Sb. The temperature map in Figure 5.7 shows that the central region of A98Sb is cooler than A98Sa. Previous *Chandra* observations by Paterno-Mahler et al. (2014) showed that A98Sb is cooler than A98Sa at a $3\text{-}\sigma$ level. With our deeper *Chandra* observations, we examined the spectra of each sub-cluster to measure the global ICM temperatures of individual sub-clusters. We extracted spectra from $50''$ regions centering at both sub-clusters’

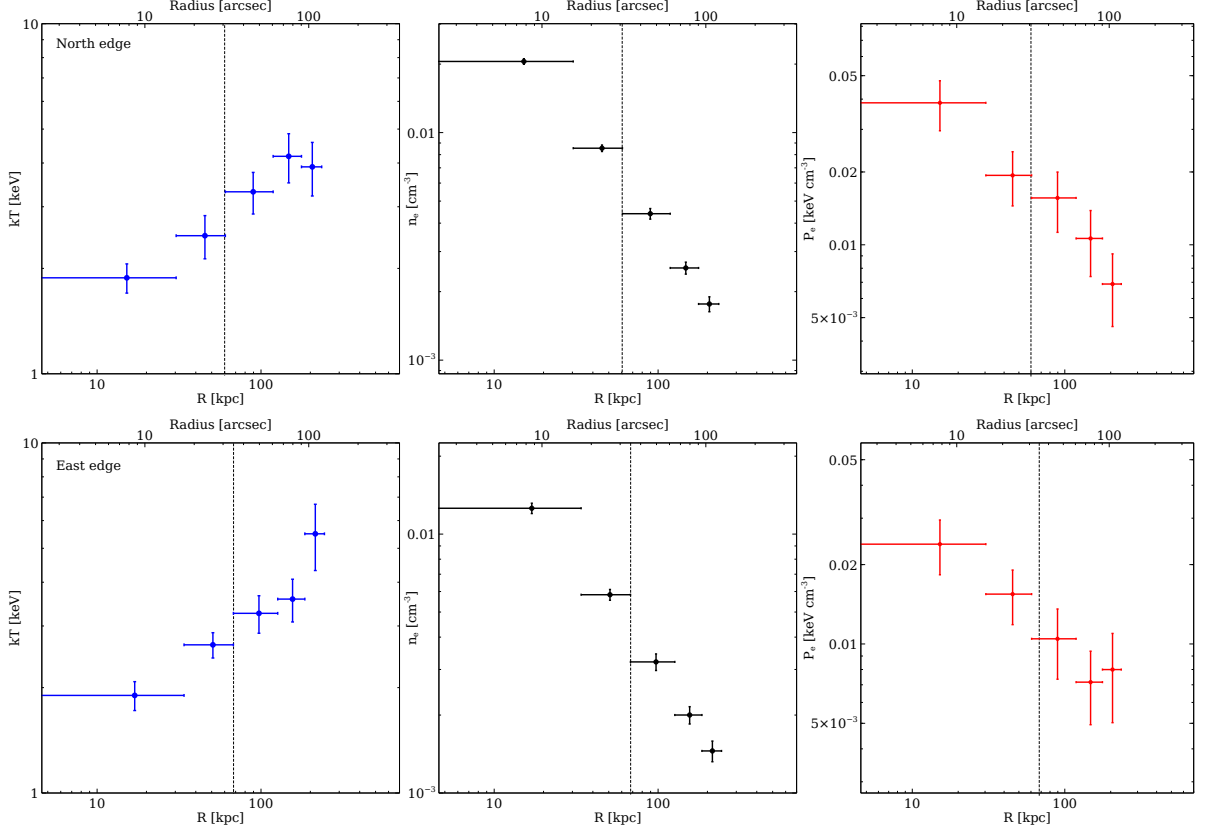


Figure 5.8: *Top panel:* Northern sector projected temperature, deprojected electron density, and projected electron pressure profiles centered on the A98N core. The metallicity was fixed to $0.4 Z_{\odot}$. The projected pressure profile was estimated using the deprojected densities and projected temperatures. Vertical dashed line represents the position of the surface brightness edges. *Bottom panel:* similar as above but for eastern sector.

core. These regions were chosen by eye estimation, assuming each of them includes the prominent extended emission from the corresponding sub-cluster. Point sources and background spectra were analyzed as described in Section 5.4. We measured a temperature of $3.70^{+0.33}_{-0.28}$ keV for the western sub-cluster (A98Sa) and $2.47^{0.21}_{-0.20}$ for the eastern sub-cluster (A98Sb). Our measured temperatures are consistent with that of Paterno-Mahler et al. (2014) within their uncertainties (90% confidence limit). We also found that the A98Sb is cooler than the A98Sa at a $5\text{-}\sigma$ level. This implies that A98Sb has a remnant cool core, whereas the core of A98Sa has been disrupted, so that this is a non cool-core cluster. Since A98Sa hosts a WAT radio source (4C 20.04; O’Donoghue et al., 1993), it may heat up the surrounding ICM via AGN jets. Similar ICM heating through AGN feedback can also be found in other galaxy clusters such as A2052 (Blanton et al., 2011), Perseus (Fabian et al., 2003), A2626 (Ignești et al., 2018, 2020), and A1795 (Kokotanekov et al., 2018). Alternatively, the core of A98Sa may have been disrupted by either the ongoing merger or a previous merger.

We next examined the “tail” like substructure of the eastern sub-cluster that

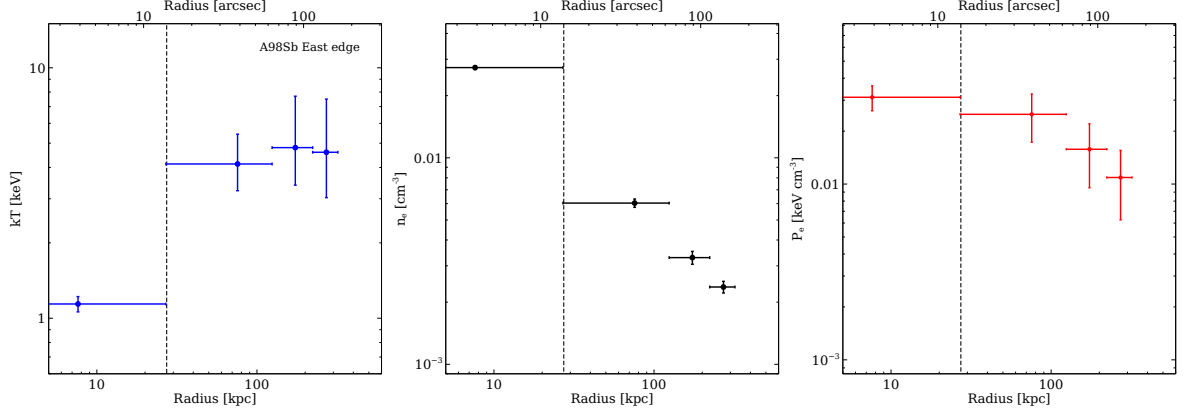


Figure 5.9: Eastern sector projected temperature, deprojected electron density, and projected electron pressure profiles centered on the A98Sb core. The metallicity was fixed to $0.4 Z_{\odot}$. The projected pressure profile was estimated using the deprojected densities and projected temperatures. Vertical dashed line represents the position of the surface brightness edge.

appeared in the unsharp masked image (Figure 5.4). We extracted spectra from three individual regions, as shown in Figure 5.4. Due to low photon counts in regions 1 and 3, we linked the parameters for those two regions while fitting, assuming they have similar temperature and electron density. For region 2, this yielded a temperature of $kT = 1.8^{+0.3}_{-0.2}$ keV and an abundance of $Z = 0.35^{+0.49}_{-0.24} Z_{\odot}$. For regions 1 and 3 together, we measured a temperature of $kT = 3.1^{+0.6}_{-0.4}$ keV and an abundance of $Z = 0.80^{+1.01}_{-0.57} Z_{\odot}$. We found the tail is significantly cooler than the surrounding gas at about $4.2\text{-}\sigma$ level, which infers that it is likely to be a cool-core remnant that is being ram pressure stripped.

Figure 5.6 shows that A98Sb has a surface brightness edge in the northeast direction at about 28 kpc from its core. To measure the temperature across the surface brightness edge, we divided the eastern sector into four individual regions and extracted spectra from them. Those regions were drawn to contain a minimum of 1000 background-subtracted photon counts in each extracted spectrum. We set this lower limit to ensure reasonable constraints on the parameters. We fitted each spectrum with the abundance fixed to $Z = 0.4 Z_{\odot}$. Figure 5.9 shows the best-fit projected temperature profile of the eastern sector. The projected temperature of the gas increases rapidly at about 28 kpc, by a factor of ~ 3.6 . This temperature jump coincides with the surface brightness edge at 28 kpc, as shown in Figure 5.9, and corresponds to a drop in the deprojected electron density by a factor of ~ 2.8 . Figure 5.9 also shows the projected electron pressure profile of the eastern sector. We found that the electron pressure is roughly constant across the surface brightness edge. We, therefore, confirm this edge as a cold front or contact discontinuity.

We next examined the surface brightness edge shown in Figure 5.10 (left) southwest of A98Sa by extracting spectra from that sector dividing it into five individual regions. We fitted the spectrum from each region with the abundance fixed to 0.4

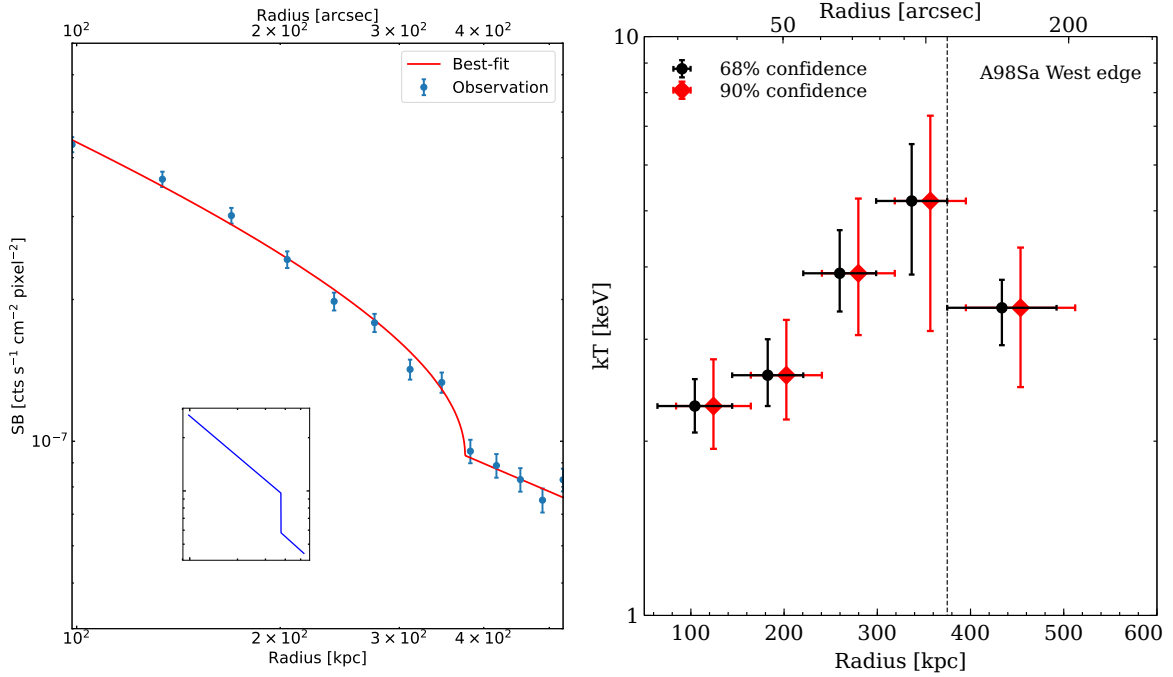


Figure 5.10: *Left*: western sector surface brightness profile of A98Sa in the 0.5-2 keV energy band fitted with a broken power-law model. Deprojected density profile is shown in inset figure. *Right*: western sector projected temperature profiles of A98Sa. Black and red represent the uncertainties estimated with 68% and 90% confidence level, respectively. The red data points are shifted to the right for the purpose of clarity and comparison. Vertical dashed line represents the position of the surface brightness edge.

Z_{\odot} . The best-fit projected temperature profiles are shown in Figure 5.10 (right) with different levels of uncertainty. Considering both levels of uncertainties, we found that the temperature profile rises to $kT = 5.1$ keV at about ~ 375 kpc, then drops suddenly to $kT = 3.3$ keV with a jump factor of ~ 1.5 . Taken all together, this implies a stronger suggestion of a shock. From the 3D density jump factor we obtained Mach number of the shock to be $\mathcal{M} \approx 1.5$, consistent with the Mach number estimated from the temperature jump. Similar Mach numbers from measurements bolster the edge as a shock front.

5.5 Summary

We have presented results from deep 227 ks *Chandra* observations of an early-stage merger A98N/A98S. Our analysis indicates that the cluster is experiencing a complex merger. While the northern sub-cluster (A98N) and southern sub-cluster (A98S) are merging along the N-S, the two sub-clusters of A98S (A98Sa and A98Sb) are

undergoing a later-stage merger in the E-W direction. We summarize our findings below -

- The residual image of A98N shown in Figure 5.2 reveals a gas sloshing spiral winding clockwise when traced inward from a large radius. The sloshing spiral in A98N indicates that it too experienced a separate merger, probably in the past few Gyr based on the timescale for the formation of the sloshing spirals seen in simulations.
- We have detected two cold fronts in the north and east directions at about 60 kpc and 70 kpc, respectively, from the A98N core. For the northern cold front, we obtain a drop in the deprojected electron density by a factor of $\rho_2/\rho_1 \approx 1.5$. This jump corresponds to an increase in the projected temperature by a factor of 1.4. Similarly, for the eastern cold front, we find a decrease in the electron density by a factor of $\rho_2/\rho_1 \approx 1.4$ and an increment in the temperature by a factor of 1.3. These two cold fronts are likely to be associated with the gas sloshing at the central region of A98N.
- With our deeper *Chandra* data, we find the average temperature of the A98Sa, $kT = 3.70_{-0.28}^{+0.33}$ keV and of the A98Sb, $kT = 2.47_{-0.20}^{+0.21}$ keV, consistent with that of Paterno-Mahler et al. (2014). We report that the eastern sub-cluster is cooler than the western sub-cluster with about a $5\text{-}\sigma$ significance.
- Figure 5.5 shows the excess X-ray emission near the central region of A98Sb appears to be a spiral pattern winding counter-clockwise if traced inward from a larger radius. The spiral structure is more likely to be associated with the gas sloshing at the central region of A98Sb, which a recent merger may trigger. We have detected a cold front in the east direction of A98Sb associated with the gas sloshing spiral. We measure a drop in the deprojected electron density by a factor of $\rho_2/\rho_1 \approx 1.3$ and a rise in the projected gas temperature by a factor of 1.4 across the front.
- The unsharp-masked image shown in Figure 5.4 exhibits a tail of X-ray emission in the south/southwest direction of the A98Sb core. Our measurement shows that the tail is considerably cooler ($1.8_{-0.2}^{+0.3}$ keV) than the surrounding gas ($3.1_{-0.4}^{+0.6}$ keV) at a $4.2\text{-}\sigma$ level and the A98Sb core ($2.47_{-0.20}^{+0.21}$ keV) at a $2.9\text{-}\sigma$ level. This implies that the tail is likely to be ram pressure stripped material from a cool-core remnant.
- We have reported detecting a surface brightness edge at 375 kpc southwest from the A98Sa core visible in Figure 5.10. The deprojected electron density drops by a factor of $\rho_2/\rho_1 \approx 1.7$ and the projected temperature drops by a factor of ≈ 1.5 , suggesting the edge is a shock front with a Mach number of $\mathcal{M} \approx 1.5$.

Chapter 6 Improved Fe II emission line models for AGN using new atomic datasets

6.1 Introduction

Emission lines of Fe II are a major contributor to the AGN spectra, with wavelengths spanning the infrared (IR) to ultraviolet (UV) regions. These emission lines provide an important laboratory for developing Fe II as a physical and geometrical diagnostic for the broad-line regions (BLRs) in AGN. Understanding the physics behind the Fe II emission is important for multiple reasons. It is the primary indicator of Eigenvector 1 (EV1), a key property to construct the quasar main sequence (e.g., Boroson and Green, 1992; Sulentic et al., 2000; Marziani et al., 2001). EV1, which relates to the black hole mass and quasar orientation (e.g., Shen and Ho, 2014; Panda et al., 2018, 2019), shows a strong anti-correlation with optical Fe II equivalent width in the Seyfert galaxies and quasars. Recent work shows correlations between the line widths of optical Fe II and UV Fe II in quasar spectra, which indicates that the emitting regions are close together (Kovačević-Dojčinović and Popović, 2015). It may be that both are emitted from the outer region of BLR or intermediate-line region (ILR).

Strong Fe II emission is also useful to investigate the energy budget of the emitting gas. The iron abundance as a function of cosmic time allows us to verify several cosmological parameters (Hamann and Ferland, 1999). In most galaxy evolution models, iron is mainly deposited in the interstellar medium (ISM) through Type Ia supernovae (SNIa), which occur about 0.3 to 1 billion years after the initial burst of star formation, because for Type Ia supernovae to occur the galaxy has to be old enough to host white dwarfs. This triggers a sudden jump in the iron abundance, as shown in Hamann and Ferland (1999) and Matteucci and Recchi (2001). The Gunn-Peterson effect in quasars suggests that the most recent onset of star formation occurred around $z \sim 6$ (e.g., Djorgovski et al., 2001; Fan et al., 2006; Bolton and Haehnelt, 2007; Kim et al., 2009; Sarkar and Samui, 2019). A properly calibrated iron chronometer would allow us to measure the iron abundance at high redshift, offering the possibility of measuring the redshift when Type Ia supernovae first happened (Baldwin et al., 2004).

The timescale for iron enrichment in the ISM is much longer than that of α -elements, such as magnesium. Magnesium is deposited in the ISM via core-collapsed (Type II) supernovae, which have much shorter timescales than Type I. The flux ratio of UV Fe II multiplet to the Mg II $\lambda 2800$ doublet (hereafter $I(\text{Fe II})/I(\text{Mg II})$) of quasars, therefore lets us probe the material deposited through Type Ia supernovae versus that processed through α -process in stars and then ejected via Type II supernovae (e.g., Kurk et al., 2007; De Rosa et al., 2011; Wu et al., 2015; Mazzucchelli et al., 2017; Shin et al., 2019). Thus, the $I(\text{Fe II})/I(\text{Mg II})$ ratio provides a powerful approach to investigate the chemical evolution of AGNs.

The theoretical and observational aspects of Fe II emission have been long-standing and important problems addressed by Osterbrock (1977); Phillips (1978); Netzer and

Wills (1983); Wills et al. (1985); Verner et al. (1999); Baldwin et al. (2004) due to its great strength in many Seyfert galaxies and quasars. Previous work with collisional excitation of Fe II in the framework of photoionization models failed to reproduce the observed strength of Fe II emission in the UV. The observed Fe II spectra of narrow-line Seyfert galaxies (e.g., Vestergaard and Wilkes, 2001) contain a so called “UV bump” between the C III λ 1909 and Mg II λ 2800 emission lines (Baldwin et al., 2004), which is produced by blending of a large number of Fe II emission lines due to transitions between high-lying states with energies $E \geq 13.25$ eV (e.g., Leighly et al., 2007; Bruhweiler and Verner, 2008). However, the collisional excitation models (Kwan and Krolik, 1981) only predict an electron temperature of $T \leq 10^4$ K at the illuminating faces of the Fe II emitting cloud which is too low to excite electrons to the high-lying energy levels ($E \geq 8$ eV).

Wills et al. (1985) first pointed out the importance of continuum fluorescence to excite the electrons to the higher energy states ($E \geq 11.6$ eV). Several spectral energy distributions (SEDs) of AGN with increasing Eddington ratio (L/L_{Edd}) have been proposed to reproduce the observed shape of the Fe II UV bump, where L_{Edd} is the Eddington luminosity of the corresponding AGN (e.g., Mathews and Ferland, 1987; Korista et al., 1997; Jin et al., 2012). However, the Fe II atomic dataset has long remained a concern for reproducing Fe II spectra. A larger Fe II model involves a large number of transitions between the high-lying energy states, producing stronger Fe II emission in the UV.

We have incorporated three recent Fe II datasets, namely those of Bautista et al. (2015), Tayal and Zatsarinsky (2018), and Smyth et al. (2019) into the spectral synthesis code CLOUDY (Ferland et al., 2017) in addition to the Mathews and Ferland (1987), Korista et al. (1997), and Jin et al. (2012) AGN SEDs. Our model predictions are compared with the observed UV (Vestergaard and Wilkes, 2001) and optical (Véron-Cetty et al., 2004) BLR templates of 1 ZW I Seyfert galaxy to constrain the physical conditions and geometrical properties of the Fe II emitting gas. We find that the Smyth et al. (2019) Fe II dataset, the Jin et al. (2012) SED, and a dense turbulent cloud, largely reproduce the Fe II emission with solar abundances.

Our goal is to reproduce the shape and strength of the Fe II UV bump and optical emission. We study the emission from a single BLR cloud in some detail. The emission lines are known to be formed in a distribution of clouds with different locations and densities. This was first measured with reverberation (Peterson, 1993) and is a consequence of atomic physics selection effects (Baldwin et al., 1995). This must be taken into account when emission from different species with a broad range of ionization potential or critical density is considered. However, emission from one particular species is generally localized to favored values of the density and ionizing photon flux, as illustrated by Korista et al. (1997) and Baldwin et al. (2004), so, when considering a single species like Fe II, a typical set of cloud parameters can be considered, as in Ferland et al. (2009). We compare Fe II and Mg II emissions later in the paper because these species are used as abundance indicators in high-redshift quasars. Figure 3f of Korista et al. (1997) shows that Fe II and Mg II lines form in very similar clouds, justifying this approach.

There are also complex interplays between different sets of model parameters

such as turbulence, the SED shape, or composition. Our primary goal is to develop a testing framework to compare theory and observations, and to document the spectral properties of these new atomic data sets. The new Fe II atomic data files, and the infrastructure needed to use them, will be included in the C17.03 update to CLOUDY and we hope that the analysis methods we demonstrate here can serve as a guide for future studies and detailed comparisons with observations.

We assume solar abundances. Studies of high-ionization lines find that the metallicity is above solar and correlates with luminosity (Hamann and Ferland, 1999). Recently Schindler et al. (2020) measured the Fe II/Mg II ratio of a large number of quasars across cosmic time. They did not find any evolution and concluded that the ratios were consistent with solar abundances. In later sections of the paper we show that this line ratio has only a weak metallicity dependence. For simplicity, we assume solar abundances in the calculations presented here.

Finally, we adopt a cosmology of $H_0 = 70 \text{ km s}^{-1} \text{ Mpc}^{-1}$, $\Omega_\Lambda = 0.7$, and $\Omega_m = 0.3$.

6.2 Basic ingredients

A complete model of the physical processes that affect the Fe II spectrum would help us to constrain the gas properties and dynamics in the BLR. However, difficulties arise because a variety of processes determine the observed Fe II emission, such as collisional excitation, pumping by the continuum photons, and fluorescence via line overlap. The spectral energy distribution (SED) of the background AGN, the cloud’s density, turbulence, and optical depth of the gas also play important roles. A realistic model should take into account all those effects while modeling the temperature and ionization structure of the gas.

We use the development version of CLOUDY, last described by Ferland et al. (2017). We adopt CLOUDY’s default solar composition, as listed in Table 6.1.

6.2.1 Fe II atomic datasets

The Fe II ion has a complex structure with 25 electrons, and is a “grand challenge” problem in atomic physics. An accurate set of radiative and collisional atomic data is therefore needed to treat the selective excitation, continuum pumping, and fluorescence, which are known to be important for the Fe II emission (e.g., Baldwin et al., 2004; Bruhweiler and Verner, 2008; Jin et al., 2012; Wang et al., 2016; Netzer, 2020). Uncertainties in the atomic data have been a longstanding limitation in interpreting line intensities. Below we discuss four different Fe II atomic datasets that are now available in the CLOUDY, while their energy levels are compared in Figure 6.1.

First, we consider the widely used Verner et al. (1999) Fe II dataset with 371 atomic levels producing 13,157 emission lines with a highest energy level of ~ 11.6 eV. Verner et al. (1999) data has collision strengths mainly calculated from the “g-bar” approximation. The original paper presented a total of $\sim 68,000$ transitions in their model atom. Most of these transitions are strongly forbidden and are assigned

Table 6.1: Solar abundances used in CLOUDY

Elements	Abundances	Elements	Abundances
H	1.0	S	1.84e-5
He	0.10	Cl	1.91e-7
Li	2.04e-9	Ar	2.51e-6
Be	2.63e-11	K	1.32e-7
B	6.17e-10	Ca	2.29e-6
C	2.45e-4	Sc	1.48e-9
N	8.51e-5	Ti	1.05e-7
O	4.90e-4	V	1.00e-8
F	3.02e-8	Cr	4.68e-7
Ne	1.00e-4	Mn	2.88e-7
Na	2.14e-6	Fe	2.82e-5
Mg	3.47e-5	Co	8.32e-8
Al	2.95e-6	Ni	1.78e-6
Si	3.47e-5	Cu	1.62e-8
P	3.20e-7	Zn	3.98e-8

Note: Solar abundances of different elements relative to H, incorporated in CLOUDY–C17. Abundances of most elements are taken from Grevesse and Sauval (1998), except for C, O which are taken from Allende Prieto et al. (2002), and N, Ne, Si, Mg, Fe are taken from Holweger (2001).

very small transition rates*. Transition probabilities between their energy levels have uncertainties $\lesssim 20\%$ for strong permitted lines and $\gtrsim 50\%$ for weak permitted and inter-combination lines. Also, forbidden lines have uncertainties $\lesssim 50\%$. We exclude all the totally forbidden lines from the 68,000 transitions because of their small transition rates. Figure 6.1 shows the energy levels predicted by the Verner et al. (1999) Fe II model.

Bautista et al. (2015) reports a Fe II model with 159 levels extending up to 11.56 eV, producing 628 emission lines. Uncertainties in the transition probabilities lie between 10% and 30%. Tests show that the Bautista et al. (2015) Fe II dataset has no lines between 2000Å and 3000Å. As our paper mainly focuses on the UV band (2000Å– 3000Å) in Fe II spectra, we do not use this data-set for our BLR modelling.

Tayal and Zatsarinny (2018) calculate 340 energy levels with a highest energy of ~ 16.6 eV, including all levels from the $3d^64s$, $3d^54s^2$, $3d^7$, $3d^64p$ configurations and a few levels from the $3d^54s4p$ configuration. Transitions between these energy levels produce 57,635 emission lines with uncertainties in transition probabilities of $\lesssim 30\%$ (in the 2200Å–7800Å). This dataset contains autoionizing levels with $E > 13.6$ eV, which are absent in Verner et al. (1999) and Bautista et al. (2015). However, the density of states in high-lying energy levels are low, as shown in Figure 6.1.

Another larger Fe II data-set is also recently available in CLOUDY. Smyth et al.

*Beginning in C17 (Ferland et al., 2017) we only predict transitions which emit photons, accounting for the much smaller number of lines.

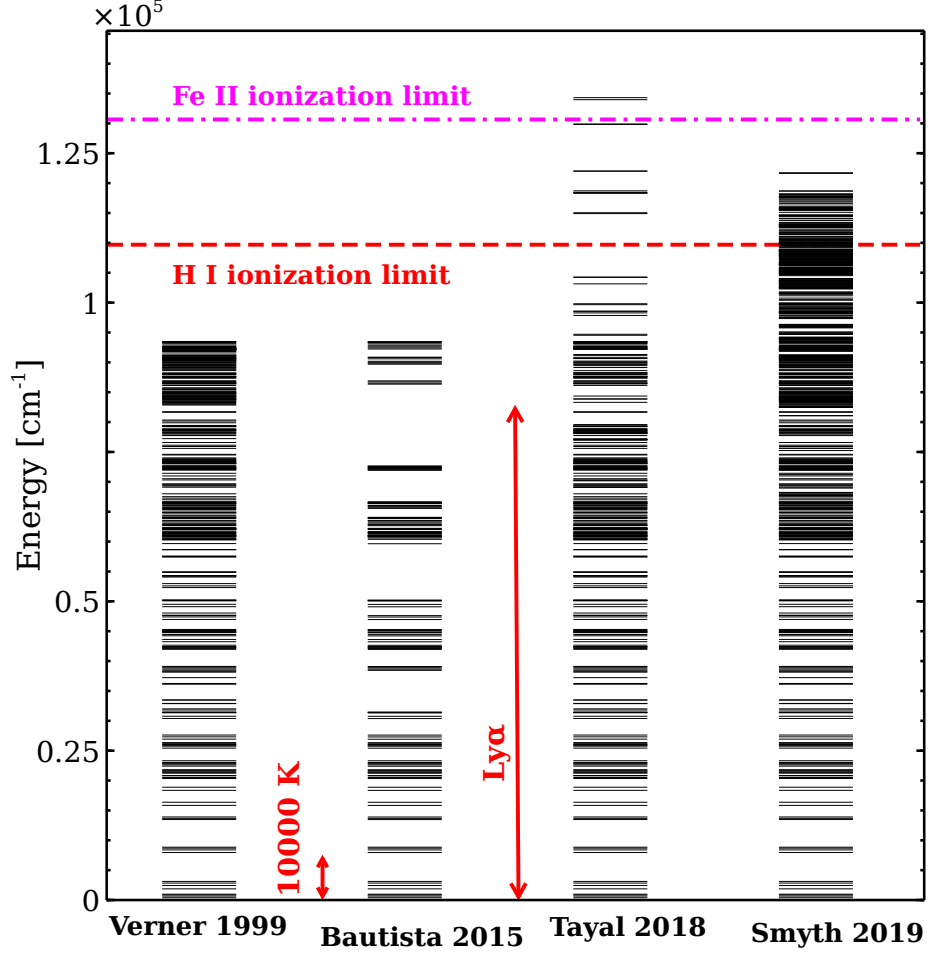


Figure 6.1: Diagram showing the energy levels of various models of the Fe II atom. From left to right : dataset derived by Verner et al. (1999), Bautista et al. (2015), Tayal and Zatsarinny (2018), and Smyth et al. (2019). The horizontal dashed lines indicate the H I and Fe II ionization limits. The energy of the Ly α transition, an important source of photoexcitation of Fe II, is also indicated, along with the thermal energy corresponding to 10^4 K.

(2019) compute energy levels taking into account 216 *LS* terms in Fe II atom arising from the $3d^64s$, $3d^7$, $3d^64p$, $3d^54s^2$, and $3d^54s4p$ configurations. The Smyth et al. (2019) model has considerably more configurations (see pg 657) in the structure but only includes 716 levels in the close coupling (scattering model), with the highest energy level reaching 26.4 eV. These levels produce 255,974 emission lines. The Smyth et al. (2019) dataset also contains autoionizing levels, but the density of states in the high-lying energy states is large compared to Tayal and Zatsarinny (2018).

We model the Fe II emitting cloud using Verner et al. (1999), Tayal and Zatsarinny (2018), and Smyth et al. (2019) and compare their predictions. Results are discussed in Section 6.3.

6.2.2 AGN SEDs

The BLR spectra in AGN mostly originate from the gas clouds photoionized by continuum radiation coming from an accretion disk around the central black hole. An accurate SED from the UV through to the soft X-ray band is therefore important to understand the Fe II emission (e.g., Wills et al., 1985; Verner et al., 1999; Korista et al., 1997; Wills et al., 1985; Baldwin et al., 2004; Bruhweiler and Verner, 2008; Jin et al., 2012; Wang et al., 2016; Netzer, 2020). The soft X-ray part of the SED can penetrate into low ionization regions to heat the gas and produce the Fe II emission by thermal collisions. We consider the three SEDs presented by Mathews and Ferland (1987), Korista et al. (1997), and Jin et al. (2012), as shown in Figure 6.2. These have been normalised to have the same flux of ionizing photons, $\phi(\text{H}^0) = 10^{20} \text{ cm}^{-2} \text{ s}^{-1}$.

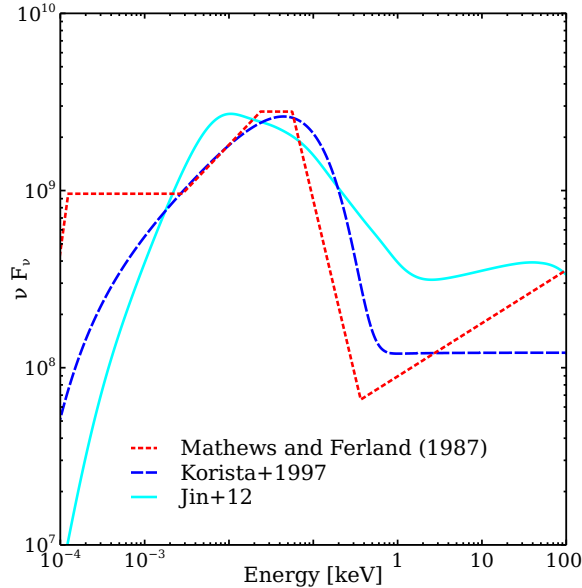


Figure 6.2: Comparing different SEDs used in CLOUDY. Red dashed line: SED derived by Mathews and Ferland (1987). Blue dashed line: SED derived by Korista et al. (1997). Cyan solid line: Jin et al. (2012) SED.

Mathews and Ferland (1987) derived a simple and phenomenological SED extending from the infrared (0.00124 eV) through the hard X-ray (10^5 eV), as shown in Figure 6.2. The shape of the continuum is approximated as a series of broken power-laws, i.e -

$$f_\nu = a\nu^{-\alpha},$$

where α is the spectral index. This can be determined by fitting the observed continuum with the power-law model in various energy bands.

We consider another standard SED derived in Korista et al. (1997), as shown in Figure 6.2. This is a baseline ionizing continuum model widely used to predict a wide range of emission lines in quasars (e.g., Ruff et al., 2012; Marziani and Sulentic, 2014;

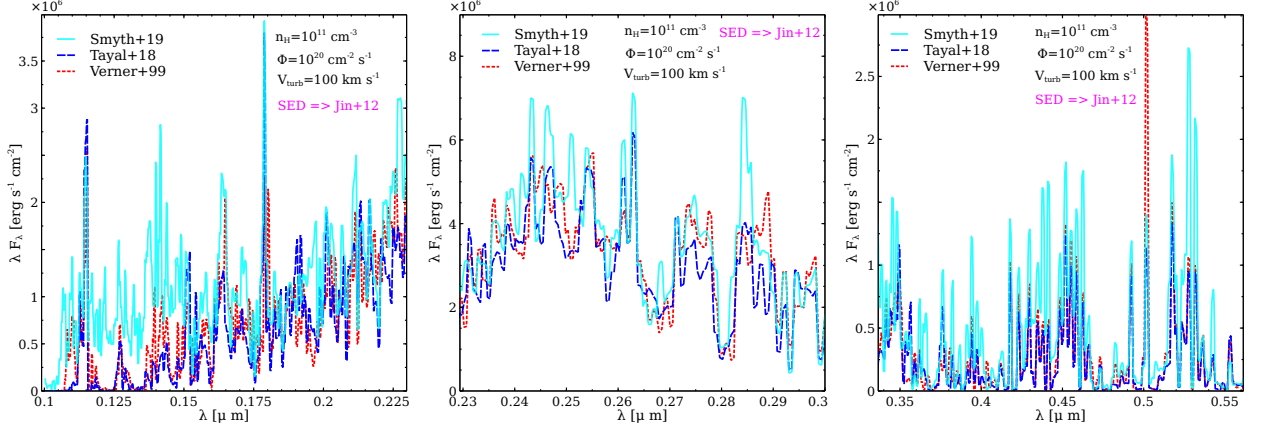


Figure 6.3: Comparing CLOUDY predicted Fe II spectra in 0.1–0.58 μm wavelength band using three different Fe II datasets and a fixed SED (Jin et al., 2012). Red dotted line: Fe II spectra using Verner et al. (1999) dataset. Blue dashed line: Tayal and Zatsarinny (2018) dataset. Cyan solid line: Smyth et al. (2019) dataset. Ranges of y-axis are different in all sub-figures.

Marinucci et al., 2018; Temple et al., 2020). The derived shape of the continuum is a combination of a UV bump and an X-ray power law, i.e.,

$$f_\nu = \nu^{-0.5} \exp(-h\nu/kT_{\text{UV}}) \exp(-kT_{\text{IR}}/h\nu) + a\nu^{-1},$$

where T_{UV} and T_{IR} are the cut-off temperatures of the UV bump and X-ray power law, respectively. The value of ‘a’ can be determined from the ratio of the UV to X-ray continua, defined as-

$$\frac{f_\nu(2 \text{ keV})}{f_\nu(2500)} = 403.3^{\alpha_{\text{ox}}},$$

where α_{ox} distinguishes the continua between different type of AGNs. As an example, for Type I Seyfert galaxies, $\alpha_{\text{ox}} = -1.2$. The shape of the continuum in the Figure 6.2 corresponds to a UV bump peaking at $\sim 44 \text{ eV}$ and an exponential decay part with a slope of -2.3 .

We also consider the new generation of SEDs which use the Eddington ratio (L/L_{Edd}) as parameter and are presented in Jin et al. (2012) and summarized by Ferland et al. (2020). These SEDs are a combination of theory and more recent observations. The SED with a $\log L/L_{\text{Edd}} = -0.55$ is shown in Figure 6.2. The derived SED has three components, namely (1) AGN disk emission, (2) Comptonization, and (3) a high energy power law tail (Done et al., 2012). Figure 6.2 represents the shape of the broadband SED. It increases as blackbody emission (emission from the outer disk) from lower energy, peaks in the UV, then falls off due to inverse Compton scattering in the inner disk and finally attains a power law tail which is due to the inverse Compton scattering in the corona. As shown, the SEDs are normalized to have the same total number of ionizing photons. Note that they disagree by ~ 1 dex in the soft X-ray region.

We next use all three SEDs in CLOUDY and compare their predicted Fe II spectra.

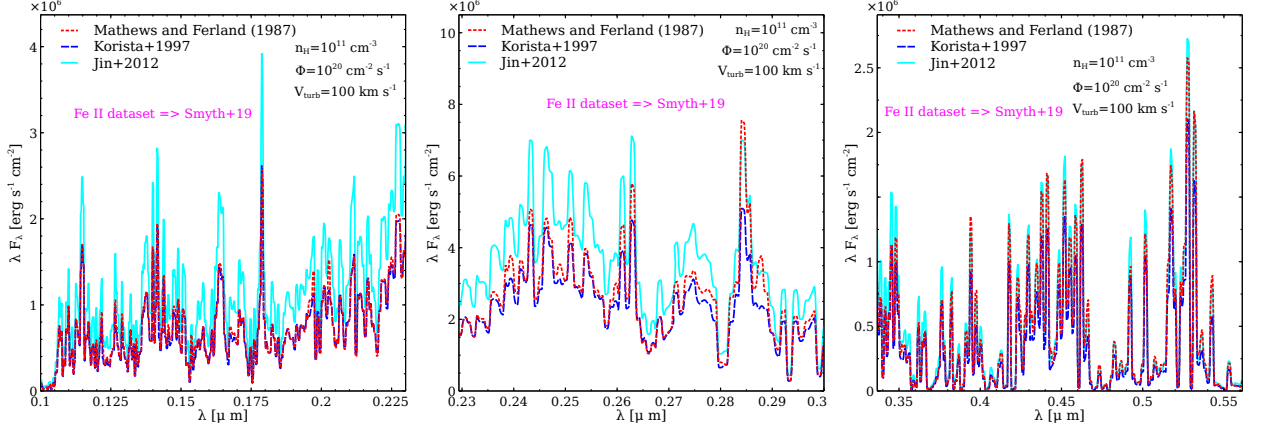


Figure 6.4: Comparing CLOUDY predicted Fe II spectra in 0.1–0.58 μm wavelength bands using three different AGN SEDs and a fixed Fe II dataset (Smyth et al., 2019). Red dotted line: Fe II spectra using Mathews and Ferland (1987) SED. Blue dashed line: Korista et al. (1997) SED. Cyan solid line: Jin et al. (2012) SED. Ranges of y-axis are different in all sub-figures.

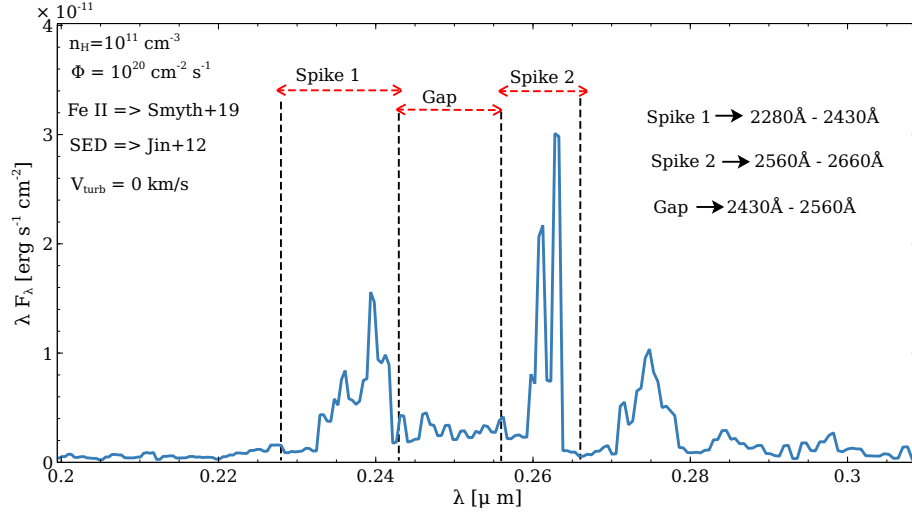


Figure 6.5: Blue spectrum shows a typical Fe II spectra in UV using Smyth et al. (2019) dataset, Jin et al. (2012) SED. The Spikes and Gap are marked with vertical dashed lines.

6.3 Applications

6.3.1 Modelling of the BLR cloud

We model the BLR gas by assuming solar abundances, as listed in table 6.1, and a cloud column density (N_{H}) of 10^{24} cm^{-2} . First, we consider the Fe II emission from a single cloud modelled using the Verner et al. (1999), Tayal and Zatsarinny (2018), and Smyth et al. (2019) datasets in addition to an intermediate L/ L_{Edd} AGN SED,

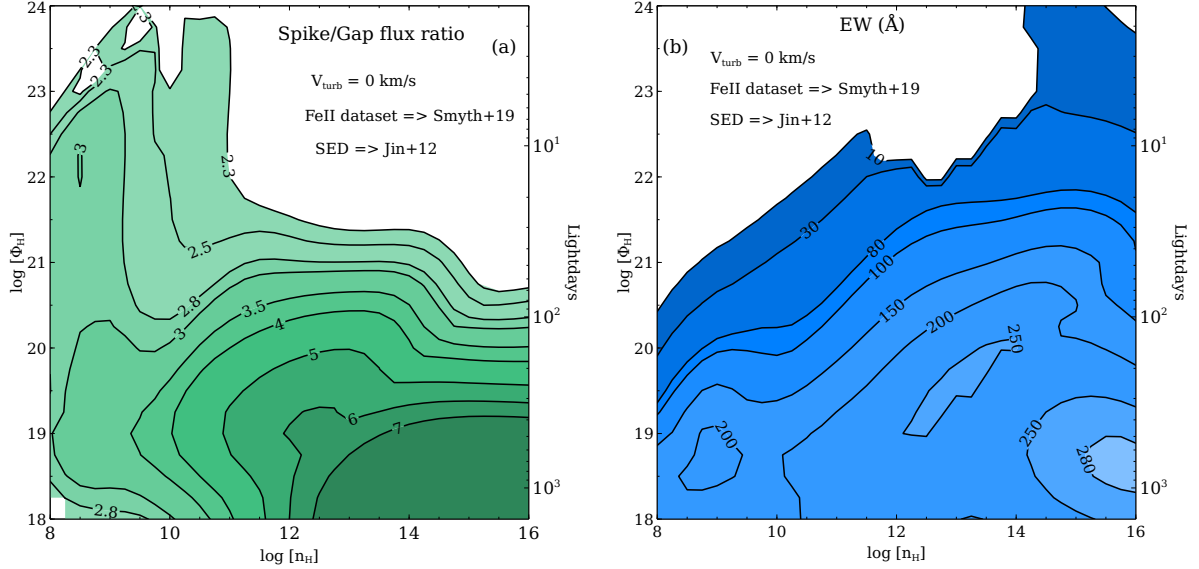


Figure 6.6: Contour plot of the Spike/gap ratio and equivalent width (EW) derived from photoionization model using the Smyth et al. (2019) Fe II dataset and Jin et al. (2012) AGN SED. Left: Spike/gap ratio of the Fe II UV bump in the $n_{\text{H}} - \Phi$ plane. Right: EW of Fe II UV bump in the $n_{\text{H}} - \Phi$ plane. An axis indicating the distance of Fe II emitting cloud from the central black hole is also added.

as described in Jin et al. (2012). Figure 6.3 compares the resulting Fe II emission spectra for the different atomic datasets in the UV and optical. In both spectral ranges, the Smyth et al. (2019) Fe II data-set produces larger line intensities compared to the other two. The Smyth et al. (2019) data-set has more very highly excited states that connect by permitted transitions to low-excitation highly-populated levels. Continuum fluorescent excitation is much stronger as a result, which brings the short-wavelength lines into better agreement with the template. The Smyth et al. (2019) dataset also better reproduces the observed Fe II pseudo-continuum, which results from the blending of a large number of high-lying lines in the UV and optical (Garcia-Rissmann et al., 2012). We therefore select the Smyth et al. (2019) dataset to generate Fe II emission lines throughout the remainder of this paper.

To find a suitable AGN SED for our BLR model, we predict Fe II spectra using the Mathews and Ferland (1987), Korista et al. (1997), and Jin et al. (2012) SEDs in addition to the Smyth et al. (2019) Fe II dataset. Figure 6.4 compares the Fe II emission spectra for all three AGN SEDs we consider. The adopted density, flux, and turbulence parameters indicated in the figures as are the best-fitting parameters derived below.

The Mathews and Ferland (1987) and Korista et al. (1997) SEDs were simple empirical fits with little physical basis. In contrast, Jin et al. (2012) SED does have a theoretical foundation, as explained in the original papers, and that family of SEDs produce significantly more soft X-ray emission between ~ 100 eV to 1 keV (see Figure 6.2) than the empirical SEDs. Soft X-rays are important because these higher

energy photons can penetrate further into the cloud, deposit more energy in neutral gas, and produce stronger Fe II lines by collisional excitation. Softer XUV and EUV[†] photons are extinguished at shallower depth into the cloud, where Fe is more highly ionized, while hard X-rays and gamma-rays encounter less opacity so are transmitted without being reprocessed into emission lines.

The two older SEDs are shown in Figure 6.4 for historical reference. The papers describing them are highly cited (Mathews and Ferland 1987 and Korista et al. 1997) and they are built into CLOUDY. Several studies have used these SEDs, and the Verner et al. (1999) atomic data set, to investigate emission properties of AGN. Although the older SEDs and the Verner et al. (1999) data have historical interest, we prefer the modern SED (Jin et al., 2012) with its foundation of observations and theory and the new generation of atomic data (Smyth et al., 2019) with more complete collision strengths.

For these reasons, we, therefore, adopt the Jin et al. (2012) SED for our BLR model throughout this paper. Additionally, the $\log L/L_{\text{Edd}}$ value for Jin et al. (2012) SED is consistent with that of IZW 1 ($\gtrsim -0.60$, Cracco et al., 2016; Giustini and Proga, 2019). This is the intermediate L/L_{Edd} SED and in Section 6.3.4 we explore the effects of varying L/L_{Edd} . We note that CLOUDY makes it easy to adopt user-defined SEDs in new calculations. It is hope that the work we present here will lead to further explorations of the effects of the SED upon the line spectrum.

With the above selections of Fe II dataset and SED, the remaining parameters are the cloud hydrogen density (n_{H}) and the flux of incoming photons striking the cloud (Φ). We estimate these by considering a grid of photoionization models by varying these two parameters over a broad range.

The computed Fe II spectra without microturbulence always show two prominent spikes at $\sim 2400\text{\AA}$ and 2600\AA , as extensively discussed by Baldwin et al. (2004) and shown in Figure 6.5. These features are absent in the observed Fe II template. Therefore, to compare the predicted Fe II spectra with the available observations of IZW 1 in the UV (Vestergaard and Wilkes, 2001), we adopt the definitions of the Spike/gap ratio and Fe II equivalent width of the UV bump given in Baldwin et al. (2004). The ‘‘Spike’’ is defined as the total Fe II flux over the wavelength ranges 2280\AA - 2430\AA and 2560\AA - 2660\AA (these are the two ‘‘Spikes’’ as seen in Figure 6.5), and gap is defined as the total Fe II fluxes over 2430\AA - 2560\AA wavelength range. The Spike/gap ratio is defined as the ratio of these two and a typical observed value is ≈ 1.4 .

We consider the equivalent width of the Fe II UV bump as the excess flux in 2200\AA - 2660\AA band over the continuum flux at 1215\AA which is then divided by the continuum flux at 1215\AA . CLOUDY calculates the equivalent width by assuming a 100% covering factor[‡]. Baldwin et al. (2004) showed that a covering factor of $\approx 20\%$ is a good indicator of a successful model. A typical CLOUDY predicted equivalent

[†]We refer to the energy band 6 – 13.6 eV (912\AA – 2000\AA) as FUV, 13.6 – 56.4 eV (228\AA – 912\AA) as EUV, and 56.4 – few hundred eV ($< 228\text{\AA}$) as XUV.

[‡]Covering factor or CF is defined as the fraction of 4π sr covered by the clouds, as seen from the central black hole. Normally, the CF is expressed as $\Omega/4\pi$, where Ω is the solid angle.

width of $> 400\text{\AA}$ is consistent with the observed value with a $\sim 20\%$ of covering factor.

Lines from the BLR are velocity broadened (by $10^3 - 10^4$ km/s), although IZW 1 has a line width of ~ 1200 km/s. Given this, we smooth the CLOUDY predicted spectra by a boxcar average with a width of 1200 km/s in order to compare with the observed IZW 1 template.

We vary the hydrogen density (n_{H}) from 10^8 cm^{-3} to 10^{16} cm^{-3} and the photon flux (Φ) between $10^{18} \text{ cm}^{-2} \text{ s}^{-1}$ and $10^{24} \text{ cm}^{-2} \text{ s}^{-1}$, as shown in Figure 6.6, resulting in a total of 825 individual BLR models with a $10^{0.25}$ step size. These parameters fully cover the possible range of clouds that produce the well-observed strong BLR lines like C IV $\lambda 1549$. In this first step we neglect any microturbulence inside the cloud so the lines are thermally broadened. For each model, we analyze the Fe II emission spectrum and calculate the Spike/gap ratio and EW of the Fe II UV bump. Figure 6.6 shows contour plots of the Spike/gap ratio and the EW of the Fe II UV bump in the $n_{\text{H}} - \Phi$ plane. No $[n_{\text{H}}, \Phi]$ pair reproduces the observed Fe II spectra. The Fe II emission is too weak, and the Spike/gap ratio too large, a problem Baldwin et al. (2004) also encountered.

We conclude that the standard baseline model cannot satisfactorily reproduce the observed UV Fe II emission even with a bigger Fe II atomic dataset and the new generation AGN SED. In addition to the Spike/gap ratio and equivalent width, each baseline model also predicts two strong emission lines, one at 2400\AA and another double-peaked at 2610\AA and 2630\AA , which are not present in the observed spectrum, as shown in Figure 6.9.

6.3.2 The effects of microturbulence

Next we consider clouds with non-zero microturbulent velocity (V_{turb}) throughout the BLR gas, as previously proposed by Netzer and Wills (1983), and later Bottorff et al. (2000); Baldwin et al. (2004). Netzer and Wills (1983) showed that the strength of the Fe II UV emission is directly proportional to the microturbulence. The Bottorff et al. (2000), Baldwin et al. (2004), and Bruhweiler and Verner (2008) obtained a better fit for the quasar emission spectra, considering a turbulent emitting cloud. Physically, microturbulence decreases the optical depth by increasing the Doppler broadening ($\tau \sim V_{\text{doppler}}^{-1}$), which helps more line photons to escape. Microturbulence also increases the importance of continuum pumping (e.g., Osterbrock, 1977; Phillips, 1978; Ferland, 1992). We present a second grid model by varying V_{turb} between 0.1 km/s and 10^3 km/s. The hydrogen density (n_{H}) is fixed to 10^{11} cm^{-3} and the photon flux (Φ) to $10^{20} \text{ cm}^{-2} \text{ s}^{-1}$, similar to the previous works (e.g., Verner et al., 2003; Véron-Cetty et al., 2004; Baldwin et al., 2004; Bruhweiler and Verner, 2008; Temple et al., 2020). Figure 6.7 shows the Spike/gap ratio and the strength of Fe II emission in the UV as a function of V_{turb} . The Spike/gap ratio decreases with increasing V_{turb} and attains a value of ~ 1.4 at $V_{\text{turb}} > 60$ km/s. In addition, to reproduce the observed strength of Fe II emission a $V_{\text{turb}} > 90$ km/s is needed. Hence we set $V_{\text{turb}} = 100$ km/s to reproduce the Fe II spectra for the remainder of the paper.

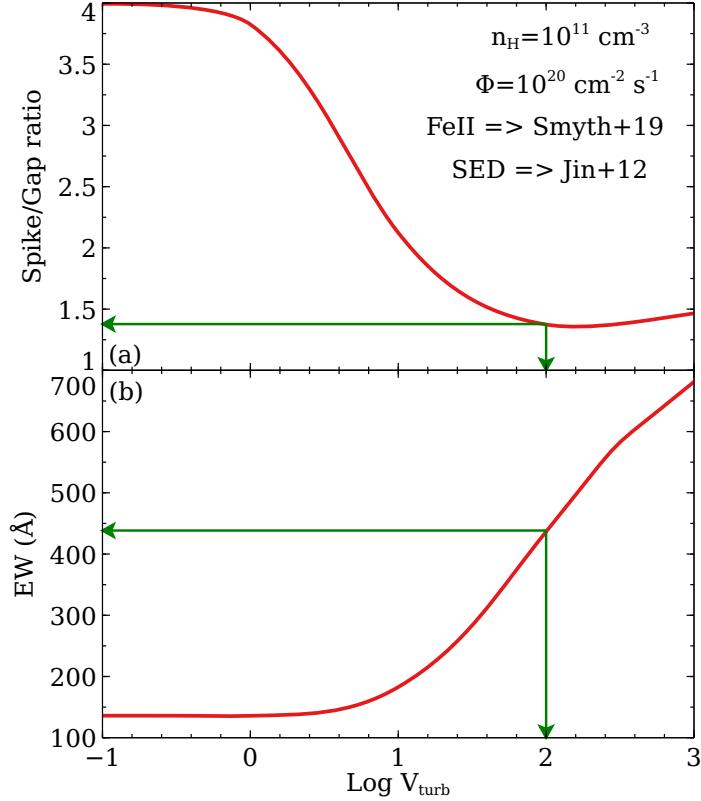


Figure 6.7: Spike/gap ratio and EW of the Fe II emission in the UV as a function V_{turb} . Green line: the Spike/gap ratio and EW of Fe II UV bump corresponding to $V_{\text{turb}} = 100$ km/s. These values are consistent with observation. Any turbulence greater than 100 km/s will reproduce the observed Fe II emission.

Next we recalculate the first grid of photoionization models assuming $V_{\text{turb}} = 100$ km/s to find the n_{H} and Φ of the emitting cloud. Similar to the previous steps, we calculate the Spike/gap ratio and the EW of the UV bump for each individual model. Figure 6.8 presents contour plots of the Spike/gap ratio and EW of the Fe II UV bump in the $n_{\text{H}}-\Phi$ plane. Clearly, a cloud with $n_{\text{H}} \approx 10^{11} \text{ cm}^{-3}$ and $\Phi \approx 10^{20} \text{ cm}^{-2} \text{ s}^{-1}$ reproduces the observed Spike/gap ratio and the strength of Fe II emission.

Next we compare the Fe II emission in the UV and optical bands with this density and flux. In Figure 6.9 we compare the predicted spectra with the observed Fe II templates in the UV (Vestergaard and Wilkes, 2001) and optical (Véron-Cetty et al., 2004). For further comparison, we include predictions for both thermal and turbulent clouds. The Smyth et al. (2019) dataset, the new-generation SED (Jin et al., 2012), and $V_{\text{turb}} = 100$ km/s reproduces AGN Fe II spectra in the UV and optical far better than found in previous work, with solar Fe/H. This is a remarkable accomplishment.

6.3.3 Fe II/Mg II ratio

The abundances of iron and magnesium are vital to probe the chemical evolution at high redshift. Iron in the solar neighborhood has mostly been produced by Type Ia

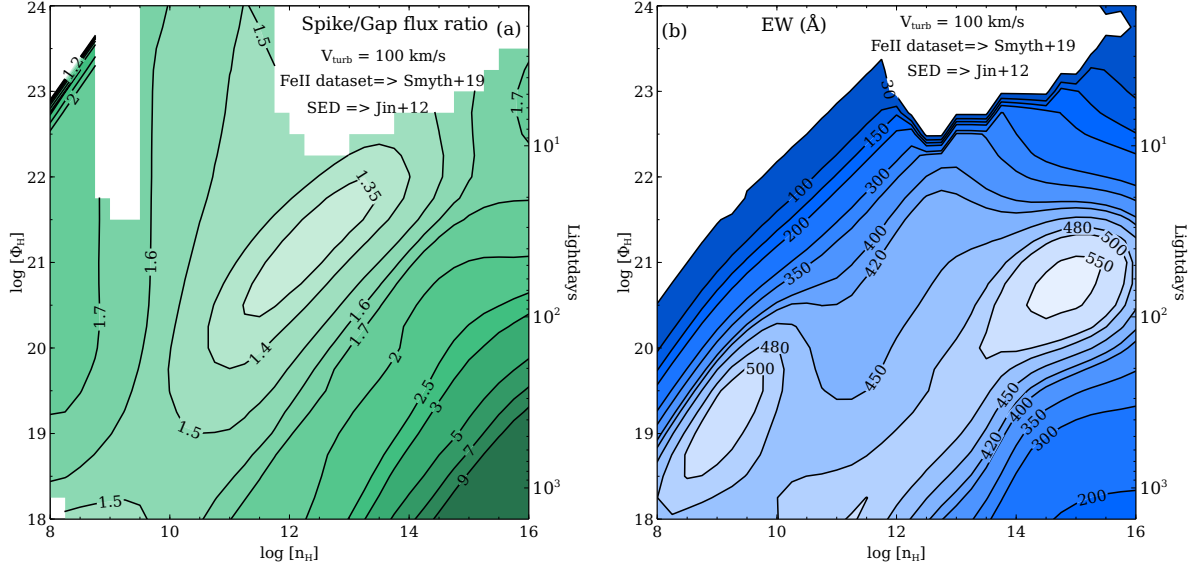


Figure 6.8: Similar to Figure 6.6 except $V_{\text{turb}} = 100 \text{ km/s}$. Large regions of parameter space reproduce the observed Spike/Gap ratio ~ 1.4 and $\text{EW} > 400 \text{ \AA}$ of the IZW 1 in the UV band.

SNe, which are the last stage of intermediate-mass stars in a close binary system. By comparison, magnesium has been deposited in the ISM by Type II SNe, a core-collapsed SN originating from the explosion of a massive star soon after the initial starburst. Type Ia SNe are delayed compared to Type II SNe. A time lag between the iron and magnesium enrichment of the solar neighborhood is therefore expected. This time delay varies from 0.3 Gyr for massive elliptical galaxies to 1-3 Gyr for Milky-Way type galaxies (Matteucci and Recchi, 2001). Previous observations have measured the $I(\text{Fe II})/I(\text{Mg II})$ as a function of look-back time to trace the Fe/Mg abundance ratio (e.g., De Rosa et al., 2011; Shin et al., 2019). More recently Schindler et al. (2020) report on an extensive data set extending over a broad range of cosmic time and find similar $I(\text{Fe II})/I(\text{Mg II})$ ratios.

We showed above that our best BLR model with solar abundances could successfully reproduce the observed template of IZW 1 in the UV and optical. To estimate the $I(\text{Fe II})/I(\text{Mg II})$, we consider the total flux of the Fe II UV bump between the $2000 \text{ \AA} - 3000 \text{ \AA}$ range and that of the Mg II doublet at 2798 \AA . We examined the $I(\text{Fe II})/I(\text{Mg II})$ for our best-fitting model with $n_{\text{H}} = 10^{11} \text{ cm}^{-3}$, $\Phi = 10^{20} \text{ cm}^{-2} \text{ s}^{-1}$, and $V_{\text{turb}} = 100 \text{ km/s}$. Our model predicts $\log(I(\text{Fe II})/I(\text{Mg II})) \approx 0.7$. Shin et al. (2019) obtained $\log(I(\text{Fe II})/I(\text{Mg II}))$ values of $0.31 - 0.79$ for a large sample of AGNs at $z \sim 3$. De Rosa et al. (2011) showed a maximum $\log(I(\text{Fe II})/I(\text{Mg II}))$ of 0.77 for AGNs with $z > 4$. Our $\log(I(\text{Fe II})/I(\text{Mg II}))$ predictions closely match those observations, as shown in Figure 6.11.

Next we vary the Fe abundance from 0.1 to 10 times the solar abundance in our best-fitting BLR model and estimate the $I(\text{Fe II})/I(\text{Mg II})$ ratio while keeping the abundances of the other elements constant. This is a test of the sensitivity of

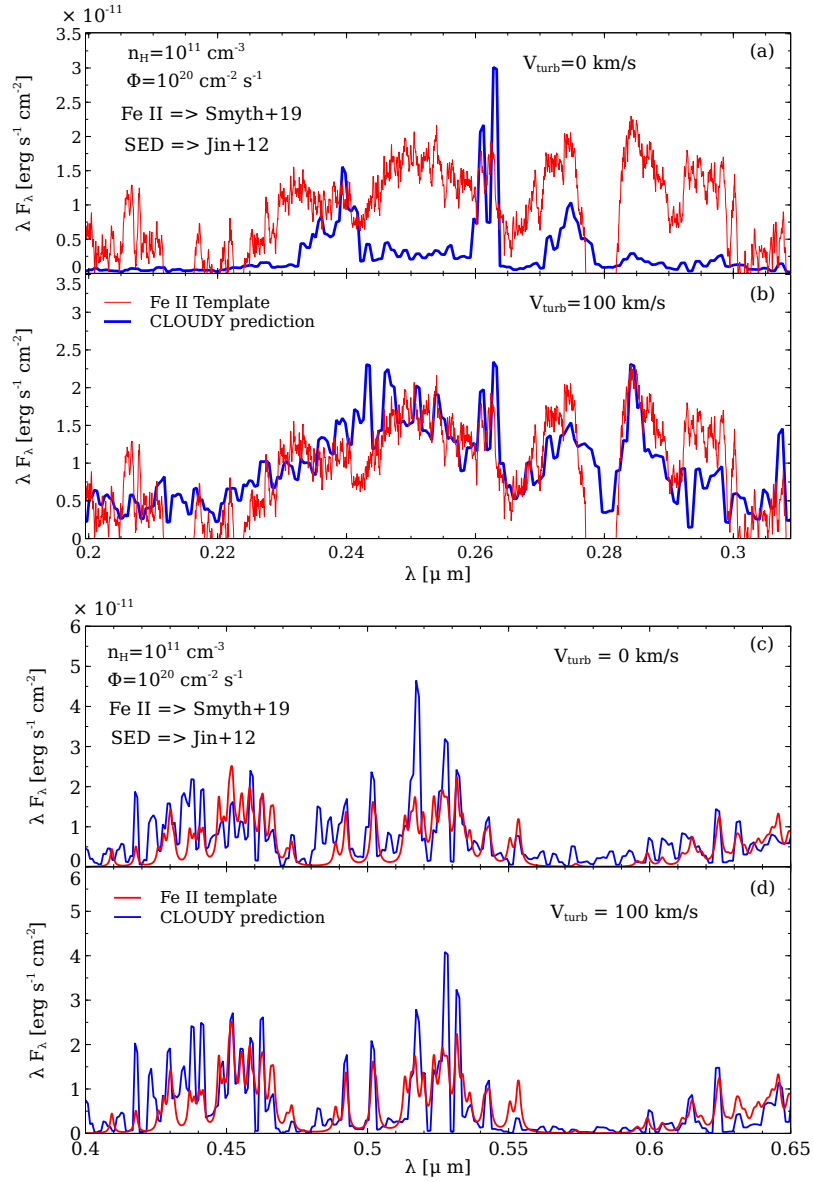


Figure 6.9: *Left:* panel (a) shows a comparison between the observed Fe II UV template (Vestergaard and Wilkes, 2001) and the CLOUDY predicted Fe II UV spectrum with $V_{\text{turb}} = 0$ km/s. Panel (b) shows the same comparison with $V_{\text{turb}} = 100$ km/s. *Right:* panel (c) compares the Fe II optical template (Véron-Cetty et al., 2004) to the CLOUDY predicted spectrum with $V_{\text{turb}} = 0$ km/s. Panel (d) presents the same comparison except $V_{\text{turb}} = 100$ km/s. The turbulent model largely reproduces the template.

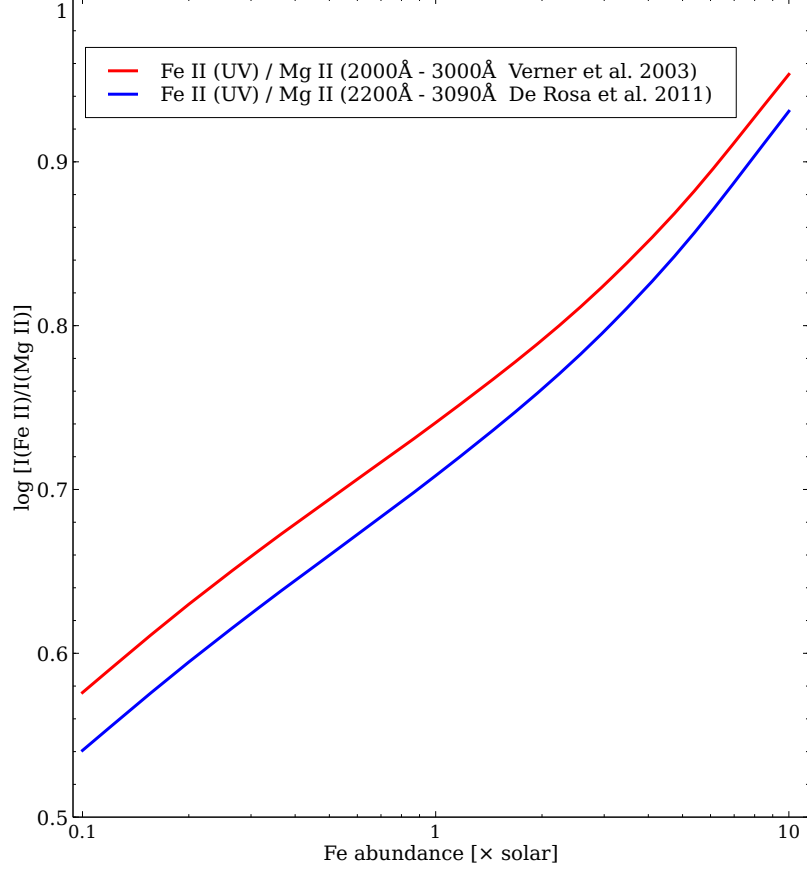


Figure 6.10: $I(\text{Fe II})/I(\text{Mg II})$ as a function of the Fe abundances. We show that the Fe II/Mg II ratio for two different UV bands – 2000Å - 3000Å and 2200Å - 3090Å band, as described in Verner et al. (2003) and De Rosa et al. (2011), respectively.

the line intensity ratio to the abundance ratio. Figure 6.10 shows the monotonic increasing nature of the $I(\text{Fe II})/I(\text{Mg II})$ ratio as a function of the Fe abundance. A similar trend of the $I(\text{Fe II})/I(\text{Mg II})$ ratio with the Fe abundance is also obtained by Verner et al. (2003). The $\log(I(\text{Fe II})/I(\text{Mg II}))$ intensity ratio increases by only ~ 0.4 dex when the Fe/Mg abundance ratio increases by 2 dex, or $I(\text{Fe II})/I(\text{Mg II}) \propto (\text{Fe}/\text{Mg})^{0.19}$. This shows that the Fe II and Mg II spectra are strongly saturated due to the large line optical depths so that the intensity ratio does not strongly depend on the abundance ratio. Chemical evolution models suggest that the Fe/Mg ratio jumps by ~ 1 dex when Type Ia supernovae start occurring in giant ellipticals (Hamann and Ferland, 1999). This would correspond to a change in the intensity ratio of $\log(I(\text{Fe II})/I(\text{Mg II})) \sim 0.19$. Clearly a large number of high quality quasar spectra will be needed to measure such a subtle change.

6.3.4 Eigenvector 1

Next we consider the Eigenvector 1 correlation. The new-generation SED models consider a wide range of L/L_{Edd} , as summarized by Ferland et al. (2020). We adopt

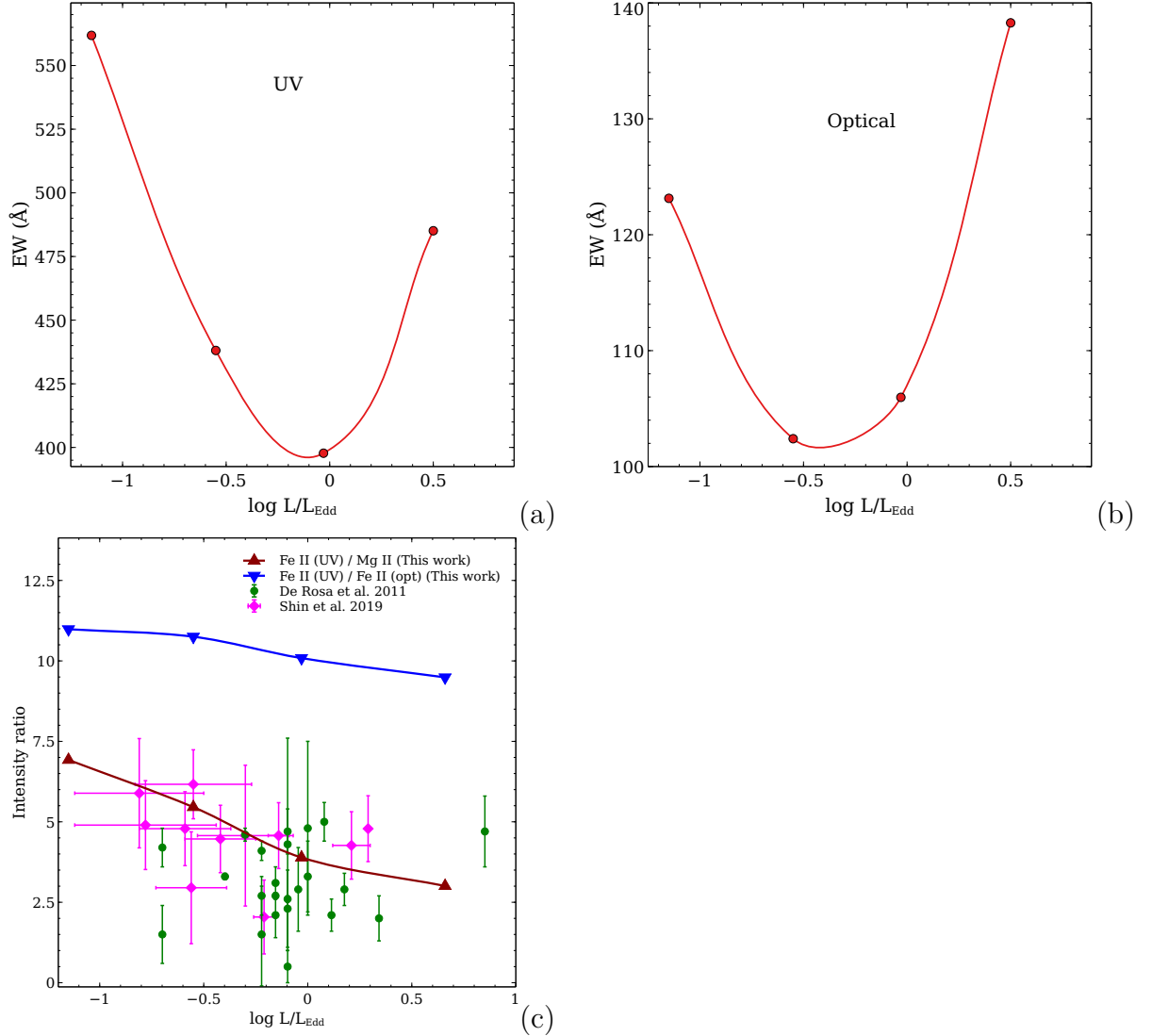


Figure 6.11: Panel (a) and (b): red circles show the EW of the Fe II UV bump and the Fe II optical band as a function of L/L_{Edd} respectively. Panel (c): red and blue triangles represent the $I(\text{Fe II})/I(\text{Mg II})$ and $I(\text{Fe II})(\text{UV})/I(\text{Fe II})(\text{Optical})$ as a function of L/L_{Edd} , respectively. For both plots we use our best obtained model parameters. Green circles and magenta squares are the observed $I(\text{Fe II})/I(\text{Mg II})$ ratios taken from De Rosa et al. (2011) and Shin et al. (2019) respectively.

four L/L_{Edd} values for Jin et al. (2012) SED. Those are $\log L/L_{\text{Edd}} = -1.15, -0.55, -0.03,$ and 0.66 . Figure 6.11 shows the predicted change in the equivalent widths of the UV bump and optical emission, defined as the total Fe II emission integrated over $4000 - 6000\text{\AA}$. Both are predicted as equivalent widths measured relative to the incident SED at 1215\AA (Baldwin et al., 2004). The rightmost panel shows the $I(\text{Fe II})/I(\text{Mg II})$ discussed above and the ratio of the UV to optical Fe II bands.

Although the predictions are in general agreement with observations, the observational scatter makes comparison difficult. De Rosa et al. (2011) and Shin et al. (2019)

obtained the $I(\text{Fe II})/I(\text{Mg II})$ for AGN samples observed at $z > 4$ and $z \sim 3$, respectively. Their results show little or no correlation between the $I(\text{Fe II})/I(\text{Mg II})$ and L/L_{Edd} . Clearly there are more parameters changing than simply the SED. A similar conclusion was reached by Ferland et al. (2020). That study used analytical theory to predict how the equivalent widths of H I and He II lines should change with the SED shape. As expected, large increases in the equivalent width were predicted as the SED grew harder with increasing L/L_{Edd} . No changes in equivalent width are observed, showing that the physics is more complex. Alternatively, the underlying theory may not, for some reason, produce the correct change in the SED as L/L_{Edd} changes. Clearly more work is needed.

6.4 Summary

We incorporated four atomic datasets, with self-consistent energy levels, transition rates, and electron impact collision strengths, for Fe II. Three of these sets include transitions in the UV and we compared the emission line predictions from these datasets for typical AGN with a set of BLR parameters and the new generation of SEDs.

- The original Verner et al. (1999) dataset largely rests on “g-bar” collision strengths, so we only presented it as a reference. By contrast, the Tayal and Zatsarinny (2018) and Smyth et al. (2019) Fe II datasets have many more transitions in the FUV, so continuum and Ly α florescent excitation, known to be important for Fe II, is better reproduced. However, the Smyth et al. (2019) dataset, with its higher density of states, produces several times more emission in the FUV compared to Tayal and Zatsarinny (2018). The Smyth et al. (2019) dataset was hence adopted throughout most of this work.
- We considered three representations of the broadband SED of an AGN, namely the original Mathews and Ferland (1987) SED (long included in CLOUDY), the Korista et al. (1997) SED derived from observations, and that of Jin et al. (2012) SED derived from a combination of theory and more recent observations. We compared the Fe II emission lines reproduced by each of the SEDs with CLOUDY. We showed that the Jin et al. (2012) SED produces the strongest Fe II emission because the soft X-rays penetrate into the low ionization region, heating it, generating more Fe II emission. Also, the $\log L/L_{\text{Edd}}$ value for the intermediate Jin et al. (2012) SED is consistent with that of IZW 1. The Jin et al. (2012) SED was hence adopted in this work.
- We presented predictions of the strength of the broad bump of Fe II UV emission and the Spike/gap ratio, defined by Baldwin et al. (2004), in the density (n_{H}) – photon flux (Φ) plane, using solar abundances and thermal line broadening ($V_{\text{turb}} = 0$ km/s). Our calculations with the Smyth et al. (2019) dataset and the Jin et al. (2012) SED also did not reproduce the observed Fe II template.

- We considered the effects of microturbulence (V_{turb}), varying it between 10^{-1} – 10^3 km/s. We showed that a cloud with $V_{\text{turb}} > 60$ km/s closely reproduces the observed Spike/gap ratio of 1.4, while the observed equivalent width ($> 400 \text{ \AA}$) requires that $V_{\text{turb}} > 90$ km/s. We adopted $V_{\text{turb}} \approx 100$ km/s in this work.
- Using the Smyth et al. (2019) dataset, Jin et al. (2012) SED, solar abundances, and the derived V_{turb} , we recalculated the strength of the Fe II UV emission and Spike/gap ratio in the density (n_{H}) – photon flux (Φ) plane. We showed that large regions in the plane reproduced the observed UV Fe II emission.
- We compared our model using the best obtained BLR parameters with the observed Fe II UV (Vestergaard and Wilkes, 2001) and optical template Véron-Cetty et al. (2004) template and found surprisingly good agreement. We concluded that the Fe II spectra are consistent with formation in relatively dense ($n_{\text{H}} = 10^{11} \text{ cm}^{-3}$) and turbulent ($V_{\text{turb}} \approx 100$ km/s) clouds about 100 – 200 light days away from the central black hole with solar abundances.
- We showed that the $I(\text{Fe II})/I(\text{Mg II})$ ratio predicted by our best-fitting model reproduces observations with solar abundances. This is a significant step in calibrating Fe II as an abundance indicator. Unfortunately, the spectrum is strongly saturated so the intensity ratio does not have a strong dependence on the abundance ratio.
- We considered how changes in the SED shape, predicted from recent models by varying L/L_{Edd} , change the resultant Fe II spectrum. In the simplest case this would provide a physical explanation for the observed Eigenvector 1 relations. The predicted changes do not agree with the observed correlations, showing that more is changing than just the SED shape. A similar conclusion was reached by Ferland et al. (2020) in their analysis of hydrogen line equivalent widths.

Chapter 7 Conclusions

My PhD thesis works involved studying the exciting physics behind the X-ray emission from the intra-cluster medium (ICM) of galaxy clusters and groups. I developed tools, analyzed spectra and high-resolution images from multiple telescopes (e.g., *Suzaku*, *Chandra*, *ROSAT*, 2MASS), and explained various physical phenomena to understand the thermal and chemical enrichment histories of ICM from cluster center out to their virial radii and beyond.

I discussed the importance of gas entropy in determining the thermal history of ICM and investigated the radial entropy profile of a cool-core galaxy group MKW4 from its center to the virial radius. Its entropy profile follows a power-law of $\propto r^{1.1}$ between R_{500} and R_{200} in all directions, as expected from the purely gravitational structure formation model. The well-behaved entropy profiles at the outskirts of MKW4 disfavor the presence of gas clumping or thermal non-equilibrium between ions and electrons in this system. I measured an enclosed baryon fraction of 11% at R_{200} , remarkably smaller than the cosmic baryon fraction of 15%. I noted that the enclosed gas fractions at R_{200} are systematically smaller for groups than for clusters from existing studies in the literature. The low baryon fraction of galaxy groups, such as MKW4, suggests that their shallower gravitational potential well may make them more vulnerable to baryon losses due to AGN feedback or galactic winds. I also measured that the azimuthal scatter of various gas properties at the outskirts of MKW4 is significantly lower than in other systems, suggesting that MKW4 is a spherically symmetric and highly relaxed system.

I extended this work by probing the chemical enrichment histories of four nearby galaxy groups, i.e., MKW4, Antlia, RXJ1159, and ESO3060170. Their peak temperatures vary over 2–3 keV, making them the smallest systems to have gas properties constrained out to their virial radii. The average Fe abundance in the outskirts ($R > 0.25R_{200}$) of their intragroup medium (IGrM) is $Z_{\text{Fe}} = 0.309 \pm 0.018 Z_{\odot}$ with $\chi^2 = 14$ for 12 degrees of freedom, which is remarkably uniform and strikingly similar to that of massive galaxy clusters, and is fully consistent with the numerical predictions from the IllustrisTNG cosmological simulation. My results support an early-enrichment scenario among galactic systems over an order of magnitude in mass even before their formation. I further constrained their O, Mg, Si, S, and Ni abundances. The abundance ratios of those elements relative to Fe are consistent with the predictions from IllustrisTNG. Their Type Ia supernovae fraction varies between 14%–21%. A pure core collapsed supernovae enrichment at group outskirts can be ruled out.

I investigated the gas properties and dynamics of ICM of a pre-merger galaxy cluster, Abell 98. I reported the first unambiguous detection of an axial merger shock between northern and central subclusters of Abell 98. The shock is about 420 kpc south from the northern subcluster with a Mach number of $\mathcal{M} \approx 2.3 \pm 0.3$. This finding of the axial merger shock front unveiled a critical epoch in the formation of a massive galaxy cluster, when two subclusters are caught in the early phase of the merging process. I established that the electron temperature in the post-shock

region favours the instant collisionless model. I also detected an intercluster gas filament, with a temperature of $kT = 1.07 \pm 0.29$ keV, along the merger axis of Abell 98. The measured properties of the gas in the filament are consistent with previous observations and numerical simulations of the hottest, densest parts of the warm-hot intergalactic medium (WHIM), where WHIM filaments interface with the virialization regions of galaxy clusters.

I further extended this study to probe the gas dynamics at the centers of two subclusters of Abell 98. I detected two gas sloshing spirals in northern and the eastern core of central subclusters, respectively. I identified a surface brightness edge in the western core of central subcluster as a shock front. I also detected a “tail” of X-ray emission associated with the eastern core of central subcluster. My measurement indicated that the tail is cooler than the surrounding gas at a $4.2\text{-}\sigma$ level, suggesting the tail is the part of a cool core remnant that has been ram-pressure stripped.

Bibliography

- G. O. Abell, J. Corwin, Harold G., and R. P. Olowin. A Catalog of Rich Clusters of Galaxies. *ApJS*, 70:1, May 1989. doi: 10.1086/191333.
- H. Akamatsu, A. Hoshino, Y. Ishisaki, T. Ohashi, K. Sato, Y. Takei, and N. Ota. X-Ray Study of the Outer Region of Abell 2142 with Suzaku. *Publications of the Astronomical Society of Japan*, 63(sp3):S1019–S1033, 11 2011. ISSN 0004-6264. doi: 10.1093/pasj/63.sp3.S1019. URL <https://doi.org/10.1093/pasj/63.sp3.S1019>.
- C. Allende Prieto, D. L. Lambert, and M. Asplund. A Reappraisal of the Solar Photospheric C/O Ratio. , 573(2):L137–L140, July 2002. doi: 10.1086/342095.
- G. E. Alvarez, S. W. Randall, H. Bourdin, C. Jones, and K. Holley-Bockelmann. Chandra and XMM-Newton Observations of the Abell 3395/Abell 3391 Intercluster Filament. *ApJ*, 858(1):44, May 2018. doi: 10.3847/1538-4357/aabad0.
- G. E. Alvarez, S. W. Randall, Y. Su, A. Sarkar, S. Walker, N. Lee, C. L. Sarazin, and E. Blanton. SUZAKU OBSERVATIONS OF THE CLUSTER OUTSKIRTS AND INTERCLUSTER FILAMENT IN THE TRIPLE MERGER CLUSTER ABELL 98. *Submitted to ApJ*, 000:0–0, Oct. 2022a. doi: 00/00.
- G. E. Alvarez, S. W. Randall, Y. Su, A. Sarkar, S. Walker, N. P. Lee, C. L. Sarazin, and E. Blanton. Suzaku Observations of the Cluster Outskirts and Intercluster Filament in the Triple Merger Cluster Abell 98. *arXiv e-prints*, art. arXiv:2206.08430, June 2022b.
- E. Anders and N. Grevesse. Abundances of the elements: Meteoritic and solar. *Geochimica et Cosmochimica Acta*, 53(1):197 – 214, 1989. ISSN 0016-7037. doi: [https://doi.org/10.1016/0016-7037\(89\)90286-X](https://doi.org/10.1016/0016-7037(89)90286-X). URL <http://www.sciencedirect.com/science/article/pii/001670378990286X>.
- M. Arnaud. The β -model of the intracluster medium. Commentary on: Cavaliere A. and Fusco-Femiano R., 1976, A&A, 49, 137. , 500(1):103–104, June 2009. doi: 10.1051/0004-6361/200912150.
- M. Arnaud, G. W. Pratt, R. Piffaretti, H. Böhringer, J. H. Croston, and E. Pointecouteau. The universal galaxy cluster pressure profile from a representative sample of nearby systems (REXCESS) and the $Y_{SZ} - M_{500}$ relation. , 517:A92, July 2010. doi: 10.1051/0004-6361/200913416.
- Y. Ascasibar and M. Markevitch. The Origin of Cold Fronts in the Cores of Relaxed Galaxy Clusters. , 650(1):102–127, Oct. 2006. doi: 10.1086/506508.
- M. Asplund, N. Grevesse, and A. Jacques Sauval. The solar chemical composition. , 777:1–4, Oct. 2006. doi: 10.1016/j.nuclphysa.2005.06.010.

- M. Asplund, N. Grevesse, A. J. Sauval, and P. Scott. The Chemical Composition of the Sun. , 47(1):481–522, Sept. 2009. doi: 10.1146/annurev.astro.46.060407.145222.
- C. Avestruz, D. Nagai, E. T. Lau, and K. Nelson. Non-equilibrium Electrons in the Outskirts of Galaxy Clusters. , 808(2):176, Aug. 2015. doi: 10.1088/0004-637X/808/2/176.
- C. Badenes, K. J. Borkowski, J. P. Hughes, U. Hwang, and E. Bravo. Constraints on the Physics of Type Ia Supernovae from the X-Ray Spectrum of the Tycho Supernova Remnant. , 645(2):1373–1391, July 2006. doi: 10.1086/504399.
- J. Baldwin, G. Ferland, K. Korista, and D. Verner. Locally Optimally Emitting Clouds and the Origin of Quasar Emission Lines. , 455:L119, Dec. 1995. doi: 10.1086/309827.
- J. A. Baldwin, G. J. Ferland, K. T. Korista, F. Hamann, and A. LaCluyz . The Origin of Fe II Emission in Active Galactic Nuclei. , 615(2):610–624, Nov. 2004. doi: 10.1086/424683.
- M. Balucinska-Church and D. McCammon. Photoelectric Absorption Cross Sections with Variable Abundances. , 400:699, Dec. 1992. doi: 10.1086/172032.
- M. A. Bautista, V. Fivet, C. Ballance, P. Quinet, G. Ferland, C. Mendoza, and T. R. Kallman. Atomic Data and Spectral Model for Fe II. , 808(2):174, Aug. 2015. doi: 10.1088/0004-637X/808/2/174.
- E. F. Bell, D. H. McIntosh, N. Katz, and M. D. Weinberg. The Optical and Near-Infrared Properties of Galaxies. I. Luminosity and Stellar Mass Functions. , 149(2):289–312, Dec. 2003. doi: 10.1086/378847.
- V. Biffi, S. Planelles, S. Borgani, D. Fabjan, E. Rasia, G. Murante, L. Tornatore, K. Dolag, G. L. Granato, M. Gaspari, and A. M. Beck. The history of chemical enrichment in the intracluster medium from cosmological simulations. , 468(1):531–548, June 2017. doi: 10.1093/mnras/stx444.
- V. Biffi, F. Mernier, and P. Medvedev. Enrichment of the Hot Intracluster Medium: Numerical Simulations. , 214(8):123, Dec. 2018. doi: 10.1007/s11214-018-0557-7.
- V. Biffi, S. Planelles, S. Borgani, E. Rasia, G. Murante, D. Fabjan, and M. Gaspari. The origin of ICM enrichment in the outskirts of present-day galaxy clusters from cosmological hydrodynamical simulations. *Monthly Notices of the Royal Astronomical Society*, 476(2):2689–2703, 02 2018. ISSN 0035-8711. doi: 10.1093/mnras/sty363. URL <https://doi.org/10.1093/mnras/sty363>.
- E. L. Blanton, S. W. Randall, T. E. Clarke, C. L. Sarazin, B. R. McNamara, E. M. Douglass, and M. McDonald. A Very Deep Chandra Observation of A2052: Bubbles, Shocks, and Sloshing. , 737(2):99, Aug. 2011. doi: 10.1088/0004-637X/737/2/99.

- H. Böhringer and N. Werner. X-ray spectroscopy of galaxy clusters: studying astrophysical processes in the largest celestial laboratories. , 18(1-2):127–196, Feb. 2010. doi: 10.1007/s00159-009-0023-3.
- J. S. Bolton and M. G. Haehnelt. The nature and evolution of the highly ionized near-zones in the absorption spectra of $z \sim 6$ quasars. , 374(2):493–514, Jan. 2007. doi: 10.1111/j.1365-2966.2006.11176.x.
- M. Bonamente, D. Landry, B. Maughan, P. Giles, M. Joy, and J. Nevalainen. Chandra X-ray observations of Abell 1835 to the virial radius. , 428(4):2812–2823, Feb. 2013. doi: 10.1093/mnras/sts202.
- S. Borgani, A. Finoguenov, S. T. Kay, T. J. Ponman, V. Springel, P. Tozzi, and G. M. Voit. Entropy amplification from energy feedback in simulated galaxy groups and clusters. *Monthly Notices of the Royal Astronomical Society*, 361(1):233–243, 07 2005. ISSN 0035-8711. doi: 10.1111/j.1365-2966.2005.09158.x. URL <https://doi.org/10.1111/j.1365-2966.2005.09158.x>.
- T. A. Boroson and R. F. Green. The Emission-Line Properties of Low-Redshift Quasi-stellar Objects. , 80:109, May 1992. doi: 10.1086/191661.
- A. Botteon, F. Gastaldello, G. Brunetti, and R. Kale. A $M \gtrsim 3$ shock in ‘El Gordo’ cluster and the origin of the radio relic. *MNRAS*, 463(2):1534–1542, Dec. 2016. doi: 10.1093/mnras/stw2089.
- A. Botteon, F. Gastaldello, and G. Brunetti. Shocks and cold fronts in merging and massive galaxy clusters: new detections with Chandra. *MNRAS*, 476(4):5591–5620, June 2018. doi: 10.1093/mnras/sty598.
- M. Bottorff, G. Ferland, J. Baldwin, and K. Korista. Observational constraints on the internal velocity field of quasar emission-line clouds. *The Astrophysical Journal*, 542(2):644–654, oct 2000. doi: 10.1086/317051. URL <https://doi.org/10.1086%2F317051>.
- R. G. Bower, I. G. McCarthy, and A. J. Benson. The flip side of galaxy formation: a combined model of galaxy formation and cluster heating. , 390(4):1399–1410, Nov. 2008. doi: 10.1111/j.1365-2966.2008.13869.x.
- J. N. Bregman. The Search for the Missing Baryons at Low Redshift. *ARAA*, 45(1): 221–259, Sept. 2007. doi: 10.1146/annurev.astro.45.051806.110619.
- F. Bruhweiler and E. Verner. Modeling Fe II Emission and Revised Fe II (UV) Empirical Templates for the Seyfert 1 Galaxy I Zw 1. , 675(1):83–95, Mar. 2008. doi: 10.1086/525557.
- F. Bruhweiler and E. Verner. Modeling FeiiEmission and revised feii(UV) empirical templates for the seyfert 1 galaxy i zw 1. *The Astrophysical Journal*, 675(1):83–95, mar 2008. doi: 10.1086/525557. URL <https://doi.org/10.1086%2F525557>.

- E. Bulbul, M. Markevitch, A. Foster, E. Miller, M. Bautz, M. Loewenstein, S. W. Randall, and R. K. Smith. Searching for the 3.5 keV Line in the Stacked Suzaku Observations of Galaxy Clusters. , 831(1):55, Nov. 2016a. doi: 10.3847/0004-637X/831/1/55.
- E. Bulbul, S. W. Randall, M. Bayliss, E. Miller, F. Andrade-Santos, R. Johnson, M. Bautz, E. L. Blanton, W. R. Forman, C. Jones, R. Paterno-Mahler, S. S. Murray, C. L. Sarazin, R. K. Smith, and C. Ezer. Probing the Outskirts of the Early-Stage Galaxy Cluster Merger A1750. , 818(2):131, Feb. 2016b. doi: 10.3847/0004-637X/818/2/131.
- D. A. Buote. Iron Gradients in Cooling Flow Galaxies and Groups. , 539(1):172–186, Aug. 2000. doi: 10.1086/309224.
- D. A. Buote and A. C. Fabian. X-ray spectral analysis of elliptical galaxies from ASCA: the Fe abundance in a multiphase medium. , 296(4):977–994, June 1998. doi: 10.1046/j.1365-8711.1998.01478.x.
- J. O. Burns, G. Rhee, F. N. Owen, and J. Pinkney. Clumped X-Ray Emission around Radio Galaxies in Abell Clusters. *ApJ*, 423:94, Mar. 1994. doi: 10.1086/173792.
- W. Cash. Parameter estimation in astronomy through application of the likelihood ratio. , 228:939–947, Mar. 1979. doi: 10.1086/156922.
- A. Cavaliere and R. Fusco-Femiano. Reprint of 1976A&A....49..137C. X-rays from hot plasma in clusters of galaxies. , 500:95–102, May 1976.
- R. Cen and J. P. Ostriker. Where Are the Baryons? *ApJ*, 514(1):1–6, Mar. 1999. doi: 10.1086/306949.
- P. Chakraborty, G. J. Ferland, M. Chatzikos, F. Guzmán, and Y. Su. X-Ray Spectroscopy in the Microcalorimeter Era. I. Effects of Fe XXIV Resonant Auger Destruction on Fe XXV $K\alpha$ Spectra. , 901(1):68, Sept. 2020a. doi: 10.3847/1538-4357/abaaab.
- P. Chakraborty, G. J. Ferland, M. Chatzikos, F. Guzmán, and Y. Su. X-Ray Spectroscopy in the Microcalorimeter Era. II. A New Diagnostic on Column Density from the Case A to B Transition in H- and He-like Iron. , 901(1):69, Sept. 2020b. doi: 10.3847/1538-4357/abaaac.
- A. O. Clarke, A. M. M. Scaife, T. Shimwell, R. J. van Weeren, A. Bonafede, G. Heald, G. Brunetti, T. M. Cantwell, F. de Gasperin, M. Brüggen, A. Botteon, M. Hoeft, C. Horellou, R. Cassano, J. J. Harwood, and H. J. A. Röttgering. Signatures from a merging galaxy cluster and its AGN population: LOFAR observations of Abell 1682. , 627:A176, July 2019. doi: 10.1051/0004-6361/201935584.
- T. E. Clarke, E. L. Blanton, and C. L. Sarazin. The Complex Cooling Core of A2029: Radio and X-Ray Interactions. , 616(1):178–191, Nov. 2004. doi: 10.1086/424911.

- P. S. Corasaniti, S. Ettori, Y. Rasera, M. Sereno, S. Amodeo, M. A. Breton, V. Ghirardini, and D. Eckert. Probing Cosmology with Dark Matter Halo Sparsity Using X-Ray Cluster Mass Measurements. , 862(1):40, July 2018. doi: 10.3847/1538-4357/aacdf.
- V. Cracco, S. Ciroi, M. Berton, F. Di Mille, L. Foschini, G. La Mura, and P. Rafanelli. A spectroscopic analysis of a sample of narrow-line Seyfert 1 galaxies selected from the Sloan Digital Sky Survey. , 462(2):1256–1280, Oct. 2016. doi: 10.1093/mnras/stw1689.
- X. Dai, J. N. Bregman, C. S. Kochanek, and E. Rasia. On the Baryon Fractions in Clusters and Groups of Galaxies. , 719(1):119–125, Aug. 2010. doi: 10.1088/0004-637X/719/1/119.
- S. Dasadia, M. Sun, C. Sarazin, A. Morandi, M. Markevitch, D. Wik, L. Feretti, G. Giovannini, F. Govoni, and V. Vacca. A Strong Merger Shock in Abell 665. *ApJL*, 820(1):L20, Mar. 2016. doi: 10.3847/2041-8205/820/1/L20.
- R. Davé, L. Hernquist, N. Katz, and D. H. Weinberg. The Low-Redshift Ly α Forest in Cold Dark Matter Cosmologies. *ApJ*, 511(2):521–545, Feb. 1999. doi: 10.1086/306722.
- R. Davé, R. Cen, J. P. Ostriker, G. L. Bryan, L. Hernquist, N. Katz, D. H. Weinberg, M. L. Norman, and B. O’Shea. Baryons in the Warm-Hot Intergalactic Medium. *ApJ*, 552(2):473–483, May 2001. doi: 10.1086/320548.
- R. Davé, B. D. Oppenheimer, and S. Sivanandam. Enrichment and pre-heating in intragroup gas from galactic outflows. , 391(1):110–123, Nov. 2008. doi: 10.1111/j.1365-2966.2008.13906.x.
- S. de Grandi and S. Molendi. Metal abundances in the cool cores of galaxy clusters. , 508(2):565–574, Dec. 2009. doi: 10.1051/0004-6361/200912745.
- A. De Luca and S. Molendi. The 2-8 keV cosmic X-ray background spectrum as observed with XMM-Newton. , 419:837–848, June 2004. doi: 10.1051/0004-6361:20034421.
- J. de Plaa, N. Werner, J. A. M. Bleeker, J. Vink, J. S. Kaastra, and M. Méndez. Constraining supernova models using the hot gas in clusters of galaxies. , 465(2):345–355, Apr. 2007. doi: 10.1051/0004-6361:20066382.
- G. De Rosa, R. Decarli, F. Walter, X. Fan, L. Jiang, J. Kurk, A. Pasquali, and H. W. Rix. Evidence for Non-evolving Fe II/Mg II Ratios in Rapidly Accreting $z \sim 6$ QSOs. , 739(2):56, Oct. 2011. doi: 10.1088/0004-637X/739/2/56.
- S. G. Djorgovski, S. Castro, D. Stern, and A. A. Mahabal. On the Threshold of the Reionization Epoch. , 560(1):L5–L8, Oct. 2001. doi: 10.1086/324175.

- K. Dolag, M. Meneghetti, L. Moscardini, E. Rasia, and A. Bonaldi. Simulating the physical properties of dark matter and gas inside the cosmic web. *MNRAS*, 370(2):656–672, Aug. 2006. doi: 10.1111/j.1365-2966.2006.10511.x.
- W. Domainko, M. Mair, W. Kapferer, E. van Kampen, T. Kronberger, S. Schindler, S. Kimeswenger, M. Ruffert, and O. E. Mangete. Enrichment of the ICM of galaxy clusters due to ram-pressure stripping. , 452(3):795–802, June 2006. doi: 10.1051/0004-6361:20053921.
- C. Done, S. W. Davis, C. Jin, O. Blaes, and M. Ward. Intrinsic disc emission and the soft X-ray excess in active galactic nuclei. , 420(3):1848–1860, Mar. 2012. doi: 10.1111/j.1365-2966.2011.19779.x.
- E. M. Douglass, E. L. Blanton, T. E. Clarke, C. L. Sarazin, and M. Wise. Chandra Observation of the Cluster Environment of a WAT Radio Source in Abell 1446. , 673(2):763–777, Feb. 2008. doi: 10.1086/523886.
- E. M. Douglass, E. L. Blanton, T. E. Clarke, S. W. Randall, and J. D. Wing. The Merger Environment of the Wide Angle Tail Hosting Cluster A562. , 743(2):199, Dec. 2011. doi: 10.1088/0004-637X/743/2/199.
- E. M. Douglass, E. L. Blanton, S. W. Randall, T. E. Clarke, L. O. V. Edwards, Z. Sabry, and J. A. ZuHone. The Megaparsec-scale Gas-sloshing Spiral in the Remnant Cool Core Cluster Abell 1763. *ApJ*, 868(2):121, Dec. 2018. doi: 10.3847/1538-4357/aae9e7.
- A. E. Blackwell, J. N. Bregman, and S. L. Snowden. The Missing Metal Problem in Galaxy Clusters: Characterizing the Early Enrichment Population. *arXiv e-prints*, art. arXiv:2105.04638, May 2021.
- D. Eckert, M. Jauzac, H. Shan, J.-P. Kneib, T. Erben, H. Israel, E. Jullo, M. Klein, R. Massey, J. Richard, and C. Tchernin. Warm-hot baryons comprise 5-10 per cent of filaments in the cosmic web. *Nature*, 528(7580):105–107, Dec. 2015. doi: 10.1038/nature16058.
- D. Eckert, V. Ghirardini, S. Ettori, E. Rasia, V. Biffi, E. Pointecouteau, M. Rossetti, S. Molendi, F. Vazza, F. Gastaldello, M. Gaspari, S. De Grandi, S. Ghizzardi, H. Bourdin, C. Tchernin, and M. Roncarelli. Non-thermal pressure support in X-COP galaxy clusters. , 621:A40, Jan. 2019. doi: 10.1051/0004-6361/201833324.
- V. R. Eke, C. M. Baugh, S. Cole, C. S. Frenk, P. Norberg, J. A. Peacock, I. K. Baldry, J. Bland-Hawthorn, T. Bridges, R. Cannon, M. Colless, C. Collins, W. Couch, G. Dalton, R. D. Propris, S. P. Driver, G. Efstathiou, R. S. Ellis, K. Glazebrook, C. Jackson, O. Lahav, I. Lewis, S. Lumsden, S. Maddox, D. Madgwick, B. A. Peterson, W. Sutherland, K. Taylor, and (the 2dFGRS Team). Galaxy groups in the 2dFGRS: the group-finding algorithm and the 2PIGG catalogue. *Monthly Notices of the Royal Astronomical Society*, 348(3):866–878, 03 2004. ISSN 0035-8711. doi: 10.1111/j.1365-2966.2004.07408.x. URL <https://doi.org/10.1111/j.1365-2966.2004.07408.x>.

- M. K. Erdim and M. Hudaverdi. Chandra observation of a cold front in Abell 2554. , 488(2):2917–2924, Sept. 2019. doi: 10.1093/mnras/stz1912.
- S. Ettori and A. C. Fabian. Coulomb interactions in the intracluster medium. , 293(1):L33–L36, Jan. 1998. doi: 10.1046/j.1365-8711.1998.01253.x.
- S. Ettori and A. C. Fabian. ROSAT PSPC observations of 36 high-luminosity clusters of galaxies: constraints on the gas fraction. , 305(4):834–848, May 1999. doi: 10.1046/j.1365-8711.1999.02460.x.
- A. C. Fabian, J. S. Sanders, S. Ettori, G. B. Taylor, S. W. Allen, C. S. Crawford, K. Iwasawa, and R. M. Johnstone. Chandra imaging of the X-ray core of Abell 1795. , 321(2):L33–L36, Feb. 2001. doi: 10.1046/j.1365-8711.2001.04243.x.
- A. C. Fabian, J. S. Sanders, S. W. Allen, C. S. Crawford, K. Iwasawa, R. M. Johnstone, R. W. Schmidt, and G. B. Taylor. A deep Chandra observation of the Perseus cluster: shocks and ripples. , 344(3):L43–L47, Sept. 2003. doi: 10.1046/j.1365-8711.2003.06902.x.
- A. C. Fabian, J. S. Sanders, S. W. Allen, R. E. A. Canning, E. Churazov, C. S. Crawford, W. Forman, J. Gabany, J. Hlavacek-Larrondo, R. M. Johnstone, H. R. Russell, C. S. Reynolds, P. Salomé, G. B. Taylor, and A. J. Young. A wide Chandra view of the core of the Perseus cluster. *MNRAS*, 418(4):2154–2164, Dec. 2011. doi: 10.1111/j.1365-2966.2011.19402.x.
- D. Fabjan, S. Borgani, L. Tornatore, A. Saro, G. Murante, and K. Dolag. Simulating the effect of active galactic nuclei feedback on the metal enrichment of galaxy clusters. , 401(3):1670–1690, Jan. 2010. doi: 10.1111/j.1365-2966.2009.15794.x.
- X. Fan, C. L. Carilli, and B. Keating. Observational Constraints on Cosmic Reionization. , 44(1):415–462, Sept. 2006. doi: 10.1146/annurev.astro.44.051905.092514.
- G. J. Ferland. N III Line Emission in Planetary Nebulae: Continuum Fluorescence. , 389:L63, Apr. 1992. doi: 10.1086/186349.
- G. J. Ferland, C. Hu, J.-M. Wang, J. A. Baldwin, R. L. Porter, P. A. M. van Hoof, and R. J. R. Williams. Implications of Infalling Fe II-Emitting Clouds in Active Galactic Nuclei: Anisotropic Properties. , 707(1):L82–L86, Dec. 2009. doi: 10.1088/0004-637X/707/1/L82.
- G. J. Ferland, M. Chatzikos, F. Guzmán, M. L. Lykins, P. A. M. van Hoof, R. J. R. Williams, N. P. Abel, N. R. Badnell, F. P. Keenan, R. L. Porter, and P. C. Stancil. The 2017 Release Cloudy. , 53:385–438, Oct. 2017.
- G. J. Ferland, C. Done, C. Jin, H. Landt, and M. J. Ward. State-of-the-art AGN SEDs for photoionization models: BLR predictions confront the observations. , 494(4):5917–5922, May 2020. doi: 10.1093/mnras/staa1207.

- D. Fielding, E. Quataert, M. McCourt, and T. A. Thompson. The impact of star formation feedback on the circumgalactic medium. *MNRAS*, 466(4):3810–3826, Apr. 2017. doi: 10.1093/mnras/stw3326.
- W. Forman, J. Bechtold, W. Blair, R. Giacconi, L. van Speybroeck, and C. Jones. Einstein imaging observations of clusters with a bimodal mass distribution. *AJ*, 243: L133–L136, Feb. 1981. doi: 10.1086/183459.
- J. Freundlich and D. Maoz. The delay time distribution of Type-Ia supernovae in galaxy clusters: the impact of extended star-formation histories. *MNRAS*, 502(4):5882–5895, Apr. 2021. doi: 10.1093/mnras/stab493.
- M. Fukugita and P. J. E. Peebles. The Cosmic Energy Inventory. *ApJ*, 616(2): 643–668, Dec. 2004. doi: 10.1086/425155.
- M. Fukugita, C. J. Hogan, and P. J. E. Peebles. The Cosmic Baryon Budget. *AJ*, 503(2):518–530, Aug. 1998. doi: 10.1086/306025.
- A. Garcia-Rissmann, A. Rodríguez-Ardila, T. A. A. Sigut, and A. K. Pradhan. A Near-infrared Template Derived from I Zw 1 for the Fe II Emission in Active Galaxies. *MNRAS*, 751(1):7, May 2012. doi: 10.1088/0004-637X/751/1/7.
- F. Gastaldello, D. A. Buote, P. J. Humphrey, L. Zappacosta, J. S. Bullock, F. Brighenti, and W. G. Mathews. Probing the Dark Matter and Gas Fraction in Relaxed Galaxy Groups with X-Ray Observations from Chandra and XMM-Newton. *MNRAS*, 669(1):158–183, Nov. 2007. doi: 10.1086/521519.
- F. Gastaldello, L. Di Gesu, S. Ghizzardi, S. Giacintucci, M. Girardi, E. Roediger, M. Rossetti, F. Brighenti, D. A. Buote, D. Eckert, S. Ettori, P. J. Humphrey, and W. G. Mathews. Sloshing Cold Fronts in Galaxy Groups and their Perturbing Disk Galaxies: An X-Ray, Optical, and Radio Case Study. *MNRAS*, 770(1):56, June 2013. doi: 10.1088/0004-637X/770/1/56.
- F. Gastaldello, A. Simionescu, F. Mernier, V. Biffi, M. Gaspari, K. Sato, and K. Matsushita. The Metal Content of the Hot Atmospheres of Galaxy Groups. *Universe*, 7(7):208, June 2021. doi: 10.3390/universe7070208.
- C. Ge, R.-Y. Liu, M. Sun, H. Yu, L. Rudnick, J. Eilek, F. Owen, S. Dasadia, M. Rossetti, M. Markevitch, T. E. Clarke, T. W. Jones, S. Ghizzardi, T. Venturi, A. Finoguenov, and D. Eckert. Chandra and XMM-Newton observations of A2256: cold fronts, merger shocks, and constraint on the IC emission. *MNRAS*, 497(4): 4704–4717, Oct. 2020. doi: 10.1093/mnras/staa2320.
- M. R. George, A. C. Fabian, J. S. Sanders, A. J. Young, and H. R. Russell. X-ray observations of the galaxy cluster PKS 0745–191: to the virial radius, and beyond. *Monthly Notices of the Royal Astronomical Society*, 395(2):657–666, 04 2009. ISSN 0035-8711. doi: 10.1111/j.1365-2966.2009.14547.x. URL <https://doi.org/10.1111/j.1365-2966.2009.14547.x>.

- V. Ghirardini, S. Ettori, D. Eckert, S. Molendi, F. Gastaldello, E. Pointecouteau, G. Hurier, and H. Bourdin. The XMM Cluster Outskirts Project (X-COP): Thermodynamic properties of the intracluster medium out to R_{200} in Abell 2319. , 614: A7, June 2018. doi: 10.1051/0004-6361/201731748.
- S. Ghizzardi, S. De Grandi, and S. Molendi. Metal distribution in sloshing galaxy clusters: the case of A496. , 570:A117, Oct. 2014. doi: 10.1051/0004-6361/201424016.
- S. Ghizzardi, S. Molendi, R. van der Burg, S. De Grandi, I. Bartalucci, F. Gastaldello, M. Rossetti, V. Biffi, S. Borgani, D. Eckert, S. Ettori, M. Gaspari, V. Ghirardini, and E. Rasia. Iron in X-COP: Tracing enrichment in cluster outskirts with high accuracy abundance profiles. , 646:A92, Feb. 2021. doi: 10.1051/0004-6361/202038501.
- M. Giustini and D. Proga. A global view of the inner accretion and ejection flow around super massive black holes. Radiation-driven accretion disk winds in a physical context. , 630:A94, Oct. 2019. doi: 10.1051/0004-6361/201833810.
- P. L. Gómez and D. Calderón. The Dynamics of the Wide-angle Tailed (WAT) Galaxy Cluster A562. , 160(4):152, Oct. 2020. doi: 10.3847/1538-3881/aba831.
- N. Grevesse and A. J. Sauval. Standard Solar Composition. , 85:161–174, May 1998. doi: 10.1023/A:1005161325181.
- L. Gu, H. Akamatsu, T. W. Shimwell, H. T. Intema, R. J. van Weeren, F. de Gasperin, F. Mernier, J. Mao, I. Urdampilleta, J. de Plaa, V. Parekh, H. J. A. Röttgering, and J. S. Kaastra. Observations of a pre-merger shock in colliding clusters of galaxies. *Nature Astronomy*, 3:838–843, June 2019. doi: 10.1038/s41550-019-0798-8.
- J. E. Gunn and I. Gott, J. Richard. On the Infall of Matter Into Clusters of Galaxies and Some Effects on Their Evolution. , 176:1, Aug. 1972. doi: 10.1086/151605.
- J.-H. Ha, D. Ryu, and H. Kang. Properties of Merger Shocks in Merging Galaxy Clusters. , 857(1):26, Apr. 2018. doi: 10.3847/1538-4357/aab4a2.
- F. Hamann and G. Ferland. Elemental Abundances in Quasistellar Objects: Star Formation and Galactic Nuclear Evolution at High Redshifts. , 37:487–531, Jan. 1999. doi: 10.1146/annurev.astro.37.1.487.
- A. D. Hincks, F. Radiconi, C. Romero, M. S. Madhavacheril, T. Mroczkowski, J. E. Austermann, E. Barbavara, N. Battaglia, E. Battistelli, J. R. Bond, E. Calabrese, P. de Bernardis, M. J. Devlin, S. R. Dicker, S. M. Duff, A. J. Duivenvoorden, J. Dunkley, R. Dünner, P. A. Gallardo, F. Govoni, J. C. Hill, M. Hilton, J. Hubmayr, J. P. Hughes, L. Lamagna, M. Lokken, S. Masi, B. S. Mason, J. McMahon, K. Moodley, M. Murgia, S. Naess, L. Page, F. Piacentini, M. Salatino, A. Schillaci, J. L. Sievers, C. Sifón, S. Staggs, J. N. Ullom, V. Vacca, A. Van Engelen, M. R. Vissers, E. J. Wollack, and Z. Xu. A high-resolution view of the filament of gas between Abell 399 and Abell 401 from the Atacama Cosmology Telescope and MUSTANG-2. *arXiv e-prints*, art. arXiv:2107.04611, July 2021.

- A. D. Hincks, F. Radiconi, C. Romero, M. S. Madhavacheril, T. Mroczkowski, J. E. Austermann, E. Barbavara, N. Battaglia, E. Battistelli, J. R. Bond, E. Calabrese, P. de Bernardis, M. J. Devlin, S. R. Dicker, S. M. Duff, A. J. Duivenvoorden, J. Dunkley, R. Dünner, P. A. Gallardo, F. Govoni, J. C. Hill, M. Hilton, J. Hubmayr, J. P. Hughes, L. Lamagna, M. Lokken, S. Masi, B. S. Mason, J. McMahon, K. Moodley, M. Murgia, S. Naess, L. Page, F. Piacentini, M. Salatino, C. L. Sarazin, A. Schillaci, J. L. Sievers, C. Sifón, S. Staggs, J. N. Ullom, V. Vacca, A. Van Engelen, M. R. Vissers, E. J. Wollack, and Z. Xu. A high-resolution view of the filament of gas between Abell 399 and Abell 401 from the Atacama Cosmology Telescope and MUSTANG-2. , 510(3):3335–3355, Mar. 2022. doi: 10.1093/mnras/stab3391.
- H. Hoekstra, B. C. Hsieh, H. K. C. Yee, H. Lin, and M. D. Gladders. Virial Masses and the Baryon Fraction in Galaxies. , 635(1):73–85, Dec. 2005. doi: 10.1086/496913.
- H. Holweger. Photospheric abundances: Problems, updates, implications. In R. F. Wimmer-Schweingruber, editor, *Joint SOHO/ACE workshop “Solar and Galactic Composition”*, volume 598 of *American Institute of Physics Conference Series*, pages 23–30, Nov. 2001. doi: 10.1063/1.1433974.
- A. Hoshino, J. P. Henry, K. Sato, H. Akamatsu, W. Yokota, S. Sasaki, Y. Ishisaki, T. Ohashi, M. Bautz, Y. Fukazawa, N. Kawano, A. Furuzawa, K. Hayashida, N. Tawa, J. P. Hughes, M. Kokubun, and T. Tamura. X-Ray Temperature and Mass Measurements to the Virial Radius of Abell 1413 with Suzaku. *Publications of the Astronomical Society of Japan*, 62(2):371–389, 04 2010. ISSN 0004-6264. doi: 10.1093/pasj/62.2.371. URL <https://doi.org/10.1093/pasj/62.2.371>.
- D. Hu, H. Xu, Z. Zhu, C. Shan, Y. Zhu, S. Fan, Y. Zhao, C. Liu, H. Siew, Z. Zhang, L. Gu, M. Johnston-Hollitt, X. Kang, Q. Tan, J. Chang, and X.-p. Wu. The Merger Dynamics of the Galaxy Cluster A1775: New Insights from Chandra and XMM-Newton for a Cluster Simultaneously Hosting a Wide-angle Tail and a Narrow-angle Tail Radio Source. , 913(1):8, May 2021. doi: 10.3847/1538-4357/abf09e.
- P. J. Humphrey, D. A. Buote, F. Brighenti, H. M. L. G. Flohic, F. Gastaldello, and W. G. Mathews. Tracing the Gas to the Virial Radius (R_{100}) in a Fossil Group. , 748(1):11, Mar. 2012. doi: 10.1088/0004-637X/748/1/11.
- Y. Ibaraki, N. Ota, H. Akamatsu, Y. Y. Zhang, and A. Finoguenov. Suzaku study of gas properties along filaments of A2744. , 562:A11, Feb. 2014. doi: 10.1051/0004-6361/201322806.
- K. Ichikawa, K. Matsushita, N. Okabe, K. Sato, Y.-Y. Zhang, A. Finoguenov, Y. Fujita, Y. Fukazawa, M. Kawaharada, K. Nakazawa, T. Ohashi, N. Ota, M. Takizawa, T. Tamura, and K. Umetsu. SUZAKUOBSERVATIONS OF THE OUTSKIRTS OF a1835: DEVIATION FROM HYDROSTATIC EQUILIBRIUM. *The Astrophysical Journal*, 766(2):90, mar 2013. doi: 10.1088/0004-637x/766/2/90. URL <https://doi.org/10.1088%2F0004-637x%2F766%2F2%2F90>.

- Y. Ichinohe, A. Simionescu, N. Werner, A. C. Fabian, and T. Takahashi. Substructures associated with the sloshing cold front in the Perseus cluster. , 483(2):1744–1753, Feb. 2019. doi: 10.1093/mnras/sty3257.
- Y. Ichinohe, A. Simionescu, N. Werner, M. Markevitch, and Q. H. S. Wang. Substructures in the core of Abell 2319. *MNRAS*, 504(2):2800–2810, June 2021. doi: 10.1093/mnras/stab1060.
- A. Ignesti, M. Gitti, G. Brunetti, E. O’Sullivan, C. Sarazin, and K. Wong. The mystery of the “Kite” radio source in Abell 2626: Insights from new Chandra observations. , 610:A89, Mar. 2018. doi: 10.1051/0004-6361/201731380.
- A. Ignesti, T. Shimwell, G. Brunetti, M. Gitti, H. Intema, R. J. van Weeren, M. J. Hardcastle, A. O. Clarke, A. Botteon, G. Di Gennaro, M. Brüggén, I. W. A. Browne, S. Mandal, H. J. A. Röttgering, V. Cuciti, F. de Gasperin, R. Cassano, and A. M. M. Scaife. The great Kite in the sky: A LOFAR observation of the radio source in Abell 2626. , 643:A172, Nov. 2020. doi: 10.1051/0004-6361/202039056.
- K. Iwamoto, F. Brachwitz, K. Nomoto, N. Kishimoto, H. Umeda, W. R. Hix, and F.-K. Thielemann. Nucleosynthesis in Chandrasekhar Mass Models for Type IA Supernovae and Constraints on Progenitor Systems and Burning-Front Propagation. , 125(2):439–462, Dec. 1999. doi: 10.1086/313278.
- C. Jin, M. Ward, and C. Done. A combined optical and X-ray study of unobscured type 1 active galactic nuclei - III. Broad-band SED properties. , 425(2):907–929, Sept. 2012. doi: 10.1111/j.1365-2966.2012.21272.x.
- R. E. Johnson, M. Markevitch, G. A. Wegner, C. Jones, and W. R. Forman. Core Gas Sloshing in Abell 1644. , 710(2):1776–1785, Feb. 2010. doi: 10.1088/0004-637X/710/2/1776.
- C. Jones and W. Forman. Einstein Observatory Images of Clusters of Galaxies. *ApJ*, 511(1):65–83, Jan. 1999. doi: 10.1086/306646.
- P. M. W. Kalberla, W. B. Burton, D. Hartmann, E. M. Arnal, E. Bajaja, R. Morras, and W. G. L. Pöppel. The Leiden/Argentine/Bonn (LAB) Survey of Galactic HI. Final data release of the combined LDS and IAR surveys with improved stray-radiation corrections. *AAP*, 440(2):775–782, Sept. 2005. doi: 10.1051/0004-6361:20041864.
- M. Kawaharada, N. Okabe, K. Umetsu, M. Takizawa, K. Matsushita, Y. Fukazawa, T. Hamana, S. Miyazaki, K. Nakazawa, and T. Ohashi. SUZAKUOBSERVATION OF a1689: ANISOTROPIC TEMPERATURE AND ENTROPY DISTRIBUTIONS ASSOCIATED WITH THE LARGE-SCALE STRUCTURE. *The Astrophysical Journal*, 714(1):423–441, apr 2010. doi: 10.1088/0004-637x/714/1/423. URL <https://doi.org/10.1088%2F0004-637x%2F714%2F1%2F423>.

- S. Kim, M. Stiavelli, M. Trenti, C. M. Pavlovsky, S. G. Djorgovski, C. Scarlata, D. Stern, A. Mahabal, D. Thompson, M. Dickinson, N. Panagia, and G. Meylan. The Environments of High-Redshift Quasi-Stellar Objects. , 695(2):809–817, Apr. 2009. doi: 10.1088/0004-637X/695/2/809.
- G. Kokotanekov, M. W. Wise, M. de Vries, and H. T. Intema. Signatures of multiple episodes of AGN activity in the core of Abell 1795. , 618:A152, Oct. 2018. doi: 10.1051/0004-6361/201833222.
- E. Komatsu, K. M. Smith, J. Dunkley, C. L. Bennett, B. Gold, G. Hinshaw, N. Jarosik, D. Larson, M. R.olta, L. Page, D. N. Spergel, M. Halpern, R. S. Hill, A. Kogut, M. Limon, S. S. Meyer, N. Odegard, G. S. Tucker, J. L. Weiland, E. Wollack, and E. L. Wright. SEVEN-YEAR WILKINSON MICROWAVE ANISOTROPY PROBE (WMAP) OBSERVATIONS: COSMOLOGICAL INTERPRETATION. *The Astrophysical Journal Supplement Series*, 192(2):18, jan 2011. doi: 10.1088/0067-0049/192/2/18. URL <https://doi.org/10.1088/2F0067-0049%2F192%2F2%2F18>.
- K. Korista, J. Baldwin, G. Ferland, and D. Verner. An Atlas of Computed Equivalent Widths of Quasar Broad Emission Lines. , 108(2):401–415, Jan. 1997. doi: 10.1086/312966.
- J. Kovačević-Dojčinović and L. Č. Popović. The Connections Between the UV and Optical Fe ii Emission Lines in Type 1 AGNs. , 221(2):35, Dec. 2015. doi: 10.1088/0067-0049/221/2/35.
- K. Koyama, H. Tsunemi, T. Dotani, M. W. Bautz, K. Hayashida, T. G. Tsuru, H. Matsumoto, Y. Ogawara, G. R. Ricker, J. Doty, S. E. Kissel, R. Foster, H. Nakajima, H. Yamaguchi, H. Mori, M. Sakano, K. Hamaguchi, M. Nishiuchi, E. Miyata, K. Torii, M. Namiki, S. Katsuda, D. Matsuura, T. Miyauchi, N. Anabuki, N. Tawa, M. Ozaki, H. Murakami, Y. Maeda, Y. Ichikawa, G. Y. Prigozhin, E. A. Boughan, B. Lamarr, E. D. Miller, B. E. Burke, J. A. Gregory, A. Pillsbury, A. Bamba, J. S. Hiraga, A. Senda, H. Katayama, S. Kitamoto, M. Tsujimoto, T. Kohmura, Y. Tsuboi, and H. Awaki. X-Ray Imaging Spectrometer (XIS) on Board Suzaku. , 59:23–33, Jan. 2007. doi: 10.1093/pasj/59.sp1.S23.
- J. D. Kurk, F. Walter, X. Fan, L. Jiang, D. A. Riechers, H.-W. Rix, L. Pentericci, M. A. Strauss, C. Carilli, and S. Wagner. Black Hole Masses and Enrichment of $z \sim 6$ SDSS Quasars. , 669(1):32–44, Nov. 2007. doi: 10.1086/521596.
- J. Kwan and J. H. Krolik. The formation of emission lines in quasars and Seyfert nuclei. , 250:478–507, Nov. 1981. doi: 10.1086/159395.
- A. M. C. Le Brun, I. G. McCarthy, J. Schaye, and T. J. Ponman. Towards a realistic population of simulated galaxy groups and clusters. , 441(2):1270–1290, June 2014. doi: 10.1093/mnras/stu608.

- A. Leccardi and S. Molendi. Radial metallicity profiles for a large sample of galaxy clusters observed with XMM-Newton. , 487(2):461–466, Aug. 2008. doi: 10.1051/0004-6361:200810113.
- K. M. Leighly, J. P. Halpern, E. B. Jenkins, and D. Casebeer. The Intrinsically X-Ray-weak Quasar PHL 1811. II. Optical and UV Spectra and Analysis. , 173(1): 1–36, Nov. 2007. doi: 10.1086/519768.
- S. H. Lim, H. J. Mo, H. Wang, and X. Yang. Detection of Missing Baryons in Galaxy Groups with Kinetic Sunyaev-Zel’dovich Effect. *ApJ*, 889(1):48, Jan. 2020. doi: 10.3847/1538-4357/ab63df.
- A. Liu, P. Tozzi, S. Ettori, S. De Grandi, F. Gastaldello, P. Rosati, and C. Norman. The chemical evolution of galaxy clusters: Dissecting the iron mass budget of the intracluster medium. , 637:A58, May 2020. doi: 10.1051/0004-6361/202037506.
- K. Lodders. Solar system abundances and condensation temperatures of the elements. *The Astrophysical Journal*, 591(2):1220–1247, jul 2003. doi: 10.1086/375492. URL <https://doi.org/10.1086%2F375492>.
- C. Loken, M. L. Norman, E. Nelson, J. Burns, G. L. Bryan, and P. Motl. A Universal Temperature Profile for Galaxy Clusters. , 579(2):571–576, Nov. 2002. doi: 10.1086/342825.
- L. Lovisari and T. H. Reiprich. The non-uniformity of galaxy cluster metallicity profiles. , 483(1):540–557, Feb. 2019. doi: 10.1093/mnras/sty3130.
- L. Lovisari, T. H. Reiprich, and G. Schellenberger. Scaling properties of a complete X-ray selected galaxy group sample. , 573:A118, Jan. 2015. doi: 10.1051/0004-6361/201423954.
- G. Macario, M. Markevitch, S. Giacintucci, G. Brunetti, T. Venturi, and S. S. Murray. A Shock Front in the Merging Galaxy Cluster A754: X-ray and Radio Observations. *ApJ*, 728(2):82, Feb. 2011. doi: 10.1088/0004-637X/728/2/82.
- P. Madau and M. Dickinson. Cosmic Star-Formation History. , 52:415–486, Aug. 2014. doi: 10.1146/annurev-astro-081811-125615.
- K. Makishima, H. Ezawa, Y. Fukuzawa, H. Honda, Y. Ikebe, T. Kamae, K. Kikuchi, K. Matsushita, K. Nakazawa, T. Ohashi, T. Takahashi, T. Tamura, and H. Xu. X-Ray Probing of the Central Regions of Clusters of Galaxies. , 53(3):401–420, June 2001. doi: 10.1093/pasj/53.3.401.
- A. B. Mantz, S. W. Allen, R. G. Morris, A. Simionescu, O. Urban, N. Werner, and I. Zhuravleva. The metallicity of the intracluster medium over cosmic time: further evidence for early enrichment. , 472(3):2877–2888, Dec. 2017. doi: 10.1093/mnras/stx2200.

- D. Maoz and O. Graur. Star Formation, Supernovae, Iron, and α : Consistent Cosmic and Galactic Histories. , 848(1):25, Oct. 2017. doi: 10.3847/1538-4357/aa8b6e.
- D. Maoz, F. Mannucci, and G. Nelemans. Observational Clues to the Progenitors of Type Ia Supernovae. , 52:107–170, Aug. 2014. doi: 10.1146/annurev-astro-082812-141031.
- F. Marinacci, M. Vogelsberger, R. Pakmor, P. Torrey, V. Springel, L. Hernquist, D. Nelson, R. Weinberger, A. Pillepich, J. Naiman, and S. Genel. First results from the IllustrisTNG simulations: radio haloes and magnetic fields. , 480(4):5113–5139, Nov. 2018. doi: 10.1093/mnras/sty2206.
- A. Marinucci, S. Bianchi, V. Braito, G. Matt, E. Nardini, and J. Reeves. Tracking the iron K α line and the ultra fast outflow in NGC 2992 at different accretion states. , 478(4):5638–5649, Aug. 2018. doi: 10.1093/mnras/sty1436.
- M. Markevitch. Chandra Observation of the Most Interesting Cluster in the Universe. In A. Wilson, editor, *The X-ray Universe 2005*, volume 604 of *ESA Special Publication*, page 723, Jan. 2006.
- M. Markevitch and A. Vikhlinin. Shocks and cold fronts in galaxy clusters. *PhR*, 443(1):1–53, May 2007. doi: 10.1016/j.physrep.2007.01.001.
- M. Markevitch, C. L. Sarazin, and A. Vikhlinin. Physics of the Merging Clusters Cygnus A, A3667, and A2065. *ApJ*, 521(2):526–530, Aug. 1999. doi: 10.1086/307598.
- M. Markevitch, T. J. Ponman, P. E. J. Nulsen, M. W. Bautz, D. J. Burke, L. P. David, D. Davis, R. H. Donnelly, W. R. Forman, C. Jones, J. Kaastra, E. Kellogg, D. W. Kim, J. Kolodziejczak, P. Mazzotta, A. Pagliaro, S. Patel, L. Van Speybroeck, A. Vikhlinin, J. Vrtilik, M. Wise, and P. Zhao. Chandra Observation of Abell 2142: Survival of Dense Subcluster Cores in a Merger. *ApJ*, 541(2):542–549, Oct. 2000. doi: 10.1086/309470.
- M. Markevitch, A. Vikhlinin, and P. Mazzotta. Nonhydrostatic Gas in the Core of the Relaxed Galaxy Cluster A1795. *ApJL*, 562(2):L153–L156, Dec. 2001. doi: 10.1086/337973.
- M. Markevitch, A. H. Gonzalez, L. David, A. Vikhlinin, S. Murray, W. Forman, C. Jones, and W. Tucker. A Textbook Example of a Bow Shock in the Merging Galaxy Cluster 1E 0657-56. *ApJL*, 567(1):L27–L31, Mar. 2002. doi: 10.1086/339619.
- M. Markevitch, F. Govoni, G. Brunetti, and D. Jerius. Bow Shock and Radio Halo in the Merging Cluster A520. *ApJ*, 627(2):733–738, July 2005. doi: 10.1086/430695.
- P. Marziani and J. W. Sulentic. Quasars and their emission lines as cosmological probes. *Advances in Space Research*, 54(7):1331–1340, Oct. 2014. doi: 10.1016/j.asr.2013.10.007.

- P. Marziani, J. W. Sulentic, T. Zwitter, D. Dultzin-Hacyan, and M. Calvani. Searching for the Physical Drivers of the Eigenvector 1 Correlation Space. , 558(2): 553–560, Sept. 2001. doi: 10.1086/322286.
- W. G. Mathews and G. J. Ferland. What Heats the Hot Phase in Active Nuclei? , 323:456, Dec. 1987. doi: 10.1086/165843.
- W. G. Mathews and F. Guo. ESTIMATE OF THE TOTAL MECHANICAL FEEDBACK ENERGY FROM GALAXY CLUSTER-CENTERED BLACK HOLES: IMPLICATIONS FOR BLACK HOLE EVOLUTION, CLUSTER GAS FRACTION, AND ENTROPY. *The Astrophysical Journal*, 738(2):155, aug 2011. doi: 10.1088/0004-637x/738/2/155. URL <https://doi.org/10.1088%2F0004-637x%2F738%2F2%2F155>.
- K. Matsushita, H. Böhringer, I. Takahashi, and Y. Ikebe. The abundance pattern of O, Mg, Si, and Fe in the intracluster medium of the Centaurus cluster observed with XMM-Newton. , 462(3):953–963, Feb. 2007. doi: 10.1051/0004-6361:20041577.
- K. Matsushita, T. Sato, E. Sakuma, and K. Sato. Distribution of Si, Fe, and Ni in the Intracluster Medium of the Coma Cluster. , 65:10, Feb. 2013. doi: 10.1093/pasj/65.1.10.
- F. Matteucci and S. Recchi. On the Typical Timescale for the Chemical Enrichment from Type Ia Supernovae in Galaxies. , 558(1):351–358, Sept. 2001. doi: 10.1086/322472.
- C. Mazzucchelli, E. Bañados, B. P. Venemans, R. Decarli, E. P. Farina, F. Walter, A. C. Eilers, H. W. Rix, R. Simcoe, D. Stern, X. Fan, E. Schlafly, G. De Rosa, J. Hennawi, K. C. Chambers, J. Greiner, W. Burgett, P. W. Draper, N. Kaiser, R. P. Kudritzki, E. Magnier, N. Metcalfe, C. Waters, and R. J. Waincoat. Physical Properties of 15 Quasars at $z \gtrsim 6.5$. , 849(2):91, Nov. 2017. doi: 10.3847/1538-4357/aa9185.
- I. G. McCarthy, J. Schaye, T. J. Ponman, R. G. Bower, C. M. Booth, C. Dalla Vecchia, R. A. Crain, V. Springel, T. Theuns, and R. P. C. Wiersma. The case for AGN feedback in galaxy groups. , 406(2):822–839, Aug. 2010. doi: 10.1111/j.1365-2966.2010.16750.x.
- M. McDonald, E. Bulbul, T. de Haan, E. D. Miller, B. A. Benson, L. E. Bleem, M. Brodwin, J. E. Carlstrom, I. Chiu, W. R. Forman, J. Hlavacek-Larrondo, G. P. Garmire, N. Gupta, J. J. Mohr, C. L. Reichardt, A. Saro, B. Stalder, A. A. Stark, and J. D. Vieira. The Evolution of the Intracluster Medium Metallicity in Sunyaev Zel’dovich-selected Galaxy Clusters at $0 < z < 1.5$. , 826(2):124, Aug. 2016. doi: 10.3847/0004-637X/826/2/124.
- D. E. McLaughlin. The Efficiency of Globular Cluster Formation. , 117(5):2398–2427, May 1999. doi: 10.1086/300836.

- F. Mernier, J. de Plaa, L. Lovisari, C. Pinto, Y. Y. Zhang, J. S. Kaastra, N. Werner, and A. Simionescu. Abundance and temperature distributions in the hot intra-cluster gas of Abell 4059. , 575:A37, Mar. 2015. doi: 10.1051/0004-6361/201425282.
- F. Mernier, J. de Plaa, C. Pinto, J. S. Kaastra, P. Kosec, Y. Y. Zhang, J. Mao, and N. Werner. Origin of central abundances in the hot intra-cluster medium. I. Individual and average abundance ratios from XMM-Newton EPIC. , 592:A157, Aug. 2016a. doi: 10.1051/0004-6361/201527824.
- F. Mernier, J. de Plaa, C. Pinto, J. S. Kaastra, P. Kosec, Y. Y. Zhang, J. Mao, N. Werner, O. R. Pols, and J. Vink. Origin of central abundances in the hot intra-cluster medium. II. Chemical enrichment and supernova yield models. , 595:A126, Nov. 2016b. doi: 10.1051/0004-6361/201628765.
- F. Mernier, J. de Plaa, J. S. Kaastra, Y. Y. Zhang, H. Akamatsu, L. Gu, P. Kosec, J. Mao, C. Pinto, T. H. Reiprich, J. S. Sanders, A. Simionescu, and N. Werner. Radial metal abundance profiles in the intra-cluster medium of cool-core galaxy clusters, groups, and ellipticals. , 603:A80, July 2017. doi: 10.1051/0004-6361/201630075.
- F. Mernier, V. Biffi, H. Yamaguchi, P. Medvedev, A. Simionescu, S. Ettori, N. Werner, J. S. Kaastra, J. de Plaa, and L. Gu. Enrichment of the Hot Intracluster Medium: Observations. , 214(8):129, Dec. 2018a. doi: 10.1007/s11214-018-0565-7.
- F. Mernier, J. de Plaa, N. Werner, J. S. Kaastra, A. J. J. Raassen, L. Gu, J. Mao, I. Urdampilleta, N. Truong, and A. Simionescu. Mass-invariance of the iron enrichment in the hot haloes of massive ellipticals, groups, and clusters of galaxies. , 478(1):L116–L121, July 2018b. doi: 10.1093/mnrasl/sly080.
- F. Mernier, N. Werner, Y. Su, C. Pinto, R. Grossová, A. Simionescu, E. Iodice, M. Sarzi, and A. Görgei. The cycle of metals in the infalling elliptical galaxy NGC 1404. *arXiv e-prints*, art. arXiv:2201.05161, Jan. 2022.
- C. A. Metzler and A. E. Evrard. A Simulation of the Intracluster Medium with Feedback from Cluster Galaxies. , 437:564, Dec. 1994. doi: 10.1086/175022.
- E. D. Miller, M. Bautz, J. George, R. Mushotzky, D. Davis, and J. P. Henry. The outer limits of galaxy clusters: Observations to the virial radius with Suzaku, XMM, and Chandra. In R. Petre, K. Mitsuda, and L. Angelini, editors, *American Institute of Physics Conference Series*, volume 1427 of *American Institute of Physics Conference Series*, pages 13–20, Mar. 2012. doi: 10.1063/1.3696144.
- E. T. Million, N. Werner, A. Simionescu, and S. W. Allen. Core-collapse supernova enrichment in the core of the Virgo cluster. , 418(4):2744–2753, Dec. 2011. doi: 10.1111/j.1365-2966.2011.19664.x.
- M. S. Mirakhor and S. A. Walker. A complete view of the outskirts of the Coma cluster. , 497(3):3204–3220, July 2020a. doi: 10.1093/mnras/staa2203.

- M. S. Mirakhor and S. A. Walker. A high coverage view of the thermodynamics and metal abundance in the outskirts of the nearby galaxy cluster Abell 2199. , 497(3): 3943–3952, July 2020b. doi: 10.1093/mnras/staa2204.
- K. Mitsuda, M. Bautz, H. Inoue, R. L. Kelley, K. Koyama, H. Kunieda, K. Makishima, Y. Ogawara, R. Petre, T. Takahashi, H. Tsunemi, N. E. White, N. Anabuki, L. Angelini, K. Arnaud, H. Awaki, A. Bamba, K. Boyce, G. V. Brown, K.-W. Chan, J. Cottam, T. Dotani, J. Doty, K. Ebisawa, Y. Ezoe, A. C. Fabian, E. Figueroa, R. Fujimoto, Y. Fukazawa, T. Furusho, A. Furuzawa, K. Gendreau, R. E. Griffiths, Y. Haba, K. Hamaguchi, I. Harrus, G. Hasinger, I. Hatsukade, K. Hayashida, P. J. Henry, J. S. Hiraga, S. S. Holt, A. Hornschemeier, J. P. Hughes, U. Hwang, M. Ishida, Y. Ishisaki, N. Isobe, M. Itoh, N. Iyomoto, S. M. Kahn, T. Kamae, H. Katagiri, J. Kataoka, H. Katayama, N. Kawai, C. Kilbourne, K. Kinugasa, S. Kissel, S. Kitamoto, M. Kohama, T. Kohmura, M. Kokubun, T. Kotani, J. Kotoku, A. Kubota, G. M. Madejski, Y. Maeda, F. Makino, A. Markowitz, C. Matsumoto, H. Matsumoto, M. Matsuoka, K. Matsushita, D. McCammon, T. Mihara, K. Misaki, E. Miyata, T. Mizuno, K. Mori, H. Mori, M. Morii, H. Moseley, K. Mukai, H. Murakami, T. Murakami, R. Mushotzky, F. Nagase, M. Namiki, H. Negoro, K. Nakazawa, J. A. Nousek, T. Okajima, y. ogasaka, T. Ohashi, T. Oshima, N. Ota, M. Ozaki, H. Ozawa, A. N. Parmar, W. D. Pence, F. S. Porter, J. N. Reeves, G. R. Ricker, I. Sakurai, W. T. Sanders, A. Senda, P. Serlemitsos, R. Shibata, Y. Soong, R. Smith, M. Suzuki, A. E. Szymkowiak, H. Takahashi, T. Tamagawa, K. Tamura, T. Tamura, Y. Tanaka, M. Tashiro, Y. Tawara, Y. Terada, Y. Terashima, H. Tomida, K. Torii, Y. Tsuboi, M. Tsumimoto, T. G. Tsuru, M. J. L. Turner, Y. Ueda, S. Ueno, M. Ueno, S. Uno, Y. Urata, S. Watanabe, N. Yamamoto, K. Yamaoka, N. Y. Yamasaki, K. Yamashita, M. Yamauchi, S. Yamauchi, T. Yaqoob, D. Yonetoku, and A. Yoshida. The X-Ray Observatory Suzaku. *Publications of the Astronomical Society of Japan*, 59(sp1):S1–S7, 01 2007. ISSN 0004-6264. doi: 10.1093/pasj/59.sp1.S1. URL <https://doi.org/10.1093/pasj/59.sp1.S1>.
- S. M. Molnar. Cluster physics with merging galaxy clusters. *Frontiers in Astronomy and Space Sciences*, 2, 2016. ISSN 2296-987X. doi: 10.3389/fspas.2015.00007. URL <https://www.frontiersin.org/articles/10.3389/fspas.2015.00007>.
- A. Moretti, S. Campana, D. Lazzati, and G. Tagliaferri. The Resolved Fraction of the Cosmic X-Ray Background. , 588(2):696–703, May 2003. doi: 10.1086/374335.
- A. Moretti, C. Pagani, G. Cusumano, S. Campana, M. Perri, A. Abbey, M. Ajello, A. P. Beardmore, D. Burrows, G. Chincarini, O. Godet, C. Guidorzi, J. E. Hill, J. Kennea, J. Nousek, J. P. Osborne, and G. Tagliaferri. A new measurement of the cosmic X-ray background. , 493(2):501–509, Jan. 2009. doi: 10.1051/0004-6361:200811197.
- C. E. Murray, S. Stanimirović, W. M. Goss, C. Heiles, J. M. Dickey, B. Babler, and C.-G. Kim. The 21-SPONGE H I Absorption Line Survey. I. The Temperature of Galactic H I. , 238(2):14, Oct. 2018. doi: 10.3847/1538-4365/aad81a.

- D. Nagai and E. T. Lau. GAS CLUMPING IN THE OUTSKIRTS OF Λ CDM CLUSTERS. *The Astrophysical Journal*, 731(1):L10, mar 2011. doi: 10.1088/2041-8205/731/1/L10. URL <https://doi.org/10.1088/2041-8205/731/1/L10>.
- J. P. Naiman, A. Pillepich, V. Springel, E. Ramirez-Ruiz, P. Torrey, M. Vogelsberger, R. Pakmor, D. Nelson, F. Marinacci, L. Hernquist, R. Weinberger, and S. Genel. First results from the IllustrisTNG simulations: a tale of two elements - chemical evolution of magnesium and europium. *MNRAS*, 477(1):1206–1224, June 2018. doi: 10.1093/mnras/sty618.
- J. F. Navarro, C. S. Frenk, and S. D. M. White. A Universal Density Profile from Hierarchical Clustering. *MNRAS*, 490(2):493–508, Dec. 1997. doi: 10.1086/304888.
- D. Nelson, A. Pillepich, V. Springel, R. Weinberger, L. Hernquist, R. Pakmor, S. Genel, P. Torrey, M. Vogelsberger, G. Kauffmann, F. Marinacci, and J. Naiman. First results from the IllustrisTNG simulations: the galaxy colour bimodality. *MNRAS*, 475(1):624–647, Mar. 2018. doi: 10.1093/mnras/stx3040.
- H. Netzer. Testing broad-line region models with reverberation mapping. *MNRAS*, 494(2):1611–1621, Mar. 2020. doi: 10.1093/mnras/staa767.
- H. Netzer and B. J. Wills. Broad emission features in QSOs and active galactic nuclei. I. New calculations of Fe II line strengths. *MNRAS*, 275:445–460, Dec. 1983. doi: 10.1086/161545.
- K. Nomoto, N. Tominaga, H. Umeda, C. Kobayashi, and K. Maeda. Nucleosynthesis yields of core-collapse supernovae and hypernovae, and galactic chemical evolution. *Publications of the Astronomical Society of Japan*, 777:424–458, Oct. 2006. doi: 10.1016/j.nuclphysa.2006.05.008.
- K. Nomoto, C. Kobayashi, and N. Tominaga. Nucleosynthesis in Stars and the Chemical Enrichment of Galaxies. *Publications of the Astronomical Society of Japan*, 51(1):457–509, Aug. 2013. doi: 10.1146/annurev-astro-082812-140956.
- P. E. J. Nulsen and H. Böhringer. A ROSAT determination of the mass of the central Virgo Cluster. *Monthly Notices of the Royal Astronomical Society*, 274(4):1093–1106, 06 1995. ISSN 0035-8711. doi: 10.1093/mnras/274.4.1093. URL <https://doi.org/10.1093/mnras/274.4.1093>.
- P. E. J. Nulsen, Z. Li, W. R. Forman, R. P. Kraft, D. V. Lal, C. Jones, I. Zhuravleva, E. Churazov, J. S. Sanders, A. C. Fabian, R. E. Johnson, and S. S. Murray. Deep Chandra Observations of A2199: The Interplay between Merger-induced Gas Motions and Nuclear Outbursts in a Cool Core Cluster. *MNRAS*, 775(2):117, Oct. 2013. doi: 10.1088/0004-637X/775/2/117.
- A. A. O’Donoghue, J. A. Eilek, and F. N. Owen. Flow Dynamics and Bending of Wide-Angle Tailed Radio Sources. *ApJ*, 408:428, May 1993. doi: 10.1086/172600.

- D. E. Osterbrock. Spectrophotometry of Seyfert 1 galaxies. , 215:733–745, Aug. 1977. doi: 10.1086/155407.
- E. O’Sullivan, J. M. Vrtilik, A. M. Read, L. P. David, and T. J. Ponman. An XMM-Newton observation of the galaxy group MKW 4. , 346(2):525–539, Dec. 2003. doi: 10.1046/j.1365-2966.2003.07108.x.
- M. S. Owers, S. W. Randall, P. E. J. Nulsen, W. J. Couch, L. P. David, and J. C. Kempner. The Dissection of Abell 2744: A Rich Cluster Growing Through Major and Minor Mergers. *ApJ*, 728(1):27, Feb. 2011. doi: 10.1088/0004-637X/728/1/27.
- M. S. Owers, P. E. J. Nulsen, W. J. Couch, C.-J. Ma, L. P. David, W. R. Forman, A. M. Hopkins, C. Jones, and R. J. van Weeren. A Merger Shock in A2034. *ApJ*, 780(2):163, Jan. 2014. doi: 10.1088/0004-637X/780/2/163.
- S. Panda, B. Czerny, T. P. Adhikari, K. Hryniewicz, C. Wildy, J. Kuraszewicz, and M. Śniegowska. Modeling of the Quasar Main Sequence in the Optical Plane. , 866(2):115, Oct. 2018. doi: 10.3847/1538-4357/aae209.
- S. Panda, P. Marziani, and B. Czerny. The Quasar Main Sequence Explained by the Combination of Eddington Ratio, Metallicity, and Orientation. , 882(2):79, Sept. 2019. doi: 10.3847/1538-4357/ab3292.
- R. Paterno-Mahler, E. L. Blanton, S. W. Randall, and T. E. Clarke. Deep Chandra Observations of the Extended Gas Sloshing Spiral in A2029. *ApJ*, 773(2):114, Aug. 2013. doi: 10.1088/0004-637X/773/2/114.
- R. Paterno-Mahler, S. W. Randall, E. Bulbul, F. Andrade-Santos, E. L. Blanton, C. Jones, S. Murray, and R. E. Johnson. Merger Signatures in the Galaxy Cluster A98. *ApJ*, 791(2):104, Aug. 2014. doi: 10.1088/0004-637X/791/2/104.
- S. Paul, R. S. John, P. Gupta, and H. Kumar. Understanding ‘galaxy groups’ as a unique structure in the universe. , 471(1):2–11, Oct. 2017. doi: 10.1093/mnras/stx1488.
- B. M. Peterson. Reverberation Mapping of Active Galactic Nuclei. , 105:247, Mar. 1993. doi: 10.1086/133140.
- M. M. Phillips. Permitted fe II Emission in Seyfert 1 Galaxies and QSOs I. Observations. , 38:187, Nov. 1978. doi: 10.1086/190553.
- A. Pillepich, D. Nelson, L. Hernquist, V. Springel, R. Pakmor, P. Torrey, R. Weinberger, S. Genel, J. P. Naiman, F. Marinacci, and M. Vogelsberger. First results from the IllustrisTNG simulations: the stellar mass content of groups and clusters of galaxies. , 475(1):648–675, Mar. 2018. doi: 10.1093/mnras/stx3112.
- Planck Collaboration, P. A. R. Ade, N. Aghanim, C. Armitage-Caplan, M. Arnaud, M. Ashdown, F. Atrio-Barandela, J. Aumont, C. Baccigalupi, A. J. Banday, and et al. Planck 2013 results. XVI. Cosmological parameters. , 571:A16, Nov. 2014. doi: 10.1051/0004-6361/201321591.

- S. Planelles, S. Borgani, D. Fabjan, M. Killedar, G. Murante, G. L. Granato, C. Ragone-Figueroa, and K. Dolag. On the role of AGN feedback on the thermal and chemodynamical properties of the hot intracluster medium. , 438(1):195–216, Feb. 2014. doi: 10.1093/mnras/stt2141.
- G. W. Pratt, M. Arnaud, R. Piffaretti, H. Böhringer, T. J. Ponman, J. H. Croston, G. M. Voit, S. Borgani, and R. G. Bower. Gas entropy in a representative sample of nearby X-ray galaxy clusters (REXCESS): relationship to gas mass fraction. , 511:A85, Feb. 2010. doi: 10.1051/0004-6361/200913309.
- S. Randall, P. Nulsen, W. R. Forman, C. Jones, M. Machacek, S. S. Murray, and B. Maughan. Chandra’s View of the Ram Pressure Stripped Galaxy M86. *ApJ*, 688(1):208–223, Nov. 2008. doi: 10.1086/592324.
- S. W. Randall, C. Jones, R. Kraft, W. R. Forman, and E. O’Sullivan. Merging Cold Fronts in the Galaxy Pair NGC 7619 and NGC 7626. *ApJ*, 696(2):1431–1440, May 2009. doi: 10.1088/0004-637X/696/2/1431.
- J. Rasmussen and T. J. Ponman. Temperature and abundance profiles of hot gas in galaxy groups - I. Results and statistical analysis. , 380(4):1554–1572, Oct. 2007. doi: 10.1111/j.1365-2966.2007.12191.x.
- J. Rasmussen and T. J. Ponman. Temperature and abundance profiles of hot gas in galaxy groups - II. Implications for feedback and ICM enrichment. , 399(1): 239–263, Oct. 2009. doi: 10.1111/j.1365-2966.2009.15244.x.
- T. H. Reiprich, A. Veronica, F. Pacaud, M. E. Ramos-Ceja, N. Ota, J. Sanders, M. Kara, T. Erben, M. Klein, J. Erler, J. Kerp, D. N. Hoang, M. Brüggen, J. Marvil, L. Rudnick, V. Biffi, K. Dolag, J. Aschersleben, K. Basu, H. Brunner, E. Bulbul, K. Dennerl, D. Eckert, M. Freyberg, E. Gatuzz, V. Ghirardini, F. Käfer, A. Merloni, K. Migkas, K. Nandra, P. Predehl, J. Robrade, M. Salvato, B. Whelan, A. Diaz-Ocampo, D. Hernandez-Lang, A. Zenteno, M. J. I. Brown, J. D. Collier, J. M. Diego, A. M. Hopkins, A. Kapinska, B. Koribalski, T. Mroczkowski, R. P. Norris, A. O’Brien, and E. Vardoulaki. The Abell 3391/95 galaxy cluster system. A 15 Mpc intergalactic medium emission filament, a warm gas bridge, infalling matter clumps, and (re-) accelerated plasma discovered by combining SRG/eROSITA data with ASKAP/EMU and DECAM data. *AAP*, 647:A2, Mar. 2021. doi: 10.1051/0004-6361/202039590.
- A. Renzini and S. Andreon. Chemical evolution on the scale of clusters of galaxies: a conundrum? , 444(4):3581–3591, Nov. 2014. doi: 10.1093/mnras/stu1689.
- E. Roediger, M. Brüggen, A. Simionescu, H. Böhringer, E. Churazov, and W. R. Forman. Gas sloshing, cold front formation and metal redistribution: the Virgo cluster as a quantitative test case. , 413(3):2057–2077, May 2011. doi: 10.1111/j.1365-2966.2011.18279.x.

- E. Roediger, L. Lovisari, R. Dupke, S. Ghizzardi, M. Brüggen, R. P. Kraft, and M. E. Machacek. Gas sloshing, cold fronts, Kelvin-Helmholtz instabilities and the merger history of the cluster of galaxies Abell 496. *MNRAS*, 420(4):3632–3648, Mar. 2012. doi: 10.1111/j.1365-2966.2011.20287.x.
- M. Rossetti, D. Eckert, S. De Grandi, F. Gastaldello, S. Ghizzardi, E. Roediger, and S. Molendi. Abell 2142 at large scales: An extreme case for sloshing? , 556:A44, Aug. 2013. doi: 10.1051/0004-6361/201321319.
- A. J. Ruff, D. J. E. Floyd, K. T. Korista, R. L. Webster, R. L. Porter, and G. J. Ferland. Near infrared hydrogen emission line ratios as diagnostics of the broad emission line region. In *Journal of Physics Conference Series*, volume 372 of *Journal of Physics Conference Series*, page 012069, July 2012. doi: 10.1088/1742-6596/372/1/012069.
- H. R. Russell, J. S. Sanders, A. C. Fabian, S. A. Baum, M. Donahue, A. C. Edge, B. R. McNamara, and C. P. O’Dea. Chandra observation of two shock fronts in the merging galaxy cluster Abell 2146. *MNRAS*, 406(3):1721–1733, Aug. 2010. doi: 10.1111/j.1365-2966.2010.16822.x.
- H. R. Russell, B. R. McNamara, J. S. Sanders, A. C. Fabian, P. E. J. Nulsen, R. E. A. Canning, S. A. Baum, M. Donahue, A. C. Edge, L. J. King, and C. P. O’Dea. Shock fronts, electron-ion equilibration and intracluster medium transport processes in the merging cluster Abell 2146. *MNRAS*, 423(1):236–255, June 2012. doi: 10.1111/j.1365-2966.2012.20808.x.
- H. R. Russell, P. E. J. Nulsen, D. Caprioli, U. Chadayammuri, A. C. Fabian, M. W. Kunz, B. R. McNamara, J. S. Sanders, A. Richard-Laferrrière, M. Beleznyay, R. E. A. Canning, J. Hlavacek-Larrondo, and L. J. King. The structure of cluster merger shocks: turbulent width and the electron heating time-scale. , 514(1):1477–1493, July 2022. doi: 10.1093/mnras/stac1055.
- E. E. Salpeter. The Luminosity Function and Stellar Evolution. , 121:161, Jan. 1955. doi: 10.1086/145971.
- C. L. Sarazin. *X-ray emission from clusters of galaxies*. 1988.
- A. Sarkar and S. Samui. On the Star Formation Efficiency in High-redshift Ly α Emitters. , 131(1001):074101, July 2019. doi: 10.1088/1538-3873/ab10ea.
- A. Sarkar, G. J. Ferland, M. Chatzikos, F. Guzmán, P. A. M. van Hoof, R. T. Smyth, C. A. Ramsbottom, F. P. Keenan, and C. P. Ballance. Improved Fe II Emission-line Models for AGNs Using New Atomic Data Sets. , 907(1):12, Jan. 2021a. doi: 10.3847/1538-4357/abcaa6.
- A. Sarkar, Y. Su, S. Randall, F. Gastaldello, I. Trierweiler, R. White, R. Kraft, and E. Miller. Joint Suzaku and Chandra observations of the MKW4 galaxy group out to the virial radius. , 501(3):3767–3780, Mar. 2021b. doi: 10.1093/mnras/staa3858.

- A. Sarkar, S. W. Randall, Y. Su, G. E. Alvarez, C. L. Sarazin, P. Nulsen, E. Blanton, W. Forman, C. Jones, E. Bulbul, J. Zuhone, F. Andrade-Santos, R. E. Johnson, and P. Chakraborty. Discovery of a pre-merger shock in an intercluster filament in Abell 98. *Submitted to ApJL*, 000:0–0, May 2022. doi: 00/00.
- T. Sasaki, K. Matsushita, and K. Sato. Metal Distributions out to $0.5 r_{180}$ in the Intracluster Medium of Four Galaxy Groups Observed with Suzaku. , 781(1):36, Jan. 2014. doi: 10.1088/0004-637X/781/1/36.
- K. Sato, K. Matsushita, and F. Gastaldello. Temperature and Metallicity in the Intra-Cluster Medium of Abell 262 Observed with Suzaku. , 61:S365, Jan. 2009. doi: 10.1093/pasj/61.sp1.S365.
- K. Sato, K. Matsushita, N. Y. Yamasaki, S. Sasaki, and T. Ohashi. Temperature and entropy profiles to the virial radius of the Abell 1246 cluster observed with Suzaku. *Publications of the Astronomical Society of Japan*, 66(5), 09 2014. ISSN 0004-6264. doi: 10.1093/pasj/psu061. URL <https://doi.org/10.1093/pasj/psu061>. 85.
- J.-T. Schindler, E. P. Farina, E. Banados, A.-C. Eilers, J. F. Hennawi, M. Onoue, B. P. Venemans, F. Walter, F. Wang, F. B. Davies, R. Decarli, G. De Rosa, A. Drake, X. Fan, C. Mazzucchelli, H.-W. Rix, G. Worseck, and J. Yang. The X-SHOOTER/ALMA sample of Quasars in the Epoch of Reionization. I. NIR spectral modeling, iron enrichment and broad emission line properties. *arXiv e-prints*, art. arXiv:2010.06902, Oct. 2020.
- Y. Shen and L. C. Ho. The diversity of quasars unified by accretion and orientation. , 513(7517):210–213, Sept. 2014. doi: 10.1038/nature13712.
- J. Shin, T. Nagao, J.-H. Woo, and H. A. N. Le. The Fe II/Mg II Flux Ratio of Low-luminosity Quasars at $z \sim 3$. , 874(1):22, Mar. 2019. doi: 10.3847/1538-4357/ab05da.
- A. Simionescu, N. Werner, H. Böhringer, J. S. Kaastra, A. Finoguenov, M. Brüggen, and P. E. J. Nulsen. Chemical enrichment in the cluster of galaxies Hydra A. , 493(2):409–424, Jan. 2009. doi: 10.1051/0004-6361:200810225.
- A. Simionescu, S. W. Allen, A. Mantz, N. Werner, Y. Takei, R. G. Morris, A. C. Fabian, J. S. Sanders, P. E. J. Nulsen, M. R. George, and G. B. Taylor. Baryons at the edge of the x-ray–brightest galaxy cluster. *Science*, 331(6024):1576–1579, 2011. ISSN 0036-8075. doi: 10.1126/science.1200331. URL <https://science.sciencemag.org/content/331/6024/1576>.
- A. Simionescu, N. Werner, O. Urban, S. W. Allen, A. C. Fabian, A. Mantz, K. Matsushita, P. E. J. Nulsen, J. S. Sanders, T. Sasaki, T. Sato, Y. Takei, and S. A. Walker. Thermodynamics of the Coma Cluster Outskirts. , 775(1):4, Sept. 2013. doi: 10.1088/0004-637X/775/1/4.
- A. Simionescu, N. Werner, O. Urban, S. W. Allen, Y. Ichinohe, and I. Zhuravleva. A Uniform Contribution of Core-collapse and Type Ia Supernovae to the Chemical

- Enrichment Pattern in the Outskirts of the Virgo Cluster. , 811(2):L25, Oct. 2015. doi: 10.1088/2041-8205/811/2/L25.
- A. Simionescu, N. Werner, A. Mantz, S. W. Allen, and O. Urban. Witnessing the growth of the nearest galaxy cluster: thermodynamics of the Virgo Cluster outskirts. , 469(2):1476–1495, Aug. 2017. doi: 10.1093/mnras/stx919.
- A. Simionescu, S. Nakashima, H. Yamaguchi, K. Matsushita, F. Mernier, N. Werner, T. Tamura, K. Nomoto, J. de Plaa, S. C. Leung, A. Bamba, E. Bulbul, M. E. Eckart, Y. Ezoe, A. C. Fabian, Y. Fukazawa, L. Gu, Y. Ichinohe, M. N. Ishigaki, J. S. Kaastra, C. Kilbourne, T. Kitayama, M. Leutenegger, M. Loewenstein, Y. Maeda, E. D. Miller, R. F. Mushotzky, H. Noda, C. Pinto, F. S. Porter, S. Safi-Harb, K. Sato, T. Takahashi, S. Ueda, and S. Zha. Constraints on the chemical enrichment history of the Perseus Cluster of galaxies from high-resolution X-ray spectroscopy. , 483(2):1701–1721, Feb. 2019. doi: 10.1093/mnras/sty3220.
- B. D. Smith, E. J. Hallman, J. M. Shull, and B. W. O’Shea. The Nature of the Warm/Hot Intergalactic Medium. I. Numerical Methods, Convergence, and O VI Absorption. *ApJ*, 731(1):6, Apr. 2011. doi: 10.1088/0004-637X/731/1/6.
- R. K. Smith, N. S. Brickhouse, D. A. Liedahl, and J. C. Raymond. Collisional Plasma Models with APEC/APED: Emission-Line Diagnostics of Hydrogen-like and Helium-like Ions. *ApJL*, 556(2):L91–L95, Aug. 2001. doi: 10.1086/322992.
- R. T. Smyth, C. A. Ramsbottom, F. P. Keenan, G. J. Ferland , and C. P. Ballance. Towards converged electron-impact excitation calculations of low-lying transitions in Fe II. , 483(1):654–663, Feb. 2019. doi: 10.1093/mnras/sty3198.
- L. Spitzer. *Physics of Fully Ionized Gases*. 1962.
- V. Springel and L. Hernquist. The history of star formation in a Λ cold dark matter universe. *Monthly Notices of the Royal Astronomical Society*, 339(2):312–334, 02 2003. ISSN 0035-8711. doi: 10.1046/j.1365-8711.2003.06207.x. URL <https://doi.org/10.1046/j.1365-8711.2003.06207.x>.
- V. Springel, R. Pakmor, A. Pillepich, R. Weinberger, D. Nelson, L. Hernquist, M. Vogelsberger, S. Genel, P. Torrey, F. Marinacci, and J. Naiman. First results from the IllustrisTNG simulations: matter and galaxy clustering. , 475(1):676–698, Mar. 2018. doi: 10.1093/mnras/stx3304.
- Y. Su, I. White, Raymond E., and E. D. Miller. Suzaku Observations of the X-Ray Brightest Fossil Group ESO 3060170. , 775(2):89, Oct. 2013. doi: 10.1088/0004-637X/775/2/89.
- Y. Su, D. Buote, F. Gastaldello, and F. Brighenti. The Entire Virial Radius of the Fossil Cluster RX J1159+5531: I. Gas Properties. , 805(2):104, June 2015. doi: 10.1088/0004-637X/805/2/104.

- Y. Su, P. E. J. Nulsen, R. P. Kraft, E. Roediger, J. A. ZuHone, C. Jones, W. R. Forman, A. Sheardown, J. A. Irwin, and S. W. Randall. Gas Sloshing Regulates and Records the Evolution of the Fornax Cluster. , 851(1):69, Dec. 2017. doi: 10.3847/1538-4357/aa989e.
- T. Sukhbold, T. Ertl, S. E. Woosley, J. M. Brown, and H. T. Janka. Core-collapse Supernovae from 9 to 120 Solar Masses Based on Neutrino-powered Explosions. , 821(1):38, Apr. 2016. doi: 10.3847/0004-637X/821/1/38.
- J. W. Sulentic, T. Zwitter, P. Marziani, and D. Dultzin-Hacyan. Eigenvector 1: An Optimal Correlation Space for Active Galactic Nuclei. , 536(1):L5–L9, June 2000. doi: 10.1086/312717.
- M. Sun, G. M. Voit, M. Donahue, C. Jones, W. Forman, and A. Vikhlinin. CHANDRA STUDIES OF THE x-RAY GAS PROPERTIES OF GALAXY GROUPS. *The Astrophysical Journal*, 693(2):1142–1172, mar 2009. doi: 10.1088/0004-637x/693/2/1142. URL <https://doi.org/10.1088/0004-637x/693/2/1142>.
- M. Sun, N. Sehgal, G. M. Voit, M. Donahue, C. Jones, W. Forman, A. Vikhlinin, and C. Sarazin. The Pressure Profiles of Hot Gas in Local Galaxy Groups. , 727(2):L49, Feb. 2011. doi: 10.1088/2041-8205/727/2/L49.
- S. S. Tayal and O. Zatsarinny. Electron-impact excitation of forbidden and allowed transitions in Fe ii. , 98(1):012706, July 2018. doi: 10.1103/PhysRevA.98.012706.
- M. J. Temple, G. J. Ferland, A. L. Rankine, P. C. Hewett, N. R. Badnell, C. P. Ballance, G. Del Zanna, and R. P. Dufresne. Fe III emission in quasars: evidence for a dense turbulent medium. , 496(3):2565–2576, June 2020. doi: 10.1093/mnras/staa1717.
- S. Thölken, L. Lovisari, T. H. Reiprich, and J. Hasenbusch. X-ray analysis of the galaxy group UGC 03957 beyond R_{200} with Suzaku. , 592:A37, July 2016. doi: 10.1051/0004-6361/201527608.
- N. Truong, E. Rasia, V. Biffi, F. Mernier, N. Werner, M. Gaspari, S. Borgani, S. Planelles, D. Fabjan, and G. Murante. Mass-metallicity relation from cosmological hydrodynamical simulations and X-ray observations of galaxy groups and clusters. , 484(2):2896–2913, Apr. 2019. doi: 10.1093/mnras/stz161.
- T. Tsujimoto, K. Nomoto, Y. Yoshii, M. Hashimoto, S. Yanagida, and F. K. Thielemann. Relative frequencies of Type Ia and Type II supernovae in the chemical evolution of the Galaxy, LMC and SMC. , 277(3):945–958, Dec. 1995. doi: 10.1093/mnras/277.3.945.
- O. Urban, A. Simionescu, N. Werner, S. W. Allen, S. Ehlert, I. Zhuravleva, R. G. Morris, A. C. Fabian, A. Mantz, P. E. J. Nulsen, J. S. Sanders, and Y. Takei. Azimuthally resolved X-ray spectroscopy to the edge of the Perseus Cluster. , 437(4):3939–3961, Feb. 2014. doi: 10.1093/mnras/stt2209.

- O. Urban, A. Simionescu, N. Werner, S. W. Allen, S. Ehlert, I. Zhuravleva, R. G. Morris, A. C. Fabian, A. Mantz, P. E. J. Nulsen, J. Sanders, and Y. Takei. Azimuthally resolved X-ray spectroscopy to the edge of the Perseus Cluster. *Monthly Notices of the Royal Astronomical Society*, 437(4):3939–3961, 12 2014. ISSN 0035-8711. doi: 10.1093/mnras/stt2209. URL <https://doi.org/10.1093/mnras/stt2209>.
- O. Urban, N. Werner, S. W. Allen, A. Simionescu, and A. Mantz. A uniform metallicity in the outskirts of massive, nearby galaxy clusters. , 470(4):4583–4599, Oct. 2017. doi: 10.1093/mnras/stx1542.
- F. Vazza, M. Roncarelli, S. Ettori, and K. Dolag. The scatter in the radial profiles of X-ray luminous galaxy clusters as diagnostic of the thermodynamical state of the ICM. *Monthly Notices of the Royal Astronomical Society*, 413(4):2305–2313, 05 2011. ISSN 0035-8711. doi: 10.1111/j.1365-2966.2010.18120.x. URL <https://doi.org/10.1111/j.1365-2966.2010.18120.x>.
- E. Verner, F. Bruhweiler, D. Verner, S. Johansson, and T. Gull. Revisited Abundance Diagnostics in Quasars: Fe II/Mg II Ratios. , 592(2):L59–L62, Aug. 2003. doi: 10.1086/377571.
- E. M. Verner, D. A. Verner, K. T. Korista, J. W. Ferguson, F. Hamann, and G. J. Ferland. Numerical Simulations of Fe II Emission Spectra. , 120(1):101–112, Jan. 1999. doi: 10.1086/313171.
- M. P. Véron-Cetty, M. Joly, and P. Véron. The unusual emission line spectrum of I Zw 1. , 417:515–525, Apr. 2004. doi: 10.1051/0004-6361:20035714.
- M. Vestergaard and B. J. Wilkes. An Empirical Ultraviolet Template for Iron Emission in Quasars as Derived from I Zwicky 1. , 134(1):1–33, May 2001. doi: 10.1086/320357.
- A. Vikhlinin, M. Markevitch, and S. S. Murray. A Moving Cold Front in the Intergalactic Medium of A3667. , 551(1):160–171, Apr. 2001. doi: 10.1086/320078.
- A. Vikhlinin, A. Kravtsov, W. Forman, C. Jones, M. Markevitch, S. S. Murray, and L. V. Speybroeck. ChandraSample of nearby relaxed galaxy clusters: Mass, gas fraction, and mass-temperature relation. *The Astrophysical Journal*, 640(2):691–709, apr 2006. doi: 10.1086/500288. URL <https://doi.org/10.1086%2F500288>.
- G. M. Voit, S. T. Kay, and G. L. Bryan. The baseline intracluster entropy profile from gravitational structure formation. , 364(3):909–916, Dec. 2005. doi: 10.1111/j.1365-2966.2005.09621.x.
- S. Walker, A. Simionescu, D. Nagai, N. Okabe, D. Eckert, T. Mroczkowski, H. Akamatsu, S. Ettori, and V. Ghirardini. The Physics of Galaxy Cluster Outskirts. , 215(1):7, Jan. 2019. doi: 10.1007/s11214-018-0572-8.

- S. A. Walker, A. C. Fabian, J. S. Sanders, and M. R. George. Further X-ray observations of the galaxy cluster PKS 0745–191 to the virial radius and beyond. *Monthly Notices of the Royal Astronomical Society*, 424(3):1826–1840, 08 2012. ISSN 0035-8711. doi: 10.1111/j.1365-2966.2012.21282.x. URL <https://doi.org/10.1111/j.1365-2966.2012.21282.x>.
- S. A. Walker, A. C. Fabian, J. S. Sanders, and M. R. George. Further X-ray observations of the galaxy cluster PKS 0745-191 to the virial radius and beyond. , 424 (3):1826–1840, Aug. 2012. doi: 10.1111/j.1365-2966.2012.21282.x.
- S. A. Walker, A. C. Fabian, J. S. Sanders, A. Simionescu, and Y. Tawara. X-ray exploration of the outskirts of the nearby Centaurus cluster using Suzaku and Chandra. , 432(1):554–569, June 2013. doi: 10.1093/mnras/stt497.
- S. A. Walker, J. S. Sanders, and A. C. Fabian. Applications for edge detection techniques using Chandra and XMM-Newton data: galaxy clusters and beyond. *MNRAS*, 461(1):684–697, Sept. 2016. doi: 10.1093/mnras/stw1367.
- S. A. Walker, J. Hlavacek-Larrondo, M. Gendron-Marsolais, A. C. Fabian, H. Intema, J. S. Sanders, J. T. Bamford, and R. van Weeren. Is there a giant Kelvin-Helmholtz instability in the sloshing cold front of the Perseus cluster? , 468(2):2506–2516, June 2017. doi: 10.1093/mnras/stx640.
- S. A. Walker, M. S. Mirakhor, J. ZuHone, J. S. Sanders, A. C. Fabian, and P. Diwanji. Is there an enormous cold front at the virial radius of the Perseus cluster? *arXiv e-prints*, art. arXiv:2006.14043, June 2020.
- T. Wang, G. J. Ferland, C. Yang, H. Wang, and S. Zhang. Evidence for Fluorescent Fe II Emission from Extended Low Ionization Outflows in Obscured Quasars. , 824 (2):106, June 2016. doi: 10.3847/0004-637X/824/2/106.
- N. Werner, J. de Plaa, J. S. Kaastra, J. Vink, J. A. M. Bleeker, T. Tamura, J. R. Peterson, and F. Verbunt. XMM-Newton spectroscopy of the cluster of galaxies 2A 0335+096. , 449(2):475–491, Apr. 2006. doi: 10.1051/0004-6361:20053868.
- N. Werner, A. Finoguenov, J. S. Kaastra, A. Simionescu, J. P. Dietrich, J. Vink, and H. Böhringer. Detection of hot gas in the filament connecting the clusters of galaxies Abell 222 and Abell 223. *AAP*, 482(3):L29–L33, May 2008. doi: 10.1051/0004-6361:200809599.
- N. Werner, O. Urban, A. Simionescu, and S. W. Allen. A uniform metal distribution in the intergalactic medium of the Perseus cluster of galaxies. , 502(7473):656–658, Oct. 2013. doi: 10.1038/nature12646.
- R. P. C. Wiersma, J. Schaye, T. Theuns, C. Dalla Vecchia, and L. Tornatore. Chemical enrichment in cosmological, smoothed particle hydrodynamics simulations. , 399 (2):574–600, Oct. 2009. doi: 10.1111/j.1365-2966.2009.15331.x.

- B. J. Wills, H. Netzer, and D. Wills. Broad emission features in QSOs and active galactic nuclei. II. New observations and theory of Fe II and HI emission. , 288: 94–116, Jan. 1985. doi: 10.1086/162767.
- K.-W. Wong, J. A. Irwin, D. R. Wik, M. Sun, C. L. Sarazin, Y. Fujita, and T. H. Reiprich. Suzaku X-ray Observations of the Nearest Non-Cool Core Cluster, Antlia: Dynamically Young but with Remarkably Relaxed Outskirts. , 829(1):49, Sept. 2016. doi: 10.3847/0004-637X/829/1/49.
- X.-B. Wu, F. Wang, X. Fan, W. Yi, W. Zuo, F. Bian, L. Jiang, I. D. McGreer, R. Wang, J. Yang, Q. Yang, D. Thompson, and Y. Beletsky. An ultraluminous quasar with a twelve-billion-solar-mass black hole at redshift 6.30. , 518(7540): 512–515, Feb. 2015. doi: 10.1038/nature14241.
- C. Zhang, I. Zhuravleva, A. Kravtsov, and E. Churazov. Evolution of splashback boundaries and gaseous outskirts: insights from mergers of self-similar galaxy clusters. *MNRAS*, 506(1):839–863, Sept. 2021. doi: 10.1093/mnras/stab1546.
- J. A. ZuHone, M. Markevitch, and R. E. Johnson. Stirring Up the Pot: Can Cooling Flows in Galaxy Clusters be Quenched by Gas Sloshing? , 717(2):908–928, July 2010. doi: 10.1088/0004-637X/717/2/908.
- J. A. ZuHone, M. Markevitch, and D. Lee. Sloshing of the Magnetized Cool Gas in the Cores of Galaxy Clusters. , 743(1):16, Dec. 2011. doi: 10.1088/0004-637X/743/1/16.

Vita

Arnab Sarkar

Place of Birth:

- West Bengal, India

Education:

- Presidency University, Kolkata, West Bengal
M.Sc. in Physics and Astronomy, Aug. 2016
- University of Calcutta, Kolkata, West Bengal
B.Sc. in Physics, May. 2014

Professional Positions:

- Graduate Teaching Assistant, University of Kentucky, Fall 2018–Fall 2020
- Pre-doctoral Fellow, Center for Astrophysics | Harvard & Smithsonian, Spring 2021–Fall 2022

Publications & Preprints:

- Arnab Sarkar, Yuanyuan Su, Scott Randall, Fabio Gastaldello, Isabella Trierweiler, Raymond White, Ralph Kraft, Eric Miller, “*Joint Suzaku and Chandra observations of the MKW4 galaxy group out to the virial radius,*” *Monthly Notices of the Royal Astronomical Society*, Volume 501, Issue 3, pp. 3767-3780, 2021 03.
- A. Sarkar, G. J. Ferland, M. Chatzikos, F. Guzmán, P. A. M. van Hoof, R. T. Smyth, C. A. Ramsbottom, F. P. Keenan, C. P. Ballance, “*Improved Fe II Emission-line Models for AGNs Using New Atomic Data Sets,*” *The Astrophysical Journal*, Volume 907, Issue 1, id.12, 11 pp., 2021 01.
- Arnab Sarkar, and Saumyadip Samui, “*On the Star Formation Efficiency in High-redshift Ly Emitters,*” *Publications of the Astronomical Society of the Pacific*, Volume 131, Issue 1001, pp. 074101, 2019 07.
- Gabriella E. Alvarez, Scott W. Randall, Yuanyuan Su, Arnab Sarkar, Christine Jones, William Forman, Esra Bulbul, Craig Sarazin, Elizabeth Blanton, Stephen Walker, Nicholas Lee, Kelly Holley-Bockelmann, “*Suzaku observations of the cluster outskirts and intercluster filament in the triple merger cluster Abell 98,*” *Submitted to The Astrophysical Journal*, 2022 07.